Observation of Cosmic-Ray Anisotropy at TeV and PeV Energies in the Southern Sky

By

Juan Marcos Santander

A dissertation submitted in partial fulfillment of
the requirements for the degree of

Doctor of Philosophy
(Physics)

at the
UNIVERSITY OF WISCONSIN–MADISON
2013

Date of final oral examination: June 25th, 2013

The dissertation is approved by the following members of the Final Oral Committee:

Paolo Desiati, Associate Scientist, Astronomy
Francis Halzen, Professor, Physics
Sebastian Heinz, Associate Professor, Astronomy
Albrecht Karle, Professor, Physics
Stefan Westerhoff, Professor, Physics
Ellen Zweibel, Professor, Astronomy

OBSERVATION OF COSMIC-RAY ANISOTROPY AT TEV AND PEV ENERGIES IN THE SOUTHERN SKY

Juan Marcos Santander

Under the supervision of Professor Stefan Westerhoff

At the University of Wisconsin-Madison

Cosmic rays in the TeV to PeV energy range are believed to originate in our galaxy, possibly in local astrophysical accelerators such as supernova remnants. After escaping from their sources, cosmic rays propagate through the interstellar medium where they scatter off turbulences in the Galactic magnetic field. This scattering process efficiently isotropizes the trajectories of cosmic rays before their arrival at Earth. However, it is predicted that a dipolar anisotropy with per-mille amplitude or lower should subsist in their arrival directions.

Such an anisotropy was observed for the first time at TeV energies by detectors in the northern hemisphere, and its study revealed the presence of both large angular scale structure (usually interpreted as the aforementioned dipole produced by cosmic-ray diffusion) and anisotropy with smaller angular size and amplitude.

Large-scale anisotropy at TeV energies in the southern hemisphere was detected for the first time using data from IceCube, a cubic-kilometer neutrino detector that is sensitive to muons created in the interaction of cosmic rays with the atmosphere. The orientation of the large-scale component is consistent with that observed in the north.

In this work, results from three analyses are presented which expand the study of cosmic-ray anisotropy in the southern sky and are aimed at characterizing its evolution as a function of angular scale, energy, and time. Data from three cosmic-ray detectors are used: IceCube, its predecessor experiment AMANDA, and the IceTop air-shower array, all located at the South Pole.

Significant anisotropy is observed over a wide range of angular scales (from large-scale to few-degrees structure), and energies (from 20 TeV to 2 PeV.) The relative amplitude of the large-scale anisotropy is $\sim 10^{-3}$, while smaller structures have amplitudes of the order

of 10^{-4}. No significant variation is observed in the TeV anisotropy pattern over the 12-year period considered in this work.

These studies provide a complete picture of the cosmic-ray anisotropy in the southern sky at TeV and PeV energies. The coordinated study of the three main cosmic-ray observables (spectrum, composition, and anisotropy) will provide information about the origin of these particles and the environment through which they propagate.

Stefan Westerhoff

ACKNOWLEDGMENTS

I dedicate this work to my daughters, Florencia and Ema, who have taught me the important things I did not know I ignored, and to my wife and friend, Elisa, for her constant support throughout this adventure and the many more to come.

My gratitude goes to my advisor, Stefan Westerhoff, for his guidance and support through these years. He convinced me that coming to the US to pursue a PhD was, perhaps, not such a crazy idea after all. This work would not have been possible without his steady advice and his inspiring dedication to the field of high-energy astrophysics. I would like to thank Segev BenZvi, for teaching me quite a few tricks on programming, the proper use of the English language in publications, and also for the many laughs. Many thanks go to the cosmic-ray anisotropy group in Madison. To Simona Toscano for introducing me to the subject of cosmic-ray anisotropy and teaching me the tools of the trade with patience and extreme generosity. Her contagious passion contributed to the great working atmosphere I found when I first arrived in Madison. To Paolo Desiati, for the many conversations about what the anisotropy results could mean, for the many coffee break talks, and for sharing the burden in the organization of the first anisotropy workshop in Madison in 2011. To Juan Carlos Díaz-Vélez and Juanan Aguilar for providing me with a much-needed Latin connection away from home, and also for the many talks and laughs. I would like to thank Rasha Abassi, who spearheaded this whole topic of research inside IceCube. My work would not have been possible without her pioneering effort.

It's been a pleasure getting to know so many great people in Madison. I would like to thank my fellow grad-students Jakob Van Santen, Nathan Whitehorn, Laura Gladstone, Jon Eisch, Jake Feintzeig, Chris Weaver, and Ben Riedel for their support and friendliness which

made the move from Argentina much easier to handle. On behalf of Mark Sanderson I would like to thank Dan Fiorino, Frank McNally, Zig Hampel, and Ian Wisher for all the fun.

To my parents, Laura and Walter, for endorsing my early interest in astronomy and science in general, and for supporting me through these years, even when that meant nearly freezing to death in the rooftop observatory of the San Rafael Natural History Museum waiting by the telescope while I watched. All this would not have been possible without their encouragement. To my sisters María del Mar and Ana Belén, and my grandmother Pilar, for always being there for me. To my many friends back in Argentina, Fernando, Ezequiel, Julio, Juan Pablo, Gustavo, Andrés, and many others for enduring my never-ending descriptions of the wonders of the night sky as we grew up.

This work is also dedicated to the memory of my grandfather, Juan Andrés Nieto Medina, who taught me the names of the constellations and showed me the Magellanic Clouds from the dark skies of his farm house in western Argentina when I was a kid. His passion for reading and learning, and his natural curiosity, is what got me here.

Gracias totales.

DISCARD THIS PAGE

TABLE OF CONTENTS

Page

Page

DISCARD THIS PAGE

LIST OF TABLES

DISCARD THIS PAGE

LIST OF FIGURES

Figure Page

Chapter 1

Cosmic Rays

1.1 Introduction

Our planet is constantly bombarded by a steady flux of energetic particles that originate somewhere in outer space. The existence of these particles, known as cosmic rays, was discovered by the Austrian physicist Victor Hess (Nobel Prize 1936) in a series of ballon flights conducted in 1912 [1]. During these flights, Hess used electroscopes to measure the level of ambient ionizing radiation as his balloon ascended to altitudes of up to 5 km. The level of radiation decreased during the first kilometer of the ascent, indicating that a fraction of the total ambient radiation originated from the ground below, but, as the balloon soared, the electroscopes showed that radiation increased steadily with altitude. This observation, later confirmed by higher-altitude flights performed by Kolhörster, led Hess to postulate that the source of this ionizing radiation had to be located somewhere outside the Earth's atmosphere.

During the first decades of cosmic ray research a lot of controversy surrounded the nature of the newly-discovered particles. Robert Millikan, who had coined the term "cosmic ray," supported the idea that cosmic rays were gamma rays, while Arthur Compton believed that they were charged particles. This lead both scientists to engage in a series of fierce debates that made it to the front page of the New York Times a total of 202 times between 1926 and 1939. In 1927, Jacob Clay from TU Delft, who had conducted balloon soundings

from the island of Java, observed a dependence of the cosmic ray flux on geomagnetic latitude. This discovery provided the first real evidence that, since cosmic rays are affected by magnetic fields, they had to be electrically charged. In 1929, Bothe and Kohlhörster developed a technique that used Geiger-Müller counters (invented the year before) operating in coincidence to study cosmic rays. Their measurements confirmed that cosmic rays are charged, and also indicated the presence of a very penetrating component in the cosmic ray flux. A key improvement to the coincidence method was introduced by Bruno Rossi in 1930, who developed an electronic circuit to tag coincident detections in order to replace the mechanical-photographic method used by Bothe and Kolhörster. During the same year, Rossi predicted and measured (together with Johnson, Alvarez, and Compton) an asymmetry in the number of particles arriving from the West. The observation of this *East-West* effect was a strong indication that most cosmic ray particles have a positive charge. Further studies carried out by Rossi in 1933 using lead absorbers of variable thickness confirmed the existence of a soft and a penetrating component in the particle flux measured at sea level.

In 1934, Rossi discovered that *air showers* of particles can simultaneously reach detectors even when placed far apart. Measurements performed by Pierre Auger in 1938 [2] using counters and cloud chambers placed in high altitude laboratories in the Alps revealed the existence of *extensive air showers* of particles in the atmosphere. The discoveries of Rossi and Auger indicated that most particles reaching ground were in fact secondary particles produced in the interaction of primary cosmic rays with atoms at the top of the atmosphere. Auger estimated that a primary cosmic ray should have an energy of more than 10^{15} eV to produce the particle density observed at ground, which Auger understood was so high that "it is actually impossible to imagine a single process able to give to a particle such an energy". In 1948, Fermi proposed an acceleration mechanism that would allow cosmic rays to reach these extreme energies.

Early cosmic ray studies also led to important discoveries in particle physics. Until the advent of high-energy particle accelerators, cosmic rays were used as a natural beam to search for new particles. This line of research led to the discovery of the positron (Anderson,

1932), the muon (Anderson, 1936), the pion (Lattes, Powell, and Occhialini, 1947), and the kaon (Rochester, 1947.)

A great source of information on the early stages of cosmic ray research is the compilation presented in [3], which includes many first-hand accounts from the main actors like Rossi, Auger, and Hess.

By the end of the first century of cosmic-ray physics, a lot of progress has been made in understanding the main characteristics of cosmic-ray particles, such as their composition and energy spectrum. Identifying the sources of cosmic rays, however, remains an enduring problem in astrophysics.

It must be noted that, although the term "cosmic ray" applies basically to any energetic particle reaching the Earth from space, in this work it will be used only to describe charged particles with energies higher than $\sim 10^{10}$ eV. Above this energy, the number of cosmic rays accelerated by the Sun is minimal, and the screening effect of the solar wind on cosmic rays (i.e. the so-called *solar modulation* effect) is negligible.

In this chapter, a summary of the main observable features of cosmic rays is presented, as well as a description of the theorized acceleration mechanisms involved in their origin and details about their propagation from their sources.

1.2 Energy Spectrum

Cosmic rays are the most energetic particles known in the Universe. The highest energy cosmic ray ever detected had an estimated energy of 3×10^{20} eV (750 TeV in the center-of-mass) [4], which corresponds to an energy eight orders-of-magnitude (two in the center-of-mass) higher than the energy of protons accelerated at the Large Hadron Collider.

The energy spectrum of cosmic rays, shown in Fig. 1.2, spans ten orders of magnitude in particle energy and about thirty orders of magnitude in flux. The energy dependence of the spectrum can be described as a power law of the form $A\,E^{-\gamma}$, where E is the primary cosmic-ray energy, γ the spectral index, and A is a normalization factor.

The spectrum is remarkably smooth given its wide energy range, but some changes in the spectral slope are observed [5, 6, 7] at different energies, the most important ones are given below:

$$\gamma = \begin{cases} 2.67 & \log(E/GeV) < 6.4, \\ 3.10 & 6.4 < \log(E/GeV) < 9.6, \\ 2.6 & 9.6 < \log(E/GeV). \end{cases}$$

At energies around 3×10^{15} eV [6], there is a spectral softening usually referred to as the cosmic ray "knee." It is believed that cosmic rays up to this energy originate inside our galaxy and that the change in spectral index is associated with a change in the chemical composition of the cosmic ray particles which will be discussed in the next Section. Another important feature is a spectral hardening at an energy of a few EeV, known as the "ankle." Based on magnetic confinement arguments, it is believed that cosmic rays with energies beyond the ankle cannot be contained by the magnetic field of the galaxy and therefore this break could mark the transition between Galactic and extragalactic cosmic rays.

A strong suppression in the flux is observed at energies above 4×10^{19} eV [8]. A spectral cutoff of this nature was originally theorized in 1966 and is known as the Greisen-Zatsepin-Kuz'min (GZK) limit [9, 10]. At energies higher than the GZK cutoff ($\sim 6 \times 10^{19}$ eV), protons lose energy through pion-production as they scatter off 2.7K Cosmic Microwave Background (CMB) photons through the Δ^+ resonance in one of the following interactions:

$$p + \gamma_{\mathrm{CMB}} \rightarrow \Delta^+ \rightarrow n + \pi^+$$
$$p + \gamma_{\mathrm{CMB}} \rightarrow \Delta^+ \rightarrow p + \pi^0.$$

This process limits the mean free path of protons with energies higher than the cutoff to a few tens of Mpc. Although the energy of the observed cutoff agrees well with the expectation for the GZK effect, it is still possible that the cutoff occurs at the source, since it is difficult to accelerate particles to these extreme energies.

The steeply-falling nature of the spectrum has important consequences for the experiments designed to measure the cosmic-ray flux at different energies. At around 10^{12} eV,

the flux corresponds to about one incident particle per square meter per second. This particle rate allows the construction of small detectors that can be mounted on balloons or spacecrafts to detect primary cosmic rays directly. Recent examples of these detectors are the CREAM balloon experiment [11], designed to measure the chemical composition and spectrum of cosmic rays up to PeV energies, and the AMS-02 detector onboard the International Space Station [12], designed to carry out precision measurements of the leptonic and hadronic components of the cosmic-ray flux.

At energies above several hundred TeV, cosmic rays are detected indirectly through the extensive air showers that they produce in the atmosphere. When a primary cosmic ray interacts at the top of the atmosphere with an air molecule, secondary particles such as pions and kaons are produced (with pions being the dominant component). This is shown schematically in Fig. 1.1.

Charged pions decay weakly through leptonic channels into muons (branching ratio: 0.999877) and electrons (branching ratio: 0.000123) accompanied by neutrinos of the corresponding flavor. The predominant muons in charged pion decays compose the hard, or penetrating component of the particle shower.

$$\begin{aligned} \pi^+ &\rightarrow \mu^+ + \nu_\mu \\ &\rightarrow e^+ + \nu_e \\ \pi^- &\rightarrow \mu^- + \bar{\nu}_\mu \\ &\rightarrow e^- + \bar{\nu}_e \end{aligned}$$

Neutral pions, on the other hand, decay through the electromagnetic force to two photons ($\pi^0 \rightarrow \gamma+\gamma$), which can then produce positron-electron pairs ($\gamma \rightarrow e^+ + e^-$). New photons are generated either through bremsstrahlung induced by electrons, or through the annihilation of positrons with atmospheric electrons. This process continues until the photon energy falls below the threshold for pair-production (~ 1 MeV) and other electron energy losses start to dominate. These particles make the electromagnetic component of the shower.

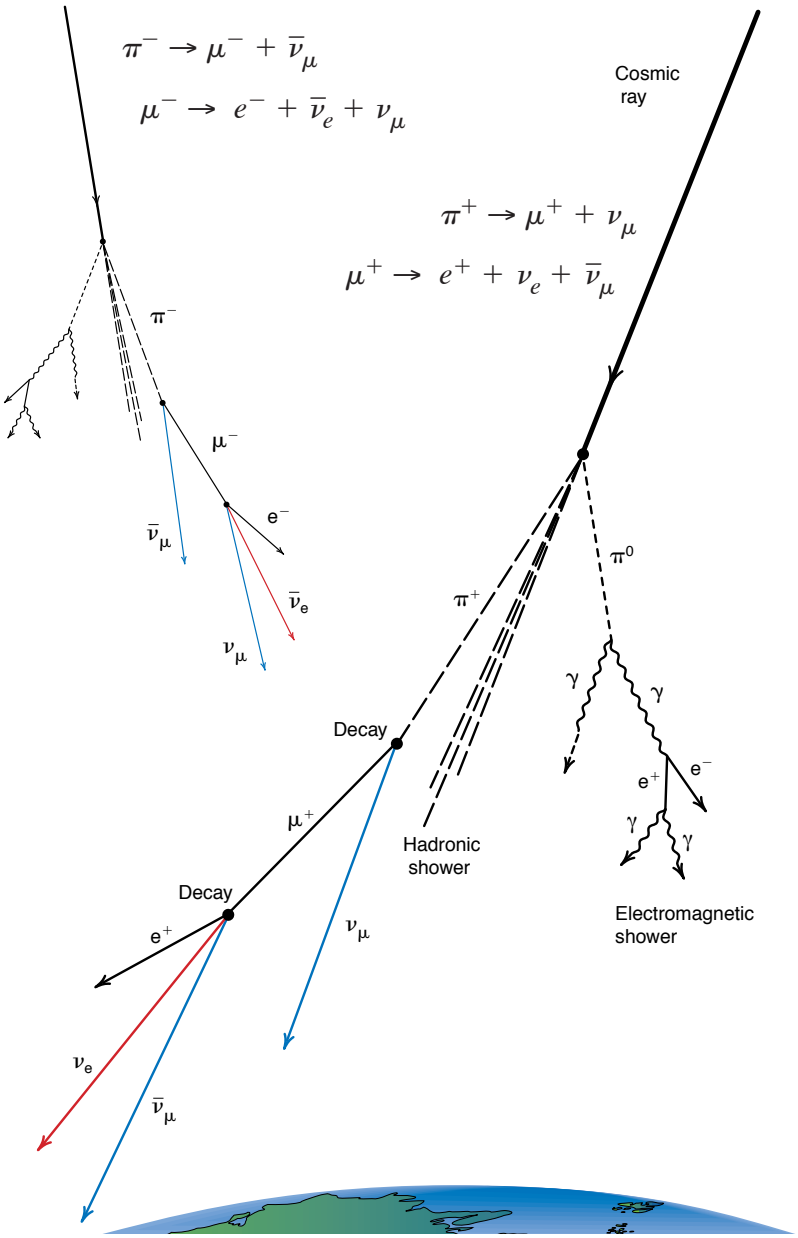

Figure 1.1: Schematic representation of an extensive air shower. The interaction of the primary cosmic ray with a molecule in the Earth's atmosphere produces high-energy pions. Charged pions decay to neutrinos and muons which in turn can decay to lighter leptons. Neutral pions decay electromagnetically to photons which can pair-produce in the atmosphere creating the electromagnetic component of the shower. (Source: Los Alamos Science, 25, 1997.)

Due to the large momentum of the incoming primary particles and the relative low density of targets in the atmosphere, extensive air showers have a small transversal size compared to their longitudinal extension. As the shower develops in the atmosphere, a particle front consisting of secondary muons and electrons travels towards the ground at speeds very close to the speed of light. The ensemble of these secondary particles retains the incoming direction of the primary particle.

The detection of extensive air showers enables the reconstruction of the energy, composition, and incoming direction of cosmic rays up to the highest energies. For this purpose, large arrays of particle detectors (air shower arrays) are deployed in regular patterns over large extensions of land. The area covered by air shower arrays is related to the energy range that they are designed to study. At energies higher than the GZK cutoff, the cosmic ray flux corresponds to one particle per square kilometer per century. Experiments designed to detect such small fluxes need an effective area of hundreds or thousands of square kilometers. The largest experiment of this kind is the Pierre Auger Observatory, located in Argentina, with a total area of 3000 km^2 [13].

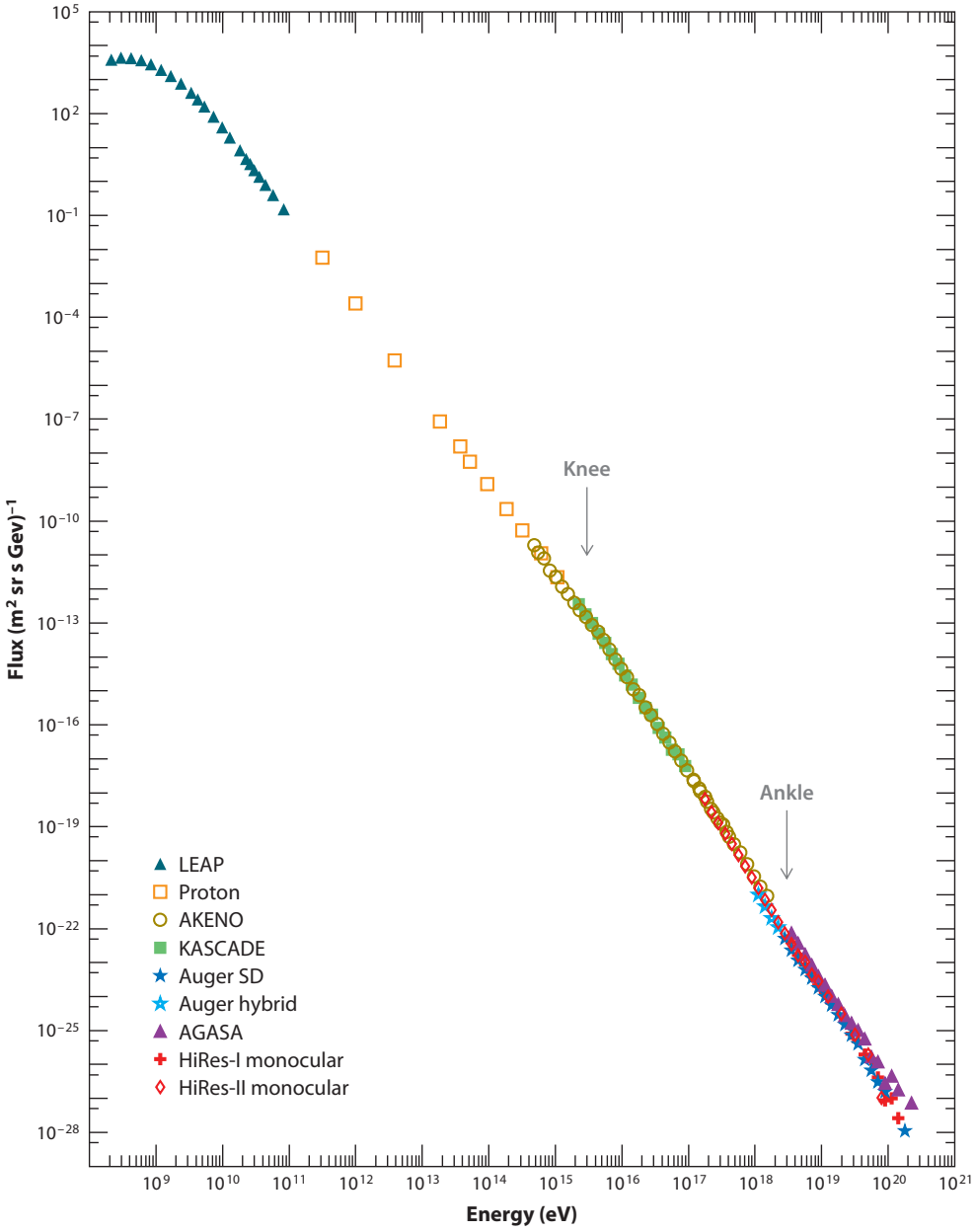

Figure 1.2: The cosmic-ray energy spectrum as measured by ground-based air-shower experiments [14]. The overall behavior of the spectrum can be characterized as a simple power law with a series of spectral breaks, the most important two being an spectral softening commonly known as the *knee* at about 3 PeV, and a spectral hardening known as the *ankle* at about 4 EeV. At energies higher than 10^{20} eV a strong suppression in the flux is observed.

1.3 Composition

Cosmic rays consist of two populations of particles: a predominant hadronic component (99%), and a small fraction of high-energy electrons and positrons (1 %). The composition of the hadronic component is dominated by protons ($\sim$ 85%), followed by helium nuclei ($\sim$ 12%), while elements with $Z > 2$ contribute with the remaining 3% of the flux. The abundance of chemical elements in the cosmic ray flux matches the chemical composition of the solar system (Fig. 1.3) except for elements like lithium, beryllium, and boron ($Z = 3-5$), and those with $Z = 20-25$ where cosmic ray abundances are larger. These secondary cosmic rays originate in the fragmentation of stable and abundant primary nuclei such as carbon ($Z = 6$), oxygen ($Z = 8$), and iron ($Z = 26$) in spallation processes that occur in the interstellar medium. The ratio of secondary to primary abundances provides information about the propagation of cosmic rays in the galaxy, and will be discussed in Section 1.6.

Recent balloon measurements [11] indicate that protons dominate the flux up to about 10 TeV. A hardening in the helium spectrum above 200 GeV makes it dominant at higher energies.

A change in composition as a function of energy is consistent with current theories of cosmic ray confinement in the galaxy. The Milky Way is known to be permeated by a large scale magnetic field that has a strength of about 2 μG in the vicinity of the Sun [16]. The Larmor radius r_g (in pc) for cosmic rays with momentum p (in TeV/c), and elemental charge Z in a magnetic field of strength B (in μG) is given by:

$$r_g = 1.1 \times 10^{-3}\ \mathrm{pc}\left(\frac{p}{\mathrm{TeV/c}}\right)\frac{1}{|Z|}\left(\frac{B}{\mu\mathrm{G}}\right)^{-1}\ . \tag{1.1}$$

As the gyroradius increases linearly with energy, higher energy particles escape the galaxy more easily as their trajectories are less deflected. This energy-dependent escape probability is thought to be the cause for the existence of the knee in the cosmic ray spectrum. Since the Larmor radius is a function of particle rigidity ($R = p/|Z|$), the location of the knee in energy should be different for different chemical elements (i.e. for different values of

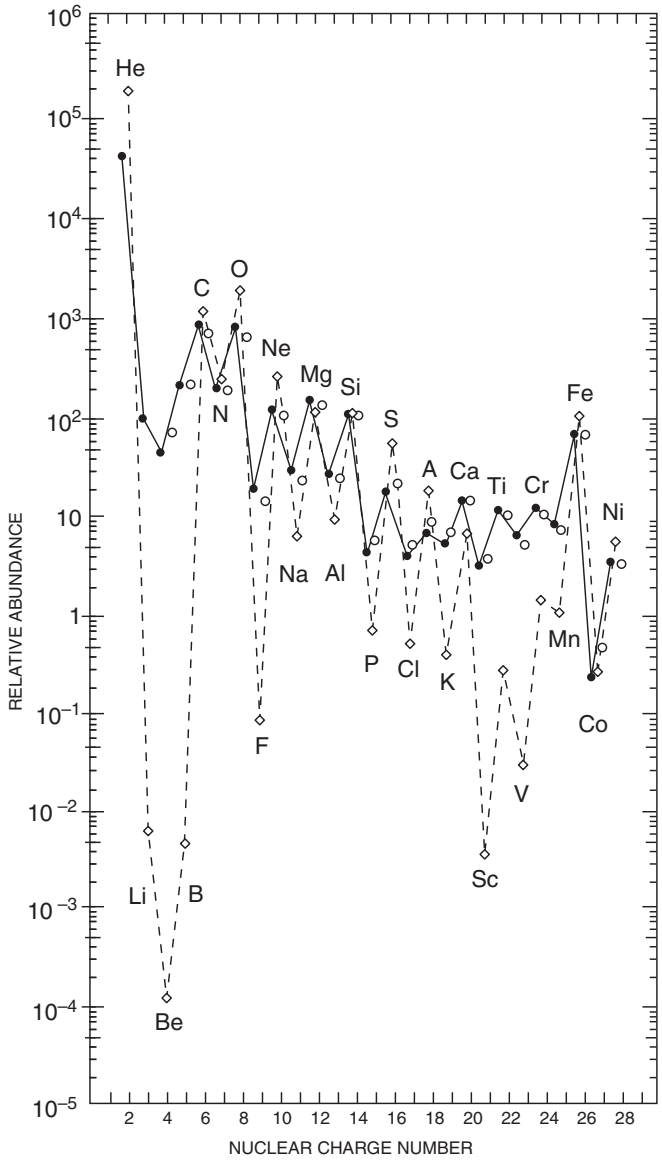

Figure 1.3: Comparison between the chemical composition of low-energy Galactic cosmic rays (solid line) and the abundances measured in the solar system (dashed line) [15]. A good agreement is found for most elements, but beryllium and boron are overabundant in the cosmic ray flux. This is caused by spallation processes on carbon nuclei that fill the Li-B "valley". A measurement of the B/C ratio as a function of energy provides information on cosmic ray propagation.

Z). This rigidity-dependence implies that the composition of Galactic cosmic rays should become heavier in the knee region, as heavier elements experience a spectral softening at higher energies. Data from air shower arrays, which are sensitive to the mean logarithmic mass of the primary particles $\langle \ln(\mathrm{A}) \rangle$, indicates that such a transition to heavier elements indeed occurs [17, 18] as is shown in Fig. 1.4. Several models exist in the literature [19, 20] that were designed to explain the spectral structure of the knee and the primary composition in this energy range.

At higher energies, near the ankle region ($E \sim 3 \times 10^{18}$ eV) where extragalactic cosmic rays are expected to become dominant, the composition turns light once again and is consistent with a proton-dominated flux. At the highest observable energies ($> 10^{19}$ eV) the results are so far inconclusive. While the Auger Collaboration has reported a composition consistent with iron nuclei [21], the Telescope Array collaboration has indicated that their measurements agree well with a proton-only composition [22]. Important systematic uncertainties in these measurements are due to the lack of knowledge about hadronic interactions at center-of-mass energies higher than several TeV. A compilation of ultra-high energy measurements is available in [23], the results from different experiments have been converted to $\langle \ln(\mathrm{A}) \rangle$ values and are shown in Fig. 1.4.

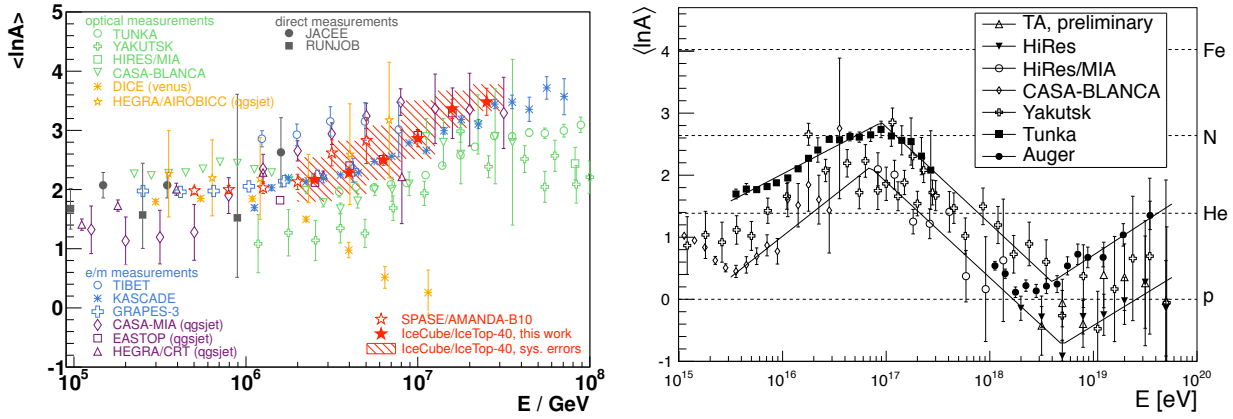

Figure 1.4: Measurements of cosmic-ray chemical composition in terms of mean logarithmic mass $\langle \ln(A) \rangle$ as a function of energy for different experiments [17]. The region around the cosmic ray knee is shown on the left ($10^{14} - 10^{17}$ eV). On the right, the value of $\langle \ln(A) \rangle$ is shown for several detectors operating at ultra-high energies. In this case, the mean logarithmic mass depends strongly on the high-energy hadronic model used to interpret the results (QGSJET01 is used for this figure, more details in [23]).

1.4 Acceleration Mechanisms

An important theoretical challenge that was recognized early on in cosmic ray research was the identification of processes that could accelerate particles up to the extreme energies observed in the cosmic ray flux. In 1949, Enrico Fermi theorized a mechanism [24] for particles to gain energy through their interaction with magnetized clouds in interstellar space.

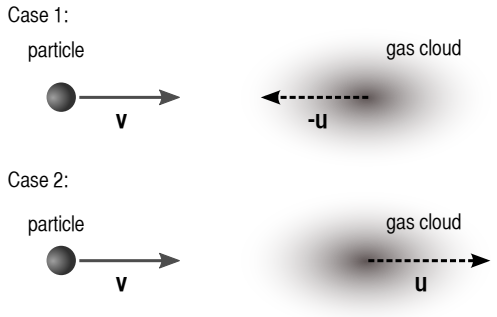

Figure 1.5: Schematic representation of the energy gained by a particle through second-order Fermi acceleration. (Adapted from [25].)

Let us assume that a charged particle of mass m that moves through space with velocity $\mathbf{v}$ is magnetically reflected by a gas cloud of mass M (where $M \gg m$) moving with velocity $\mathbf{u}$. If $\mathbf{u}$ and $\mathbf{v}$ are antiparallel (case 1 in Fig. 1.5, the increase in the energy of the particle in the non-relativistic case is given by:

$$\Delta E_1 = \frac{1}{2}m(v+u)^2 - \frac{1}{2}mv^2 = \frac{1}{2}m(2uv+u^2)\ . \tag{1.2}$$

For case 2 in Fig. 1.5 (where $\mathbf{u}$ and $\mathbf{v}$ are parallel) the particle experiences an energy *decrease*, which can be calculated as:

$$\Delta E_2 = \frac{1}{2}m(v-u)^2 - \frac{1}{2}mv^2 = \frac{1}{2}m(-2uv+u^2)\ \ . \tag{1.3}$$

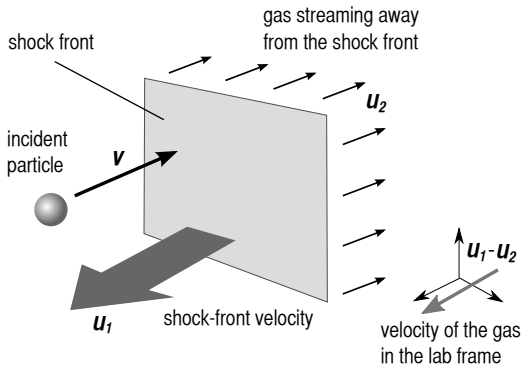

Figure 1.6: Schematic representation of the energy gained by a particle through first-order Fermi acceleration. (Adapted from [25].)

On average, the particle gains energy, since $\Delta E = \Delta E_1 + \Delta E_2 = mu^2$. This results in a relative energy increase of

$$\frac{\Delta E}{E} = 2\left(\frac{u}{v}\right)^2 \quad . \tag{1.4}$$

Since the energy gain is quadratic in the velocity of the particle, this process is known as *second order Fermi acceleration*. Due to the low cloud velocities ($u \ll v \sim c$), the energy gain per collision is very small ($\propto u^2$) which implies that this process requires very long times to accelerate particles. Due to energy losses that may occur between collisions, this mechanism is only efficient for particles with a minimum injection energy. The injection energy could be provided by a different process, such as acceleration in astrophysical shocks.

In Fig. 1.6, an idealized representation of the interaction of a particle with a shock is shown. The shock travels through the interstellar medium with velocity u_1, while gas recedes from the shock with velocity u_2, which means that the gas has a lab-frame velocity $u_1 - u_2$.

The increase in energy of a particle moving with velocity v towards the shock and being reflected is:

$$\begin{aligned} \Delta E &= \tfrac{1}{2}m(v+(u_1-u_2))^2 - \tfrac{1}{2}mv^2 \\ &= \tfrac{1}{2}m(2v(u_1-u_2)+(u_1-u_2)^2) \\ &\approx mv(u_1-u_2) \quad , \end{aligned} \tag{1.5}$$

where the simplification in the last step is due to the fact that $v \gg u_1, u_2$, which makes the linear term dominate. The relative energy increase $\Delta E/E$ is then simply $2(u_1-u_2)/v$; a full relativistic treatment changes the final result to $4(u_1-u_2)/3c$. Since the final energy increase is linear in the velocity of the gas in the lab-frame, this process is known as *first order Fermi acceleration*, even though it was not originally postulated by Fermi. Particles can be accelerated to energies of up to 100 TeV through this process, which provides the second order mechanism with the required injection energy to go to higher energies.

If we assume that in every interaction with the shock the particle experiences a small fractional increase ϵ in its original energy E_0, the energy after n collisions would be $E_n = E_0(1+\epsilon)^n$. To reach energy E_n, the number of collisions needed is

$$n = \frac{\log E_n/E_0}{\log 1+\epsilon} \quad . \tag{1.6}$$

If there is a certain probability p_e of escaping the acceleration region in every encounter, the probability of the particle not escaping after n collisions is $(1-p_e)^n$. This implies that the number of particles accelerated to energies higher than E is

$$N(\geq E) \propto \sum_{m=n}^{\infty}(1-p_e)^m \sim \frac{(1-p_e)^n}{p_e} \quad . \tag{1.7}$$

Combining Eq. 1.4 and Eq. 1.7 leads to the integral energy spectrum

$$N(\geq E) \propto \frac{1}{p_e}\left(\frac{E}{E_0}\right)^{-\alpha} \quad , \tag{1.8}$$

where

$$\alpha = \log \frac{1}{1-p_e} / \log(1+\epsilon) \sim \frac{p_e}{\epsilon} \quad . \tag{1.9}$$

For the case of shock acceleration,

$$\alpha = \frac{p_e}{\epsilon} = \frac{3}{u_1/u_2 - 1} \quad . \tag{1.10}$$

The shock is only formed for supersonic flows where u_1 is larger than c_1, the sound speed of the gas. In other words, the Mach number of the flow M has to be larger than unity, where $M = u_1/c_1$. The mass continuity of the gas on both sides of the shock ensures that $\rho_1 u_1 = \rho_2 u_2$. Combining this equation with the kinetic theory of the gases, we arrive at

$$\frac{u_1}{u_2} = \frac{\rho_2}{\rho_1} = \frac{(c_p/c_v + 1)M^2}{(c_p/c_v - 1)M^2 + 2} \quad , \tag{1.11}$$

where c_p/c_v for a monoatomic gas is 5/3. Replacing the above equation for u_1/u_2 into Eq. 1.10, we obtain

$$\alpha \approx 1 + \frac{4}{M^2} \quad . \tag{1.12}$$

For strong shocks, $M \gg 1$ which results in $\alpha \sim 1$. The differential spectral index is ~ 2, which is close to the measured value of the cosmic ray spectral index γ of ~ 2.7 discussed in Section 1.2. The difference between the spectral index at the source and that observed at Earth is believed to be related to propagation effects that will be discussed in Section 1.6.

1.5 Candidate Sources of Cosmic Rays

In order to accelerate particles to high energies, not only powerful shocks are needed but also strong magnetic fields that can confine the particles while being accelerated. Once the Larmor radius of a particle is comparable to the size of the acceleration region, the probability of escape from the region increases significantly. This relation between maximum achievable

energy $E_{\max}$, size R, and magnetic field strength B is known as the "Hillas criterion" [26], which can be expressed as

$$E_{\max} \sim 10^{18}\text{eV}\ \beta_s\ Z \left(\frac{B}{\mu\text{G}}\right) \left(\frac{R}{\text{kpc}}\right) \ , \tag{1.13}$$

where Z is the cosmic ray charge, β_s is the velocity parameter of the shock wave. This relation is represented graphically in Fig. 1.7, where several types of astrophysical objects are shown according to their potential to accelerate cosmic rays up to energies of $\sim 10^{20}$ eV or higher.

The production of ultra-high energy cosmic rays through their acceleration in astrophysical sources is known as the "bottom-up" scenario. More exotic "top-down" scenarios exist where ultra-high energy cosmic rays (UHECRs) are created in the decay of high-mass topological defects left as relics from phase transitions after the Big Bang, or super-heavy dark matter particles. Top-down models usually predict an important flux of ultra-high energy gamma rays and neutrinos associated with the creation of cosmic rays, and have been constrained using data from air-shower arrays [28].

The search for sources of cosmic rays is performed in two different ways: either directly by searching for correlations in the arrival direction of cosmic rays, or indirectly by looking for high-energy neutrino or gamma-ray emission that would reveal sites where high-energy hadronic interactions are taking place. Both approaches have advantages and draw-backs.

Direct detection is only possible at ultra-high energies (above 10^{19} eV) where the magnetic deflection experienced by charged cosmic rays propagating through the magnetic field of the galaxy is below a few degrees [14, 29]. This is the goal of large air-shower arrays like Telescope Array and the Pierre Auger Observatory. The down side to this detection technique is that, as was already mentioned, the fluxes are very low at ultra-high energies, and also that ambient cosmic rays lose energy as they propagate through the cosmic microwave background. Recent results on the search of ultra-high energy cosmic ray sources will be presented in Section 1.7.

If the density of target nucleons around a cosmic-ray source is high, high-energy neutrino emission is expected as protons or nuclei interact with the medium producing mesons that

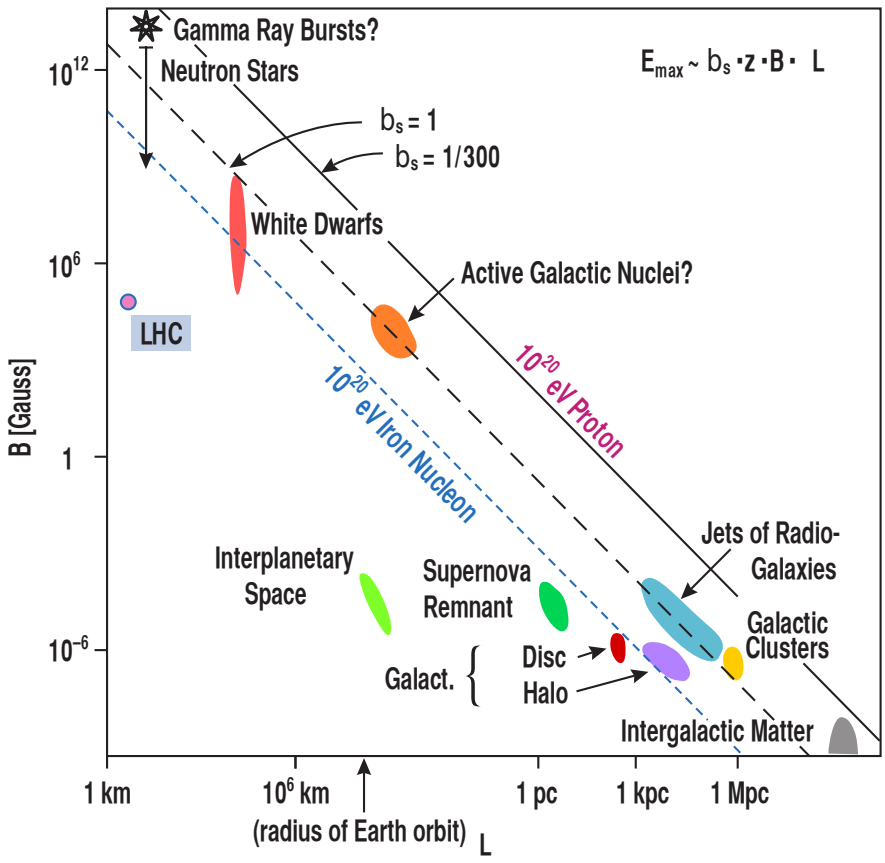

Figure 1.7: Hillas diagram indicating different classes of astrophysical objects capable of accelerating cosmic rays up to very high energies. The maximum energy that can be achieved while containing particles in the acceleration region depends on the size of the source and its magnetic field strength. (Adapted from [27].)

subsequently decay to neutrinos. Since neutrinos are electrically neutral, they experience no magnetic deflection and therefore can point back to their sources. Their interaction probability is very small given their weak cross-sections, which allows them to propagate without absorption over cosmological distances. The small cross-section, however, also represents a challenge to their detection. This is the reason why astrophysical neutrino detectors, like IceCube or the proposed KM3NET, require volumes of at least 1 km^3 to reach reasonable sensitivities [30]. Muons and neutrinos from cosmic-ray interaction in the atmosphere represent a high background for this search technique.

The neutrino emission from charged meson decays at the source should be accompanied by gamma rays produced in the decay of neutral pions [31]. By studying the spectral characteristics of the gamma-ray emission from known sources it is possible to determine if pion decays (and hence, hadron acceleration) is taking place at the source. This kind of search is conducted in the GeV range with the Large Area Telescope onboard the Fermi gamma-ray satellite [32], and in the TeV range using ground-based Imaging Air Cherenkov Telescopes (IACTs) such as VERITAS, HESS, or MAGIC.

The main challenge for this search technique is that the pion decay signature can be overwhelmed by inverse Compton emission at the source which is purely leptonic in origin. Also, gamma rays above GeV energies experience energy losses through pair-production on infrared photons from the Extragalactic Background Light (EBL), which significantly reduces their mean-free-path. The recent discovery of hadronic emission from supernova remnants in our galaxy by Fermi [33] shows promise for this search method.

1.5.1 Galactic Sources

Supernova explosions in our galaxy produce powerful shocks capable of accelerating particles to high energies. The possible connection between supernovae and cosmic rays was first suggested in 1934 by Baade and Zwicky [34], and further developed by Ginzburg and Syrovatskii [35]. The energy density of Galactic cosmic rays in our galaxy is ~ 1 eV/cm^3. Assuming a typical cosmic-ray escape time of 6×10^6 years, the power needed to fill the

Galactic disk (volume $\sim 4 \times 10^{66}$ cm^3) with cosmic rays is approximately 5×10^{40} erg/s. Type II (core collapse) supernovae can eject several solar masses of material with bulk velocities of around 5×10^7 m/s. This corresponds to a total kinetic energy of around 10^{51} ergs, meaning that the power delivered by all Type II supernova is $\sim 3 \times 10^{42}$ erg/s, given a supernova rate of about three explosions per century in the galaxy. There are large uncertainties in this order-of-magnitude estimates, but even with a cosmic-ray efficiency of just a few percent, supernova remnants (SNRs) are important candidates for Galactic cosmic ray sources. The Fermi collaboration has recently reported [33] on the observation of gamma-ray emission from two Galactic SNRs (W44, shown in Fig. 1.8, and IC443) that is consistent with neutral pion decays. This represents the first evidence for hadronic acceleration in a SNR, although only for GeV protons.

Since hadronic emission is linked with harder gamma-ray spectra, it is expected that sources with significant emission in VHE gamma rays (i.e. at TeV energies) may be cosmic ray accelerators. The Milagro gamma-ray detector observed a significant number of extended gamma-ray emission regions distributed along the galactic plane, specially in the direction of the constellation Cygnus [36]. Imaging Air Cherenkov Telescopes such as MAGIC, HESS, and VERITAS have identified a total of 144 sources of TeV gamma-rays (including extragalactic objects) [37]. A source catalog is available through the TeVCat website[1]. The location in the sky of the Galactic sources in TeVCat and their place in the galaxy relative to the Sun is shown in Fig. 1.9.

1.5.2 Extragalactic Sources

Two classes of objects, Gamma Ray Bursts (GRBs) and Active Galactic Nuclei (AGN), have for a long time been considered as the most likely candidates for the sources of UHECRs. However, if the composition near the GZK cutoff is heavy, as the Pierre Auger Observatory data seems to indicate, it is very unlikely that these cosmic rays could have come from GRBs. GRBs produce a huge number of MeV gamma rays, and any atomic nucleus that

[1] http://tevcat.chicago.edu

Figure 1.8: Candidate sources of cosmic rays. *Left:* Composite image of the SNR W44. The colors indicate regions with X-ray (blue), radio (orange), infrared (red), and gamma-ray (magenta) emission. Credit: NASA/DOE/Fermi LAT Collaboration, ROSAT, JPL-Caltech, and NRAO/AUI. *Right:* Composite image of the nearest Active Galactic Nucleus, the Centaurus A radio galaxy. Sub-millimeter data (orange) show the jets and radio lobes emanating from the galaxy center. X-ray (blue) and optical (true color) data are also shown. Credit: ESO/WFI (Optical); MPIfR/ESO/APEX/A.Weiss et al. (submillimeter); NASA/CXC/CfA/R.Kraft et al. (X-ray)

could remain in its vicinity long enough to be accelerated to ultra-high energies will most likely photo-dissintegrate into its constituent protons and neutrons before escaping.

Even if ultra-high energy cosmic rays consist mostly of protons, photon-proton interactions in the GRB fireball should produce TeV neutrinos detectable by neutrino telescopes such as IceCube. A recent analysis of IceCube data shows no neutrino emission associated with GRBs, which heavily constraints neutrino emission models from GRBs and also their contribution to the cosmic ray flux near GZK energies [38]. AGN are still considered potential sources of extragalactic cosmic rays. Recent correlation studies between the arrival directions of UHECRs and nearby AGNs will be discussed in Section 1.7.

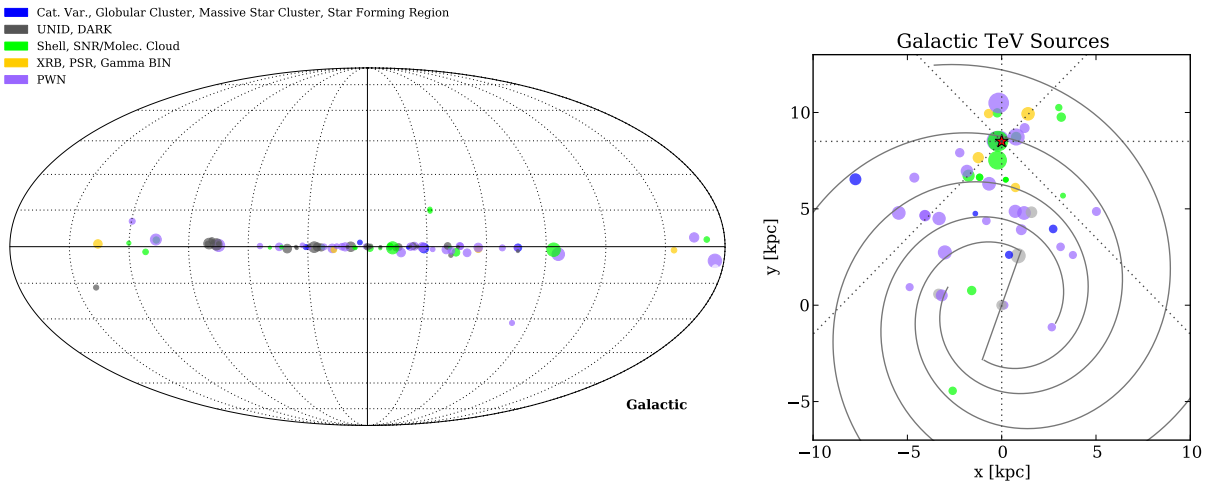

Figure 1.9: *Left:* Sky map in Galactic coordinates of known Galactic sources of TeV gamma-rays included in TeVCat. The legend indicates the type of source. Galactic longitude is $-180°$ on the right edge of the map and increases towards the left. *Right:* Location in the galaxy of each known TeV gamma-ray source for which a distance has been determined. The red star represents the location of the Sun. (Credit: S. BenZvi).

1.6 Propagation

As cosmic rays propagate over long distances from their sources, they interact with magnetic fields, dust, background photons, and other contents of the medium. As they reach Earth, cosmic rays carry information about the characteristics of the medium through which they have propagated. The propagation of Galactic and extragalactic cosmic rays is discussed in this section, as well as its observables. A review of cosmic-ray propagation in the galaxy is available in [39], while a more in-depth discussion about certain aspects of the diffusion approximation is given in the classical work of Berezinskii et al. [40], and also in [41] and [42].

1.6.1 Propagation of Galactic Cosmic Rays

Our home galaxy, the Milky Way, is a vast collection of about 100,000 million stars, dark matter, dust, and gas held together by gravity. The galaxy has a disc shape with a radius of about 15 kpc and a width of 300 pc. Our Solar System is located on one of the spiral arms that stretch outwards from the Galactic center, located at a distance of about 8 kpc from us. A schematic view of the galaxy is shown in Fig. 1.10.

Measurements of starlight polarization, Zeeman splitting, and Faraday rotation indicate that the galaxy is permeated by a large-scale magnetic field with a strength of about 2 μG oriented along the spiral arms. This "regular component" of the field is accompanied by a turbulent component of almost the same strength but with a shorter characteristic scale of the order of 10-100 pc. The energy density of the magnetic field is $\sim 0.4 \times 10^{-12}$ erg/cm^3, which is comparable to the cosmic-ray energy density of 1.5×10^{-12} erg/cm^3.

The magnetic field and the ionized gas of the galaxy form a magnetohydrodynamic (MHD) fluid through which Alfvén waves can propagate, where magnetic line tension provides the restoring force and the density of the ionized gas provides the inertia to the medium. The streaming of cosmic rays can generate Alfvén waves which can then act as scattering centers for cosmic rays.

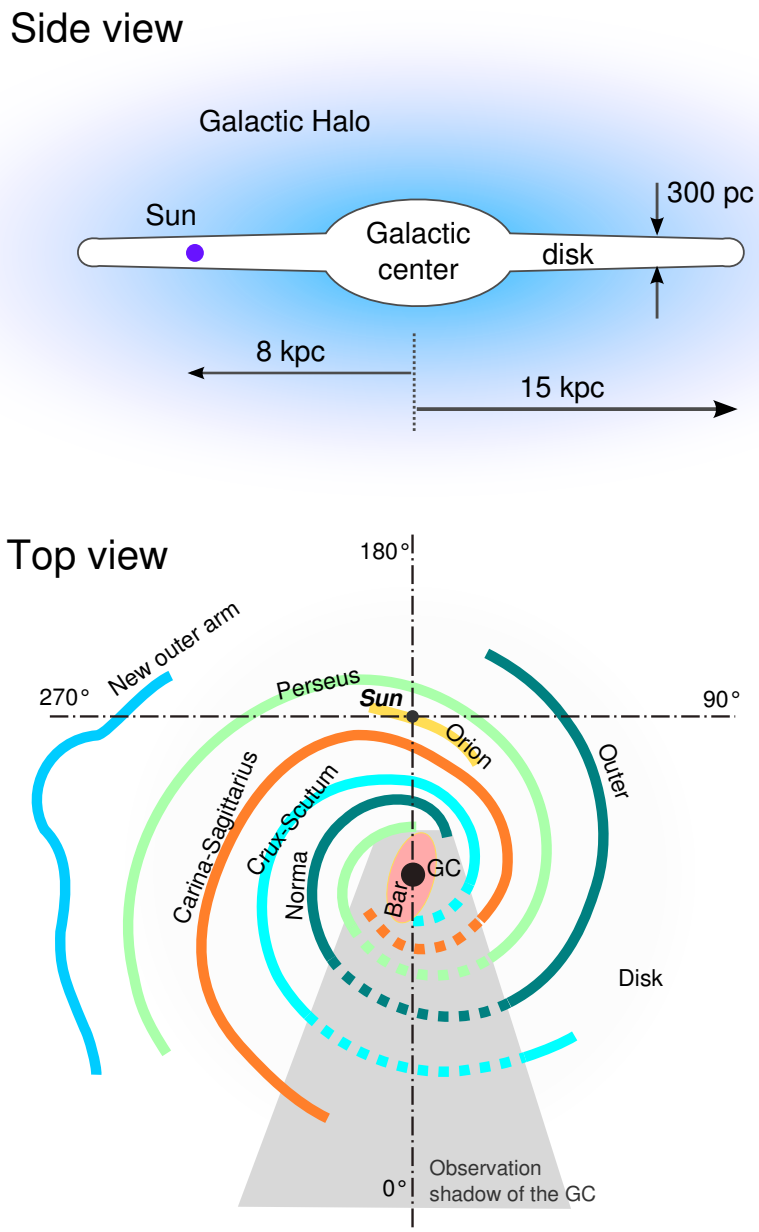

Figure 1.10: Simplified model of the structure of the Milky Way galaxy.

A significant part of our current knowledge of the propagation of cosmic rays in the galaxy comes from the study of their chemical abundances. Using spallation cross sections, it is possible to estimate the amount of matter that primary cosmic rays need to traverse in order to account for the observed secondary abundances. Data indicates that, on average, a cosmic ray travels through $6 - 10$ g/cm^2 before reaching the top of the Earth's atmosphere. Since the column depth along the Galactic plane is of the order of 10^{-3} g/cm^2, this means that Galactic cosmic rays have long confinement times of the order of several million years. The high level of isotropy in Galactic cosmic rays (discussed in Section 1.7) also favors long confinement times over which the cosmic rays trajectories are scrambled by the Galactic magnetic field. The evolution of the secondary-to-primary ratio indicates that higher energy cosmic rays travel through less matter than low energy ones. This observation has two important consequences: high energy cosmic rays have shorter confinement times (because they sense less matter), and also that propagation and acceleration are two separate processes that occur in distinct places (otherwise a constant ratio would be expected.)

Over the years, several propagation models of varying degree of sophistication have been postulated where cosmic rays perform random walks in the galaxy as a way of producing long storage times compatible with those derived from the data. One of the early models is the so-called "leaky box approximation," which is considered outdated nowadays but has interesting properties. In the leaky box model, the distribution of cosmic rays is assumed to be uniform inside a containment volume surrounded by a three-dimensional absorbing wall. Inside the volume, each particle has a constant probability per unit time of escape. Each cosmic ray spends a mean time $\tau_{\rm esc}$ in the volume, which is much longer than the direct escape time, and traverses a mean amount of matter $\lambda_{\rm esc} = \rho\beta c\tau_{\rm esc}$ if the particle is moving with a velocity βc through the interstellar medium (ISM) of density ρ.

Gaisser [41] discusses the scenario of a source with injection spectrum

$$Q(E,t) = \mathcal{N}_0(E)\ \delta(t - t_0)\ , \tag{1.14}$$

where particles are injected instantaneously at time t_0 with energy spectrum $\mathcal{N}_0(E)$. The observed spectrum in the leaky box model will then be $\mathcal{N}(E,t) = \mathcal{N}_0(E)\exp(-t/\tau_{\rm esc})$. Neglecting energy losses and gains, the transport equation for cosmic rays of species i can be written as

$$\frac{N_i(E)}{\tau_{\rm esc}(E)} = Q_i(E) - \left(\frac{\beta c\rho}{\lambda_i} + \frac{1}{\gamma\tau_i}\right) N_j(E) + \frac{\beta c\rho}{m}\sum_{k>i}\sigma_{i,k}N_k(E) \ , \tag{1.15}$$

where $\sigma_{i,k}$ is the spallation cross section for the production of secondaries of species i from heavier nuclei of species k, and $\gamma\tau_i$ is the Lorentz dilated lifetime of the nucleus. The energy dependence of $\lambda_{\rm esc}$ is implicit due to its dependence on the velocity βc. Gaisser [41] cites a fit to the ratio of secondaries to primaries as:

$$\lambda_{\rm esc} = 10.8\ \beta \times \left(\frac{4}{R}\right)^{\delta} \ , \tag{1.16}$$

where $\lambda_{\rm esc}$ is expressed in g/cm^2, R is the particle rigidity in GV, and $\delta \simeq 0.6$. If we assume a primary nucleus P with a very long lifetime (so that the decay term in Eq. 1.15 vanishes) that receives no contribution from spallation of heavier nuclei (so that the spallation term vanishes) we can write a solution for the flux at Earth as

$$\mathcal{N}_P(E) = \frac{Q_P(E)\tau_{\rm esc}(R)}{1+\lambda_{\rm esc}(R)/\lambda_P} \ . \tag{1.17}$$

For protons, where $\lambda_P \sim 55$ g/cm^2, $\lambda_{\rm esc} \ll \lambda_P$, which implies

$$\mathcal{N}_P(E) \approx Q_P(E)\tau_{\rm esc}(R) \ . \tag{1.18}$$

From Eq. 1.16 we know that $\tau_{\rm esc} \propto R^{-\delta}$, or similarly, $\tau_{\rm esc} \propto E^{-\delta}$ for a particle of known charge. The spectrum observed at Earth is known to be a power law with spectral index γ, which can be expressed as $\mathcal{N}_P \propto E^{-(\gamma+1)}$. The source spectrum can also be written as a power law with spectral index α, so that $Q_P(E) \propto E^{-\alpha}$. Replacing the power law spectra and the energy dependence of the containment time into Eq. 1.18 we can see that, in order for the proportionality to hold, α must satisfy $\alpha = (\gamma + 1 - \delta)$. From the fit in Eq. 1.16 we

obtained $\delta \simeq 0.6$ (although with large uncertainties), and we know that the spectral index of cosmic rays observed at Earth is $\gamma \simeq 2.7$, which means that the spectral index at the source should be $\alpha \simeq 2.1$, which is in good agreement with the expected spectrum for acceleration in astrophysical shocks discussed in Section 1.4.

It is interesting to see how a simplistic model as the leaky box approximation can reproduce some important propagation observables. However, in order to obtain a better understanding of the propagation processes a more precise model is needed that accounts for the discrete nature of the sources, the gradients in the cosmic ray density across the galaxy, and a model of the known structure of the galaxy. A more realistic description of cosmic-ray propagation was proposed by Ginzburg & Syrovatskii [35] where cosmic-ray transport is treated as a diffusion problem. The transport equation for a particle of type i can be written as

$$\frac{\partial \mathcal{N}}{\partial t} = \nabla \cdot (D_i \nabla \mathcal{N}_i) - \frac{\partial}{\partial E}[b_i(E)\mathcal{N}_i(E)] - \nabla \cdot \mathbf{u}\, \mathcal{N}_i(E) \tag{1.19}$$

$$+ \quad Q_i(E,t) - p_i \mathcal{N}_i + \frac{v\ \rho}{m} \sum_{k \geq i} \int \frac{d\sigma_{i,k}(E,E')}{dE} \mathcal{N}_k(E') dE' \ . \tag{1.20}$$

On the right-hand side, the first term corresponds to diffusion, where D is the diffusion coefficient that can be expressed as a function of particle velocity v and diffusion mean free path λ_D as

$$D = \frac{1}{3} \lambda_D v \ . \tag{1.21}$$

Typical values for D are obtained by fitting cosmic-ray data such as the B/C (boron-to-carbon) ratio. At an energy of ~ 1 GeV/nucleon, $D \sim (3-5) \times 10^{28} \mathrm{cm}^2/\mathrm{s}$, and increases with magnetic rigidity R as $R^{0.3} - R^{0.6}$ for different diffusion models. A recent example of this type of measurement is shown in Fig. 1.11 obtained with the TRACER detector [43]. For the TRACER data, the best fit for the rigidity index is $\delta = 0.53 \pm 0.06$, but there seems to be a flattening in the ratio at high energies which may indicate the existence of a constant residual grammage of less than ~ 0.8 g/cm^2.

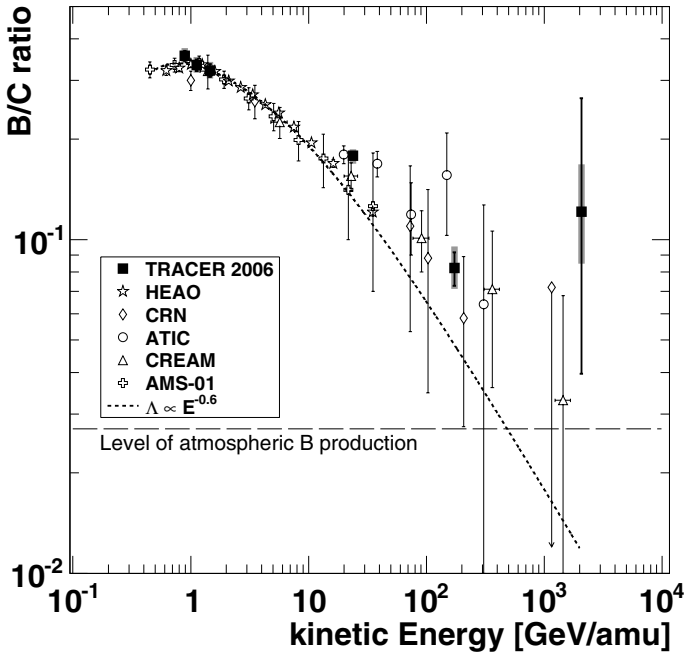

Figure 1.11: Measurements of the B/C ratio up to energies of about 1 TeV/amu. Taken from [43]. A fit to the data points with an spectral index of 0.6 is shown for reference.

The second term in Eq. 1.20 represents the change in energy of the particle during propagation (either losses through ionization or gains through reacceleration), with $b_i(E) = dE/dt$.

The third term is the convection term, characterized by the convection, or Galactic wind, velocity $\mathbf{u}$, which corresponds to the bulk motion of the cosmic ray plasma. It is not entirely clear from the literature if convection is an important ingredient in the equation or not. A discussion in [39] mentions that convection may be important since Galactic winds have been observed in other galaxies and could be relevant at large distances from the disk as the wind speed increases. However, no strong evidence for a Galactic wind exists today, so the actual value of the velocity has not been settled. In order to agree with secondary-to-primary ratios and anisotropy measurements, one model divides the galaxy in two zones: one at vertical distances < 1 kpc from the disk with pure diffusion, and a second one with a mix of diffusion and convection at larger distances. However, experimental evidence would be needed to support such models.

The forth term is the source term $Q_i(\mathbf{x}, E, t)$, where a cosmic ray source located at position $\mathbf{x}$ injects particles of type i with energy E at time t into the medium.

The fifth term represents the loss of particles of type i through decay or collisions. In this term, p_i can be written as

$$p_i = \frac{v\rho\sigma_i}{m} + \frac{1}{\gamma\tau_i} = \frac{v\rho}{\lambda_i} + \frac{1}{\gamma\tau_i} \ , \tag{1.22}$$

where λ_i is the mean free path for collisions in a medium with density ρ and $\gamma\tau_i$ is the lifetime of the nucleus already mentioned in the discussion of the leaky box model.

The last term represents the feed down of particles of type k into type i from spallation processes, where $\sigma_{i,k}$ is the energy dependent spallation cross section.

As was mentioned before, diffusion occurs when cosmic rays scatter off MHD waves and discontinuities in the ISM. The scattering is resonant, and particles scatter preferentially off waves where the projection of the wave vector along the average magnetic field direction is $k = \pm s/(r_g)\mu$, where r_g is the particle gyroradius, μ is the pitch angle, and s is an

integer, with $s = 1$ being the most important contributor to the scattering process. Strong fluctuations over long distances ($L \sim 100$ pc), where the strength of the random field δB is larger than the regular field B, the scattering becomes isotropic in the galaxy. For $r_g < L$, the diffusion coefficient can be estimated as $D \sim (\delta B_{\rm res}/B)^{-2} v r_g/3$, where $B_{\rm res}$ is the random field amplitude for the resonant mode $k_{\rm res} = r_g^{-1}$. The energy density of interstellar turbulence can be characterized by a power law of the form $w(k)\ dk \propto k^{-2+a}\ dk$, with $a \sim 1/3$ for waves with $1/(10^{20}\ {\rm cm}) < k < 1/(10^{8}\ {\rm cm})$. For $\delta B \approx 5\mu$G, the diffusion coefficient is $D \approx 2 \times 10^{27} \beta R_{\rm GV}^{1/3}$. An index $a = 1/3$ is characteristic of a Kolmogorov spectrum, while smaller values of the random field would yield a spectrum with $a = 1/2$, called Kraichnan spectrum. This range of spectral indices ($a = 0.3 - 0.5$) for the rigidity dependence of the diffusion coefficient agrees well with observational data.

Solutions to the diffusion equation can be found analytically by assuming symmetries in the geometry of the halo, the distribution of sources, or by setting reasonable boundary conditions. Several software packages exist that find numerical solutions, such as GALPROP [44], and DRAGON [45], with GALPROP being the most widely used one by the community.

One of the main differences of the diffusion model compared to the leaky box approximation is that the density of cosmic rays at different locations in the galaxy is not homogeneous. This introduces density gradients and, subsequently, directional anisotropy. The implications of the diffusion model for anisotropy of Galactic cosmic rays is one of the key topics of this work, and will be described in Section 1.7.1.

1.6.2 Propagation of Extragalactic Cosmic Rays

Cosmic rays with energies above 10^{18} eV cannot be contained by the magnetic field of the galaxy and can propagate over intergalactic distances. As was already mentioned in Section 1.2, cosmic rays with energies $\gtrsim 6 \times 10^{19}$ eV experience energy losses due to the GZK effect, which reduces their mean free path to a few tens of Mpc. Since the trajectories of ultra-high-energy cosmic rays (UHECRs) are less affected by Galactic and extragalactic magnetic fields, they can be used to search for cosmic rays sources as they point back to

their origin. For instance, for a cosmic ray propagating from the direction of the Centaurus A galaxy (located at a distance of 3-5 Mpc, within the GZK radius), the expected deflection angle $\Delta\theta_{\rm Gal}$ (in degrees) due to the regular component of the Galactic magnetic field is:

$$\Delta\theta_{\rm Gal} = (2.3^\circ \pm 0.24^\circ)(Z/E) \quad , \tag{1.23}$$

where E is the cosmic ray energy in units of 10^{20} eV, and Z is the cosmic ray charge in units of proton charge [46]. The uncertainties in the deflection angle are associated with our incomplete knowledge of the Galactic magnetic field. However, substantial progress has been made in recent years in creating a more precise field model [47].

An additional deflection $\delta\theta_{\rm XGal}$ is due to the extragalactic component:

$$\delta\theta_{\rm XGal} \approx 0.15^\circ \left(\frac{D}{3.8\ {\rm Mpc}} \cdot \frac{\lambda_{\rm XGal}}{100\ {\rm kpc}}\right)^{\frac{1}{2}} \left(\frac{B_{\rm XGal}}{1{\rm nG}}\right)\left(\frac{Z}{E}\right) \quad , \tag{1.24}$$

for a source at a distance D and an extragalactic magnetic field with coherence length $\lambda_{\rm XGal}$ and rms value $B_{\rm XGal}$. Note that for the above equations, deflection angles are small enough (i.e. $\lesssim 10^\circ$) to allow correlation studies with potential sources only for very light primary particles like protons or He nuclei. A heavier composition, such as that reported by the Auger Collaboration at ultra-high energies, would represent a challenge to such correlation studies. The results from recent searches for sources of UHECRs will be presented in Section 1.7.3.

If neutrons form a significant fraction of the UHECR flux, they would not be affected by magnetic fields and therefore their trajectories would point back to their sources. However, since neutrons have a lifetime of about 15 min in their rest frame, they would need to be highly boosted to propagate over Galactic and intergalactic distances without decaying. For example, a neutron with an energy of about 10^{20} eV (boost $\Gamma \sim 10^{11}$) would on average travel 1 Mpc before decaying. Limits on point sources of EeV (i.e. Galactic) neutrons have been set by the Pierre Auger Observatory [48].

1.7 Anisotropy

A natural way of searching for the sources of cosmic rays is to study their arrival directions at Earth and look for significant excess regions that could be correlated with the positions of known astrophysical objects. However, as was discussed in the previous chapter, Galactic and extragalactic magnetic fields significantly limit this search methodology. In this section, the anisotropy of cosmic rays is discussed for different energy ranges.

1.7.1 Anisotropy of TeV Cosmic Rays

1.7.1.1 Large-Scale Anisotropy

Cosmic rays with TeV energies propagate diffusively through the galaxy as described in Section 1.6.1. Their arrival directions cannot be used to search for point sources of cosmic rays directly, but it is expected that their distribution in the sky should present some degree of anisotropy, probably at the per-mille level.

A model to explain early anisotropy claims by Hess was published in 1935 by Compton & Getting [49]. In this model, the rotation of the Solar system around the Galactic center should induce an anisotropy due to our relative motion with respect to the unknown rest frame of Galactic cosmic rays. The Solar system moves towards a point in the sky located at $(\alpha, \delta) = (315°, +49°)$ at a velocity estimated at $200 - 240$ km/s, depending on the type of Galactic objects used as a rest frame [50]. This so-called Compton-Getting anisotropy should appear as a dipolar structure with its maximum pointed in the direction of motion of the Sun and a relative intensity change $\Delta I/\langle I \rangle$ given by:

$$\frac{\Delta I}{\langle I \rangle} = (\gamma + 2)\frac{v}{c}\cos\rho. \tag{1.25}$$

where the I is the cosmic ray intensity, γ is the index of the cosmic-ray energy spectrum, v is the Earth's velocity as a result of the motion of the Solar system, ρ is the opening angle between the velocity vector and the cosmic-ray direction, and c is the speed of light [51]. Replacing the known values for the parameters in the above equation gives a dipole amplitude of $\sim 0.35\%$. This effect has not been observed.

Note that the power law spectral index has a systematic uncertainty (see for example [52] for a discussion) and the Earth's velocity is not precisely constant, but both of these uncertainties are too small to be relevant.

A similar anisotropy, which may be called the Solar Compton-Getting effect, or solar dipole, is expected due to the rotation of the Earth around the Sun. The orbital velocity of the Earth is $\sim$ 30 km/s, which should produce a dipole with a relative strength of $\sim 4.7 \times 10^{-4}$. The orientation of the dipole is parallel to the Earth's velocity vector, which is fixed at a location about 90° away from the Sun in the sky on the ecliptic plane (i.e. the projection of the orbit of the Earth on the sky). This effect has been routinely observed with cosmic-ray detectors.

The diffusive propagation of cosmic rays in our galaxy should also produce anisotropy. In Section 1.6.1, it was discussed that one of the main differences between the leaky box approximation and the diffusion formalism of cosmic ray transport is that the latter produces gradients in the density of cosmic rays as a function of distance from the source and the time of injection. At the location of the Earth, the gradient in the cosmic ray number density $n(E)$ appears as a dipole anisotropy of amplitude δ, which is related to the diffusion coefficient D through the equation:

$$\delta(E) = \frac{3D(E)}{c} \frac{\nabla n(E)}{n(E)} \ , \tag{1.26}$$

where the dipole vector would point in the direction of the density gradient [40]. From the B/C measurements discussed in Section 1.6.1, it is known that $D \propto E^{\alpha}$, with $\alpha = 0.3 - 0.6$. This implies that for diffusive propagation the dipole should increase in amplitude as $\delta \propto E^{\alpha}$. The amplitude of the anisotropy expected from diffusion should be in the 10^{-3} to 10^{-2} range.

Many claims for the detection of anisotropy at this level have been published over the last 40 years. However, most of the claims are based on data from small detectors, with poorly-determined energy responses and usually afflicted by rate instabilities that may affect the validity of the anisotropy observations, specially given the small amplitudes involved.

An important claim was published in 1998 [53] based on data from underground muon telescopes located in Japan. A significant sidereal anisotropy was detected at energies of a few hundred GeV that was described as a superposition of two effects: a large-scale Galactic anisotropy with its maximum oriented towards ($\alpha = 0°, \delta = -20°$) similar to that previously reported in [54], and an excess flux from a cone with a half opening angle of $\sim 68°$ pointed in the direction ($\alpha = 90°, \delta = -29°$). This excess points close to the expected direction of the magnetic tail created by motion of the heliosphere through the interstellar medium. For this reason, this excess region is usually called the "tail-in" anisotropy. Also in [53], a claim is presented for the observation of seasonal variation of this anisotropy, which is maximal in December when the Earth is closest to the tail and reaches a minimum in June, which is interpreted as evidence for the heliospheric origin of this feature. No Compton-Getting anisotropy associated with the motion of the Sun in the galaxy is observed. A wide deficit region in the direction ($\alpha = 180°, \delta = 20°$) is usually referred to as the "loss cone."

At higher energies, the Tibet-ASγ collaboration conducted a search for anisotropy [55] with a data set of 37 billion events and energies between 4 and 300 TeV collected between 1997 and 1999 with the Tibet II array, and between 1999 and 2005 with the Tibet III array located in Yangbajing, Tibet. The analysis showed a dipolar anisotropy in the distribution of cosmic ray arrival directions with respect to the position of the Sun with a relative amplitude of $\sim 4 \times 10^{-4}$, compatible with the solar Compton-Getting effect.

The arrival direction distribution in the equatorial (i.e. sidereal) coordinate frame (which is fixed with respect to the stars, and will be discussed in Chapter 4) also showed a significant large-scale anisotropy which in principle could be described as a dipole at energies of about 3 TeV. The location of the strongest excess region and the wide deficit in the Tibet sky map (Fig. 1.12) roughly match the "tail-in" and "loss cone" regions already mentioned. Also in this case, the observed anisotropy is not consistent with the expectation for a Compton-Getting dipole both in orientation and in amplitude. Moreover, Tibet claimed that the null observation of the Compton-Getting anisotropy in their 300 TeV energy band (fitted dipole amplitude $0.03\% \pm 0.03\%$) implies that the cosmic ray plasma corotates with the Galactic

magnetic field. A systematic study of the anisotropy as a function of time shows that the large-scale pattern is stable over a period of about nine years (1999 to 2008) [56], without any noticeable influence from the 11-years solar activity cycle.

Other experiments in the Northern hemisphere, such as Super-Kamiokande [57], Milagro [58] and ARGO-YBJ [59], have reported on the observation of a large-scale anisotropy compatible with that observed by Tibet-ASγ at energies of a few TeV. It must be noted that while Tibet observes no change in the anisotropy as a function of time, Milagro reports a three-fold increase in the amplitude of the fundamental harmonic of the cosmic ray anisotropy for a similar sky and time coverage (2000 to 2007).

The large scale anisotropy is usually characterized as either a simple dipole, or the combination of dipole and quadrupole components with their respective amplitudes A and phases ϕ. A fit of this kind to the anisotropy profile δI as a function of right ascension α was applied to ARGO-YBJ data and reported in [59] using the expression:

$$\delta I(\alpha) = A_1 \cos(\alpha - \phi_1) + A_2 \cos(2(\alpha - \phi_2)). \tag{1.27}$$

The best fit amplitudes and phases are $A_1 = 6.8 \times 10^{-4}, A_2 = 4.9 \times 10^{-4}$ and $\phi_1 = 39.1^\circ, \phi_2 = 281^\circ$ which are compatible with results from Tibet.

The large scale structure reported by these experiments is usually interpreted in the framework of diffusive propagation as corresponding to the dipole anisotropy produced by the presence of gradients in the cosmic-ray density in our Galactic vicinity. Erlykin & Wolfendale [60] postulate that these observations point towards the existence of a nearby source of cosmic rays (possibly a young supernova remnant). If a single source is in fact a major contributor to the flux of cosmic rays observed at Earth, some structure in the energy spectrum should be visible, specially a progression of sharp breaks for increasingly heavier chemical elements for higher energies. Their suggestion is to study the anisotropy of cosmic rays as a function of energy and chemical composition, as a change in the anisotropy phase with energy could indicate a transition between different sources contributing to the cosmic ray flux in difference energy ranges. In their study, Erlykin & Wolfendale compare

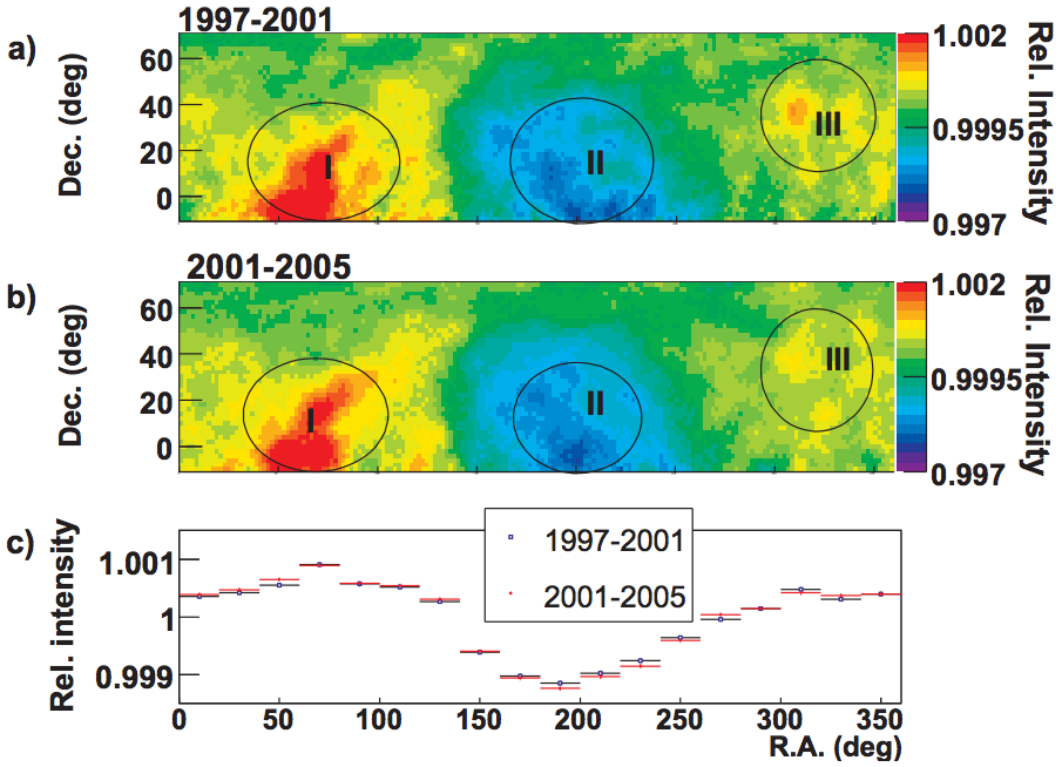

Figure 1.12: Anisotropy skymap produced by the Tibet-ASγ Collaboration [55] showing the so-called "tail-in" excess (I), the "loss cone" deficit (II), and a wide excess that is claimed to be associated with the Cygnus Galactic region (III). The anisotropy pattern appears to be stable in time (a) and (b). A one-dimensional projection of the anisotropy is shown in (c).

the anisotropy measurements to expectations for random realizations of a Galactic source population, where the sources follow the spatial distribution of supernova remnants in our galaxy.

A more recent example of this type of study is the work of Blasi & Amato [61] that explores the implications of diffusive propagation from Galactic sources on the three main cosmic-ray observables: energy spectrum, composition, and anisotropy in different scenarios. The observables are studied for different Galactic configurations with varying spatial source distributions, halo scale heights, diffusion spectral indices, and supernova rates. It is found that for typical values, most realizations produce an anisotropy that is too large compared to current observations and limits, as can be seen in Fig. 1.13. The phase of the anisotropy shows important changes as a function of energy depending on the geometry of the galaxy. For small halo heights, for instance, the containment volume is small so the cosmic-ray flux and anisotropy are dominated by very nearby sources. As a result of this, the phase of the anisotropy shows very fast transitions pointing towards different nearby source for this kind of Galactic model.

The anisotropy has also been modeled using nearby astrophysical objects that are potential cosmic ray accelerators instead of random source realizations. The results from one of these studies [62] shows that the Vela SNR in the southern sky should be a major contributor to the observed anisotropy. A younger SNR, known as Vela X, may also be an important source depending on its distance to Earth, which is very uncertain but could be as small as 200 pc. The authors remind us of an important caveat for this and the propagation studies already discussed: a strong assumption is made by considering diffusion as being isotropic and uniform everywhere in the galaxy, which is unlikely to be true. An update of this study with real sources is presented in [63] for a larger number of sources and for a wider energy range (TeV to EeV). Since this study makes use of several results presented in this thesis, the interpretations will be discussed in the corresponding chapters.

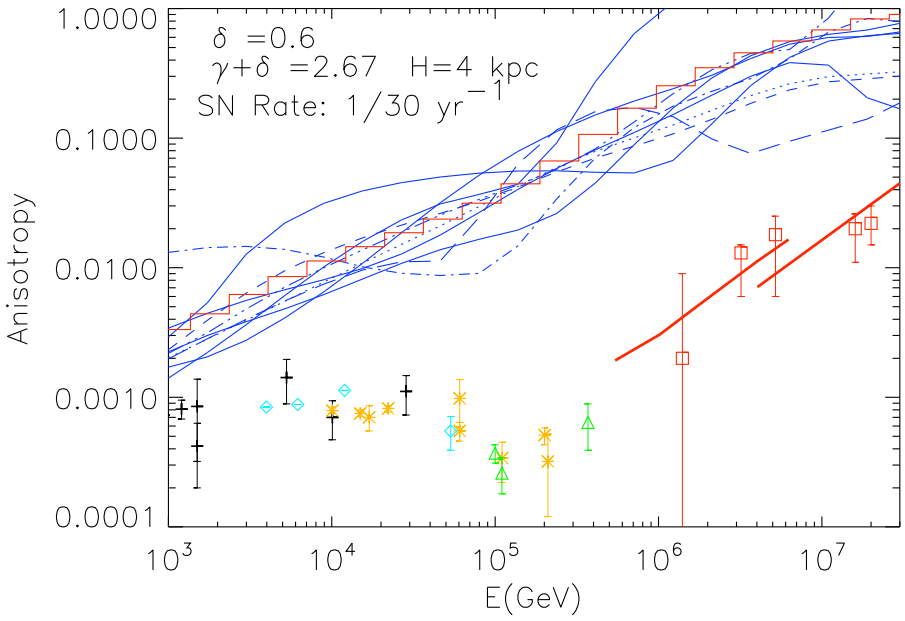

Figure 1.13: Comparison between the anisotropy amplitude as a function of energy for a collection of measurements and upper limits and the expected anisotropy from several realizations of a Galactic source population with the parameters given in the figure. See [61] for details.

1.7.1.2 Small-Scale Anisotropy

Besides the large angular scale component, localized excess regions have been detected. In 2008, the Milagro collaboration reported on the observation of regions of excess flux in the northern sky based on the analysis of a data set of 2.2×10^{11} events collected over a seven-year period [64]. The median energy of the data set was about 10 TeV. Shown in Fig. 1.14 are the two observed regions (labeled A and B). Region A shows a fractional excess of $\sim 6 \times 10^{-4}$, while for region B it is $\sim 4 \times 10^{-4}$. The spectrum of cosmic rays from each region was modeled using a power-law with an energy cutoff. The spectral index found by the fit to each region has large uncertainties. The 1σ interval for the spectral index of region A is between 0 and -2, while for region B the interval is between -1.2 and -2.6. The cutoff energy for both region is constrained to $\log_{10}(E/\mathrm{GeV}) = 4.0^{+0.4}_{-0.5(\mathrm{stat})}$ for region A and $\log_{10}(E/\mathrm{GeV}) = 4.0^{+0.3}_{-0.5(\mathrm{stat})}$ for region B.

While the large scale structure is relatively easy to explain in terms of diffusive propagation in our galaxy, the hotspots represent a challenge to the current view of Galactic cosmic-ray propagation. Several possible models have been proposed that could produce these small angular scale structures. Drury & Aharonian [65] speculate that cosmic rays may be transported along magnetic field lines from a nearby "magnetic mirror" or "nozzle" that has a field strength about 20 times that near the Sun. On the other side (or inside) of the mirror, a source that produces a higher intensity of cosmic rays with a harder spectrum may be located. Only those cosmic rays approaching the mirror at very small pitch angles would make it through, creating a collimated beam that could be producing both regions observed by Milagro. For this to work the source should be fairly close ($\sim$ 100 pc).

Due to the proximity of region A to the heliotail, the authors also explore the possibility of a heliospheric origin of both excesses. In this case, secondary neutrons produced in the tail of ISM material that forms downstream from the Sun could be creating the hotspots. Unfortunately, the column density towards the heliotail is too low to explain the observations. Accounting for the possible gravitational focusing of the ISM material increases the density, but not enough to match the Milagro data. Salvati & Sacco [66] propose that both regions are

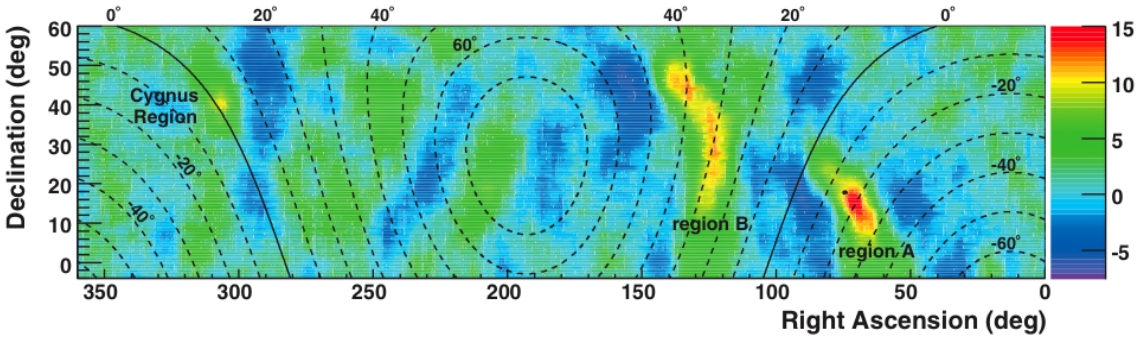

Figure 1.14: Sky map of the small scale anisotropy observed with Milagro in equatorial coordinates taken from [64]. Two regions (A and B) are clearly visible. The map was produced without removing gamma-rays, which makes the Cygnus region (bright in TeV gamma-rays) appear. Note the reversal in the right ascension coordinate axis (now with 0° on the right) compared to the Tibet maps. This convention will be used for sky maps in this work.

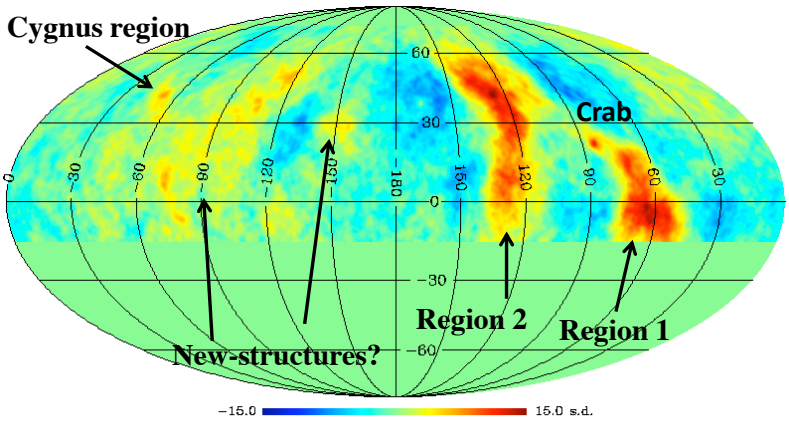

Figure 1.15: Small-scale anisotropy observed with the ARGO-YBJ detector taken from [68]. The observed anisotropy is compatible with that reported by Milagro.

connected through magnetic nozzles (similar to what was proposed by Drury & Aharonian) to one or two nearby supernova remnants (possibly Geminga). Malkov et al. [67] propose a different scenario in which a "beam" arises from propagation effects in a turbulent medium. The existence of this beam is linked to the large-scale anisotropy (i.e. the dipole). The model predicts the width, fractional excess, and maximum energy of region A, which all depend on the longest turbulence wave-particle interaction scale (of about 1 pc for the Milagro data). The model points to a break in the source spectrum at 3 PeV, which is coincidentally near the cosmic ray "knee." The authors point out that this could be the indication that the knee and the hotspot have a shared origin.

More recent studies of the small scale anisotropy in the northern sky (Fig. 1.15) with the ARGO-YBJ experiment located in Yianbaijing, Tibet [68] have confirmed the results obtained by Milagro and possibly revealed the existence of new small-scale excess regions.

1.7.2 Anisotropy of PeV Cosmic Rays

Since the gyroradii of cosmic rays increase linearly with energy, it is expected that at high energies the effect of the Galactic magnetic field should be less noticeable on the trajectories of cosmic rays. Above a certain energy, particle paths are no longer compatible with random

walks in the galaxy and the diffusion approximation to cosmic-ray propagation should not hold anymore. The energy where this transition occurs is not known due to the uncertainties in the Galactic magnetic field and the composition of the particles, but it is likely that it may happen somewhere in the PeV to EeV energy range. For this reason, this energy range is interesting since it may include the transition between Galactic and extragalactic cosmic rays.

The first claim of observation of cosmic ray anisotropy at energies above a few hundred TeV was presented by the EAS-TOP collaboration [69] in 2009. The search was based on a data set of about 2 billion cosmic ray events taken with the EAS-TOP array in Campo Imperatore, Gran Sasso, Italy between 1992 and 1999. One-dimensional projections of the anisotropy profiles in right ascension were reported for two energy bins with median energies of 110 and 370 TeV. The amplitude and phase of the observed anisotropy were parametrized by fitting first and second harmonic functions.

A search for anisotropy was conducted at higher energies (approximately between 1 and 100 PeV) by the KASCADE collaboration using data from the KASCADE array and its extended configuration, KASCADE-Grande. No anisotropy was observed in a data set of about 10^8 events detected by KASCADE between 1998 and 2002 [70]. The 95% upper limit on the amplitude of a large scale anisotropy goes from about 10^{-3} at primary energies of approximately 300 TeV, to 10^{-2} at an energy of about 6 PeV. The analysis of KASCADE-Grande data [71] extended the search to higher energies, with no positive results so far. Upper limits at 95% confidence level from this analysis were set on the amplitude and go from $\sim 5 \times 10^{-3}$ at 3 PeV, to 0.3 at 300 PeV.

The EAS-TOP measurements and the KASCADE and KASCADE-Grande upper limits are shown in Fig. 1.16 in comparison to results from searches at higher energies that will be discussed in Subsection 1.7.3.

1.7.3 Anisotropy at the Highest Energies

As discussed in Section 1.6.2, cosmic rays with energies above $\sim 10^{19}$ eV are not completely scrambled by Galactic and extragalactic magnetic fields and therefore can be use to search for cosmic-ray sources directly. Air shower arrays with areas large enough to collect reasonable statistics at ultra-high energies have conducted such searches with so far inconclusive results. A review of recent anisotropy searches is available in [14] and [29]. Here we discuss recent results on the search for large-scale and point source anisotropy of ultra-high energy cosmic rays.

1.7.3.1 Large-Scale Anisotropy

The composition of UHECRs has important consequences for directional anisotropy. If the composition at the highest energies is indeed heavy, as the Pierre Auger Observatory data seems to indicate, there is little chance that cosmic rays would point back to their sources even for the most optimistic magnetic field models. Despite the scrambling of event directions introduced by magnetic fields, it is possible that some anisotropy may survive, specially in the form of a large angular scale structure which could be due to the distribution of nearby sources or a potential extragalactic Compton-Getting effect. A search for large scale anisotropy using Pierre Auger Observatory data has been reported in [73, 74] with so far no significant evidence for anisotropy. The search was performed in declination and right ascension and reported in terms of the dipolar and quadrupolar coefficients of the Legendre spherical harmonics. Upper limits derived at 99% C.L. for both coefficients as a function of energy are shown in Fig. 1.17. As a comparison, the expected anisotropy due to stationary Galactic sources of proton and iron primaries are shown, where the width of the bands is due to the stochasticity of the turbulent component of different Galactic magnetic field realizations. At around 1 EeV, the composition measured by the Auger Observatory is significantly light. The upper limits on large-scale anisotropy exclude the possibility that the light component could come from sources in the galaxy, although the expected anisotropy depends strongly on the magnetic field model, the spatial distribution of sources, and their

spectra. The exclusion of Galactic proton sources agrees with the absence of a neutron flux produced by EeV protons also investigated by the Auger Observatory [48]. The current limits are compatible with both a Galactic population of iron sources, or an extragalactic population of proton sources.

Even though the anisotropy search in the UHECR data has not revealed large scale structure of significant amplitude, the Auger Collaboration reports a smooth transition (Fig. 1.18) in the orientation of the best fit dipole as a function of energy [72]. The orientation changes from the general direction of the Galactic Center at $E \sim 0.3$ EeV, to the direction of the anti-center at $E \sim 5$ EeV. This correlation between independent energy bins could be the first hint of the existence of large scale anisotropy in the UHECR data.

1.7.3.2 Searches for Point Sources

An important claim of observation of anisotropy at ultra-high energies was presented by the AGASA collaboration in 1999 [75], when a 4.5σ excess was reported near the location of the Galactic center, at $(\alpha, \delta) \sim (280°, -17°)$ for a $20°$ integration window and for energies range between 8×10^{17} eV and 3.2×10^{18} eV. It must we noted that the Galactic center, located at $(\alpha, \delta) \sim (266.3°, -29.0°)$, is outside the field of view of AGASA ($\delta \geq -24.2°$). An analysis of data taken with the SUGAR detector which operated in Australia between 1968 and 1979 observed a 2.9σ excess from the location of the Galactic center. The analysis of a larger data set, with better angular and energy resolution, taken with the Auger Observatory, has failed to find a significant excess at the same location [76].

Since the amount of magnetic deflection is largely unknown due to the uncertainties in magnetic field models and the distances from the sources, a possible way to look for anisotropy is to study the autocorrelation of UHECR data sets over different angular scales. Using this kind of analysis, the existence of small-scale anisotropy was claimed by AGASA based on an analysis of 57 events with $E > 4 \times 10^{19}$ eV [77]. However, no evidence of statistically significant clustering was found in an analysis of 271 events recorded by the HiRes detector between 1999 and 2004 in the same energy range [78].

In 2007, the Auger Collaboration published the results of a study [79, 80] on the angular correlation between cosmic rays with energies above $\sim 6\times10^{19}$ eV and the positions of AGN as defined in the 12$^{\text{th}}$ edition of the Véron-Cetty & Véron catalog of quasars and active nuclei [81]. Using data taken between January 2004 and May 2006, the correlation probability was scanned for a minimum in a three-dimensional space defined by the maximum angular separation ψ between each cosmic ray and an AGN, the minimum energy of the cosmic rays E_{min}, and the maximum redshift of the galaxies z_{max}. A minimum was found for $\psi = 3.1°$, $z_{max} = 0.018$, and $E_{min} = 56$ EeV. For these parameters, 12 events correlated out of 15 detected. A test was designed for events detected after May 2006 with an energy greater than E_{min}. The test ended when the isotropic hypothesis was rejected with a p-value of 1% or less. Between May 2006 and August 2007, 13 new events were detected, with 8 of them correlating with AGNs by the above definitions with 2.7 expected on average for the null hypothesis. The chance probability of this configuration for an isotropic flux was 1.7×10^{-3}.

After the Auger Collaboration publication, the HiRes collaboration presented the results of an analysis [82] performed using the Auger Observatory parameters that showed no evident anisotropy in their data. Out of 13 events observed by HiRes above the energy, only two were found to correlate (with 3.2 correlated events expected by chance) which resulted in an 82% chance probability. A scan over the same parameter space as that used by the Auger Collaboration found a minimum chance probability of 24% for (E_{min}, ψ, z_{max}) = (15.8 EeV, 2.0°, 0.016) with 36 correlated events out of a total of 198. The autocorrelation study indicated that the probability that the HiRes data set is isotropic is 97%. In 2010, the Auger Collaboration published an update on the correlation analysis [83]. The correlation of the new data with the VCV catalog is weaker than in the previous analysis, decreasing from $\sim$ 69% to $\sim$ 38%, with 21% being the expected correlation for the isotropic case.

It is possible that the galaxies included in the VCV catalogue are not the actual sources of UHECRs but just tracers of the matter distribution in the local universe, in which case there may be other galaxy catalogues that could show a better correlation. Several catalogues were tested but with the current level of statistics no strong correlation was found. The

autocorrelation of the data shows a deviation from isotropy at an angular scale of 11°, with a corresponding p-value of $\sim 1.3\%$. The region with the largest overdensity of events is centered 4° away from the location of the Centaurus A radiogalaxy (the closest AGN to Earth). In a separate publication [84], it is reported that the correlation with Cen A is maximal for events within a 18° angular window, with 10 events observed over an expectation of 2.44 events for the isotropic case. Additional data will be needed to determine if this excess turns statistically significant.

A recent publication by the TA collaboration uses data taken during the first 40 months of operation of the Telescope Array detector located in Utah to search for anisotropy and to conduct a correlation study with large scale structure in the local universe. From these analyses, TA reports the following results [85]:

- No significant clustering is evident in the TA data. A hint of clustering is present at angular scales of $20° - 30°$ for energies $E > 57$ EeV. The statistical significance of the clustering is still too low at this point to draw conclusions.

- The correlation between the VCV catalog and the data using the parameters defined in the original Auger Collaboration analysis gives a chance probability of 2% (11 events are correlated from a total of 25, with 5.9 expected from random coincidences). The statement from the TA collaboration is that this implies no correlation; no further scan of the parameter space is attempted. While a 2% chance probability is certainly not significant enough to claim a positive correlation, it is interesting enough to draw attention to a future follow-up analysis.

- Data sets with $E > 10$ EeV, $E > 40$ EeV, and $E > 40$ EeV seem compatible with an isotropic distribution. The two higher energy sets are compatible at 95% C.L. with sources that follow the large-scale structure (LSS) of the universe.

- The data set with $E > 10$ EeV can be made compatible with the LSS model for smearing angles larger than 3° by including magnetic field deflections.

The search for the sources of cosmic rays at the highest energies will benefit from new data currently being taken with the TA array and the Pierre Auger Observatory, the two largest cosmic ray detectors currently in operation. The combination of the data sets from both detectors and the coordination of analysis strategies may shed new light on this important topic. In terms of extending the anisotropy search to even higher energies ($E > 10^{20-21}$ eV), the strong flux suppression observed in the energy spectrum at those energies implies that areas > 10000 km^2 would have to be instrumented. In order to reduce the cost of such large detectors, there are two possibilities being currently explored: either the construction of large arrays based on cost-effective radio [86] or microwave [87] detectors, or the large-area coverage provided by an orbiting air fluorescence telescope [88].

1.7.4 Anisotropy Studies in the Southern Hemisphere

Searches for cosmic-ray anisotropy at TeV and PeV energies were limited to the northern-hemisphere sky before the construction of the AMANDA and IceCube detectors. The first report of significant anisotropy in the southern sky at TeV energies was presented by IceCube in [89]. In that work, a significant large angular scale anisotropy was detected using a data set of 4.3 billion events recorded with the IC22 configuration of IceCube. The median angular resolution of the data set used for that analysis is about 3° and the median energy of the parent cosmic-ray particles is approximately 20 TeV. A map of relative intensities is shown in Fig. 1.19 where the large scale structure in the southern sky is visible. The one-dimensional projection of the anisotropy sky map in the right ascension coordinate was parametrized using the first two components of a harmonic expansion:

$$\delta I(\alpha) = A_0 + A_1 \cos(\alpha - \phi_1) + A_2 \cos(2(\alpha - \phi_2)). \tag{1.28}$$

The best fit amplitudes and phases are given in Table 1.1. The χ^2/dof of the fit was 22/19. The anisotropy is similar in amplitude, angular size, and orientation as that observed by experiments in the north what were discussed in Subsection 1.7.1.

Harmonic order n	A_n	ϕ_n
0	$(1.0 \pm 2.1_{\text{stat}} \pm 10_{\text{sys}}) \times 10^{-6}$	-
1	$(6.4 \pm 0.2_{\text{stat}} \pm 0.8_{\text{sys}}) \times 10^{-4}$	$66.4^\circ \pm 2.6^\circ_{\text{stat}} \pm 3.8^\circ_{\text{sys}}$
2	$(2.1 \pm 0.3_{\text{stat}} \pm 0.5_{\text{sys}}) \times 10^{-4}$	$-65.6^\circ \pm 4.0^\circ_{\text{stat}} \pm 7.5^\circ_{\text{sys}}$

Table 1.1: Fit coefficients for the harmonic fit to the 1d relative intensity projection of IceCube data [89].

The work presented in this thesis expands the scope of anisotropy studies in the southern sky using the IceCube, IceTop and AMANDA detectors (Chapter 2). Several analyses were performed to extend the search for anisotropy to smaller angular scales (Chapter 5), higher energies (Chapter 6), and to probe the stability of anisotropy on time scales of over a decade (Chapter 7). A validation of the pointing capabilities of the IceCube detector, a prerequisite to any anisotropy search, is presented in Chapter 3, while the anisotropy search method is described in Chapter 4.

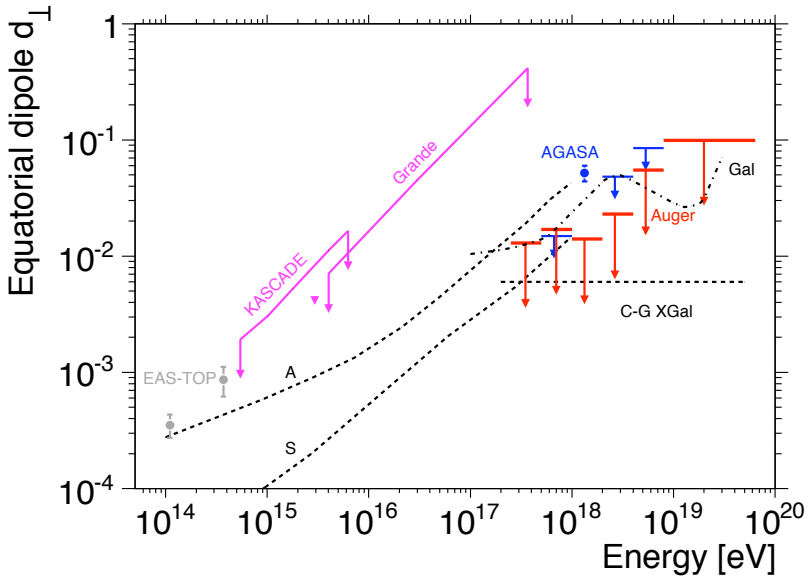

Figure 1.16: Measurements and upper limits on the amplitude of a dipole anisotropy from EAS-TOP, KASCADE, and KASCADE-Grande. Limits at higher energies (as well as an observation claim) are shown from the Auger Observatory and AGASA and will be discussed in Subsection 1.7.3. For comparison, the plot shows the expected anisotropy amplitude up to 1 EeV due to Galactic sources given two different magnetic field configurations (*A* and *S*), as well as the amplitude due to a purely Galactic origin of UHECRs (*Gal*), and the Compton-Getting dipole induced by our motion with respect to the CMB rest frame (*C-G XGal*). See [72] for more details.

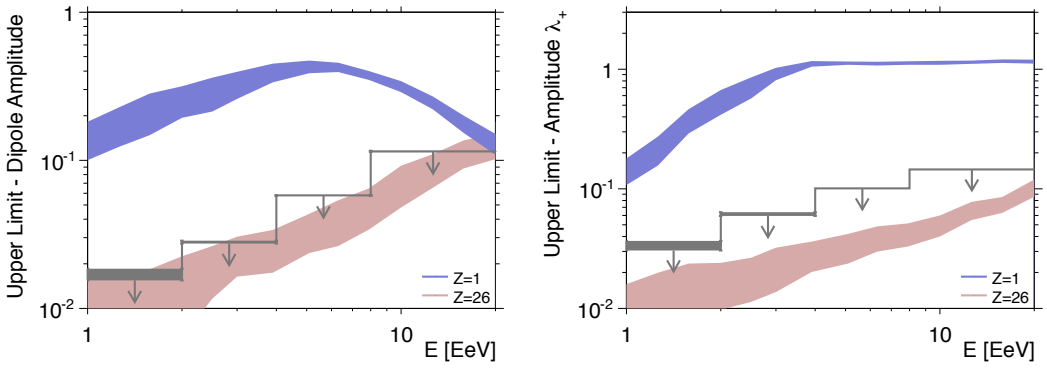

Figure 1.17: Upper limits at 99% C.L. on dipole (*left*) and quadrupole (*right*) amplitudes as a function of energy as determined by an analysis of UHECR data from the Auger Observatory [74]. The color bands represented the expected anisotropy level for sources of cosmic rays with two compositions: proton (*blue*), and iron (*red*). The width of the bands corresponds to fluctuations induced by the stochastic nature of the fluctuations in the turbulent Galactic magnetic field.

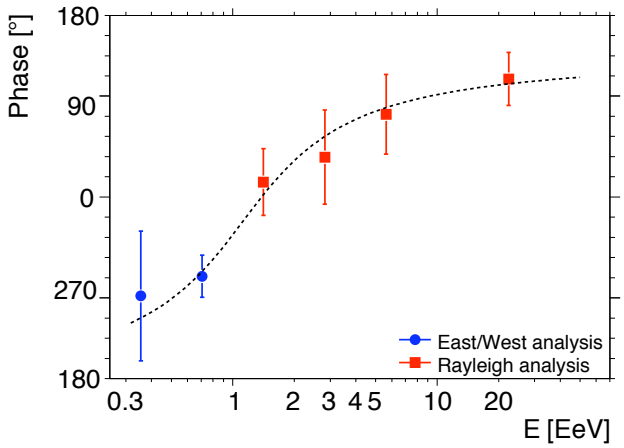

Figure 1.18: Orientation in right ascension of the best fit dipole to the UHECR data from the Pierre Auger Observatory for independent energy bins. The smooth change in orientation may be indicating a real anisotropy with an amplitude below current limits. Taken from [72].

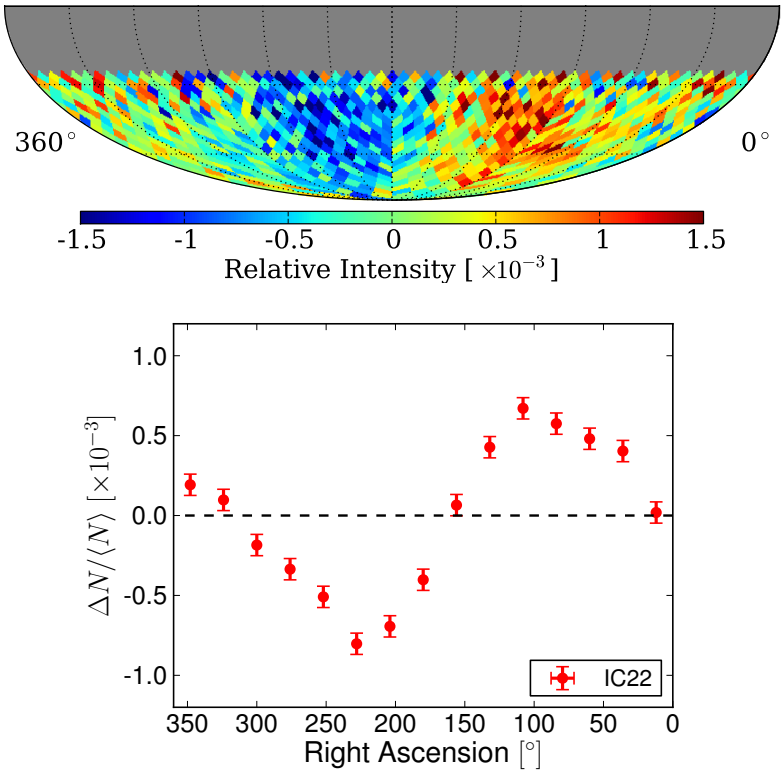

Figure 1.19: Large-scale anisotropy observed in the IC22 cosmic-ray data. *Right:* IC22 relative intensity sky map in equatorial coordinates. A broad excess with an amplitude of $\sim 10^{-3}$ is visible accompanied by a wide deficit of similar strength. *Left:* One-dimensional projection of the anisotropy map showing relative intensity as a function of right ascension for the declination range $-75 < \delta < -35$.

Chapter 2

Cosmic-Ray Detectors

The results presented in this work are based on data collected using three cosmic-ray detectors: the IceCube neutrino telescope, the IceTop air-shower array, and the AMANDA neutrino telescope. These three instruments are located next to the Amundsen-Scott research station, at the geographic South Pole. The design and operation of these detectors is described in this chapter.

2.1 Working Principle

High-energy cosmic rays are studied through the detection of the secondary particles that they produce after interacting with air molecules in the Earth's atmosphere. As was described in Section 1.2, this interaction produces energetic mesons that subsequently decay to produce muons and electrons that can be detected at ground.

2.1.1 Propagation of Charged Leptons through Matter

Electrons and muons lose energy as they propagate through matter. The rate of energy loss is dictated by the physical process that occurs in the propagation medium. Continuous energy losses are usually associated with the ionization of material in the path of the charged particle, while other processes such as pair production, bremsstrahlung, or photonuclear interactions are stochastic in nature.

Electrons with energies below $\sim$ 1 GeV lose energy predominantly through ionization, while bremsstrahlung losses dominate at higher energies. The significant losses suffered by

electrons limit their range of propagation in a dense medium. For this reason, electrons usually do not reach depths of more than a few meters water equivalent (mwe) and subsequently can only be detected at ground level. Since bremsstrahlung losses are inversely proportional to the mass squared of the charged particle, muons have a smaller energy loss rate than electrons and therefore a much longer range due to their larger mass (about 2000 times that of the electron).

Muon energy losses at high energies are usually parametrized through the equation

$$-\frac{dE}{dX} \approx a(E) + b(E)\ E, \tag{2.1}$$

where $a \sim 0.26$ GeV/mwe and $b \sim 3.57 \times 10^{-4}$/mwe [90], both quantities being only mildly dependent on energy. The equation shown above implies a maximum range for energetic muons. The mean range x_0 of a muon with initial energy E_0 is given by

$$x_0 \approx \frac{1}{b} \ln \left[1 + \frac{b}{a} E_0 \right] . \tag{2.2}$$

As an example, the mean range of muons with energies of 2, 20, and 200 TeV corresponds to about 3.7, 9.4, and 15.8 km in ice, respectively.

2.1.2 Cherenkov Radiation

When a relativistic electron or muon enters a refractive medium, Cherenkov radiation is emitted if the velocity v of the charged particle is larger than the speed of light in the medium. The speed of light in a medium is given by c/n where c is the speed of light in vacuum and n is the index of refraction of the medium, which implies that the condition for Cherenkov emission is $v > c/n$. The constructive interference of electromagnetic waves creates a cone-shaped wavefront that is characteristic of Cherenkov light. The opening angle of the cone θ_c is given by

$$\cos \theta_c = \frac{1}{\beta n} \tag{2.3}$$

with $\beta = v/c$. The process is shown schematically in Fig. 2.1 for a highly relativistic particle ($\beta \sim 1$). As an example, a relativistic muon traveling through ice ($n \sim 1.35$) would produce a light cone with an angle of $\theta \sim 42°$.

Particle detectors that record the Cherenkov light emitted by relativistic charged particles can be built by placing light sensors in a medium that is dark and optically transparent, such as ice or water. The three cosmic-ray detectors used in this work (AMANDA, IceCube, and IceTop) are Cherenkov detectors of this kind.

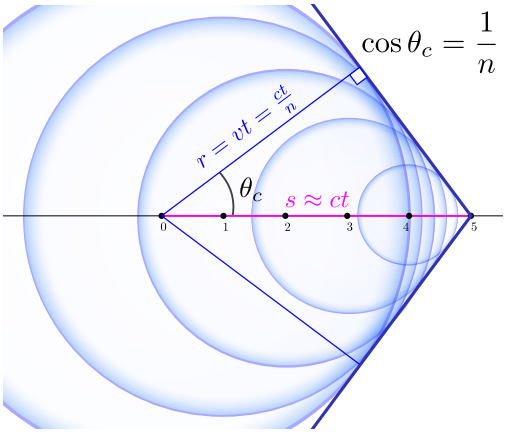

Figure 2.1: Illustration of Cherenkov radiation emission by a highly relativistic particle ($\beta \sim 1$) as it moves through a medium with refractive index n. Waves emitted at the numbered positions add constructively to form a conic wavefront with opening angle θ_c.

2.2 IceCube

IceCube is a km^3-scale particle detector deployed in the glacial ice at the South Pole. Its main scientific goal is to search for astrophysical sources of high-energy neutrinos, but it is also used as a cosmic-ray detector due to its sensitivity to high-energy muons produced in air showers.

The Cherenkov light produced by cosmic-ray muons in the ice is detected by a three-dimensional array of 5160 Digital Optical Modules (DOMs, which will be described in Section 2.2.1) deployed at depths between 1450 m and 2450 m below the ice surface. DOMs are

attached to 86 vertical cables, or "strings," that provide mechanical support, electrical power, and a data connection to the surface. Each string supports 60 DOMs, each separated from its neighbor by a vertical distance of about 17 m. The horizontal spacing between strings is about 125 m. A compact group of eight strings with a smaller DOM and string spacing forms the DeepCore detector [91], located at the bottom of IceCube, which is designed to extend the energy reach of neutrino studies to lower energies. A detector diagram is shown in Fig. 2.2.

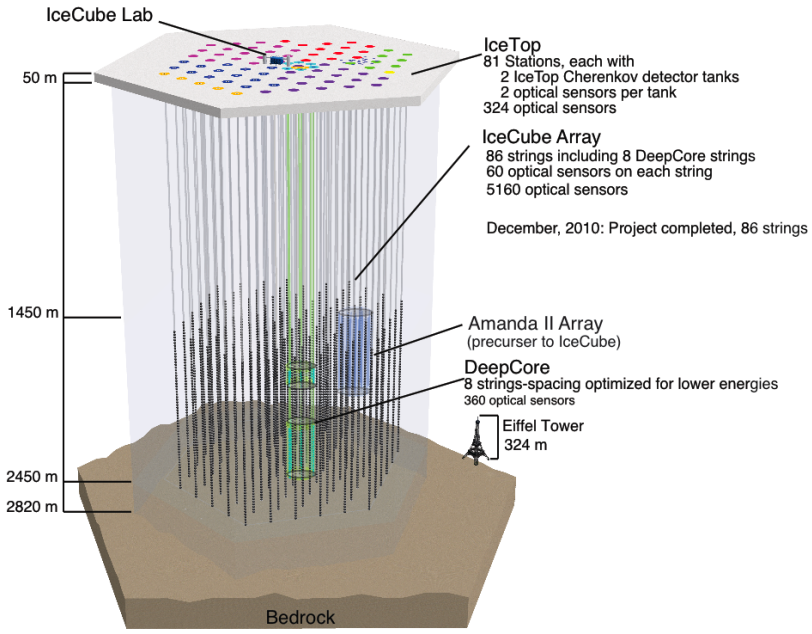

Figure 2.2: Model view of IceCube, IceTop, AMANDA, and DeepCore.

Strings were deployed in holes about 60 cm in diameter that were drilled using a high-pressure hot-water drill. The harsh weather conditions at the South Pole allow for drilling to take place only during the warmest months of the Austral summer (December and January), so the detector was operated in a series of stable configurations for about a year before the start of the next drilling season. The first IceCube string was deployed during the 2004/05 season, and construction was finished in December 2010. The chronology of the string deployment process is shown in Fig. 2.3. Each detector configuration is named according to

Name	Start	End
IC22	06/2007	04/2008
IC40	04/2008	05/2009
IC59	06/2009	06/2010
IC79	06/2010	04/2011
IC86	05/2011	-

Table 2.1: Operation time of each detector configuration in IceCube.

the number of working strings that were deployed in the ice and participated in the data acquisition (the IC59 configuration, for instance, had 59 active strings). The operation time of each configuration used in this work is given in Table 2.1.

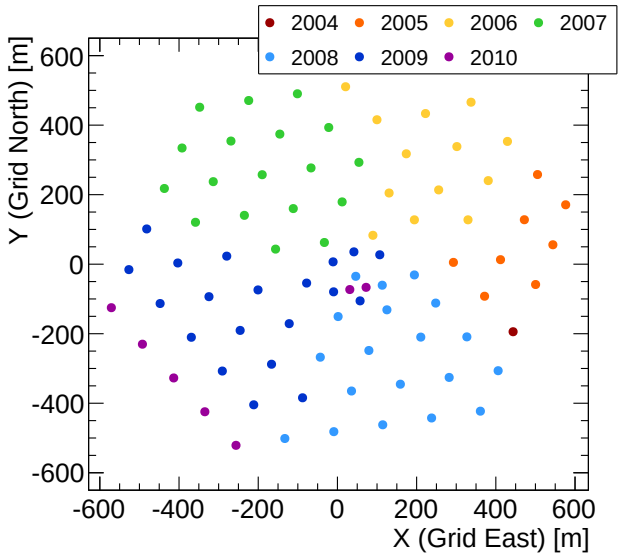

Figure 2.3: Chronology of the IceCube string deployment. The deployment season usually started during the month of December of the year indicated in the legend and continued until the beginning of the following year.

2.2.1 Digital Optical Modules

The Digital Optical Module (DOM), shown schematically in Fig. 2.4, is the main building block of the IceCube detector. A DOM consists of a 35 cm diameter pressure sphere that houses a 10-inch diameter R7081-02 photomultiplier tube (PMT) manufactured by Hamamatsu Photonics [92]. Besides the PMT, the DOM houses a power supply, a set of calibration light sources, and the electronics for the digitization of PMT signals [93]. The pressure sphere is made of 0.5 in-thick borosilicate glass capable of withstanding pressures of up to 690 atm. Before deployment, the sphere is filled with nitrogen gas at a pressure of about 1/2 atm.

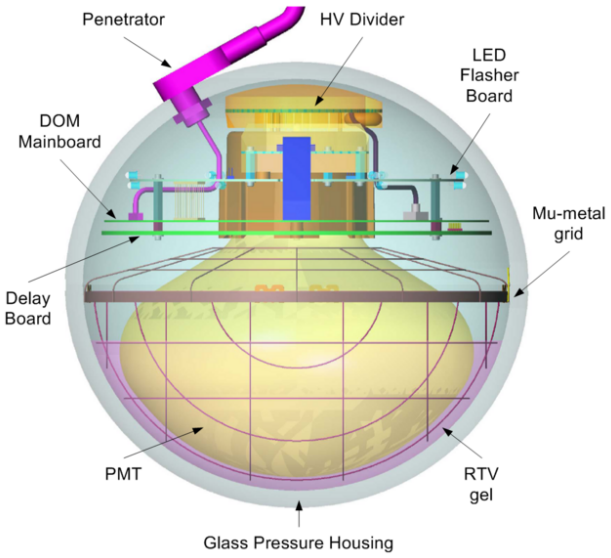

Figure 2.4: Schematic view of a Digital Optical Module, with main components labeled.

A layer of RTV gel provides optical coupling between the PMT and the glass sphere. The glass introduces a short wavelength cutoff at about 350 nm, which matches nicely the spectral response of the PMT (300-650 nm). The PMT bialkali photocathode has a peak quantum efficiency of about 25% at a wavelength of 390 nm. Radioactive decays in the glass induce fluorescence, a major contributor to the dark noise rate of the PMT (< 500 Hz). The DOM PMTs are operated at voltages between 1300 and 1500 V, which results in an electronic gain of about 10^7. The PMT cathode is grounded and the anode is connected to

high potential; a toroidal transformer provides the AC coupling between the anode and the digitization electronics.

Inductive coupling is used because high-voltage power supply noise couples more weakly into the DOM main board than with capacitor coupling. A drawback caused by the use of inductive coupling, however, are the non-linearities introduced by saturation effects in the transformer core in the presence of large electric currents. This effect, usually referred to as "droop," can be corrected for in data analysis, but in some extreme cases some information can be lost.

The photocathode is surrounded by a mu-metal grid, designed to shield the PMT from the magnetic field of the Earth.

The DOM response to a single photoelectron (SPE) is an electric pulse with a typical amplitude of 10 mV and a width of 5 ns. The time resolution for single photoelectrons is about 2 ns. The digitization of the PMT signals is performed by two independent systems: the Analog Transient Waveform Digitizer (ATWD) and the Fast Analog-to-Digital Converter (FADC). The DOM's Field-Programmable Gate Array (FPGA) starts the digitization cycle with the FADC and the ATWD jointly when a signal crosses a discriminator threshold of 1/4 SPE. The ATWD is a low-power custom-designed digitizer that consists of an array of 128 switched capacitors used to store the analog signal operating at 300 megasamples per second (MSPS). Each ATWD has four parallel channels with different input gains (gain ratios are 16:2:1/4) that provide 14 bits of dynamic range. The voltages in the capacitors are digitized by 128 10-bit ADCs multiplexed to the four parallel channels. Since the digitization of each waveform takes 29 μs, each DOM is equipped with two ATWD chips operating in ping-pong mode to reduce readout-induced dead time.

The FADC system consists of a commercial 10-bit 40 MSPS digitizer connected to a three-stage amplifier. After a trigger, 256 FADC samples are recorded that correspond to 6.4 μs. Even though the FADC dynamic range is limited compared to the ATWD, they provide time coverage for specially long signals. Each DOM "launch" is comprised of the

FADC and ATWD waveforms plus a timestamp provided by the 40 MHz system clock and additional information about locally coincident signals from nearby DOMs.

The operation of the DOM is controlled by a 400k-gate Altera Excalibur EPXA-4 FPGA. Two memory banks are available to the FPGA: an 8 Mbit read-only memory that stores basic functionality instructions, and a second 8-Mbit flash memory that can be reprogrammed. The FPGA includes a 4-bit scaler that counts the number of pulses recorded in each 1.6 ms interval and is read out periodically. The scaler system enables the possibility of searching for supernova signals with IceCube by looking for an overall increase in the noise rate of the detector. Additional control functions are performed by a Complex Programmable Logic Device (CPLD) that provides an interface to the calibration LEDs, reads 24 ADC channels used for monitoring, and 16 DAC channels used as analog control voltages. The signals are transmitted using an 8-bit DAC and read out with a 10-bit ADC at 40 MSPS.

The power consumed by each DOM is about 3.5 W. The power is provided via a single twisted pair cable that feeds ± 48 V from the surface and is also used to transmit the data from every pair of adjacent DOMs.

DOMs are operated in two coincidence modes: Hard Local Coincidence (HLC) and Soft Local Coincidence (SLC). In the HLC mode, data is stored and sent to the surface only if two nearest neighbor or next-to-nearest-neighbor DOMs observe a signal within a 1 μs coincidence window. The rate of HLC hits at the DOM level is between 3 and 15 Hz. For the SLC mode, a "Coarse Charge Stamp" for isolated hits is sent to the surface together with the coincident waveform information. SLC hits have the same rate as the dark noise rate of the DOM of around 350 Hz and are mostly composed of noise hits, although for some events this information allows to recover some information about the event.

The main event trigger in IceCube is a simple multiplicity trigger called SMT8 that requires coincident hits in eight DOMs within 5 μs. For each trigger, all locally-coincident hits within a $\pm 10\mu$s window are recorded, and overlapping windows are merged. The SMT8 trigger rate shows a seasonal variation of $\pm 10\%$ over the year, due to the change of atmospheric conditions that affect the muon production in air showers. The average trigger rate

has increased over the years with the deployment of more strings in the ice, as shown in Fig. 2.5. The average trigger rate for IC86 is about 2700 Hz.

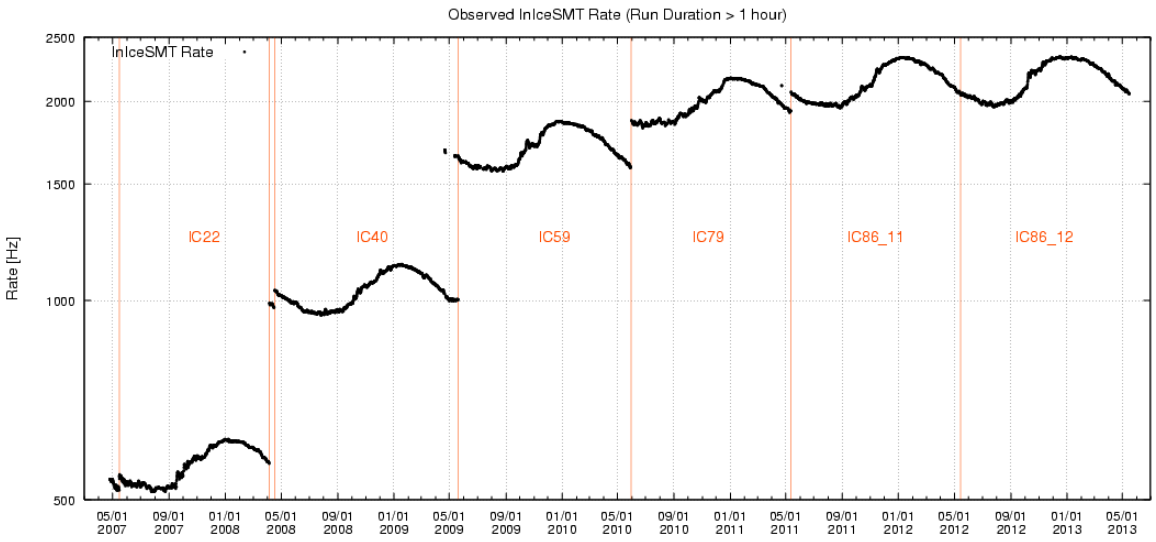

Figure 2.5: Seasonal variation of the IceCube trigger rate for different detector configurations. Note that the both years of operation of the final IC86 configuration are shown. Only the first year is used in this work.

Before deployment, DOMs were subjected to stress tests to verify their survival rate. These tests indicate that the survival probability after 15 years is about 94%.

Each DOM also incorporates a "flasher" board with 12 UV LEDs mounted on its periphery, where six LEDs are pointing radially outwards and the remaining six are inclined in an angle of around 42° which is meant to emulate the Cherenkov angle of an energetic charged particle in the detector. DOMs can be flashed individually while the rest of the detector records the emitted light. This information is then used for geometry calibrations, and the determination of the optical properties of the ice, which will be discussed in the following Subsection.

2.2.2 Ice Properties

The quality of event reconstructions in IceCube relies on the level of understanding of light propagation in the ice. The optical properties of the glacial ice at the South Pole are described in terms of the amount of scattering and absorption that UV light experiences as it propagates through the detection medium. The ice slowly accumulated layer by layer over the last 100,000 years, giving rise to a depth-dependent structure that is reflected in its optical characteristics.

A layer of compacted snow, or "firn," sits immediately below the ice surface up to a depth of 50 m. Below this layer, the ice is solid and dark, but the presence of air bubbles embedded in it strongly scatters light and prevents it from propagating further than 10 m, at most. Scattering in air bubbles dominates up to a depth of about 1300 m, while at greater depths both the effective scattering and absorption lengths increase significantly.

At depths between 1450 m and 2450 m (where IceCube sensors are deployed) the optical properties of the ice have been determined using the LED light sources included in each DOM. In a "flasher run," the LEDs in one DOM are operated to emit short light pulses while the remaining detector records the resulting light distribution of the flash as a function of time and position. The study of arrival time distributions relative to the flash and of the recorded pulse amplitudes is used to reconstruct the ice properties in terms of effective scattering and absorption coefficients. The latest study of this sort is presented in [94].

IceCube data indicates that the average scattering length increases from about 25 m to 70 m in the 1450-2450 m depth range; the absorption length increases from 70 m to about 200 m in the same range. Besides the overall increase in absorption and scattering lengths, the most important optical feature of the ice is the presence of several dust peaks which are evident in Fig. 2.6. These dust peaks are associated with periods of lower temperature that occurred in the late Pleistocene. The strongest peak (usually referred to as the "dust layer") is about 65,000 years old and is located at a depth of about 2025 m; the absorption length in the layer is less that 20 m, while the scattering length is only 5 m.

The ice layers remain mostly parallel to the ice surface, but near the bottom of the detector the layers exhibit a certain amount of tilt which is believed to reflect the shape of the bedrock under the ice. The tilt in the deep ice produces differences in the depths at which the same layer would appear as a function of position in the detector, with depth differences being as large as about 50 m in the most extreme case. These differences are accounted for in the current ice model used in IceCube reconstructions.

The description above refers to the characteristics of the naturally-ocurring "bulk" ice that makes most of the detection medium of IceCube. A current topic of study is the characterization of the hole ice that formed after the drilling process as water refroze around the DOMs. This ice contains more air bubbles than its surroundings as well as a different dust distribution.

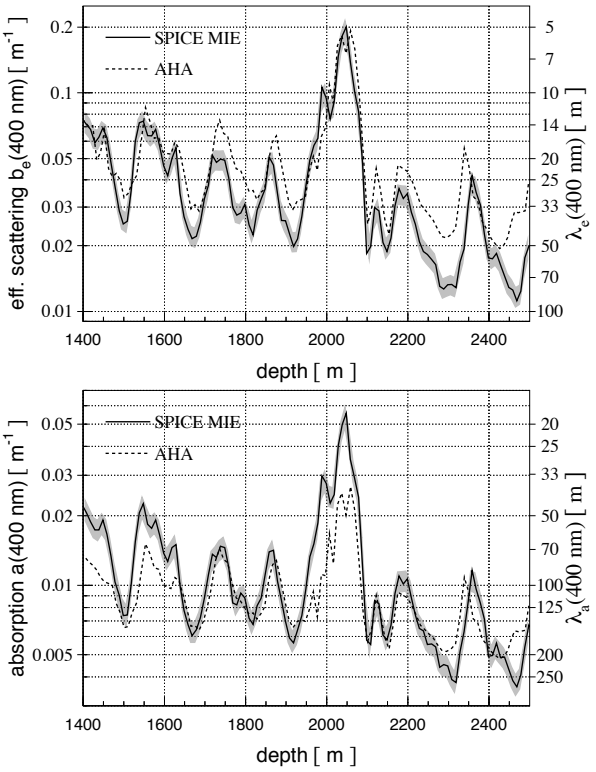

Figure 2.6: Effective scattering coefficient (top) and absorption coefficient of the South Pole ice as a function of depth from the ice surface. The most current ice model (Spice Mie [94]) is shown in a comparison to a previous model (AHA [95]).

2.2.3 Angular Reconstruction

The light signals produced by muons in the IceCube DOMs can be used to reconstruct the arrival direction of the original cosmic-ray particles. The inputs to the reconstruction algorithms are the positions of the triggered DOMs and the times at which they recorded photon hits.

A first guess of the event direction is obtained by performing a linear-track fit to the DOM hits using an analytical χ^2 minimization procedure. This algorithm, called `linefit`, assumes that the event can be described as a simple plane wave propagating through the detector, therefore ignoring the geometry of the Cherenkov cone and the light propagation

effects in the ice. Even with these simplifications, `linefit` is able to achieve an angular resolution of a few degrees while being very fast, making it a good seed for more complex reconstructions.

Better angular resolutions are achieved by reconstruction algorithms that rely on a maximum likelihood method and implement more details of the light generation and propagation in the ice. The general purpose of these methods is to obtain the muon track parameters $\vec{a}$ that maximize the log-likelihood equation:

$$\log \mathcal{L} = \sum_i \log p(\vec{x}_i|\vec{a}) \ , \tag{2.4}$$

where $\vec{a} = (\vec{r}_0, t_0, \theta, \phi)$ for a muon located at position $\vec{r}_0$ at time t_0 with its velocity vector pointed in a direction with zenith angle θ and azimuth angle ϕ. The function $p(\vec{x}_i|\vec{a})$ represents the probability of observing each hit $\vec{x}_i$ given a track with parameters $\vec{a}$. Since the problem has no analytic solution, numerical minimization algorithms such as `MINUIT` are used to search for the minimum of $-\log \mathcal{L}$. Due to the complexity of the likelihood space, it is possible that the minimizer would only find local minima depending on the starting conditions. To avoid this, the minimization is carried out in an iterative fashion with different starting conditions to increase the probability of finding the global minimum. Pseudo-random directions on the sky are drawn from a Sobol sequence and used as the minimization seed in each iteration, and between 1 and 32 iterations are performed for each event.

In the fit, an analytic expression, known as the Pandel parametrization [96], is used to describe the likelihood that a photon arrives at a time t at a given DOM. The parametrization is based on a gamma distribution that takes into account the geometry of the Cherenkov cone and the average behavior of light scattering in the ice. The residual time t is measured with respect to the calculated time of arrival of a photon that propagates directly from the Cherenkov cone to the DOM with no scattering (i.e. a "direct hit"). The Pandel function provides a fast and reasonable approximation to more detailed simulations, as can be seen in the distributions of residual times for two different distances shown in Fig. 2.7.

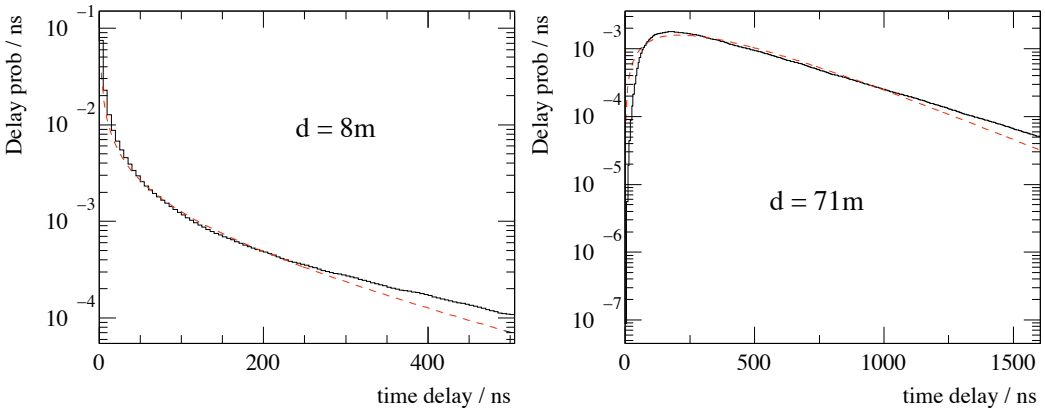

Figure 2.7: Distribution of time residuals with respect to the arrival time of direct photons for a detailed simulation (solid black line) and for the Pandel function (dashed red line) at two distances from the muon track: 8 meters (left), and 71 meters (right). A good agreement between the simulation and the Pandel parameterization is observed in both cases.

Two fit approaches are used for muon track reconstructions in IceCube:

– **Single Photo-Electron (SPE)**: In this implementation only the arrival time of the first photon at each DOM enters the likelihood calculation. The algorithm uses the `linefit` reconstruction result as a starting seed and returns a muon track solution with better angular resolution. Due to its speed, this reconstruction is run online in single-iteration mode at the South Pole to search for events that pass different classification criteria in almost real time. Unless stated otherwise, the reconstruction used in the IceCube anisotropy studies presented in this work is the SPE reconstruction performed at the South Pole. An example IceCube event and the corresponding SPE reconstruction is shown in Fig. 2.8.

– **Multi Photo-Electron (MPE)**: The SPE reconstruction ignores all photon hits but the first in the likelihood calculation. It is clear, however, that a better reconstruction quality may be achieved by using the timing information of all hits. For this reason, the MPE reconstruction computes the likelihood that the first of N photons arrived at

a given time. The MPE reconstruction provides a better angular resolution than the SPE method, usually of the order of a degree or better.

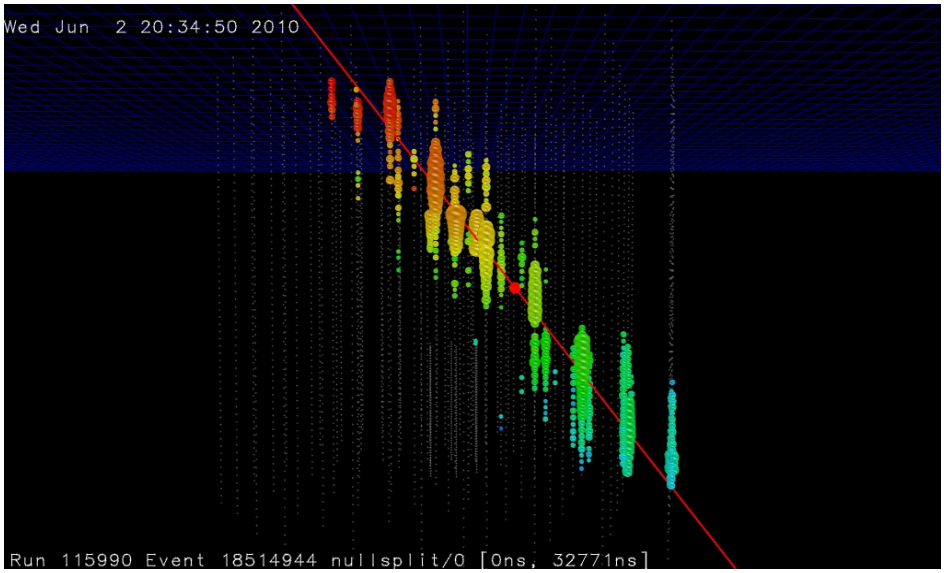

Figure 2.8: A down-going event recorded by IceCube with one or more cosmic-ray muons reaching the detector with a total energy of the order of hundreds of TeV. The color scale indicates the time at which light reached the triggered DOMs, where red corresponds to earlier times and blue to later times. The red line indicates the best muon track solution for the observed distribution of hits.

2.2.4 DST Data Stream

The high trigger rate of IceCube ($\sim$ 2.6 kHz in IC86) sets a practical limit on the amount of information that can be stored for every event. For this reason, the raw data is only stored for those events that pass one of several DAQ filters that select events deemed interesting according to predefined criteria. Since down-going cosmic ray muons dominate the trigger rate, the storage of raw data for all of them is not possible. Instead, a more compact Data Storage and Transfer (DST) format is used to store the results of the online reconstruction performed on all events that trigger IceCube.

The DST format stores the time of the event, the direction angles (θ, ϕ) of the reconstructed SPE track, the number of triggered strings and DOMs, the number of photon hits in the detector, and the result of a muon energy estimation, among other information. The data are encoded in a compressed format that allows the transfer of about 3 Gb per day via the South Pole Archival and Data Exchange (SPADE) satellite communication system.

The DST stream is the main source of information on cosmic-ray arrival directions for the anisotropy analysis. The median energy and the median angular resolution of the events in the DST stream has been determined using simulated air showers generated using the CORSIKA Monte Carlo program[1] [97]. The median angular resolution of the simulated DST events is about 3°, and the median energy of the sample is about 20 TeV. A more detailed description of the resolution and the median energy scale of the DST data set is given in Chapter 5.

2.3 IceTop

The IceTop air shower array consists of 81 stations distributed over an area of $1\,\mathrm{km}^2$ as shown in Fig. 2.2. Each station is located near an IceCube string hole, so that neighboring stations are placed at a distance of about 125 m from each other on a hexagonal grid. The detector is described in detail in [98].

The construction of IceTop was conducted in parallel to the installation of IceCube strings between 2005 and 2010. The data used in this work was collected in three different periods: between May 2009 and May 2010 when the detector was operated in a 59-station configuration (IT59); between May 2010 and May 2011 when IceTop operated with 73 stations (IT73); and between May 2011 and May 2012 when the detector operated in its final 81-station configuration (IT81). Each IceTop station is made up of two light-tight ice Cherenkov tanks separated by about 10 m. The positions of the tanks in each station relative to the IceCube string holes is shown in Fig. 2.9.

[1] COsmic Ray SImulations for KAscade: `http://www-ik.fzk.de/corsika/`

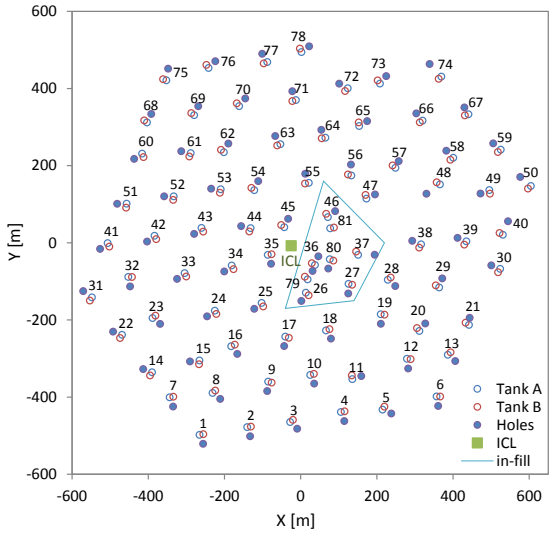

Figure 2.9: Detector diagram for IceTop showing the location of each station next to an IceCube string hole. Both tanks in each station are represented.

Each IceTop tank is 1.8 m in diameter, 1.3 m in height, and is filled with transparent ice up to a height of 0.9 m (Fig. 2.10). Frozen into the ice are two DOMs (Fig. 2.10) identical to those used in IceCube and already described in Subsection 2.2.1. DOMs in IceTop detect the Cherenkov light produced inside the tank by energetic muons and electrons in the cosmic-ray air shower. The two DOMs inside each IceTop tank are operated at different PMT gains (about 5×10^6 for the high-gain, and 10^5 for the low-gain) in order to increase the dynamic range of the detector. The two high-gain DOMs in each station (one located in each tank) are operated in Hard Local Coincidence (HLC) mode, and data readout is enabled if both observe photon hits within ± 1 μs of each other. The HLC requirement reduces the trigger rate from 1600 Hz per DOM to 3000 Hz for all DOMs in the detector. The Simple Majority Trigger (SMT) in IceTop requires at least six HLC hits within a time window of 5 μs, which implies that at least two stations participated in the event. This further reduces the trigger rate to about 30 Hz across the array.

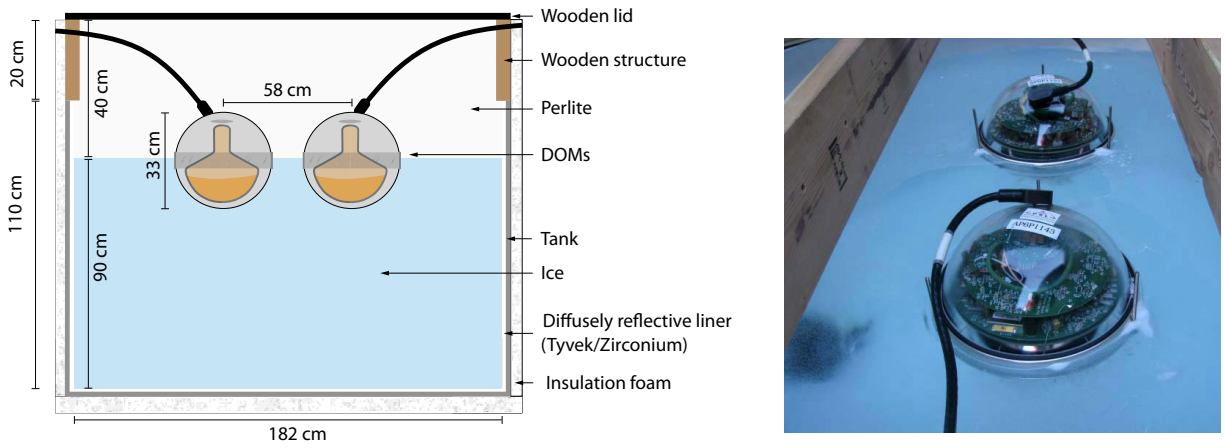

Figure 2.10: Schematic representation of an IceTop tank with its main components (left). A picture of the two DOMs already frozen into the ice inside the tank is shown on the left.

Most time traces recorded by IceTop DOMs have a similar shape. An IceTop waveform is characterized by a fast, linear rise leading to a sharp peak, followed by an exponential fall off. The pulse shape is due to the size of the tank and the reflectivity of its inner surface. As particles enter the tank, many Cherenkov photons reach the DOMs with little or no scattering. This produces the fast rise of the leading edge, taking about 10 ns to go from 10% to 90% of the total signal amplitude. After the shower front passes the tank, internal reflections produce the exponential fall off. The time constant of the exponential tail is 31 ns for most tanks, namely those equipped with a zirconium internal liner (70% - 80% UV reflectivity). For the 8 tanks installed in 2005 that were equipped with a Tyvek liner (90% reflectivity) the time constant is 43.5 ns.

The signal recorded by IceTop tanks is measured in units of "vertical equivalent muons" (VEM), which is the signal charge produced by a single muon that enters the tank vertically. The calibration of the number of observed photoelectrons that correspond to a VEM is obtained from data for each individual tank. Starting in 2009, a single-muon calibration trigger is run in continuous mode together with normal data taking to avoid the down-time

associated with dedicated calibration runs. The calibration plot for one tank is shown in Fig. 2.11.

Due to the limited bandwidth available for data transmission from the South Pole, only a fraction of all events are transferred over the satellite for further analysis. For this reason, the data is filtered according to the number of stations that participated in each event. The main filter for IceTop is known as `IceTopSTA3`, and requires at least 3 stations to have an HLC hit. Similarly, a `IceTopSTA8` filter was implemented during the operation of IT59, IT73, and the first year of IT81 that selects events with HLC hits in at least 8 stations. The `IceTopSTA3` filter sets an effective energy threshold of about 300 TeV on the air showers that are capable of meeting the filter criteria. To further reduce the high rate of `IceTopSTA3` events, events were prescaled by a factor of eight during the operation of IT59, and by a factor of three during IT73 and IT81. Events that passed the `IceTopSTA8` filter (i.e. with at least 8 stations) were not prescaled. Other filters select for IceCube/IceTop coincident events or for events that have triggered the infill array shown in Fig. 2.9 but were not used in this work.

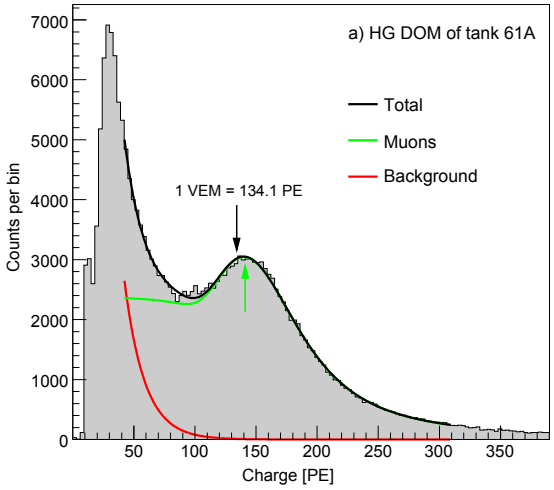

Figure 2.11: VEM calibration plot for the high-gain DOM of tank 61A. From this plot it is determined that 1 VEM corresponds to a charge of 134.1 photoelectrons recorded by the DOM.

2.3.1 Angular Reconstruction

The angular reconstruction used for anisotropy studies with IceTop assumes that the shower front reaching the detector array can be described as a plane wave propagating at the speed of light. A solution is fully constrained by defining a unit vector $\vec{s}$ perpendicular to the shower plane passing the origin at time t_0. The position of the origin $\vec{b}$ is defined as the signal-weighted average of the tank positions that participated in the event.

For a plane wave, the time t at which each tank is hit is a function of the position $\vec{x}$ of the tank in the ground relative to the origin $\vec{b}$, the orientation of the plane $\vec{s}$, and t_0:

$$t(\vec{x}) = t_0 - \frac{|\vec{x} - \vec{b}|}{c}\vec{s}\,. \tag{2.5}$$

A fit to the shower plane using the observed hit times can be obtained by minimizing the χ^2 expression:

$$\chi^2 = \frac{1}{\sigma_t^2}\sum_i [t_i - t(\vec{x_i})]^2 = \frac{1}{(c\sigma_t)^2}\sum_i [ct_i - ct_0 + (x_i u + y_i v + z_i w)]^2 \tag{2.6}$$

where the vector components correspond to $\vec{s} = (u, v, w)$ and $\vec{x_i} = (x_i, y_i, z_i)$ and σ_t is the uncertainty in the measured trigger time. By requiring $\vec{s}$ to be a unit vector, it can be written as $\vec{s} = (u, v, \sqrt{1 - u^2 - v^2})$, which makes the problem non-linear. A linear solution can be found for the simplified case where all the tank coordinates in z are equal. This is a good approximation for the case of IceTop (and also for most air shower arrays) as height differences between tanks across the array are at most 5 m (Fig. 2.12), implying that $z_i \ll x_i, y_i$. The algorithm used in IceTop, called `ShowerPlane`, neglects the z coordinate of the tanks and analytically minimizes the χ^2:

$$\sigma^2 = \frac{1}{(c\sigma_t)^2}\sum_i [c(t_i - t_0) + x_i u + y_i v]^2 \tag{2.7}$$

assuming that σ_t is 5 ns for all tanks. Once the direction of the shower is found for a flat geometry, a second iteration is performed that corrects the signal times for the tank altitudes:

$$t_i' = t_i + \frac{z_i - \langle z \rangle}{c} cos\theta. \tag{2.8}$$

where $\langle z \rangle$ is the average tank altitude, and θ is the zenith angle of the shower found in the first iteration. The event is reconstructed again using the corrected times.

The `ShowerPlane` reconstruction has an angular resolution of about 3°, which is well suited for anisotropy studies in the TeV-PeV energy range. More detailed reconstructions exist for IceTop that are mostly intended for cosmic ray energy spectrum and composition studies. These reconstructions require some quality cuts to be performed, which reduces the statistics of the sample, while improving only slightly the angular resolution.

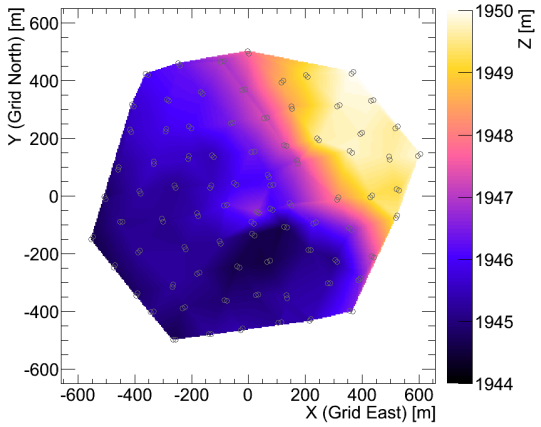

Figure 2.12: Measured heights of IceTop stations with respect to the center of the IceCube array. A total amplitude of about 6 m is found for the heights of all stations across the array.

As with IceCube, the median energy of the IceTop data sets was determined using air shower simulations. The median energy of events triggering at least eight stations (i.e. those that pass the `IceTopSTA8` filter) have a median energy of about 2 PeV, while those with more than three but less than eight stations have a median energy of about 400 TeV. A more detailed description of the energy estimation of the data set is given in Chapter 6.

2.4 AMANDA

The Antarctic Muon and Neutrino Detector Array (AMANDA) [99] was the predecessor experiment to IceCube. AMANDA consisted of 19 vertical strings equipped with 677 optical modules (OMs) that instrumented a cylindrical volume with a diameter of 200 m. Most optical modules were deployed at depths between 1500 m and 2000 m below the ice surface, as shown in Fig. 2.13. The location of AMANDA relative to IceCube and IceTop is shown in Fig. 2.2. The inner ten strings of the detector (302 OMs) were installed between 1995 and 1997, and constituted the AMANDA-B10 configuration. The installation of nine additional strings by early 2000 gave way to the start of operation of the AMANDA-II detector, which stopped running in 2009. All AMANDA data contained in this work was recorded during the operation of the AMANDA-II configuration.

The AMANDA OM consists of a 30 cm glass pressure sphere that contains an 8-inch Hamamatsu R5912-2 PMT with a bialkali photocathode (20% peak quantum efficiency). A layer of silicone gel optically couples the PMT to the glass sphere. The high voltage for the PMT was provided through the cables connecting it to the surface. As a contrast to the IceCube design, digitization of the PMT signals was not performed *in situ*, signals were instead transmitted in analog form to the surface. The long transmission cables ($\sim$ 2 km in length) attenuated the amplitude of the signals from about 10 mV in the ice to 1 mV at the surface. For this reason, OMs were operated at very high electronic gains of about 10^9, which occasionally caused the PMTs to spark and produce light.

The long cables used for signal transmission (either coaxial or twisted-pair) also broadened the PMT pulses, with typical time-over-thresholds of 550 ns and rise times of 180 ns. The muon-DAQ system amplified the signals and fed them to two outputs, one direct and one delayed by 2 μs. The direct signal was connected to a discriminator, and then to a trigger and a Time-to-Digital Converter (TDC) that recorded successive crossings of the discriminator threshold. The delayed output was connected to a Analog-to-Digital Converter (ADC) that determined the maximum amplitude of all the pulses.

The delay time introduced by the signal propagation through the cables was determined by injecting short pulses of laser light through an optical fiber from the surface at known times. A measured delay time was found for each OM in the detector, and then applied as a correction in data analyses. The resulting timing uncertainty across the detector was about 15 ns, while the individual OM timing resolution was < 5 ns. In a later version, OMs transmitted PMT signals to the surface using an optical fiber, which improved the OM timing resolution to 3.5 ns.

Two main triggers were used in AMANDA:

– Multiplitiicy trigger: Requires that 24 OMs should register hits within a 2.5 μs window.

– String trigger: Mainly oriented towards low-energy muons. It required 6 hit OMs from the inner four strings, or 7 hit OMs from the remaining strings within 2.5 μs.

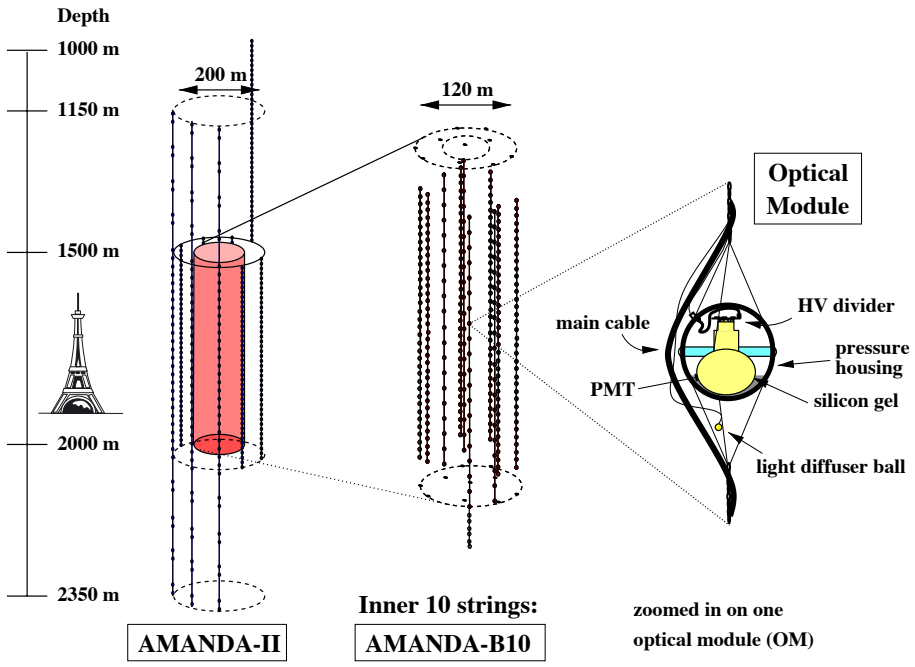

Figure 2.13: Detector diagram for AMANDA. The data used in this work was collected using the AMANDA-II configuration. The location of AMANDA inside the IceCube detector volume is shown in Fig. 2.2.

Similarly to IceCube, a compressed readout format was implemented in AMANDA, called `nano-dst`, that included a reduced number of event variables and the results of fast reconstructions done at the pole for monitoring and quality assurance studies. The AMANDA analysis presented in this work is based on data from the `nano-dst` data stream. The angular reconstruction included in the `nano-dst` data is described in the next Subsection.

2.4.1 Angular Reconstruction

A first guess for the arrival direction of muons in AMANDA was obtained using the `DirectWalk` algorithm [100], which selects hits most likely to be caused by direct photons.

The event reconstruction involves four separate steps:

1. *Track elements* are constructed by creating straight lines between any two hits at distance d. The track element is constrained by a direction (θ, ϕ), a vertex (the average of the two OM positions), and a vertex time t_0 (the average of the two hit times). The time difference between the two hits Δt should satisfy

$$|\Delta t| < \frac{d}{c_{\text{vac}}} + 30 \text{ ns} \tag{2.9}$$

   with $d > 50$ m.

2. The number of *associated hits* (AH) is calculated for each track element, which are defined as the hits for which -30 ns $< t_{\text{res}} <$ 300 ns, and $d < 25\text{m} \cdot (t_{\text{res}} + 30)^{1/4}$, with t_{res} in ns. The definition of the residual time t_{res} is the same as for IceCube: the time with respect to the arrival of direct photons with no scattering. After the hit selection, track elements of poor quality are removed by requiring that $N_{\text{AH}} \geq 10$ and the standard deviation of L

$$\sigma_L = \sqrt{\frac{1}{N_{\text{AH}}} \sum_i (L_i - \langle L \rangle)^2} \geq 20 \text{ m}, \tag{2.10}$$

   where L is the distance between the track element vertex and the nearest distance between OM i and the track element, and $\langle L \rangle$ is the average over all L_i. Track elements that pass these requirements are considered *track candidates* (TC).

3. Since it is possible that more that one TC is found, a cluster search is performed on the track candidates using the quality parameter Q_{TC}, defined as $min(N_{\mathrm{AH}}, 0.3\mathrm{m}^{-1}\cdot\sigma_L+7)$. The quality condition for a TC j is $Q^j_{\mathrm{TC}} > 0.7Q_{\mathrm{max}}$ where Q_{max} is the maximum Q_{TC} for all track candidates. The number of "neighbors" (track candidates with an opening angle less that 15° from each other) for each TC is counted. The cluster with the most TC is selected.

4. The final track direction is defined as the average direction of all TCs inside the cluster. The track vertex and time are taken from the central track candidate in the cluster.

The `DirectWalk` algorithm has been shown [101] to reconstruct atmospheric muons with a resolution of about 5°, which makes it suitable for anisotropy studies. Events triggering AMANDA have a median energy of approximately 10 TeV [102]. The primary energy is lower than in IceCube because of the shallower depth at which AMANDA is deployed and its smaller volume, which makes it sensitive to lower energy muons.

Chapter 3

Moon-Shadow Analysis

3.1 Introduction

The search for cosmic-ray anisotropy relies on understanding the absolute pointing capabilities and the angular resolution of the detectors employed in the study. The pointing and angular resolution of IceCube can be tested by studying the deficit of cosmic-ray muons from the direction of the Moon. This effect, due to the absorption of cosmic-ray primary particles by the Moon, is shown schematically in Fig. 3.1 and was first predicted by Clark in 1957 [103]. Its observation has been used by several experiments as a way of calibrating the angular resolution and the pointing accuracy of their particle detectors (see [104], [105], [106], [107], or [108] for recent results.)

The cosmic-ray "Moon shadow" is employed as a verification tool for the track reconstruction algorithms presented in Section 2.2.3 that are used in the search for cosmic-ray anisotropy and point-like sources of astrophysical neutrinos [109], among other analyses. In this chapter we will report on the observation of the Moon shadow using data taken between April 2008 and May 2010, which corresponds to the IC40 and IC59 configurations of the IceCube detector (Table 2.1).

Two independent analysis methods were used in the search for the Moon shadow. The first analysis performs a binned, one-dimensional search for the Moon shadow that compares the number of events detected from the direction of the Moon to the number of background events recorded at the same declination as the Moon but at a different right ascension.

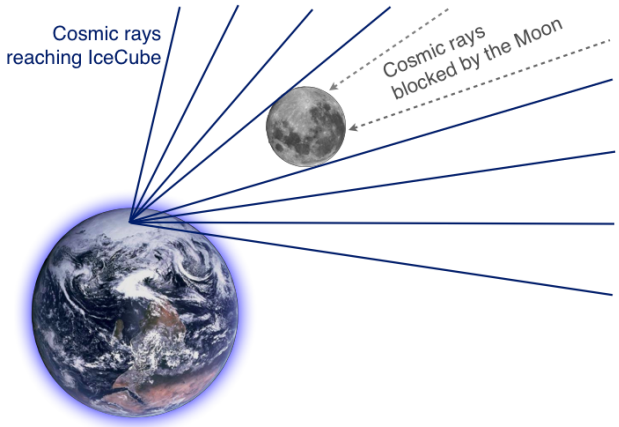

Figure 3.1: Schematic representation of the shadowing of cosmic rays by the Moon.

The second method uses an unbinned, two-dimensional maximum likelihood algorithm that retrieves the best fit value for the total number of events shadowed by the Moon.

Both methods show consistent results and were published in [110]. This observation constitutes the first statistically significant detection of the shadow of the Moon using a high-energy neutrino telescope.

3.2 Detector Configuration and Data Sample

The layout of the two detector configurations used in this work is shown in Fig. 3.2. During the operation of IC40, the cosmic muon-induced trigger rate was about 1.1 kHz, which increased to about 1.7 kHz during the IC59 data-taking period. This high rate of cosmic-ray muon events provides a high-statistics data set that can be used to search for the Moon shadow. In order to limit the number of muon events transmitted to the North, a dedicated online filter was used to store events passing minimum quality cuts and that are reconstructed within a predefined angular acceptance window around the Moon.

A fast single-iteration SPE reconstruction is performed at the South Pole to obtain the arrival direction of each event. The reconstructed direction of the muon track is then

compared to the position of the Moon in the sky, which is calculated using the publicly-available `SLALIB` library of astronomical routines [111].

An event satisfies the Moon filter selection criterium if at least 12 DOMs in 3 different strings record photon hits, and if the reconstructed direction is within 10° of the Moon position in declination and $40°/\cos(\delta_\mu)$ in right ascension (where δ_μ is the declination of the event and the cosine factor accounts for projection effects.)

The filter is enabled when the Moon is at least 15° above the horizon. Due to the particular geographic location of IceCube at the South Pole, the Moon crosses this threshold only once per month, as its elevation above the horizon changes slowly over the course of days. Since the number of muon events recorded by IceCube is a strong function of the elevation angle, the rate of events that pass the acceptance window condition changes during this period as this window follows the apparent motion of the Moon at the South Pole. The strong correlation between Moon elevation and rate of events passing the Moon filter is shown in Fig. 3.3. The maximum event rate is also modulated over a longer time scale of 18.6 years (known as the lunar draconic period [112]) in which the maximum elevation of the Moon above the horizon at the South Pole oscillates between the extreme values of 18.4° and 28.4°. The maximum Moon elevation during the IC40 data-taking period was 26.9°, while for IC59 it was 25.6°. Approximately 1.29×10^8 muon events passing the Moon filter condition were recorded during the IC40 data-taking period, and about 1.77×10^8 events were recorded during the operation of the IC59 configuration.

Once these events have been transferred from the South Pole, the SPE reconstruction is performed again with a larger number of iterations (32 for IC40 and 8 for IC59), which improves the angular resolution of the reconstruction. An algorithm, usually called "paraboloid fit," is used to determine the angular uncertainty in the reconstructed track direction by mapping the likelihood space around the best track solution and fitting it with a paraboloid function [113]. A narrow paraboloid indicates a precise reconstruction, while a wide paraboloid indicates a larger uncertainty in the reconstructed direction of the muon track. The 1σ contour line of the paraboloid function defines an error ellipse for the reconstructed direction of

the track. In this analysis, a single, one dimensional estimator of the uncertainty is obtained by adding in quadrature the semi-major axes of that error ellipse.

The results presented in this chapter are based on the SPE reconstruction, which is the reconstruction used for the cosmic-ray anisotropy analysis. For a discussion on the observation of the Moon shadow based on the MPE reconstruction commonly used in neutrino analysis the reader is referred to [110].

The track reconstruction algorithms use the local detector coordinate system and the direction of a reconstructed track is given as a zenith and azimuth angle. Using the event times as recorded by the data acquisition system these are transformed into a right ascension α_μ and declination δ_μ.

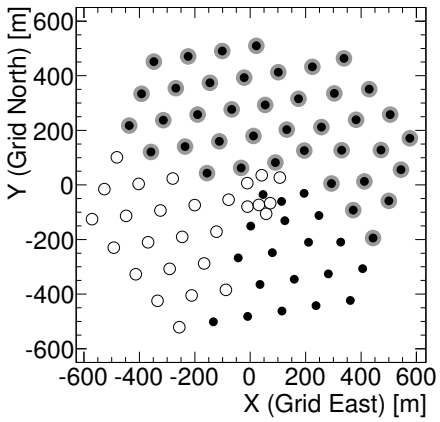

Figure 3.2: Layout of the two detector configurations considered in this analysis. IC40 (*gray*) operated between 2008 and 2009. The deployment of more strings initiated the IC59 configuration (*black*) operated between 2009 and 2010. The remaining strings that form the final 86-string configuration, the last of them installed in December 2010, are shown as open circles. The y axis (Grid North) is aligned with the Greenwich Prime Meridian.

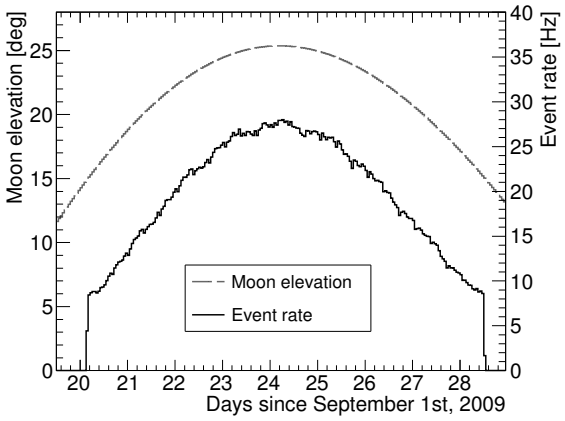

Figure 3.3: Rate of muon events passing the Moon filter during the month of September 2009, when IceCube was operating in its IC59 configuration. The correlation between Moon elevation (*dashed line*) and event rate (*solid line*) is clearly visible.

3.3 Cosmic-Ray Energy and Composition

The muons produced in the interaction between cosmic rays and the atmosphere must traverse several kilometers of ice before reaching the IceCube detector, losing energy in the process. This sets a lower limit of several hundred GeV on the energy of the muons at ground level that would trigger the detector. By extension, the primary cosmic-ray particle needed to produce this kind of muon should have an energy of at least several TeV.

Given that this analysis deals with cosmic-ray showers near the energy threshold of the detector, the number of muons produced in each shower that reach the detector is small. Most events in the Moon data sample are composed of one or two energetic muons, and only 2% of the events have muon multiplicities higher than ten.

The detailed energy scale for the IC40 and IC59 data sets was determined using simulated cosmic-ray air showers created with the CORSIKA Monte Carlo code [97] using the SIBYLL model of high-energy hadronic interactions [114]. The chemical composition and spectral shape of the cosmic rays generated in this simulation follow the polygonato model [20].

From these simulations, we estimate that the median energy of the primary cosmic rays that trigger the IceCube detector is 20 TeV, while the median energy of events that satisfy the Moon filter condition is about 40 TeV for both IC40 and IC59, with 68% of the events between 10 TeV and 200 TeV. The increased median energy of the filtered sample is due to the greater average zenith angles of the cosmic rays that pass the filter, which requires primary particles with enough energy to produce muons able to traverse more ice and trigger IceCube. The muons produced by cosmic rays passing the Moon filter have a mean energy of about 2 TeV at ground level and reach the detector with a mean energy of 200 GeV. The distribution of the average muon energy in air showers that trigger IceCube is shown in Fig. 3.4. Events from two filters are compared: the Moon filter and the "minimum bias" filter, where every 2000th event is selected from the data stream which creates an unbiased event sample.

The energy spectrum of all primary cosmic rays triggering the IceCube detector is shown in Fig. 3.5 and compared to the spectrum of those that pass the Moon filter. Also shown in the figure are the five main chemical elements (protons, He, C, O, and Fe) that make more than 95% of the Moon filter data sample assuming the polygonato composition model. The two main components of the sample are proton (68% of the events) and helium (23%).

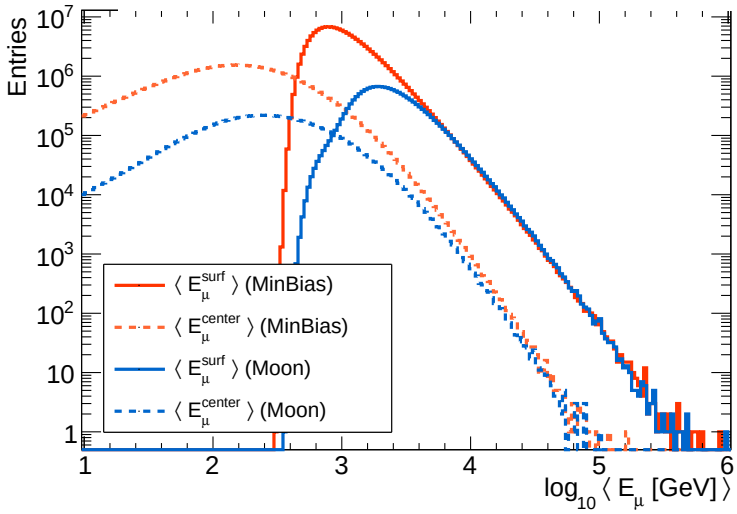

Figure 3.4: Distribution of average muon energies for air showers triggering IceCube. Events passing the Moon (*blue*) and Minimum Bias (*orange*) filters are shown, where the average energy of the muons is calculated at the ice surface (*solid line*) or near the center to the detector (*dashed line*). The decrease in average muon energy from about 2 TeV at the surface to about 200 GeV in the detector is due to energy losses in the ice. The average energy of the Moon events is higher due to their higher inclination compared to the all-sky Minimum Bias sample.

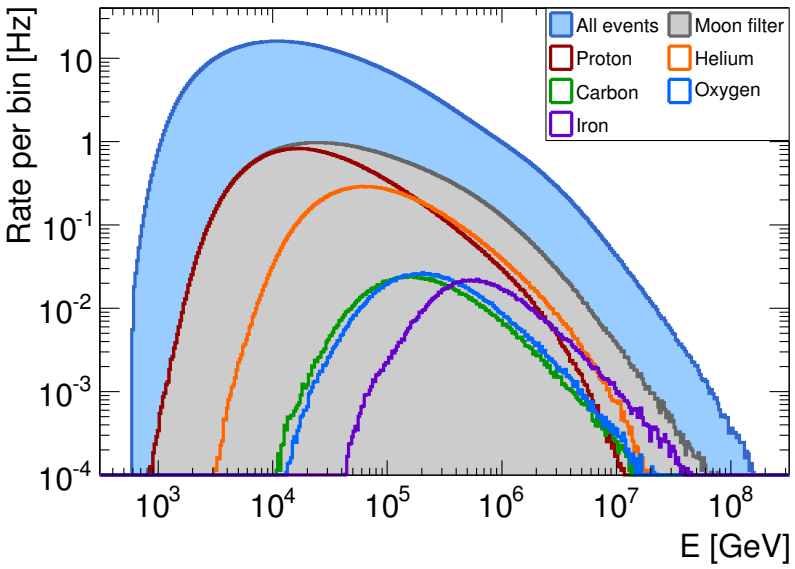

Figure 3.5: Differential event rate as a function of cosmic-ray primary energy for all events in IC59 (*light blue*) and for only those passing the Moon filter (*gray*) as determined from simulation studies. The main chemical elements that make up the events passing the Moon filter are shown with lines of different color. The width of the energy bins is 0.014 in $\log_{10}(E)$. The IC40 configuration shows a similar energy response.

3.4 Geomagnetic Field Effects

Cosmic rays with TeV energies should experience a small deflection in their trajectories due to the influence of the geomagnetic field as they propagate towards the Earth. This deflection would appear in this analysis as a shift in the position of the shadow with respect to the true Moon position, which could be wrongly interpreted as a systematic offset produced by the event reconstruction.

A particle propagation code that can trace cosmic rays through the Earth's magnetic field has been developed to quantify this offset and compare it with any possible shift observed in the data. The results of this propagation study are presented in this section.

3.4.1 The Magnetic Field of the Earth

The magnetic field of the Earth has a highly complex and time-dependent structure that can be mathematically approximated in a number of ways. The simplest model assumes a perfect dipole field, so that its strength at any point around the Earth can be characterized by a radial (B_r) and an azimuthal (B_θ) component [115]. These components can be calculated using the equations:

$$B_r = -2B_0 \left(\frac{R_E}{r}\right)^3 \cos\theta, \tag{3.1}$$

$$B_\theta = -B_0 \left(\frac{R_E}{r}\right)^3 \sin\theta \ . \tag{3.2}$$

Here, r is the distance from the center of the Earth and has the same units as R_E (the Earth's radius), B_0 is typically 3.11×10^{-5} T, and θ is the angle from the North magnetic pole. The magnetic axis of the Earth is tilted with respect to the axis of rotation by $\sim 11.5°$.

This first order approximation works well near the surface of the Earth, and away from the magnetic poles. A more accurate model includes not only the dipole term, but several more components in a spherical harmonics expansion of the real magnetic field. The most

widely used of these models is the International Geomagnetic Reference Field (IGRF)[1] [116], currently in its eleventh revision, which includes a spherical multipole expansion up to order 13 and can account for time variations of the magnetic field as measured by satellites.

Both the dipole and the IGRF-11 models describe what is known as the *internal* magnetic field of the Earth, which is presumably produced by electrical currents in the outer core of the planet and represents $\sim 95\%$ of the total field strength. The remaining 5% is produced by *external* sources, namely by electrical currents in the ionosphere produced by ionizing solar radiation.

While the internal field is stable in time scales of days, it gradually changes over the years. The external field, on the other hand, is extremely variable and can change over very short time scales of the order of minutes in the occurrence of a solar magnetic storm. The standard model for the external component of the magnetic field has been produced by Tsyganenko [117, 118]. The model is based on magnetometer data from seven spacecrafts (Geotail, Polar, ISEE 2, AMPTE/CCE, AMPTE/IRM, CRRES, and DE 1), and can account for the variability of the space weather if given parameters such as the solar wind direction and ram pressure, which can be retrieved from a database as time-dependent quantities. The model itself has been made publicly available as a suite of FORTRAN routines called GEOPACK-2008[2].

The total strength of the magnetic field for the IGRF-11 and Tsyganenko models (as well as the sum of both) is shown in Fig. 3.6.

3.4.2 Propagation Algorithm

The propagation algorithm used to calculate the trajectory of cosmic-ray particles in the Earth's magnetic field is similar to others available in the literature [115, 119]. The trajectory is computed by tracking particles outwards from the detector towards the Moon through the magnetic field. The particles are given the opposite electrical charge to those

[1] IGRF website (with code implementation of the model): `http://www.ngdc.noaa.gov/IAGA/vmod/igrf.html`

[2] Tsyganenko's GEOPACK website: `http://geo.phys.spbu.ru/~tsyganenko/modeling.html`

being considered. This significantly simplifies the problem since the deflection experienced by, say, a proton as it approaches the Earth has the same magnitude and direction as that experienced by an *antiproton* as it travel *away* from the Earth.

For the calculation, let us assume a cosmic-ray particle with energy E, mass m, and charge Z that travels through the Earth's magnetic field starting from position $\mathbf{x}$ with velocity $\mathbf{v}$, where the position is defined with respect to a coordinate frame with its origin at the center of the Earth.

For TeV particles, we can consider that the energy losses that occur during propagation in the vicinity of the Earth, and the possible energy gains associated with electric fields in the local interplanetary medium are both negligible. In this energy range, the ultrarelativistic limit applies, which means that for the particle $|\mathbf{v}|$ remains close to c during propagation while only the direction of the velocity vector is affected by the geomagnetic field through the Lorentz force.

A fast numerical calculation of the effect of the Lorentz force on the trajectory of the particle can be performed by introducing small rotations in the velocity vector of the cosmic ray. The direction in which the velocity vector is rotated depends only on the relative orientation between the magnetic field vector and the direction of motion of the particle, while the rotation angle $d\theta$ depends on the strength of the magnetic field.

The cyclotron frequency for a particle of charge Z, mass m, and Lorentz factor γ located at position $\mathbf{x}$ where the strength of the magnetic field is $|\mathbf{B}(\mathbf{x})|$, is:

$$\omega_g = \frac{Z|\mathbf{B}(\mathbf{x})|}{\gamma m} \quad . \tag{3.3}$$

After a time dt the CR velocity vector is rotated by an amount $d\theta$:

$$d\theta = \omega_g dt \quad . \tag{3.4}$$

This rotation is performed with respect to an axis defined by an unit vector $\mathbf{b}(\mathbf{x})$ that points in the same direction as the local magnetic field $\mathbf{B}(\mathbf{x})$. The new velocity vector of the particle $\mathbf{v}'$ is obtained from the expression:

$$\mathbf{v}' = \mathbf{R}(\mathbf{b}(\mathbf{x}), d\theta)\ \mathbf{v} \quad , \tag{3.5}$$

where $\mathbf{R}(\mathbf{b}(\mathbf{x}), d\theta)$ is a rotation matrix that is used to rotate the velocity vector around $\mathbf{b}$, and that can be written as:

$$\mathbf{R}(\mathbf{b}(\mathbf{x}), d\theta) = \begin{bmatrix} C + b_x^2\,(1-C) & b_x b_y\,(1-C) - b_z S & b_x b_z\,(1-C) + b_y S \\ b_y b_x\,(1-C) + b_z S & C + b_y^2\,(1-C) & b_y b_z\,(1-C) - b_x S \\ b_z b_x\,(1-C) - b_y S & b_z b_y\,(1-C) + b_x S & C + b_z^2\,(1-C) \end{bmatrix} \quad ,$$

where $C = \cos d\theta$, and $S = \sin d\theta$. The new position of the particle after time dt is obtained simply by calculating:

$$\mathbf{x}' = \mathbf{x} + \mathbf{v}'\ dt \quad . \tag{3.6}$$

Using this method, the trajectory of the particle is obtained by calculating in each step n a new position and velocity based only on the current values of both quantities and the magnetic field at that location:

$$\mathbf{x}^{(n+1)} = \mathbf{x}^{(n)} + \mathbf{R}^{(n)}(\mathbf{b}, d\theta)\ \mathbf{v}^{(n)}\ dt \quad . \tag{3.7}$$

The value of the time interval dt is selected so that the distance traveled by the particle during that time $d\ell = \mathbf{v}dt$ is small compared to the total distance over which the particle will be propagated. The time interval can also be made a function of the gyroradius of the particle in the magnetic field (Eq. 1.1) in order to increase the number of points in the trajectory in regions where the magnetic field is high (e.g. near the Earth), but reduce it when the field strength decreases (e.g. far away from the Earth).

Several tests were performed to verify the performance of the code in different particle energy regimes. An example of the trajectory of a 50 MeV proton injected at a distance of 3 R_E from the center of the Earth is shown in Fig. 3.7. The resulting particle path shows the characteristic pattern associated with the trapping and mirroring of protons in the magnetosphere of the Earth at these energies.

More examples of three-dimensional trajectories for protons with MeV, GeV, and TeV energies are given in Fig. 3.8. In this case, the protons are injected far away from the Earth on a regular grid and experience different degrees of deflection depending on their energy. While MeV protons drape around the magnetosphere, GeV protons are strongly scattered, and TeV protons show only small deflections. These simulations illustrate the shielding effect of the magnetic field to low-energy particles. The field induces a position-dependent "geomagnetic cutoff," which represents the minimum particle rigidity that is necessary to reach the surface of the Earth. Due to its proximity to the magnetic south pole, the geographic south pole has a very low cutoff (< 1 GV), which is sensitive to the level of solar activity.

Shown in Fig. 3.9 is the angular deflection of a 10 TeV proton as a function of distance from the Earth. Most of the bending in the particle trajectory occurs relatively close to the Earth ($r < 5R_E$), which is due to the $1/r^3$ dependence of the field strength. For this reason, particle paths are calculated up to a distance of 30 R_E (about half the total distance to the Moon) at which point the opening angle between the initial and final velocity vectors is computed (i.e. the deflection angle). The plot also shows that the dipole model gives results that are similar to the IGRF model, or even to the case where the Tsyganenko external field has been included. Since the calculation of the field using IGRF is fast, we use this model for the propagation studies presented in this work. The inclusion of the Tsyganenko field significantly slows down computations, and since its impact is small it has been omitted in this study.

3.4.3 Results

Using the algorithm described above, the deflection angle induced by the geomagnetic field was calculated. In our simulation, primary cosmic rays are propagated in the direction of the Moon as seen from the South Pole for different times during the data taking period. The cosmic-ray energy and chemical composition is sampled from the event distributions that pass the Moon filter, shown in Fig. 3.5. The resulting total deflection $\Delta\lambda$ is shown in Fig. 3.10 as a function of energy for 10^5 simulated cosmic ray particles for the five main chemical elements that contribute to the Moon dataset. The energy and charge dependence of the deflection angle is evident in the plot. Different bands in the plot correspond to different chemical elements. The width of each band is due to particles that were propagated in different directions in the sky (i.e. through different regions of the Earth's magnetic field) experiencing different deflections. A power-law fit to the simulation results has been performed to estimate the deflection angle as a function of energy and charge. The fit gives a good agreement for the following expression:

$$\Delta\lambda[^\circ] = 1.9^\circ \frac{Z}{E[\mathrm{TeV}]} \quad , \tag{3.8}$$

where Z is the cosmic-ray charge in units of elementary charge e, E is its energy in TeV, and $\Delta\lambda$ is given in degrees. This expression has the same functional form as the one found in [120] with a higher normalization in our simulation, which could be due to the difference in geographic location and other simulation details.

The deflection of each cosmic ray with arrival direction (α_μ, δ_μ) in sidereal coordinates is calculated with respect to the position of the Moon at the time of the event $(\alpha_{\mathrm{Moon}}, \alpha_{\mathrm{Moon}})$. The two coordinates that characterize the position of an event in this system are a right ascension difference $\Delta\alpha = (\alpha_\mu - \alpha_{\mathrm{Moon}}) \cos\delta_\mu$, and a declination difference $\Delta\delta = \delta_\mu - \delta_{\mathrm{Moon}}$ with respect to the nominal Moon position. The median shift in right ascension $\Delta\alpha$ for all particles in our simulation is 0.08°, with 68% of the particles having deflection angles in the interval $0.02^\circ < \Delta\alpha < 0.24^\circ$. The median shift in declination $\Delta\delta$ is 0.0°, with 68% of the events contained in the interval $|\Delta\delta| < 0.035^\circ$.

The cosmic-ray muons that ultimately trigger IceCube are also deflected by the geomagnetic field. However, since their total track length is in the 50-100 km range and their energy is about 2 TeV, their contribution to the total deflection angle should be at most $\sim 0.015°$. For this reason, the muon contribution has been ignored in calculating the expected total deflection angle.

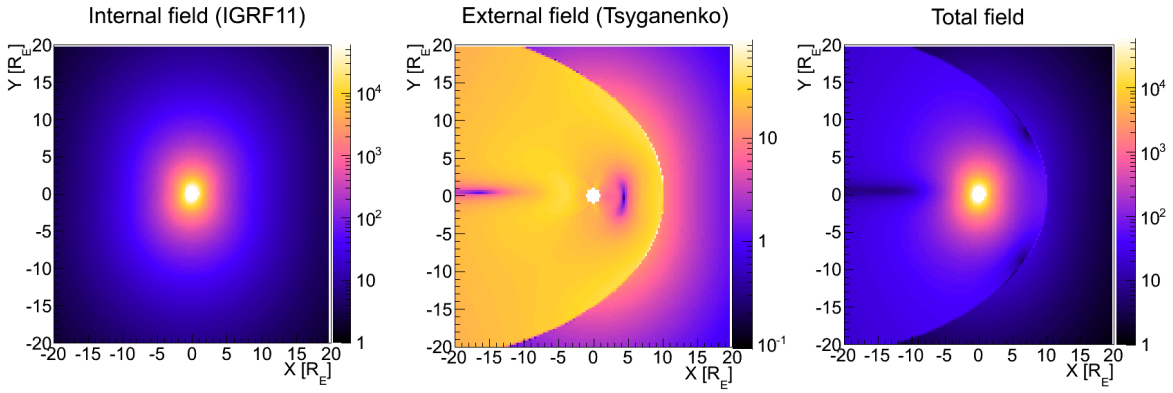

Figure 3.6: Comparison between magnetic field strengths (in nanoteslas) predicted by models of the internal (*left*), external (*center*), and total (*right*) field of the Earth. Position is indicated relative to the center of the Earth in Earth's radii (R_E) with the X axis pointing towards the direction of the Sun and the Y axis in the perpendicular direction towards North. The dipole behavior of the field is reproduced by the IGRF-11 internal field model, while a more complex structure is visible in the Tsyganenko model of the external component. The ram pressure of the solar wind creates a characteristic bow shock in the Earth's magnetosphere. Note the difference in strength between the internal and external fields. The total field is largely dominated by the internal component.

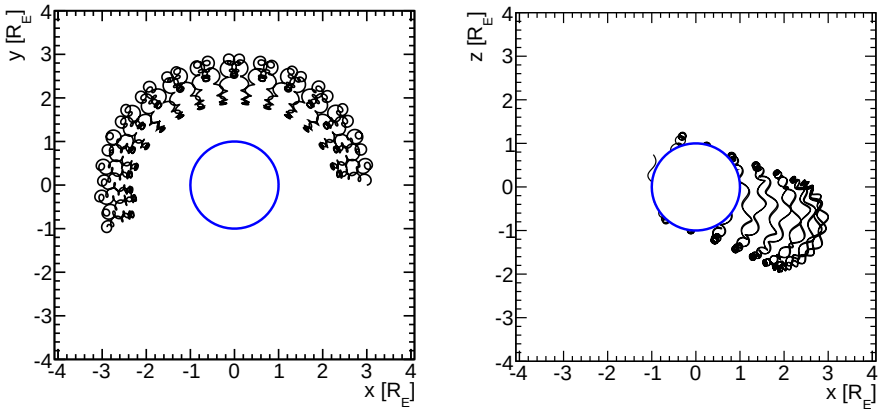

Figure 3.7: A 50 MeV proton trapped in the Earth's magnetosphere, as simulated with the propagation code. Distances are expressed in Earth radii (R_E).

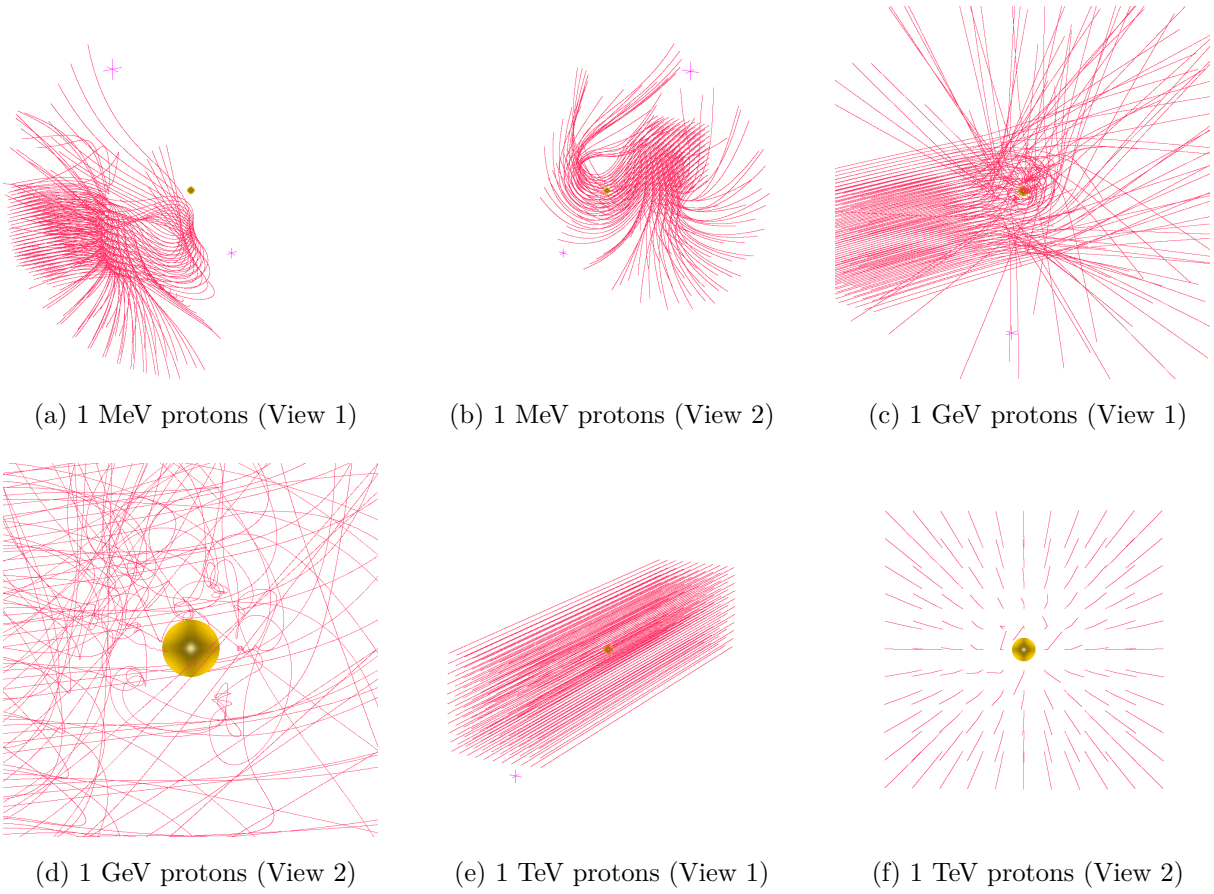

(a) 1 MeV protons (View 1) (b) 1 MeV protons (View 2) (c) 1 GeV protons (View 1)

(d) 1 GeV protons (View 2) (e) 1 TeV protons (View 1) (f) 1 TeV protons (View 2)

Figure 3.8: Examples of charged particle propagations in the magnetic field of the Earth. Shown here are two views of three-dimensional trajectories for protons with energies of 1 MeV (Figs. 3.8a and 3.8b), 1 GeV (Figs. 3.8c and 3.8d), and 1 TeV (Figs. 3.8e and 3.8f) injected on a regular grid at a large distance from the Earth and moving in parallel directions. While MeV protons mostly drape around the magnetosphere, GeV protons are strongly scattered by the field, with some of them reaching the Earth's surface (shown here as a yellow sphere in the middle of each plot). TeV protons, on the other hand, experience small deflections.

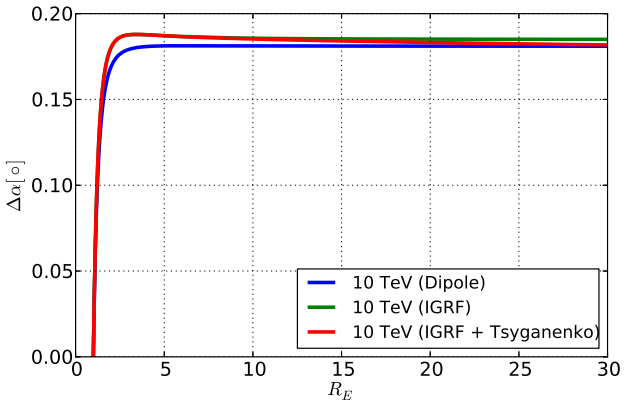

Figure 3.9: Deflection angle in degrees as a function of distance for a 10 TeV proton propagation outwards from the surface of the Earth through three different magnetic field models: dipole field (*blue*), IGRF field (*green*), and IGRF with Tsyganenko field (*red*).

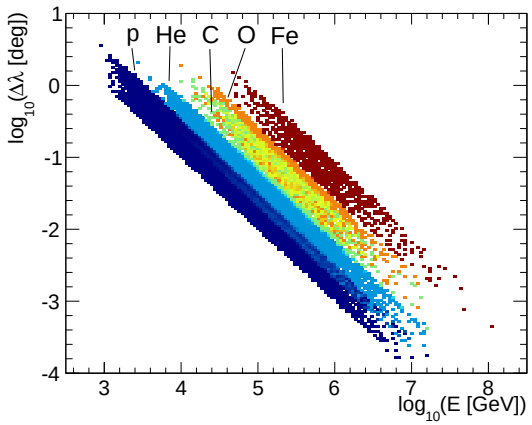

Figure 3.10: Angular deflection as a function of energy for the different chemical elements simulated using the particle propagation code described in Section 3.4.

3.5 Binned Analysis

3.5.1 Description of the Method

The main goal of the binned analysis is to obtain a profile view of the Moon shadow and measure its width, which can be used as a direct estimator of the angular resolution of the event reconstruction. This is accomplished by comparing the observed number of events as a function of angular distance from the Moon to an estimate of how many events would have been observed if there was no shadow.

For this comparison, the angular distance between the reconstructed muon tracks and the expected position of the Moon is binned in constant increments of 0.2° up to a maximum angular distance of 5°. This defines the so-called *on-source* distribution of events. The same binning procedure is applied to eight *off-source* regions centered around points located at the same declination as the Moon, but offset from it in right ascension by $\pm 5^\circ$, $\pm 10^\circ$, $\pm 15^\circ$, and $\pm 20^\circ$, where it is assumed that the shadowing effect is negligible. The average number of counts as a function of radius for these eight *off-source* regions represents the expectation in the case of no Moon shadow.

The relative difference between the number of events in the i-th bin in the *on-source* region N_i^{on}, and the average number of events in the same bin in the *off-source* regions $\langle N_i^{\text{off}} \rangle$ is calculated using the following expression:

$$\frac{\Delta N_i}{\langle N \rangle_i} = \frac{N_i^{\text{on}} - \langle N_i^{\text{off}} \rangle}{\langle N_i^{\text{off}} \rangle} \quad . \tag{3.9}$$

The uncertainty in the relative difference is given by:

$$\sigma_{\Delta N/\langle N \rangle} = \frac{N_i^{\text{on}}}{\langle N_i^{\text{off}} \rangle} \sqrt{\frac{1}{N_i^{\text{on}}} + \frac{1}{s \langle N_i^{\text{off}} \rangle}} \quad , \tag{3.10}$$

where $s = 8$ is the number of *off-source* regions. The distribution of relative differences as a function of angular radius from the Moon constitutes a profile view of the shadow.

Simulation studies indicate that the point spread function (PSF) of the detector can be approximated by a two-dimensional Gaussian function. We use this approximation to obtain

an estimate of the angular resolution of the track reconstruction by fitting the distribution of $\Delta N_i/\langle N\rangle_i$ for the events in the Moon data set.

Following [121], we treat the Moon as a point-like cosmic-ray sink that removes $\Phi\pi R_M^2$ events from the muon sample, where R_M is the angular radius of the Moon ($R_M \sim 0.26^\circ$) and Φ is the cosmic ray flux at the location of the Moon in units of events per square degree. This deficit is smeared by the PSF of the detector, which results in radially-symmetric two-dimensional Gaussian distribution of shadowed events which is a function of radial distance ψ from the center of the Moon. Integrating over the azimuthal coordinate of the symmetric Gaussian distribution yields:

$$f(\psi) = -\frac{\Phi\pi R_M^2}{\sigma^2} e^{-\psi^2/2\sigma^2} \quad , \tag{3.11}$$

where σ is the angular resolution of the directional reconstruction. The number of shadowed events in the i-th bin of width $\Delta\psi$ is given by the two-dimensional integral:

$$N_s(\psi_i) = \int_{\psi_i-\Delta\psi/2}^{\psi_i+\Delta\psi/2} \psi\ f(\psi)\ d\psi \tag{3.12}$$

$$\approx -\frac{\Phi\pi R_M^2 \Delta\psi}{\sigma^2} \psi_i\ e^{-\psi_i^2/2\sigma^2} \quad . \tag{3.13}$$

The number of events N_e that would have been observed in the same bin with no shadowing is $2\pi\Phi\psi_i\Delta\psi$. The ratio of equations 3.13 and N_e gives us the expected distribution of relative differences $\Delta N_i/\langle N\rangle_i$ for a detector with a Gaussian PSF of angular resolution σ:

$$\frac{N_s}{N_e}(\psi_i) = -\frac{R_M^2}{2\sigma^2} e^{-\psi_i^2/2\sigma^2} \quad . \tag{3.14}$$

This expression is used to fit the experimental data, and the resulting value of σ is compared to an estimate of the angular resolution of the data set obtained from simulation studies. Our treatment ignores the finite angular size of the lunar disc, which may affect the result of the fit. However, for the expected angular resolution of the Moon data set (of order 1° or less) this effect should influence the fit value of σ only at the few-percent level.

A set of cuts was developed to optimize for the statistical significance of the detection of the Moon shadow. Under the assumption of Poisson statistics, the relation between the significance S, the fraction η of events passing the cuts, and the resulting median angular resolution Ψ_{med} after cuts is:

$$S \propto \frac{\sqrt{\eta}}{\Psi_{\text{med}}} \quad . \tag{3.15}$$

The optimization of the cuts was performed on the CORSIKA-simulated air showers. Two cut variables were used in this analysis: the angular uncertainty σ_i in the reconstruction of the muon track direction estimated individually for each event, and the reduced log-likelihood *rlogl*, which is the log-likelihood for the best track solution divided by the number of degrees of freedom in the fit. The number of degrees of freedom in the track fit is equal to the number of DOMs triggered by the event minus the number of free parameters in the fit (five for this fit.) Both *rlogl* and σ are standard cut variables used in the search for point-like sources of astrophysical neutrinos [109], the search for a diffuse flux of high-energy neutrinos [122], and several other analyses of IceCube data.

Once the cuts have been determined, the number of events falling inside a circular search bin around the Moon is compared to the number of events contained in a bin of the same angular radius for the average *off-source* region. The statistical significance of an observed deficit in the number of events in the search bin is calculated using the method given by [123].

The optimal radius of the search bin ψ_b can be found by maximizing the S' parameter in the following expression:

$$S'(\psi_s) \propto \frac{\int_0^{\psi_s} \psi' \ \text{PSF}(\psi') \ d\psi'}{\psi_s} \quad , \tag{3.16}$$

where ψ_s is the radius of the bin and $\text{PSF}(\psi')$ is the point spread function of the detector after cuts obtained from simulations. Due to its symmetry, the PSF has already been integrated over the azimuthal coordinate and only the radial dependence remains. The optimization

of the search bin radius is also performed using simulated CORSIKA showers generated for each detector configuration.

3.5.2 Results

A set of cuts was determined independently for both the IC40 and IC59 detector configurations using the optimization procedure described above on simulated data. For IC40, only events with $rlog < 9$ and $\sigma_i < 1.01^\circ$ were used in the analysis, with 26% of the events surviving the cuts. After cuts, the median angular resolution of the reconstruction was estimated from simulation to be 0.93°, with 68% of the events having angular uncertainties σ_i between 0.38° and 2.18°. A two-dimensional fit to the simulated data shows that for the two-dimensional Gaussian approximation the corresponding resolution σ is about 0.74°.

In the case of IC59, the events selected for the analysis were those with $rlog < 8.8$ and $\sigma_i < 1.04^\circ$, which resulted in a passing rate of 34%. The median resolution after cuts was 0.78°, with the 68% containing interval located between 0.33° and 1.78°, with a Gaussian width σ of about 0.71°.

After the cuts were applied to both data sets, the radius of the optimal search bin (ψ_b) and the number of events contained in that bin for both the *on-source* ($N^b_{\rm on}$), and *off-source* ($N^b_{\rm off}$) windows were calculated. In both detector configurations, a deficit in the number of events in the *on-source* bin when compared to the *off-source* bin was observed at high statistical significance ($> 6\sigma$), as expected due to the shadowing effect of the Moon. A complete list of the number of events observed on each bin, the observed deficit in the *on-source* bin, as well as the statistical significance associated with such deficit is given in Table 3.1.

The Moon shadow profile shown in Fig. 3.11 was fit using the expression given in Eq. 3.14, where σ is the only free parameter. A list of fit results is given in Table 3.2. In both cases, the observed angular resolution shows good agreement with the one obtained from the above-mentioned simulation studies.

	IC40	**IC59**
ψ_b	0.75°	0.79°
N^b_{on}	52967	96412
N^b_{off}	54672	100442
ΔN	-1705	-4030
Significance	6.9σ	12.1σ

Table 3.1: Optimal bin radius (ψ_b), number of observed events in the *on-source* (N^b_{on}) and *off-source* (N^b_{off}) bins, event deficit in the *on-source* bin (ΔN), and statistical significance of the deficit for the binned analysis of IC40 and IC59 data sets.

	IC40	**IC59**
σ	$0.71° \pm 0.07°$	$0.63° \pm 0.04°$
χ^2/dof	31.4 / 24	13.0 / 24

Table 3.2: Gaussian angular resolution σ obtained from the fit to the Moon shadow profile shown in Fig. 3.11. The χ^2/dof of the fit is also given for the two results.

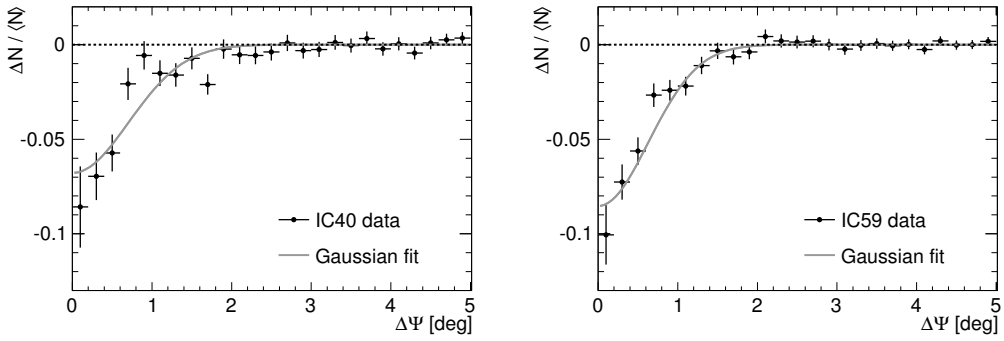

Figure 3.11: Relative difference between the number of events in the *on-source* and the average *off-source* region as a function of the angular distance from the nominal position of the Moon for the IC40 *(left)* and IC59 *(right)* datasets. A Gaussian fit to the deficits is shown in gray.

3.6 Unbinned Analysis

The second algorithm used to search for the Moon shadow is based on an unbinned maximum likelihood method analogous to that used in the search for point-like sources of high-energy neutrinos [124].

In this analysis, performed by Jan Blumenthal (see [125]) and Rene Reimann (see [126]), a maximum-likelihood fit to the data is performed that returns the most likely position of the Moon shadow and the total number of shadowed events. This kind of likelihood analysis was first proposed in [127], and was applied for the first time to a Moon shadow search in [128].

The total number of shadowed events for IC40 and IC59 are 5320 ± 501 and 8700 ± 550, respectively. These values agree with the expected number of shadowed events: 5734 ± 76 for IC40, and 8192 ± 91 for IC59. The statistical significance of the observed deficits is 10.2σ for IC40, and 13.9σ for IC59.

The position of the center of the Moon shadow returned by the fit can be compared to the expected location after accounting for geomagnetic field deflection effects. The best

fit shadow positions for both detector configurations are shown in Fig. 3.12 together with 1σ, 2σ, and 3σ contours. The expected locations are shown as white circles. In both detector configurations, the observed position of the minimum is consistent with its expected location within statistical fluctuations. These measurements imply that the absolute pointing accuracy of the detector during the IC40 and IC59 data-taking periods was better than about 0.2°.

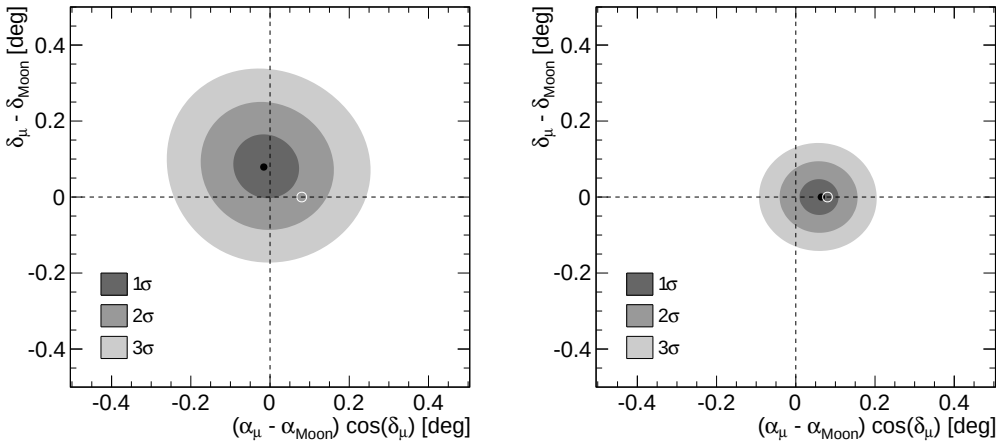

Figure 3.12: Contour plot for the position of the minimum of the Moon shadow in the IC40 (*left*) and IC59 data (*right*) in the $(\Delta\alpha, \Delta\delta)$ coordinate system. The reconstructed position for the Moon shadow from the maximum likelihood analysis is shown as a black point, while the expected position of the Moon shadow after accounting for magnetic deflection is shown as a white circle.

3.7 Conclusions

The shadow of the Moon in TeV cosmic rays has been detected to high significance ($> 6\sigma$) using data taken with the IC40 and IC59 configurations of the IceCube Neutrino Observatory. For both detector configurations, the observed positions of the shadow minimum show good agreement with expectations given the statistical uncertainties. An important implication of this observation is that any systematic effects introduced by the detector geometry and the event reconstruction on the absolute pointing capabilities of IceCube are smaller than about 0.2°.

The average angular resolution of both data samples was estimated by fitting a Gaussian function to the shadow profile. In both cases, the 1σ width of the Moon shadow was found to be about 0.7° , which is in good agreement with the expected angular resolution based on simulation studies of down-going muons. The degree-level angular resolution of the detector makes it suitable for precise studies of the cosmic-ray anisotropy.

The total number of shadowed events estimated using an unbinned analysis is also consistent with expectations for IC40 and IC59.

Chapter 4

Anisotropy Search Method

The anisotropy search method is presented in this chapter. First, a general description of the time and coordinate systems used in this work is given in Section 4.1, followed by a description of the time-scrambling algorithm used to estimate the detector exposure in Section 4.2. Finally, several examples of the application of the time-scrambling algorithm on simulated data sets are given in Section 4.3.

4.1 Time and Coordinate systems

4.1.1 Time Frame Definition

This work uses the Modified Julian Date (MJD) convention for event times. The MJD system is based on the historical Julian Date (JD) dating method traditionally used in astronomy. The start of the JD count is from 0 at noon 01/01/4713 BC. For instance, the Julian Date for 07:30, 22 June 2006 (UTC) is 2453908.8125. The Modified Julian Date was introduced in the late 1950's, and is defined as

$$\mathrm{MJD} = \mathrm{JD} - 2400000.5 \tag{4.1}$$

The half day is subtracted so that each julian day starts at midnight with the new civil day. For example, 02:00, 2 July 2011(UTC) corresponds to MJD 55744.0833.

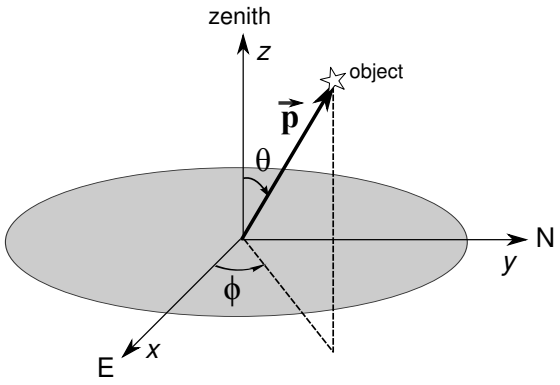

Figure 4.1: Definition of the local coordinate frame. The azimuth and zenith angles (ϕ and θ, respectively) a an object in the sky are shown.

4.1.2 Local Coordinates

The local, or horizontal, coordinate system is fixed to the detector itself. For detectors used in this work, a right-handed coordinate system (shown in Fig. 4.1) is defined as follows:

- The origin is located near the center of the IceCube detector, shown in Fig. 2.3.
- The y axis (or Grid North) is contained in a plane parallel to the ice surface, and is aligned with the Prime Meridian that points towards Greenwich, UK (geographic longitude 0°).
- The x axis (or Grid East) is coplanar with y, and points in a direction that is 90° from Grid North measured clockwise.
- The z axis is normal to the xy plane, pointing towards the local zenith point.

Arrival directions of events in this coordinate system are defined by two angles in spherical coordinates: the azimuth angle ϕ, and the zenith angle θ, which are defined as follows:

- Azimuth angle ϕ: Measured counterclockwise from the x axis (Grid East) from 0° to 360°. In this convention, the y axis points in the $\phi = 90°$ direction.

– Zenith angle θ: Measured with respect to the z axis from 0° to 180°. The convention implies that the zenith point has $\theta = 0°$, the local horizon is at $\theta = 90°$, and the nadir point has $\theta = 180°$.

4.1.3 Equatorial Coordinates

Astronomical positions are defined in the usual equatorial coordinate system (shown in Fig. 4.2), which is also referred to in this work as "sidereal" coordinate frame. The reference points in the celestial sphere are the *celestial equator*, which is the projection of the equatorial plane of the Earth to infinity; the *vernal equinox*, which is the intersection of the celestial equator and the ecliptic plane (i.e. the projection of the orbit of the Earth to infinity); and the celestial poles (north and south) defined by the projection of the rotation axis of the Earth. Due to the precession motion of the Earth, the vernal point moves slowly with respect to the stars, completing a cycle in about 26,000 years. For this reason, positions in equatorial coordinates are usually referred to the vernal point for a particular epoch. In this work, we use the J2000 epoch. For the anisotropy study, corrections for higher order effects such as nutation are neglected.

Positions in the celestial sphere are characterized by two angles:

– Right ascension α: The angular distance from the vernal point measured counterclockwise along the celestial equator from 0° to 360°.

– Declination δ: Measured as the angular distance between the celestial equator and the parallel line that contains the object. The angles are measured from $-90°$ to $+90°$, where negative (positive) declinations correspond to objects in the southern (northern) sky.

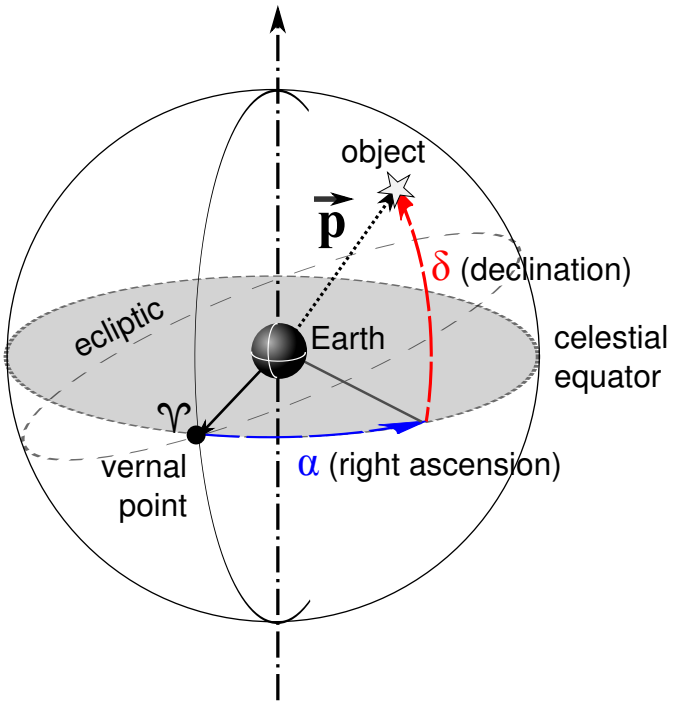

Figure 4.2: Definition of the equatorial, or sidereal, coordinate system. The right ascension and declination angles (α and δ, respectively) of an object in the sky are shown.

4.1.4 Coordinate Transformations

For the purpose of the anisotropy analysis, a cosmic-ray event is fully characterized by its arrival time in MJD and its arrival direction in local coordinates (θ, ϕ). Local coordinates can be transformed into equatorial coordinates using the equations:

$$\tan h = -\frac{\cos\phi}{\cot\theta\cos\lambda - \sin\lambda\sin\phi} \tag{4.2}$$

$$\sin\delta = \sin\lambda\cos\theta + \cos\lambda\sin\theta\sin\phi, \tag{4.3}$$

where h is the hour angle, and λ is the latitude of the detector. For the particular location at the South Pole ($\lambda = -90°$), the above equations simplify to

$$h = \phi + 90° \tag{4.4}$$

$$\delta = \theta - 90° \tag{4.5}$$

The conversion has been adapted from [129] to meet the local coordinate convention defined in Subsection 4.1.2. The hour angle h can be transformed into right ascension α using

$$\alpha = t_s - h, \tag{4.6}$$

where t_s is the mean sidereal time at 0^{h} UTC, defined (in degrees) as

$$t_s = 280.46061837 + 1.31850007701\times10^{7}\cdot T + 3.87933\times10^{-4}\cdot T^2 - 2.58331181\times10^{-8}\cdot T^3\ , \tag{4.7}$$

and T is defined as

$$T = \frac{\mathrm{MJD} - 51544.5}{36525}\ . \tag{4.8}$$

These transformations are performed using the `SLALIB` library of astronomical routines [111].

4.1.5 Solar Coordinate Frame

As was described in Chapter 1, a solar dipole anisotropy caused to the motion of the Earth around the Sun should be observed in cosmic rays. The direction of the dipole is fixed with respect to the position of the Sun in the sky. For this reason, we define a "solar" coordinate frame where the right ascension of events are measured with respect to the right ascension of the Sun $\alpha_{\odot}$, and their declination remains unchanged:

$$\alpha_s = \alpha_{\rm CR} - \alpha_{\odot} \tag{4.9}$$

$$\delta_s = \delta_{\rm CR} \ . \tag{4.10}$$

Since the origin of this frame in right ascension is fixed to the Sun, it moves with respect to the sidereal frame (i.e. with respect to the stars), completing one revolution in a solar year (365.25 days). For experiments with perfect uptime and sky coverage, any signal in the sidereal frame should average to zero over the course of the solar year. Gaps in the data acquisition time or seasonal variations in the observed cosmic ray flux could produce an anisotropy in sidereal coordinates of solar origin. The effect can also work in the opposite direction: the sidereal anisotropy could distort the anisotropy observed in the solar frame. Anisotropy of astrophysical origin is expected in the sidereal and solar frame, so it is hard to disentangle those signals from the effect that data-taking gaps could cause. For this reason, two additional frames are studied: the anti-sidereal, and the extended-sidereal coordinate systems, which can be used for stability studies since no signal of astrophysical origin is expected to appear in either of them [130].

4.1.6 Anti-Sidereal and Extended-Sidereal Coordinate Frames

A sidereal year has 366.25 days (i.e. complete revolutions in the coordinate frame), one more day than the solar year (365.25 days). This means that each sidereal day is *shorter* by about 4 minutes than the solar day. The anti-sidereal frame is constructed by reversing the sign of the correction necessary to go from solar to sidereal time, which means that an

anti-sidereal day is about 4 minutes *longer* than a solar day. As a result, the anti-sidereal year has 364.25 days.

Similarly, another frame, called "extended-sidereal," can be defined where a day is 4 minutes shorter than the sidereal day (8 minutes shorter than the solar day). Therefore, a year in this time frame has 367.25 days.

These two time frames are used to investigate different effects: a seasonal variation of the solar dipole causing a distortion of the sidereal anisotropy would produce a "signal" in the anti-sidereal frame, and similarly, a distortion of the solar dipole caused by fluctuations in the sidereal anisotropy would induce a "signal" in the extended-sidereal frame. Both frames are studied to estimate systematic effects due to seasonal modulations in the solar and sidereal anisotropies.

4.1.7 Map-Making Technique

The sky maps produced in this analysis are generated using the Hierarchical Equal-Area isoLatitude Pixelization (HEALPix) of the sphere [131], which is available as a coding library [1]. In HEALPix, the unit sphere is divided into pixels that subtend the same solid angle. The number of pixels in a map $N_{\rm pix}$ is set by the parameter $N_{\rm side}$, where $N_{\rm pix} = 12 \cdot N_{\rm side}^2$. $N_{\rm side}$ is defined by the resolution parameter r, an integer number between 0 and 10, with $N_{\rm side} = 2^r$. For example, for $N_{\rm side} = 8$ ($r = 3$) the sky is divided in 768 pixels, which means that the mean spacing between pixels is about 7.3°. The default map resolution used in this work is $N_{\rm side} = 64$, which divides the sphere in 49152 pixels with a mean pixel size of $\sim 0.92°$. This pixel size is smaller than the angular resolution of the detectors used in this work ($\sim 2-5°$).

Maps shown in this work use the Mollweide projection of the sphere, with $\alpha = 0°$ on the right of the map increasing towards the left.

[1] Hierarchical Equal-Area isoLatitude Pixelization of the sphere: `http://healpix.jpl.nasa.gov`.

4.2 Reference level estimation

4.2.1 Overview

Due to the design and working principle of cosmic-ray detectors, the probability of detecting a cosmic-ray event is usually a strong function of its arrival direction. For instance, the regular grid layout commonly used in large air-shower arrays creates lines of detectors along which events are preferentially detected, producing an uneven event rate as a function of local azimuth angle. The flat geometry of air-shower arrays also induces a strong dependence of the observed cosmic-ray rate on local zenith angle.

A key component of any search for cosmic-ray anisotropy is a method that would remove these detector effects and provide an unbiased estimation of the real cosmic-ray distribution in the sky. To accomplish this, an estimation of what the arrival distributions in detector coordinates would have been if the cosmic-ray flux was isotropic is desired. The response of a detector to an isotropic flux can be used as a reference to which we can compare the distribution of detected events.

The ideal procedure to obtain this estimate would be to inject an isotropic flux of simulated air showers to a Monte Carlo model of the detector and then study the arrival distributions of events that pass the same trigger requirements as those in the real data. However, this is only feasible when anisotropies are large (i.e. $> 10\%$), since detector simulations are usually not precise at a level better than a few percent. For anisotropies with amplitudes in the $\sim 10^{-4} - 10^{-3}$ range such as those expected in the TeV-PeV energy range, this approach is not realistic due to the required level of agreement between data and simulation.

For this reason, the calculation of this estimate, or *reference level*, is based on the data itself. The algorithm used for the calculation of the reference level in this work is called "time scrambling," and will be described in the next subsection. A recent study of the capabilities and limitations of the time-scrambling method is presented in [132].

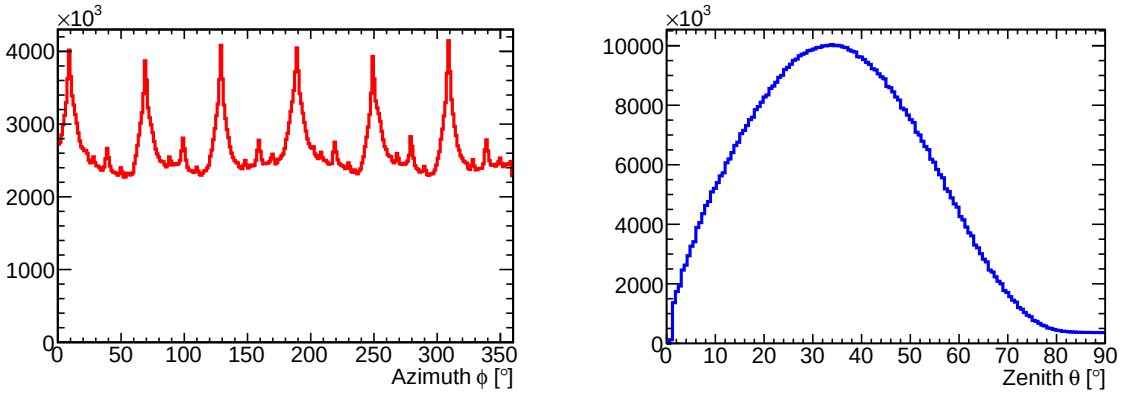

Figure 4.3: Example distributions of event arrival directions in local coordinates of one day of data taking with the IC86 configuration of IceCube.

4.2.2 Time-Scrambling Algorithm

The time-scrambling algorithm is a widely used method to estimate an exposure-weigthed isotropic reference level to which the observed distribution of events is compared.

Two HEALPix maps are produced where event coordinates in the sky are binned in a fine grid. The first one of these maps, which we will call the *data* map, contains event directions in sidereal coordinates (α, δ) that were calculated from their local coordinates (θ, ϕ) and arrival times t. The distribution of events in this map is still very anisotropic, since it retains the uneven exposure of the detector to different parts of the sky.

The anisotropy in the data map has two origins: one due to detector exposure effects as already mentioned and a second one, potentially, of astrophysical origin. These two sources of anisotropy can be considered stable in their respective frames: the sidereal frame for the astrophysical source, and the detector (or local) frame for the exposure anisotropy. The time-scrambling algorithm disentangles these two sources by keeping the local coordinates of each event fixed while shuffling the astrophysical coordinates. To do this, each event in the data set is assigned a random time which is sampled from the distribution of all event times in the data in order to keep track of gaps in the data acquisition. In order to reduce statistical fluctuations, 20 "fake" events are generated for each real event in the data. The fake events

are used to build the second map, which we will call *reference* map. This process effectively shuffles the right ascension of the event (Eq. 4.6) while keeping the local coordinates (shown in Fig. 4.3 for IceCube as an example) and the detector rate unchanged with respect to the real data. This procedure destroys the autocorrelation of events in sidereal coordinates that may have existed in the data and is an estimation of what the distribution of events would have been if there was no sidereal anisotropy.

The amount by which each event is scrambled in right ascension depends on the length of time window Δt from which event times are sampled, where the time window length can be anything from minutes to 24-hours long. The length of the window indicates the time scale over which the detector acceptance in local coordinates is believed to be stable so that events are not scrambled over times when the detector operated in different configurations. For detectors at the South Pole, the environmental conditions change very slowly and detector operation is very stable, which allows the use of a 24 hours time window. In fact, the stability of the detector allows the use of even longer time windows, but since a full rotation of the celestial sphere is observed during a 24 hours period, longer time windows are not needed. Even with a stable detector, Δt could be made shorter for other reasons. Since the Earth rotates 15° around its axis per hour, the range over which right ascension are scrambled is given by $15°/\text{hour} \times \Delta t$, which means that any structure larger in right ascension than $15°/\text{hour} \times \Delta t$ will be suppressed from the analysis. This "high-pass" filter can be used to search for structure smaller than a particular angular scale, and will be used in parts of this work.

4.2.3 Dipole and Quadrupole Fit

A different approach to remove the large-scale structure to focus on smaller-scale structure in the sky map is to subtract the dominating dipole and quadrupole moments from the data and study the residuals. This requires a dipole and quadrupole fit, which can be seen as the two-dimensional equivalent of the usual one-dimensional harmonic fit used in

previous anisotropy studies. For this procedure, we fit the relative intensity map (described in Subsection 4.2.4) using the function:

$$\delta I(\alpha,\delta) = m_0 + p_x \cos\delta\cos\alpha + p_y \cos\delta\sin\alpha + p_z \sin\delta$$
$$+ \frac{1}{2}Q_1(3\cos^2\delta - 1) + Q_2 \sin 2\delta\cos\alpha + Q_3 \sin 2\delta\sin\alpha + Q_4\cos^2\delta\cos 2\alpha + Q_5\cos^2\delta\sin 2\alpha \ . \tag{4.11}$$

Equation (4.11) is a multipole expansion of the relative count distribution in terms of real-valued spherical harmonic functions, and follows a normalization convention commonly used in Cosmic Microwave Background physics [133]. The quantity m_0 is the "monopole" moment of the distribution, and corresponds to a constant offset of the data from zero. The values (p_x, p_y, p_z) are the components of the dipole moment, and the quantities $(Q_1, \ldots, Q_5)$ are the five independent components of the quadrupole moment.

The estimation of the reference level given by the time-scambling method has some disadvantages. As can be seen in Eq. 4.5, the declination of an event δ is completely degenerate with the zenith angle θ at the South Pole, regardless of the arrival time of the event. As events are time-scrambled, they remain in the same declination band, which reduces the sensitivity of the anisotropy search to structures oriented mostly along declination parallels. For instance, a dipole anisotropy aligned with the axis of the rotation of the Earth would produce a distribution of events that would be impossible to distinguish from a detector effect in zenith angle using the time-scrambling method and would therefore not be detected. The limitations of this reference estimation technique are discussed in Section 4.3.

4.2.4 Relative Intensity and Significance Maps

Once the data and reference maps have been built using the time-scrambling algorithm, they are compared to establish if any anisotropy in sidereal coordinates is visible. This comparison is performed by constructing two types of maps: a relative intensity map, and

an statistical significance map. Pixel values in the relative intensity map are calculated using the equation:

$$\delta I_i = \frac{\Delta N_i}{\langle N \rangle_i} = \frac{N_i(\alpha,\delta) - \langle N_i(\alpha,\delta)\rangle}{\langle N_i(\alpha,\delta)\rangle} \ , \tag{4.12}$$

where N_i and $\langle N_i \rangle$ are the number of events in the i^{th} pixel of the data and reference maps, respectively. The statistical uncertainty on δI is calculated in the same way as in the binned analysis of the Moon shadow:

$$\sigma_{\delta I} = \frac{N_i}{\langle N \rangle_i} \sqrt{\frac{1}{N_i} + \frac{\alpha}{\langle N \rangle_i}} \ , \tag{4.13}$$

where $\alpha = 1/n$, for n resamples of the data during the time-scrambling process ($\alpha = 1/20$ in this work). The statistical significance of any deviation from the reference level can be calculated using the method of Li & Ma [123], where the significance s for pixel i is given by the expression:

$$s_i = \sqrt{2} \left\{ N_i \log \left[\frac{1+\alpha}{\alpha} \Big(\frac{N_i}{N_i + N_o} \Big) \right] + N_o \log \left[(1+\alpha) \Big(\frac{N_o}{N_i + N_o} \Big) \right] \right\}^{1/2} \ , \tag{4.14}$$

with $N_o = \langle N \rangle_i / \alpha$. This method of statistical significance calculation is widely used in gamma ray astronomy, and takes into account the statistical fluctuations of the data and reference counts.

In order to increase the sensitivity of the search to excess regions with different angular sizes, a smoothing procedure is applied to the data and reference maps before the calculation of the relative intensity and significance maps. The smoothing process sums all events in a pixel to the events inside a certain angular distance (the smoothing radius). This produces a sky map of pixels with correlated counts but with Poisson uncertainties that has an improved sensitivity to structures with angular sizes similar to the smoothing radius.

4.3 Application Examples

To test the time-scrambling algorithm, data sets were generated where known signals were injected on top of an isotropic background. The signals have similar sizes and amplitudes (part per-mille or less) to those expected in real data. For each data set, two HEALPix maps were created: a *signal* map where the relative intensity of the input signal is stored after being zero-supressed; and a *background* map, which is usually flat across the sky.

Local coordinates and the time for each simulated event in the set are generated using a Monte Carlo acceptance/rejection algorithm as follows:

1. The time for each event is taken from real data (the IC40 data set in this case) to replicate the gaps in data acquisition and other changes in the event rate that occur in a real detector. Since all event times in the real data set are used, the size of the fake and real sets is the same ($\sim 3.4 \times 10^{10}$ events in IC40).

2. For each event, random local coordinates (θ, ϕ) are sampled from the arrival distributions of the IC40 data. The distributions are built using the entire IC40 data set.

3. The event sidereal coordinates are determined from the local coordinates and the arrival time.

4. The value of the signal map in the direction of the event is retrieved. If this value is smaller than a random number sampled from a uniform distribution, the event is kept and tagged as a "signal" event. If the event is rejected in the signal test, the same test is done using now the value of the background map at the same position and the event is tagged as background if accepted. The process continues until all events have been recorded as either being "signal" or "background".

A list of injected signals is given below:

– Sidereal Compton-Getting dipole.

– Gaussian excess region.

– Dipole + Quadrupole.

– Gaussian excess on top of dipole and quadrupole.

The results for each of these sets are discussed in the following subsections.

4.3.1 Compton-Getting Dipole

A dipole signal was injected with an orientation and amplitude predicted by the sidereal Compton-Getting effect. The dipole (shown in Fig. 4.4a) has an amplitude of 3.5×10^{-3} and its maximum points towards ($\alpha = 315°, \delta = 48°$). A time-scrambling window of 24 hours was used to analyze the simulated data. A map of the best fit dipole and quadrupole to the data, and a relative intensity map for a 20° smoothing radius are shown in Figs. 4.4b and 4.4c, respectively. Only two of the harmonic coefficients of Eq. 4.11 dominate the fit, the dipole components $p_2 = (-1.56 \pm 0.07) \times 10^{-3}$, and $p_3 = (1.72 \pm 0.07) \times 10^{-3}$.

The detected dipole vector has an amplitude of $(2.32 \pm 0.03) \times 10^{-3}$, and a phase of $317.7° \pm 1.6°$ which agrees with the input signal phase. The best-fit dipole, however, is oriented along the equatorial plane, which implies that the original inclination of the injected signal is lost. This is a known issue of time-scrambling methods. Since the algorithm estimates the reference level by essentially averaging the number of counts over a declination band, different declination bands may have different normalizations, and whether this is due to detector acceptance effects or an astrophysical origin cannot be determined using this method.

The implication for this study is that the method is sensitive to the *projection* of the anisotropy profile on the equatorial plane. In the case of the Compton-Getting dipole, an amplitude of 3.5×10^{-3} and an inclination of $\delta = 48°$ results in an equivalent equatorial dipole with amplitude $3.5 \times 10^{-3} \cos(48°) = 2.34 \times 10^{-3}$, which agrees well with the amplitude of the fit.

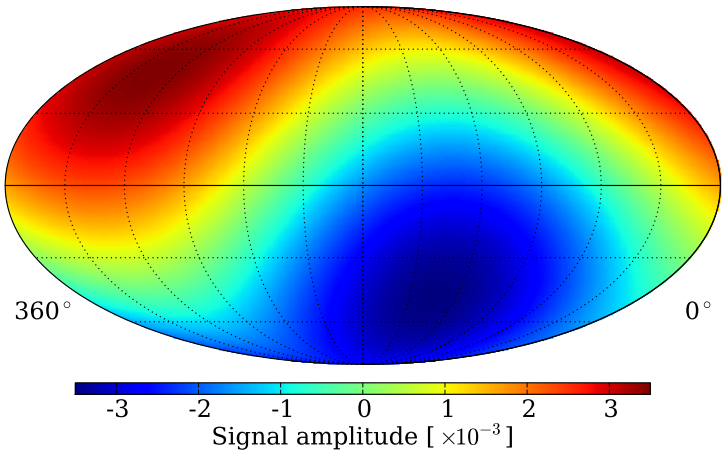

(a) Injected Compton-Getting dipole.

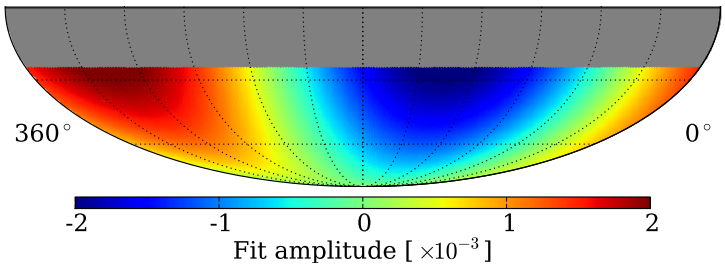

(b) Dipole and quadrupole fit to Compton-Getting map.

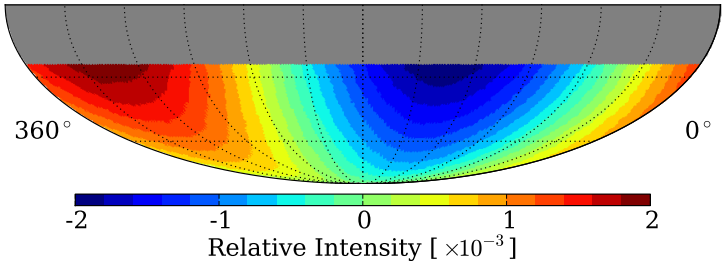

(c) Relative intensity map (20° smoothing).

Figure 4.4: Density map of the injected Compton-Getting dipole signal. Best fit (*left*) and relative intensity map (*right*) for the Compton-Getting dipole data.

4.3.2 Gaussian excess

In order to test the response of the time-scrambling method on a source with limited angular extent, we inject a Gaussian excess with the following parameters:

- Amplitude: 10^{-3}.
- Radius (1σ): 20°.
- Location: ($\alpha = 270^{\circ}$, $\delta = -10^{\circ}$).

A map of the input signal density is shown in Fig. 4.5a. The performance of the time-scrambling method is evaluated in terms of the length of the time-scrambling window (in hours) and the smoothing radius.

Six time-scrambling window lengths Δt were tested, $\Delta t = \{2, 3, 4, 6, 8, 24\}$ hours, and smoothing radii up to 50° were used. After smoothing, the significance maps are scanned for the highest significance value. A contour plot of highest significance values as a function of smoothing and time-scrambling window length is shown in Fig. 4.5. The significance reaches a maximum for smoothing radii in the range between 20° and 40°. This optimal range in smoothing radius is defined by the geometry of the source. The shape of the injected signal dictates the rate at which more signal events are included in the smoothing window and therefore the maximum significance that can be reached. For increasingly larger radii, the total number of signal events is basically constant because all events from the source have been included but the number of reference events keeps increasing quadratically with the radius, which results in a decrease of the maximum significance. Statistical significance in the presence of the Gaussian source also increases as a function of window length, reaching its maximum for a Δt of 24 hours. Significance and relative intensity maps for a smoothing radius of 20° are shown in Figs. 4.5d and 4.5e, respectively.

The effect of the different time window lengths is evident in Fig. 4.5c, where a profile view of the number of events in the declination range $-35^{\circ} < \delta < -10^{\circ}$ is shown for the data and for reference maps with different window lengths. Since the time-scrambling method works

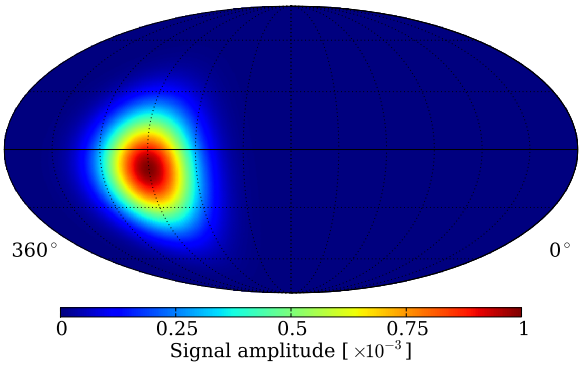

(a) Density map of the injected Gaussian signal.

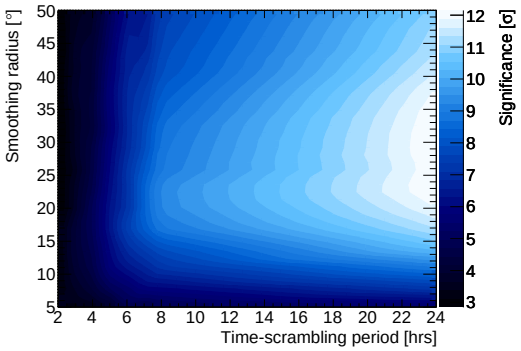

(b) Maximum significance as a function of smoothing radius and time-scrambling window length.

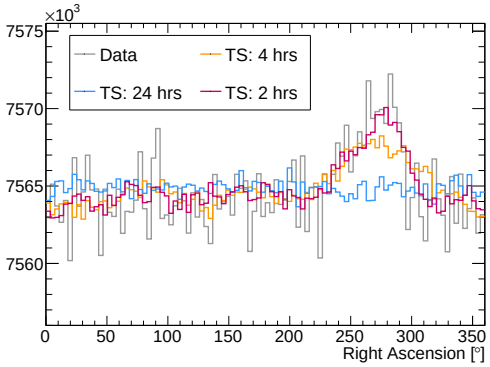

(c) Number of events in the declination range $-35° < \delta < -10°$ for the data and reference maps for 2,4, and 24 hour time scrambling.

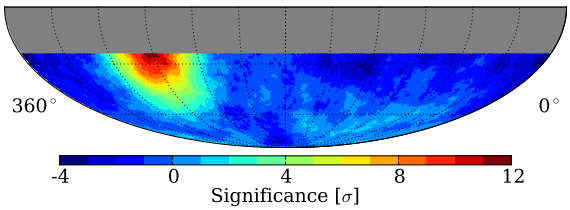

(d) Significance map for 20° smoothing and 24 hour time-scrambling.

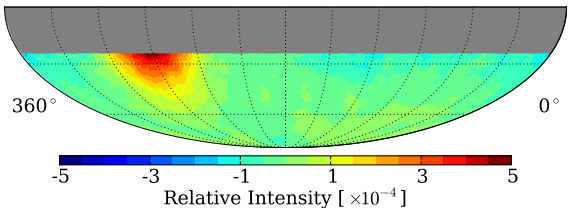

(e) Relative intensity map for 20° smoothing and 24 hour time-scrambling.

Figure 4.5: Result plots for the Gaussian source data set.

as a running average of the data over a declination band, longer time scrambling windows will be more sensitive to localized excess and deficit regions. For instance, a time-scrambling window of 2 hours (which corresponds to $\sim 30^\circ$ in right ascension) shows no sensitivity to the Gaussian excess, which is evidenced by the lack of a clear significance maximum in the Fig. 4.5b regardless of the smoothing angle for that value of Δt. The reason for this is that the Gaussian excess region (with a 1σ width of 20°) is closely tracked by the reference level and therefore is not seen as an excess. Longer windows make the excess stand out more clearly from the reference level, with the best case being the 24 hour scrambling time.

The 24 hour window, however, overestimates the reference level over the entire right ascension range. This can also be seen in the significance map shown in Fig. 4.5d, where regions of the sky in the same declination band as the Gaussian source are observed as a $\sim 4\sigma$ underfluctuation due to the bias introduced in the reference level estimation by the presence of the source. This effect is a well known limitation of the method, which can not estimate the *absolute* number of events expected in a declination band for the isotropic case. For this reason, if a sky map presents a series of wide excess and deficit regions it is not possible to determine the "floor" level with respect to which the anisotropy should be measured. This behavior could be exemplified by the detection of a deficit region of limited extent. Using the time scrambling method alone, it is not possible to claim that the observation of the deficit is not, in fact, due to a wide excess flux region in the same declination band as the excess, which may lead to a different physical interpretation of the anisotropy observation.

The significance map shown in Fig. 4.5d can be compared to the injected signal shown in Fig. 4.5a. It can be seen that the region with high significance extends farther away from the celestial equator than the injected signal may indicate. The reason for this is that in the case of the statistical significance, the combination of the relative amplitude of the excess and the number of events (which increases towards the poles for IceCube data) is important.

4.3.3 Dipole and Quadrupole

The dipole and quadrupole modes of the spherical harmonic functions were injected to test the performance of the method on large-scale signals. The orientation and amplitudes of both components is given below:

- Dipole amplitude: 5×10^{-4}.
- Dipole orientation: $\alpha = 90°$, $\delta = 0°$.
- Quadrupole amplitude: 1×10^{-4}.
- Quadrupole orientation: $\alpha = 0°$, $\delta = 0°$.

The injected signal is shown in Fig. 4.6a. The maximum significance as a function of Δt and smoothing radius is shown in Fig. 4.6b. As expected for a large-scale signal, the significance steadily increases both with Δt and smoothing radius. Scrambling periods of less than about 4 hours do not produce significant excesses regardless of the selected smoothing radius.

The purpose of this study is to determine if the presence of large-scale anisotropy by itself would induce a signal which could be interpreted as a small scale anisotropy if a time-scrambling period shorter than 24 hours was selected. The absence of a significant anisotropy detection for a Δt shorter than 6 hours indicates that no leakage of the large-scale anisotropy into smaller scales is evident, and if a positive anisotropy detection occurs at such time-scrambling periods, it has to be due to small angular-scale anisotropy.

Dipole and quadrupole harmonic moments were fit to the relative intensity sky map. The result for the best fit is shown in Fig. 4.6c, which can be compared to the input signal shown in Fig. 4.6a. Some of the amplitude of the dipole and quadrupole modes is lost, mostly because of the limited statistics close to the equator where the signal strength is larger. The residual maps of the fit show no significant structure. Sample significance and relative intensity maps for a smoothing radius of 20° are shown in Figs. 4.6d and 4.6e, respectively.

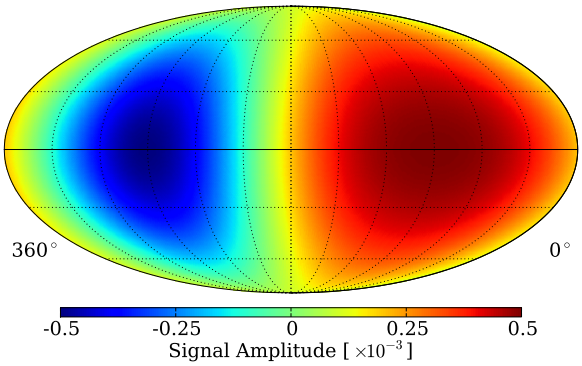

(a) Density map of the injected dipole and quadrupole signal.

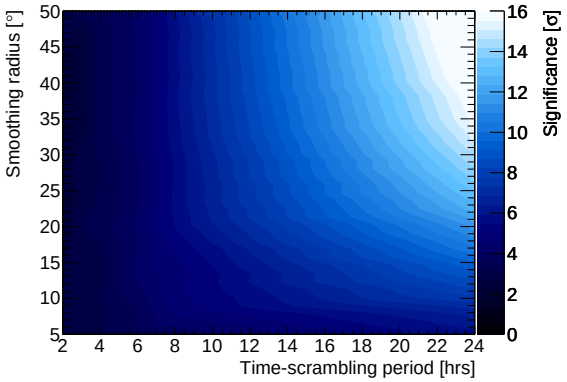

(b) Maximum significance as a function of smoothing radius and time scrambling window length.

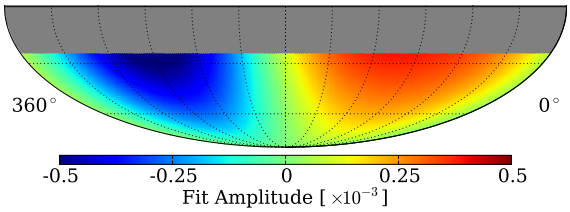

(c) Best fit dipole and quadrupole map.

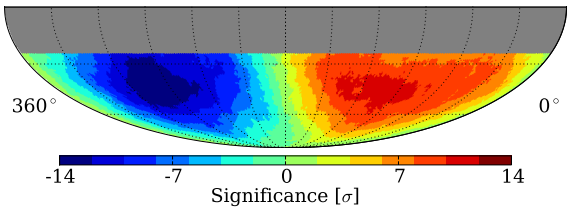

(d) Significance map for 20° smoothing with 24 hour time-scrambling.

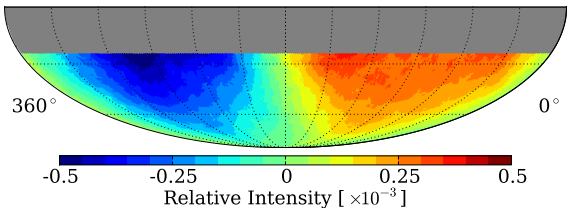

(e) Relative intensity map for 20° smoothing with 24 hour time-scrambling.

Figure 4.6: Result plots for the dipole and quadrupole data set.

4.3.4 Dipole and Quadrupole with a Gaussian Excess

Cosmic-ray data collected with experiments in the northern hemisphere indicates that the anisotropy presents structure both at large and small angular scales. For this reason, we produced a map that includes dipole and quadrupole structure with a Gaussian excess on top. Two data sets were created, the first with the Gaussian source located near the minimum and the second one near the maximum of the large-scale anisotropy. The signal parameters for both sets are given below:

- Dipole amplitude and orientation: 6.4×10^{-4}, ($\alpha = 66.4°$, $\delta = 0°$).
- Quadrupole amplitude and orientation: 2.1×10^{-4}, ($\alpha = 294.4°$, $\delta = 0°$).
- Gaussian amplitude: 6.4×10^{-4}.
- Gaussian radius (1σ): $20°$.
- Gaussian location 1 (near minimum): $\alpha = 270°$, $\delta = -30°$.
- Gaussian location 2 (near maximum): $\alpha = 66.4°$, $\delta = -30°$.

Both data sets were analyzed using different time-scrambling windows and smoothing radii. A dipole and quadrupole fit was performed and subtracted from the data to increase the sensitivity to the Gaussian source.

4.3.4.1 Gaussian Source located near the Large-Scale Minimum

The input signal map for the data set with a Gaussian source located near the large-scale minimum is shown in Fig. 4.7a. The maximum significance as a function of Δt and smoothing radius is shown in Fig. 4.7b. The overall evolution of the maximum significance for this set can be interpreted as a superposition of the significance evolution for the Gaussian-only (Fig. 4.5b) data set and the dipole and quadrupole-only (Fig. 4.6b) data set.

For small values of Δt (of about 6 hours or less), the maximum significance is found for smoothing radii around $20°$. This is due to the filtering of the large scale anisotropy

which makes the Gaussian excess the most significant structure in the map. For longer time-scrambling windows, the point of maximum significance in the map moves to the maximum of the large scale anisotropy and therefore larger smoothing radii are favored.

The best harmonic fit is shown in Fig. 4.7c. It can be seen that some of the Gaussian feature is absorbed into the dipole and quadrupole structure which results in a smaller amplitude of the large-scale anisotropy when compared to the input signal shown in Fig. 4.7a. The fit residuals for a smoothing radius of 20° are shown both in terms of statistical significance (Fig. 4.7d) and relative intensity (Fig. 4.7e). The most significant excess is observed at the location of the Gaussian source. Due to the fit and subtraction procedure the shape of the Gaussian has been distorted.

4.3.4.2 Gaussian Source located near the Large-Scale Maximum

For this data set, the Gaussian excess was injected on top of the large-scale anisotropy maximum. The input signal map is shown in Fig. 4.8a. It is possible that for a data set with partial sky coverage such as that from IceCube, a small-scale excess near the maximum could be masked by the large-scale anisotropy. The maximum significance as a function of Δt and smoothing angle is shown in Fig. 4.8b. The contour plot shows some differences with the one produced for the set where the Gaussian source was located near the large-scale minimum. For instance, even though there is a clear evolution that favors progressively larger smoothing radii for longer time scrambling periods, the transition is not as fast as in the previous case.

The best fit dipole and quadrupole fit to the data is shown in Fig. 4.8c. Also in this case, part of the amplitude of the anisotropy due to the presence of the Gaussian source is absorbed by the fit which leads to an overestimation of the large-scale component in the regions surrounding the excess. This is evident in the significance (Fig. 4.8d) and relative intensity (Fig. 4.8e) maps shown for a smoothing radius of 20°.

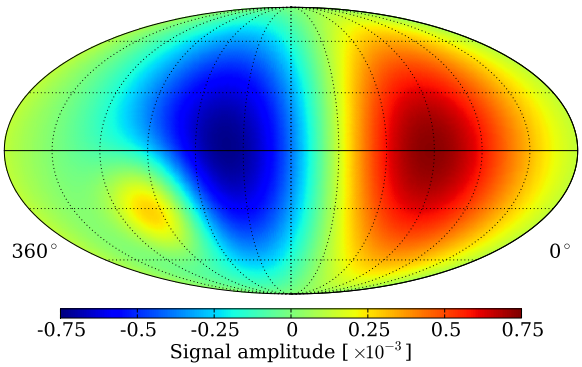

(a) Input map for a dipole and quadrupole signal with Gaussian source near the minimum.

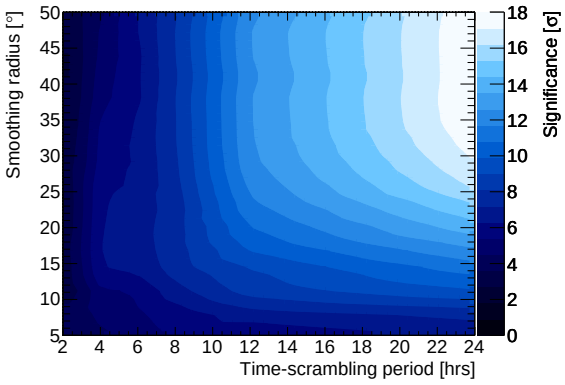

(b) Maximum significance as a function of smoothing radius and time scrambling window length.

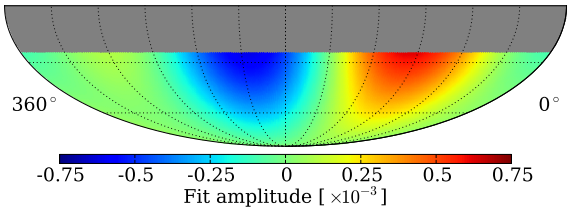

(c) Best fit dipole and quadrupole map.

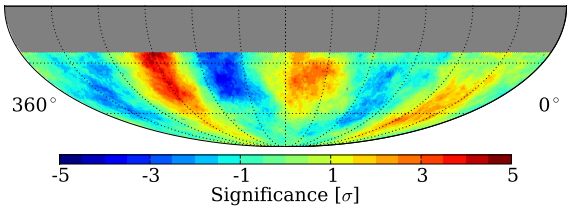

(d) Significance map for 20° smoothing of the dipole and quadrupole fit residuals with 24 hour time-scrambling.

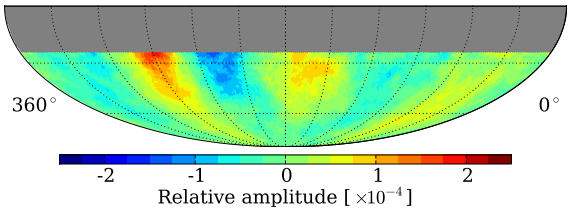

(e) Relative intensity map for 20° smoothing of the dipole and quadrupole fit residuals with 24 hour time-scrambling.

Figure 4.7: Result plots for the dipole and quadrupole data set with a Gaussian source located near the large-scale minimum.

Even though the dipole and quadrupole fit reduces the amplitude of the Gaussian source located near the maximum, it is still clear in the relative intensity and significance maps that the excess is present at small angular scales.

4.3.5 Conclusions

Toy Monte Carlo data sets were generated to test the performance of the time-scrambling algorithm and a procedure to remove large-scale structure for realistic anisotropy patterns of varying angular size, amplitude, and orientation. A number of important conclusions can be drawn for this study that must be taken into account when interpreting the results of the anisotropy search presented in this work.

It was shown in the analysis of the Compton-Getting dipole that for large-scale anisotropy the method is only sensitive to the component of the anisotropy projected on the equatorial plane. This is equivalent to decomposing the anisotropy in terms of the Laplace spherical harmonics Y_ℓ^m on the celestial sphere and canceling all the harmonic coefficients a_ℓ^m oriented along the z axis ($a_\ell^0 = 0$).

A Gaussian excess on top of a flat background is correctly found by the method, although the amplitude of the feature is underestimated, which implies that the real amplitude of any anisotropy observed in experimental data may actually be larger than measured. The presence of the Gaussian source induces an overestimation of the isotropic floor for the entire declination band where it is located. This is a known issue of the time-scrambling method.

The injection of large-scale anisotropy in the form of dipole and quadrupole modes does not induce anisotropy at smaller angular scales by itself, regardless of time-scrambling window length and smoothing radius. This was originally a concern in the study for small-scale anisotropy. A small scale anisotropy such as a Gaussian excess located on top of different parts of large-scale structure can be correctly identified by fitting and subtracting the large scale components and smoothing the fit residuals. Some distortion of the small-scale anisotropy due to the fit and subtraction procedure is unavoidable.

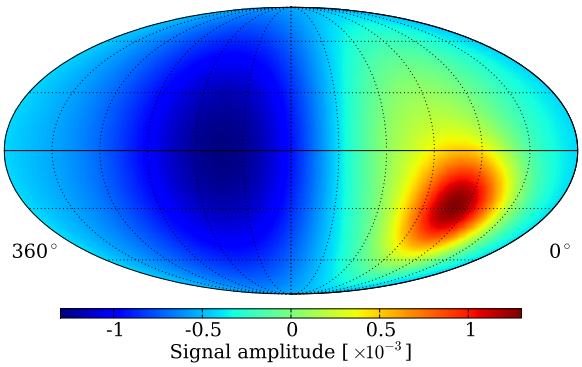

(a) Input map for a dipole and quadrupole signal with Gaussian source near the maximum.

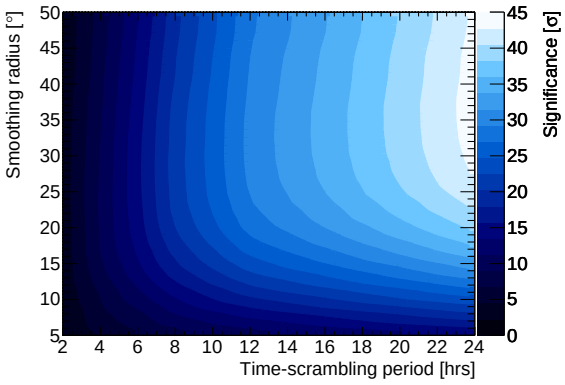

(b) Maximum significance as a function of smoothing radius and time scrambling window length.

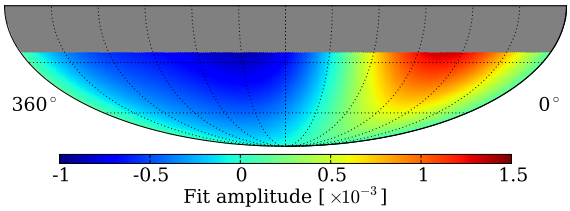

(c) Best fit dipole and quadrupole map.

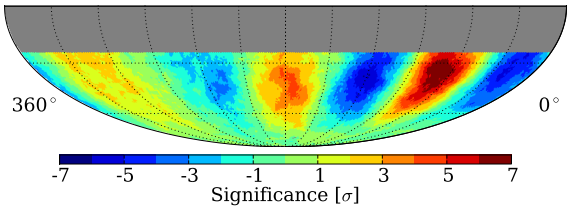

(d) Significance map for 20° smoothing of the dipole and quadrupole fit residuals with 24 hour time-scrambling.

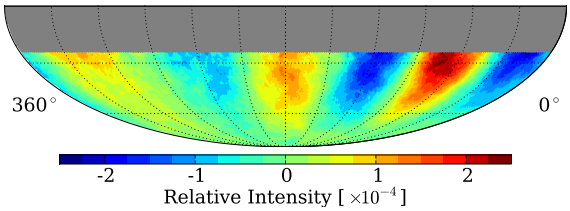

(e) Relative intensity map for 20° smoothing of the dipole and quadrupole fit residuals with 24 hour time-scrambling.

Figure 4.8: Result plots for the dipole and quadrupole data set with a Gaussian source located near the large-scale maximum.

Despite its intrinsic limitations, the time-scrambling algorithm has been demonstrated to be a powerful tool to search for anisotropy at per-mille scale or lower.

Chapter 5

Anisotropy as a Function of Angular Scale

5.1 Introduction

The analysis of IC22 data (described in Chapter 1) revealed the presence of a large-anisotropy at TeV energies in the southern sky for the first time. It is possible that the southern sky presents small-scale anisotropy similar to that observed by Milagro in the north. For this reason, in this work we search for anisotropy over a wide range of angular scales.

The basis of this study is the angular power spectrum of the arrival direction distribution. A power spectrum analysis decomposes the skymap into spherical harmonics and provides information on the angular scale of the anisotropy in the map. The power spectrum indicates which multipole moments $\ell = (0, 1, 2, \ldots)$ in the spherical harmonic expansion contribute significantly to the observed arrival direction distribution. To produce a skymap of the contribution of the $\ell \geq 3$ multipoles, the strong contributions from the dipole ($\ell = 1$) and quadrupole ($\ell = 2$) have to be subtracted first. The residual map can then be studied for structure on angular scales corresponding to $\ell \geq 3$.

The analysis presented in this chapter is based on data collected using the IC59 configuration of IceCube, which operated between May 2009 and May 2010. The results of this search were published in [134] and represent the first search for structure at multiple angular scales in the arrival direction distribution of TeV cosmic rays in the southern sky. An update on these studies is also presented using all currently available cosmic-ray data from IceCube, which consists of 150 billion events recorded between 2007 and 2012. This

corresponds to data recorded by all partial configurations of IceCube between IC22 and the first year of operation of the full detector, IC86 (see Table 2.1 for the start and end times for each configuration).

5.2 The DST Data Set

For the anisotropy study, we make use of the DST data stream presented in Section 2.2.4. The DST data contain the results of an SPE reconstruction, the number of DOMs and hits participating in each event, the total number of triggered strings, and the position of the center of gravity of the event. The number of DOMs in the event can be used as a measure of the energy of the primary cosmic ray. Above 1 TeV, the energy resolution is of order of 0.5 in $\Delta(\log(E))$, where E is the energy of the primary cosmic ray. Most of the uncertainty originates in the physics of the air shower. In this energy range, we are dominated by air showers containing muons with energies near the threshold necessary to reach the deep ice. Fluctuations in the generation of these muons are the main contribution to the uncertainty in the determination of the energy of the primary cosmic ray.

The IC59 data used in the first search for anisotropy at multiple angular scales was collected between 2009 May 20 and 2010 May 30. The data set contains approximately 3.4×10^{10} muon events detected with an integrated livetime of 334.5 days. A cut in zenith angle to remove misreconstructed tracks near the horizon (see below) reduces the final data set to 3.2×10^{10} events.

Simulated air showers are used to evaluate the median angular resolution of the likelihood reconstruction and the median energy of the DST sample. The simulated data are created using the standard air shower Monte Carlo program CORSIKA [97]. The cosmic ray spectrum and composition are simulated using the polygonato model [20], and the air showers are generated with the SIBYLL model of high-energy hadronic interactions [114].

The simulations show that, for zenith angles smaller than 65°, the median angular resolution is 3°. This is not to be confused with the angular resolution of IceCube for neutrino-induced tracks (better than 1°), where more sophisticated reconstruction algorithms and

more stringent quality cuts are applied. The resolution depends on the zenith angle of the muon. Fig. 5.1 (left) shows the median angular resolution as a function of zenith angle. The resolution improves from 4° at small zenith angles to about 2.5° near 60°. The larger space angle error at small zenith angles is caused by the detector geometry, which makes it difficult to reconstruct the azimuth angle for near-vertical showers. Consequently, with the azimuth angle being essentially unknown, the angular error can be large. For zenith angles greater than 65°, the angular resolution degrades markedly. The reason is that more and more events greater than 65° are misreconstructed tracks of smaller zenith angle and lower energy. The energy threshold for muon triggers increases rapidly with slant depth in the atmosphere and ice, and the statistics at large zenith angle become quite poor. We restrict our analysis to events with zenith angles smaller than 65°. Within this range, the angular resolution is roughly constant and much smaller than the angular size of arrival direction structure we are trying to study.

Using simulated data, we estimate that the overall median energy of the primary cosmic rays that trigger the IceCube detector is 20 TeV. Simulations show that at this energy the detector is more sensitive to protons than to heavy nuclei like iron. The median energy increases monotonically with the true zenith angle of the primary particle (Fig. 5.1 (right)) due to the attenuation of low-energy muons with increasing slant depth of the atmosphere and ice. The median energy also increases as a function of reconstructed zenith angle. Near the horizon, the large fraction of misreconstructed events causes the median energy to fall.

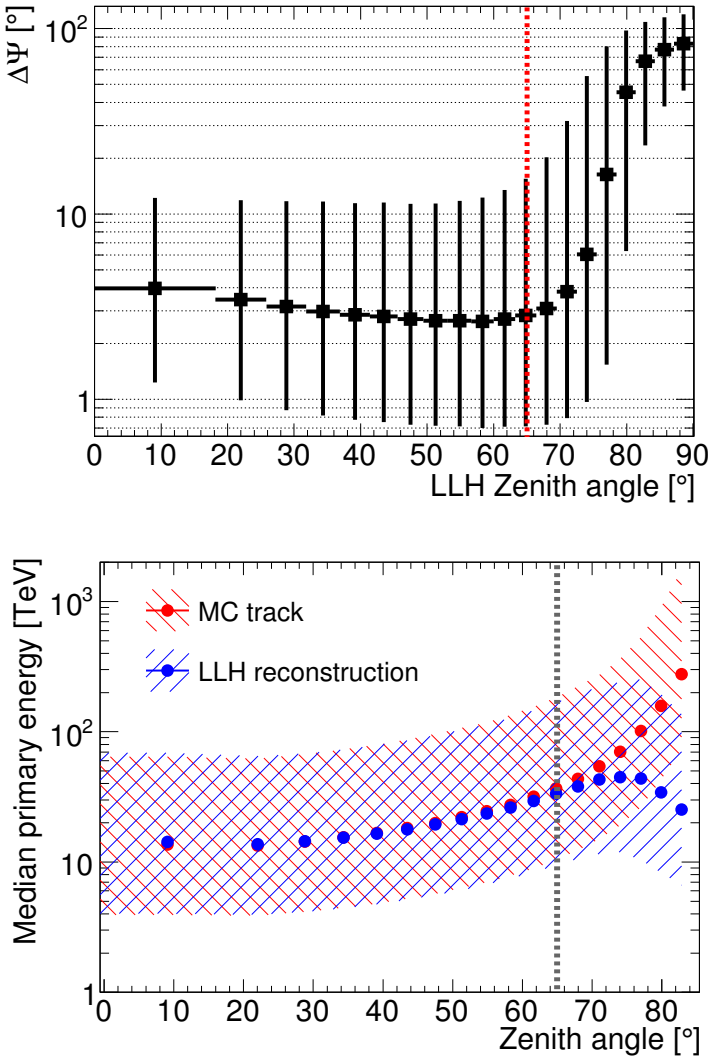

Figure 5.1: Median angular resolution *(top)* and median energy *(bottom)* as a function of zenith angle for simulated cosmic-ray events. The error bars on the left plot and the hatched regions on the right one correspond to a 68% containing interval. The median primary energy is shown both as a function of the true zenith angle (MC track) and the reconstructed zenith angle (LLH reconstruction), while the median angular resolution *(left)* is shown as a function of the reconstructed zenith angle only. The dotted vertical line at $\theta = 65°$ indicates the cut in zenith angle performed in this work.

5.3 Analysis

The search for anisotropy is conducted by calculating data and reference level maps as described in Chapter 4 and by searching for significant deviations with respect to the isotropic level in the relative intensity and statistical significance maps.

The selected resolution for the HEALPix maps ($N_{\text{side}} = 64$) divides the sky into 49 152 pixels with an average pixel size of about 0.9°. Due to the zenith angle cut of 65° discussed in Section 5.2, the pixels above declination $\delta = -25°$ are masked in the analysis. This leaves 14 196 pixels in the region between $\delta = -25°$ and the celestial South Pole at $\delta = -90°$.

Fig. 5.2 (left) shows the relative intensity when a 24-hour time window is used to estimate the reference level. The map exhibits clear structures. The most obvious features are a broad excess in the relative counts near right ascension 105°, and a broad deficit near 225°. The relative intensity in the excess (and deficit) region is of order 10^{-3}. This structure is the large-scale anisotropy first observed in the analysis of the IC22 data set and reported in [135]. Since the IC59 data set is larger than the IC22 data set by an order of magnitude, it is now possible to see the large scale structure directly in the data without further rebinning or averaging over many pixels.

Fig. 5.2 (right) shows the statistical error on the relative intensity map calculated using the expression presented in Section 4.2.4. Relative intensity skymaps have declination-dependent statistical uncertainties due to the fact that the detector acceptance decreases with larger zenith angle. Since IceCube is located at the South Pole, the relative intensity exhibits large fluctuations near the horizon, corresponding to declinations $\delta > -30°$. Such edge effects are not as severe for skymaps of the significance of the fluctuations, though one must note that the location of structures with large (or small) significance may not coincide with regions of large (or small) relative intensity.

Fig. 5.3 (left) shows the significance map corresponding to the relative intensity map shown in Fig. 5.2. The right panel also shows a distribution of the significance values in all 14196 statistically independent pixels. In an isotropic skymap, the distribution of the

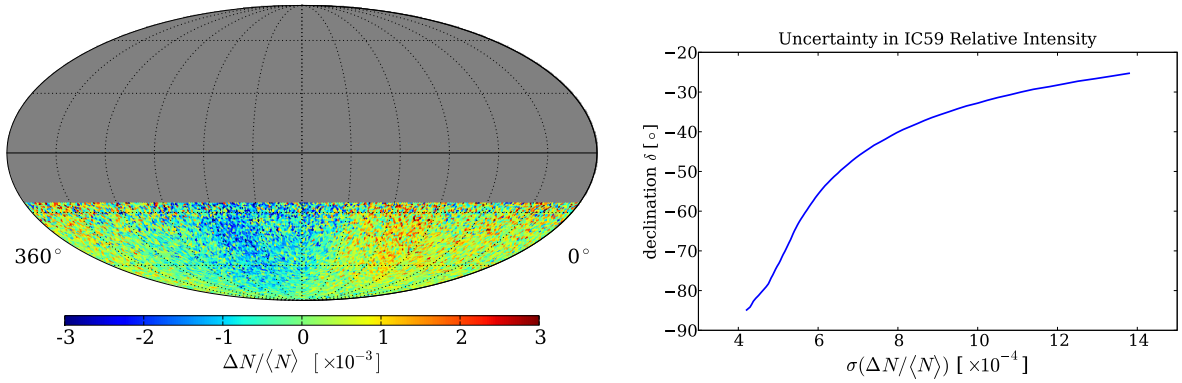

Figure 5.2: *Left:* Relative intensity $\Delta N/\langle N\rangle$ of the IC59 data in equatorial coordinates, produced with a time window of 24 hours. *Right:* Dependence of the statistical error on the declination.

significance values should be normal (red dashed line). However, the best Gaussian fit to the distribution (black solid line) exhibits large deviations from a normal distribution caused by the large-scale structure.

5.3.1 Angular Power Spectrum Analysis

To observe correlations between pixels at several angular scales, we calculate the angular power spectrum of the relative intensity map $\delta I = \Delta N/\langle N\rangle$. The relative intensity can be treated as a scalar field which we expand in terms of a spherical harmonic basis,

$$\delta I(\mathbf{u}_i) = \sum_{\ell=1}^{\infty} \sum_{m=-\ell}^{\ell} a_{\ell m} Y_{\ell m}(\mathbf{u}_i) \tag{5.1}$$

$$a_{\ell m} \sim \Omega_p \sum_{i=0}^{N_{\rm pix}} \delta I(\mathbf{u}_i) Y^*_{\ell m}(\mathbf{u}_i) \quad . \tag{5.2}$$

In Eqs. (5.1) and (5.2), the $Y_{\ell m}$ are the Laplace spherical harmonics, the $a_{\ell m}$ are the multipole coefficients of the expansion, Ω_p is the solid angle observed by each pixel (which is

constant across the sphere in HEALPix), $\mathbf{u}_i = (\alpha_i, \delta_i)$ is the pointing vector associated with the i^{th} pixel, and N_{pix} is the total number of pixels in the skymap. The power spectrum for the relative intensity field is defined as the variance of the multipole coefficients $a_{\ell m}$,

$$\mathcal{C}_\ell = \frac{1}{2\ell+1} \sum_{m=-\ell}^{\ell} |a_{\ell m}|^2 \quad . \tag{5.3}$$

The amplitude of the power spectrum at some multipole order ℓ is associated with the presence of structures in the sky at angular scales of about $180^\circ/\ell$. In the case of complete and uniform sky coverage, a straightforward Fourier decomposition of the relative intensity maps would yield an unbiased estimate of the power spectrum. However, due to the limited exposure of the detector, we only have direct access to the so-called pseudo-power spectrum, which is the convolution of the real underlying power spectrum and the power spectrum of the relative exposure map of the detector in equatorial coordinates. In the case of partial sky coverage, the standard $Y_{\ell m}$ spherical harmonics do not form an orthonormal basis that we can use to expand the relative intensity field directly. As a consequence of this, the pseudo-power spectrum displays a systematic correlation between different ℓ modes that needs to be corrected for.

The deconvolution of pseudo-power spectra has been a longstanding problem in CMB astronomy, and there are several computationally efficient tools available from the CMB community. (For a discussion on the bias introduced by partial sky coverage in power spectrum estimation and a description of several bias removal methods, see [136].) To calculate the power spectrum of the IC59 data, we use the publicly available `PolSpice`[1] software package [137, 138].

In `PolSpice`, the correction for partial sky bias is performed not on the power spectrum itself, but on the two-point correlation function of the relative intensity map. The two-point correlation function $\xi(\eta)$ is defined as

$$\xi(\eta) = \langle \delta I(\mathbf{u}_i)\, \delta I(\mathbf{u}_j) \rangle \quad , \tag{5.4}$$

[1] `PolSpice` website: `http://www2.iap.fr/users/hivon/software/PolSpice/`.

where $\delta I(\mathbf{u}_k)$ is the observed relative intensity in the direction of the k^{th} pixel. Note that $\xi(\eta)$ depends only on the angle η between any two pixels. The two-point correlation function can be expanded into a Legendre series,

$$\xi(\eta) = \frac{1}{4\pi} \sum_{\ell=0}^{\infty} (2\ell + 1)\ \mathcal{C}_\ell\ P_\ell(\cos\eta) \quad , \tag{5.5}$$

where the $\mathcal{C}_\ell$ are the coefficients of the angular power spectrum and the P_ℓ are the Legendre polynomials. The inverse operation

$$\mathcal{C}_\ell = 2\pi \int_{-1}^{1} \xi(\eta)\ P_\ell(\cos\eta)\ d(\cos\eta) \tag{5.6}$$

can be used to calculate the angular power spectrum coefficients from a known two-point correlation function.

In order to obtain an unbiased estimator of the true power spectrum, `PolSpice` first calculates the $a_{\ell m}$ coefficients of both the relative intensity map and the relative exposure map doing a spherical harmonics expansion equivalent to that shown in Eq.(5.2). Pseudo-power spectra for both maps are computed from these coefficients using Eq.(5.3), and these spectra are subsequently converted into correlation functions using Eq.(5.5). An unbiased estimator $\tilde{\xi}(\eta)$ of the true correlation function of the data is computed by taking the ratio of the correlation functions of the relative intensity map and the relative exposure map. An estimate $\tilde{\mathcal{C}}_\ell$ of the true power spectrum can then be obtained from the corrected two-point correlation function using the integral expression shown in Eq.(5.6).

This process reduces the correlation between different ℓ modes introduced by the partial sky coverage. Further corrections performed in η-space are used to eliminate ringing artifacts introduced by the limited angular range over which the correlation function is evaluated.

Fig. 5.4 (blue points) shows the angular power spectrum for the IC59 relative intensity map from Fig. 5.2. In addition to a strong dipole and quadrupole moment ($\ell = 1, 2$), higher order terms up to $\ell = 12$ contribute significantly to the skymap. The error bars on the $\tilde{\mathcal{C}}_\ell$ are statistical. The grey bands indicate the one and two sigma bands for a large number of power spectra for isotropic data sets (generated by introducing Poisson fluctuations in the

reference skymap.) As the $\tilde{\mathcal{C}}_\ell$ are still not entirely independent (even after the correction for partial sky coverage is performed), a strong dipole moment in the data can lead to significant higher order multipoles, and it is important to study whether the structure for $3 \leq \ell \leq 12$ is a systematic effect caused by the strong lower order moments $\ell = 1, 2$. Fig. 5.4 (red points) shows the angular power spectrum after the strong dipole and quadrupole moments are removed from the relative intensity map by a fit procedure described in the previous chapter. The plot illustrates that after the removal of the lower order multipoles, indicated by the drop in $\tilde{\mathcal{C}}_\ell$ for $\ell = 1, 2$ (both are consistent with 0 after the subtraction), most of the higher order terms are still present. Only the strength of $\tilde{\mathcal{C}}_3$ and $\tilde{\mathcal{C}}_4$ is considerably reduced (the former to a value that is below the range of the plot).

Regarding systematic uncertainties, for $\ell = 3$ and $\ell = 4$ the effects of the strong dipole and quadrupole suggest that there is significant coupling between the low-ℓ modes. Therefore, we cannot rule out that $\tilde{\mathcal{C}}_3$ and $\tilde{\mathcal{C}}_4$ are entirely caused by systematic effects. For the higher multipoles, the systematic effects of this distortion are much lower. After explicit subtraction of the $\ell = 1$ and $\ell = 2$ terms (Fig. 5.4), the residual power spectrum agrees with the original power spectrum within the statistical uncertainties. Therefore, we conclude that the systematic uncertainties in these data points are, at most, of the same order as the statistical uncertainties.

In summary, the skymap of cosmic ray arrival directions contains significant structures on scales down to $\sim 15^\circ$. In the next sections, we describe analysis techniques to make the smaller scale structure visible in the presence of the much stronger dipole and quadrupole moments.

5.3.2 Subtraction of the Dipole and Quadrupole Moments

The two-dimensional harmonic expansion of Eq. (4.11) was fit to the 14 196 pixels in the IC59 data that lie between the celestial South Pole and declination $\delta = -25^\circ$. The best-fit dipole and quadrupole coefficients are provided in Table 5.1, and the corresponding sky distribution is shown in Fig. 5.5. By themselves, the dipole and quadrupole terms can

account for much of the amplitude of the part-per-mille anisotropy observed in the IceCube data. We note that the quadrupole moment is actually the dominant term in the expansion, with a total amplitude that is about 2.5 times larger than the dipole magnitude.

The fit $\chi^2/\mathrm{ndf} = 14743/14187$ corresponds to a χ^2-probability of approximately 0.05%. The dipole and quadrupole are dominant terms in the arrival direction anisotropy, but they do not appear to be sufficient to explain all of the structures observed in the angular distribution of $\Delta N/\langle N \rangle$. This result is consistent with the angular power spectrum analysis in Section 5.3.1, which also indicates the need for higher-order multipole moments to describe the structures in the relative intensity skymap.

Subtraction of the dipole and quadrupole fits from the relative intensity map shown in Fig. 5.2 yields the residual map shown in Fig. 5.6. The fit residuals are relatively featureless at first glance, and the significance values are well-described by a normal distribution, which is expected when no anisotropy is present. However, the bin size in this plot is not optimized for a study of significant anisotropy at angular scales larger than the angular resolution of the detector. To improve the sensitivity to larger features, we apply a smoothing procedure which simply takes the reference level and residual data counts in each bin and adds the counts from pixels within some angular radius of the bin. This procedure results in a map with Poisson uncertainties, though the bins are no longer statistically independent.

The actual size of any possible excess or deficit region (and thus the optimal smoothing scale) is not known *a priori*. Furthermore, the skymap may contain several significant structures of different size, with the optimal smoothing radius differing for each structure. To make the search as comprehensive as possible, we study the skymap on all smoothing scales from 3° (the angular resolution) to 45° in steps of 1° and search for regions of high significance at any location. Applying this procedure, the two most significant localized excesses on the sky are a region with a peak significance of $7.0\,\sigma$ at a smoothing radius of 22° at $(\alpha = 122.4°, \delta = -47.4°)$, and a region of peak significance 6.7σ at a smoothing radius of 13° at $(\alpha = 263.0°, \delta = -44.1°)$. These values do not account for statistical trials due to the scan over smoothing radii or the scan for the peak significance in the 14 196 pixels. We

have estimated the trial factors using a Monte Carlo simulation of isotropic data. After trial factors are applied, the maximum significance of the "hot spot" with an optimal smoothing radius of 22° is reduced to 5.3σ, and the "hot spot" at 13° is reduced to 4.9σ.

Skymaps of the relative intensity and the significance of the residual data are plotted in Fig. 5.7, where a smoothing radius of 20° has been used. The radius is not optimal for any of the most significant excesses, but with this choice all of the significant features can be seen with reasonable resolution. Compared to the intensity of the dipole and quadrupole shown in Fig. 5.2, the smaller structures are weaker by about a factor of 5.

Table 5.2 contains the location and optimal smoothing scales of all the regions in the IC59 skymap which have a pre-trials significance beyond $\pm 5\sigma$. The data also exhibit additional regions of excess and deficit. As described in Chapter 2, it is possible that the deficits are at least in part artifacts of the reference level estimation procedure, which can produce artificial deficits around regions of significant excess counts (or in principle, excesses in the presence of strong physical deficits). While several of the deficit and excess regions are observed at large zenith angles near the edge of the IC59 exposure region, we do not believe these features are statistical fluctuations or edge effects. The deficit identified as region 6 will be important for the discussion on the study of the anisotropy at higher energies in Chapter 6, since it is located at the same position as a broad deficit observed with IceCube and IceTop at energies above 400 TeV.

Fig. 5.8 shows the significance maps with regions with a pre-trial significance larger than $\pm 5\sigma$ indicated according to the numbers used in Table 5.2. Since the optimal scales vary from region to region and no single smoothing scale shows all regions, we show the maps with two smoothing scales, 12° (left), and 20° (right).

The angular power spectrum of the residual map is shown in red in Fig. 5.4. As expected, there is no significant dipole or quadrupole moment left in the skymap, and the $\ell = 3$ and $\ell = 4$ moments have also disappeared or have been weakened substantially. However, the moments corresponding to $5 \leq \ell \leq 12$ are still present at the same strength as before the

subtraction, and indicate the presence of structure of angular size 15° to 35° in the data. The excesses and deficits in Fig. 5.7 correspond in size to these moments.

5.3.3 A Filter for Structure on Small Angular Scales

In previous works [64, 68], a different method is applied to filter the lower ℓ terms and create skymaps showing the small-scale structure. In these analyses, the dipole and quadrupole moments are not fit and subtracted, but suppressed by varying the time window Δt over which the reference level is estimated (*i.e.*, the length of time in which the time scrambling, or any other method for generating an isotropic sky, is performed). We apply this method to the IC59 data to compare the results to the dipole and quadrupole subtraction outlined in Section 5.3.2.

Different time windows probe the presence of anisotropy at different angular scales. The time scrambling fits structures that are larger than $15^\circ/\text{hour} \times \Delta t$, and the angular size of a multipole of order ℓ in the sky is $\sim 180^\circ/\ell$. This implies that the technique filters out modes with $\ell < 12\ \text{hours}/\Delta t$ and reduces the magnitude of the modes near this threshold.

The efficiency of the method in suppressing larger structures (low-ℓ moments) is demonstrated in Fig. 5.9, where the angular power spectra are plotted for relative intensity maps constructed with seven values of Δt between 2 hours and 24 hours. As expected, the strength of the low-order multipoles decreases monotonically with Δt. However, the power spectrum also reveals that the low-ℓ moments, in particular the quadrupole term, are not completely removed from the data unless Δt is as small as 3 hours. In addition, the choice of $\Delta t \leq 3\,\text{hours}$ also appears to weaken the power observed in the modes $3 \leq \ell \leq 12$. Consequently, the residual map from Section 5.3.2 and the skymaps produced by choosing a small Δt cannot be expected to agree in all details. Nevertheless, a comparison of the skymaps produced with the two methods provides an important crosscheck.

To best compare this analysis to the results of Section 5.3.2, the reference level is calculated using a scrambling time window of $\Delta t = 4\,\text{hours}$. This choice of Δt is motivated by the angular power spectrum in Fig. 5.9. With $\Delta t = 4\,\text{hours}$, the spectrum shows the strongest

suppression of the dipole and quadrupole while still retaining most of power in the higher multipole moments.

Skymaps of the relative intensity and significance for $\Delta t = 4$ hours are shown in Fig. 5.10. The maps have been smoothed by 20° to allow for a direct comparison with Fig. 5.7. The most prominent features of the map are a single broad excess and deficit, with several small excess regions observed near the edge of the exposure region. The broad excess is centered at $\alpha = (121.7^{+4.8}_{-7.1})^\circ$ and $\delta = (-44.2^{+12.1}_{-7.8})^\circ$, at the same position as Region 1 in Table 5.2. The optimal smoothing scale of the excess is 25°, with a pre-trials significance of 9.6σ. A second significant excess is observed at $\alpha = (341.7^{+1.4}_{-5.6})^\circ$ and $\delta = (-34.9^{+3.6}_{-6.8})^\circ$ with a peak significance of 5.8σ at a smoothing scale of 9°. This feature does not appear to have a direct match in Fig. 5.7, but is roughly aligned in right ascension with the excess identified in Table 5.2 as Region 4. We also note that the second-largest excess in Table 5.2, Region 2, is visible near $\alpha = 263.0^\circ$ in Fig. 5.10, but with a pre-trials peak significance of 4.5σ after smoothing by 13°.

The differences in significance between Figs. 5.7 and 5.10 can be attributed to the fact that some contributions from the low-ℓ moments are still present in this analysis. The broad excess observed here is co-located with the maximum of the large-scale structure shown in Fig. 5.5, enhancing its significance. By comparison, the excess in Region 2 is close to the minimum of the large-scale structure, weakening its significance. The leakage of large-scale structure into the $\Delta t = 4$ hour skymap also explains the large deficit near $\alpha = 220^\circ$; due to its co-location with the minimum of the dipole and quadrupole, the size of the deficit is enhanced considerably.

This effect is illustrated in Fig. 5.11, which shows the relative intensity for the declination range $-45^\circ < \delta < -30^\circ$, projected onto the right ascension axis. This declination range is chosen because it contains some of the most significant structures of the skymaps. The blue points show the relative intensity corresponding to Fig. 5.7, *i.e.*, the skymap after subtraction of dipole and quadrupole moments. The black and red points show the relative intensity for skymaps obtained with the method described in this section; the black points correspond

to $\Delta t = 24$ hours, the red points to $\Delta t = 4$ hours. In the case of $\Delta t = 24$ hours, the large-scale structure dominates. For $\Delta t = 4$ hours, the large-scale structure is suppressed, and the smaller features become visible. The blue and red curves show excesses and deficits at the same locations, but with different strengths. As the red curve still contains some remaining large-scale structure, maxima and minima are enhanced or weakened depending on where they are located with respect to the maximum and minimum of the large-scale structure. The systematic error for the relative intensity values in Fig. 5.11 is taken from the analysis of the data in anti-sidereal time as described in the next section.

Finally, we note that the presence of the small-scale structure can be verified by inspection of the raw event counts in the data. Fig. 5.12 shows the observed and expected event counts for declinations $-45^\circ < \delta < -30^\circ$, projected onto the right ascension axis. The seven panels of the figure contain the projected counts for seven time scrambling windows $\Delta t = \{2, 3, 4, 6, 8, 12, 24 \text{ hours}\}$. For small values of Δt, the expected counts agree with the data; for example, when $\Delta t = 2$ hours, the data exhibit no visible deviation from the expected counts. For larger values of Δt, the expected count distribution flattens out as the technique to estimate the reference level no longer over-fits the large structures. When $\Delta t = 24$ hours, the reference level is nearly flat, and the shape of the large-scale anisotropy is clearly visible from the raw data.

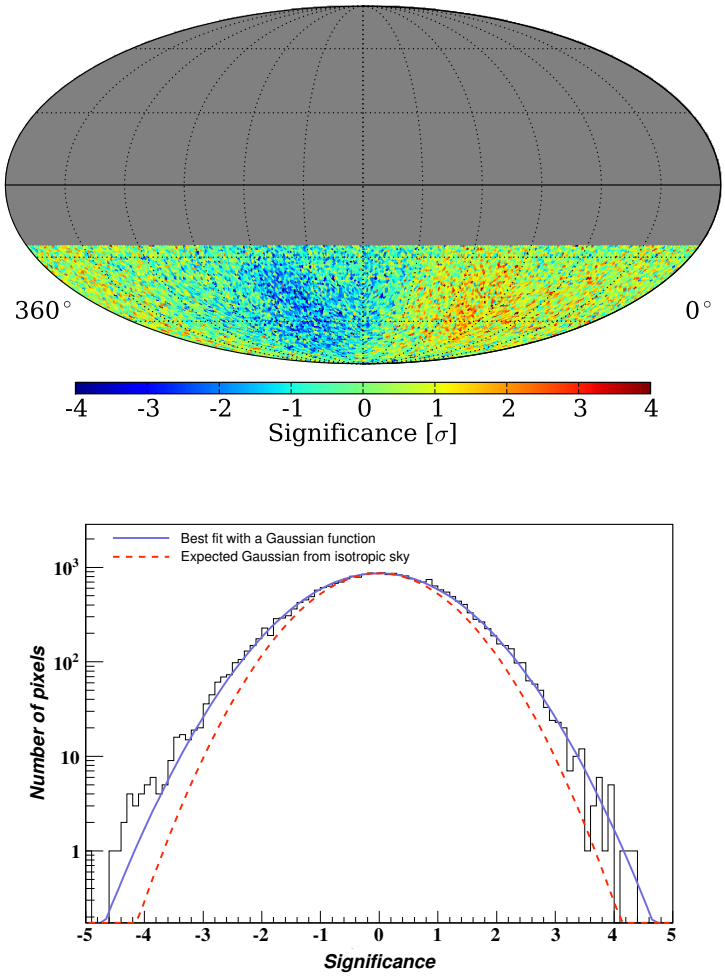

Figure 5.3: *Left*: Significance sky map of the IC59 data in equatorial coordinates, produced using a time window of 24 hours. *Right*: 1d-distribution of the significance values together with the best-fit (black solid line) performed with a Gaussian function. For comparison, a Gaussian function of mean zero and unit variance (red dashed line), expected from an isotropic sky, has been superimposed.

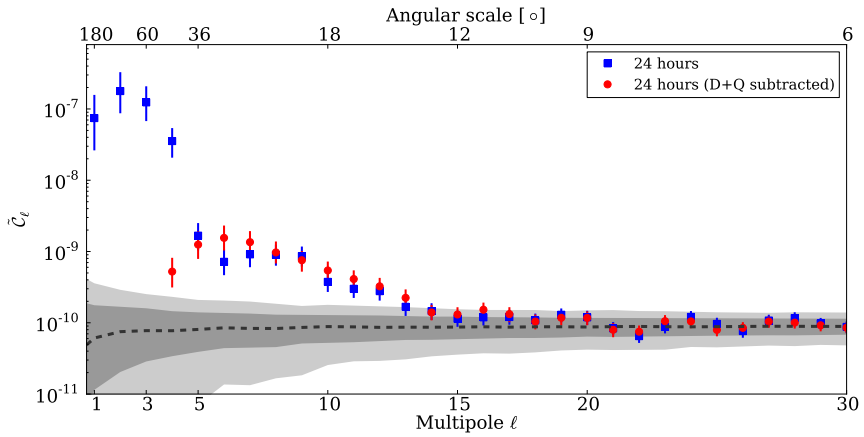

Figure 5.4: Angular power spectra for the relative intensity map shown in Fig. 5.2. The blue and red points show the power spectrum before and after the subtraction of the dominant dipole and quadrupole terms from the relative intensity map. Errors bars are statistical, but a possible systematic error is discussed in the text. The grey bands show 1 and 2 sigma bands for a large set of isotropic sky-generated skymaps.

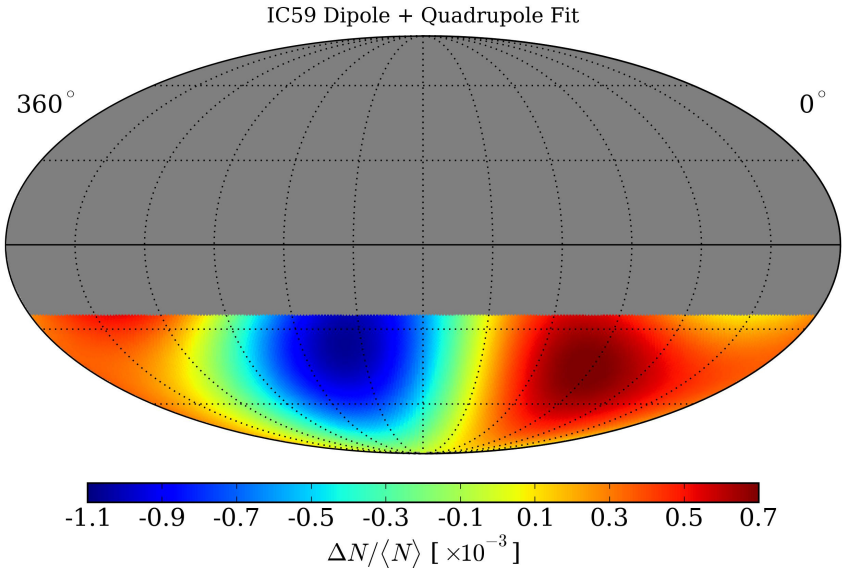

Figure 5.5: Fit of Eq. (4.11) to the IC59 relative intensity distribution $\Delta N/\langle N\rangle$ shown in Fig. 5.2.

Coefficient	Value (stat. + syst.)	Correlation Coefficients								
	$(\times 10^{-4})$	$\chi^2/\text{ndf} = 14743/14187 :\ \Pr(\chi^2\|\text{ndf}) = 5.5 \times 10^{-4}$								
m_0	$0.32 \pm 2.26 \pm 0.28$	1.00								
p_x	$2.44 \pm 0.71 \pm 0.30$	0.00	1.00							
p_y	$-3.86 \pm 0.71 \pm 0.94$	0.00	0.00	1.00						
p_z	$0.55 \pm 3.87 \pm 0.45$	1.00	0.00	0.00	1.00					
Q_1	$0.23 \pm 1.70 \pm 0.17$	0.99	0.00	0.00	0.99	1.00				
Q_2	$-2.95 \pm 0.49 \pm 0.74$	0.00	0.98	0.00	0.00	0.00	1.00			
Q_3	$-8.80 \pm 0.49 \pm 0.50$	0.00	0.00	0.98	0.00	0.00	0.00	1.00		
Q_4	$-2.15 \pm 0.20 \pm 0.50$	0.00	0.00	0.00	0.00	0.00	0.00	0.00	1.00	
Q_5	$-5.27 \pm 0.20 \pm 0.06$	0.00	0.00	0.00	0.00	0.00	0.00	0.00	0.00	1.00

Table 5.1: Coefficients for the fit of Eq. (4.11) to the IC59 relative intensity distribution. The correlation coefficients indicate that there is some degeneracy between the contributions of p_x and Q_2, p_y and Q_3, and p_z and Q_1 due to the fact that the IceCube detector only has a partial view of the sky. The systematic error on the fit parameters is estimated using the results of a fit using anti-sidereal time as described in Section 5.4.2.

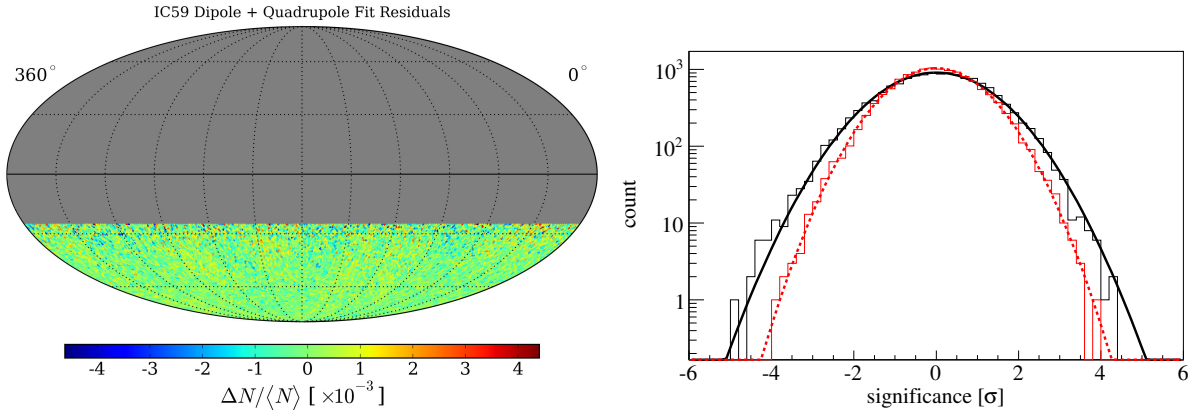

Figure 5.6: *Left*: Residual of the fit of Eq. (4.11) to the relative intensity distribution shown in Fig. 5.2. *Right:* Distribution of pixel significance values in the IC59 skymap before subtraction of the dipole and quadrupole (solid black line) and after (dashed red line). Gaussian fits to the data yield a mean of $(-0.20 \pm 1.05) \times 10^{-2}$ and a width of 1.23 ± 0.01 before the dipole and quadrupole subtraction, and $(0.28 \pm 0.89) \times 10^{-2}$ and 1.02 ± 0.01 after.

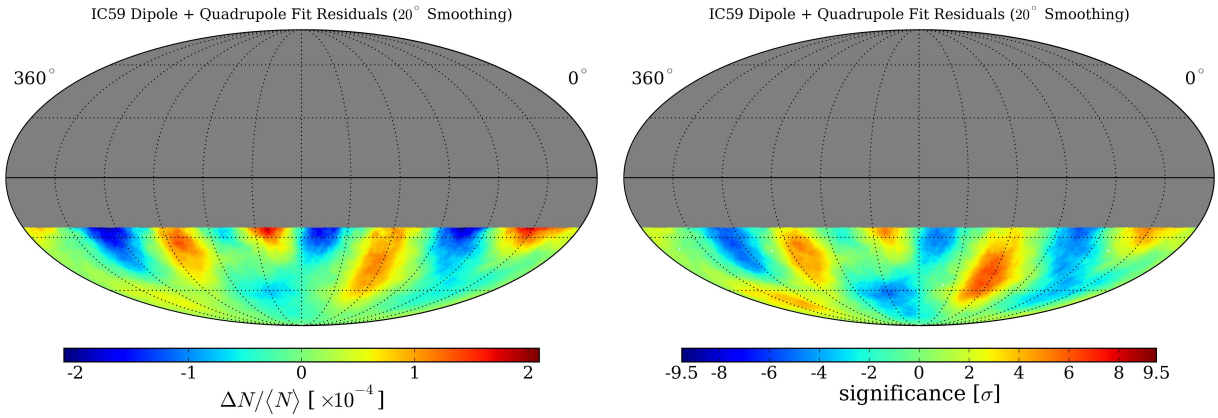

Figure 5.7: *Left*: Residual intensity map plotted with 20° smoothing. *Right*: Significances of the residual map (pre-trials), plotted with 20° smoothing.

region	right ascension	declination	optimal scale	peak significance	post-trials
1	$(122.4^{+4.1}_{-4.7})^\circ$	$(-47.4^{+7.5}_{-3.2})^\circ$	22°	7.0σ	5.3σ
2	$(263.0^{+3.7}_{-3.8})^\circ$	$(-44.1^{+5.3}_{-5.1})^\circ$	13°	6.7σ	4.9σ
3	$(201.6^{+6.0}_{-1.1})^\circ$	$(-37.0^{+2.2}_{-1.9})^\circ$	11°	6.3σ	4.4σ
4	$(332.4^{+9.5}_{-7.1})^\circ$	$(-70.0^{+4.2}_{-7.6})^\circ$	12°	6.2σ	4.2σ
5	$(217.7^{+10.2}_{-7.8})^\circ$	$(-70.0^{+3.6}_{-2.3})^\circ$	12°	-6.4σ	-4.5σ
6	$(77.6^{+3.9}_{-8.4})^\circ$	$(-31.9^{+3.2}_{-8.6})^\circ$	13°	-6.1σ	-4.1σ
7	$(308.2^{+4.8}_{-7.7})^\circ$	$(-34.5^{+9.6}_{-6.9})^\circ$	20°	-6.1σ	-4.1σ
8	$(166.5^{+4.5}_{-5.7})^\circ$	$(-37.2^{+5.0}_{-5.7})^\circ$	12°	-6.0σ	-4.0σ

Table 5.2: Location and optimal smoothing scale for regions of the IC59 skymap with a pre-trials significance larger than $\pm 5\sigma$. The errors on the equatorial coordinates indicate the range over which the significance drops by $1\,\sigma$ from the local extremum.

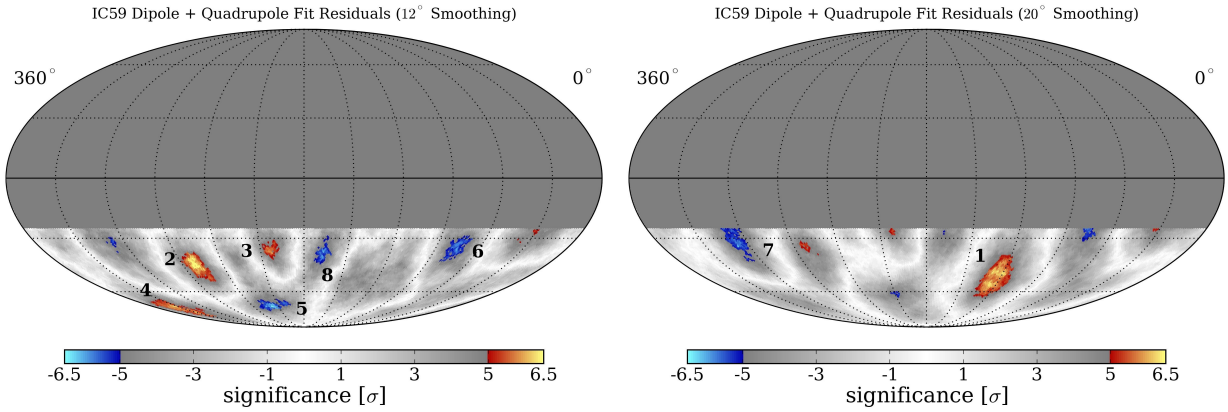

Figure 5.8: *Left*: Significances of the IC59 residual map plotted with 12° smoothing. *Right*: Significances of the IC59 residual map plotted with 20° smoothing. The regions with a pre-trial significance larger than $\pm 5\sigma$ are indicated according to the numbers used in Table 5.2.

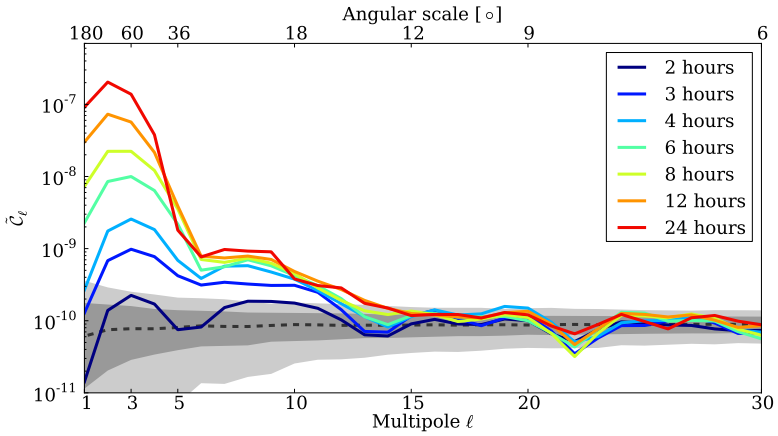

Figure 5.9: Power spectra for different time values of the time scrambling period Δt. The filtering effect of the time scrambling on large-scale structure can be easily seen as a monotonic reduction in the strength of low-ℓ components of the power spectrum. The grey bands show 1 and 2 sigma bands for a large set of isotropic skymaps. See Fig. 5.4 and Section 5.3.1 for statistical uncertainties and a discussion of systematic uncertainties.

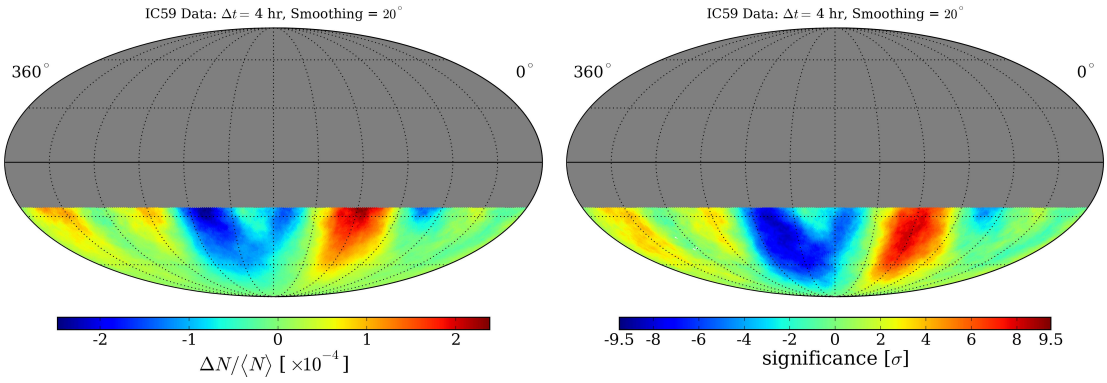

Figure 5.10: Relative intensity *(left)* and significance *(right)* map in equatorial coordinates for $\Delta t = 4$ hours and an integration radius of 20°.

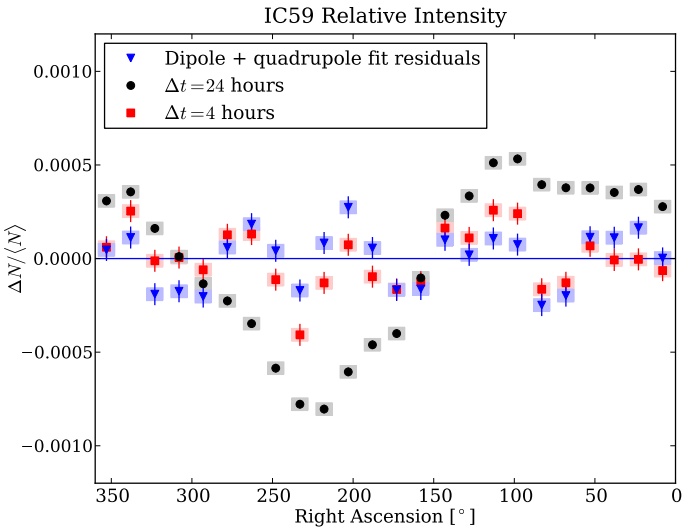

Figure 5.11: Relative intensity in the declination band $-45° < \delta < -30°$ in IC59 data. The blue points show the result after subtracting the dipole and quadrupole moments. The black points correspond to Δt =24 hours and show the large-scale structure, the red points correspond to $\Delta t = 4$ hours. The error boxes represent systematic uncertainties.

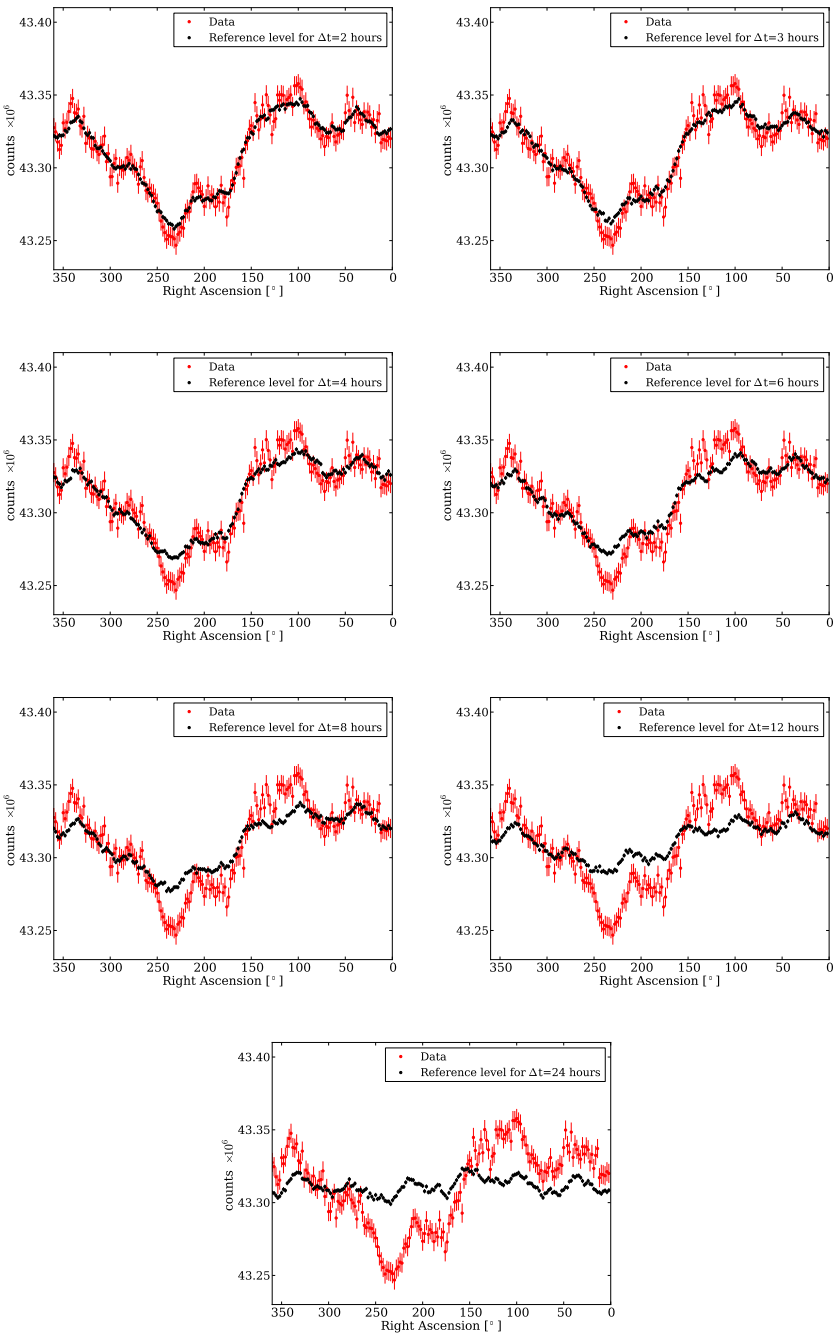

Figure 5.12: Number of signal and isotropic-generated events, with statistical uncertainties, as a function of right ascension for the declination range $-45° < \delta < -30°$, with the reference level estimated in different time windows, from 2 hours (*top-left*) to 24 hours (*bottom*). Each plot has been created using independent $15°\delta \times 2°$ bins in right ascension.

5.4 Systematic Checks

Several tests have been performed on the data to ensure the stability of the observed anisotropy and to rule out possible sources of systematic bias. Among the influences that might cause spurious anisotropy are the detector geometry, the detector livetime, nonuniform exposure of the detector to different regions of the sky, and diurnal and seasonal variations in atmospheric conditions. Due to the unique location of the IceCube detector at the South Pole, many of these effects play a lesser role for IceCube than for detectors located in the mid-latitudes. The southern celestial sky is fully visible to IceCube at any time, and changes in the event rate tend to affect the entire visible sky. Seasonal variations are of order $\pm 10\%$ [139], but the changes are slow and the reference level estimation technique is designed to take these changes into account. This is also true for any effects caused by the asymmetric detector response due to the geometrical configuration of the detector. In this section, we test the accuracy of these assumptions.

5.4.1 Solar Dipole Analysis

As mentioned in Section 1.7.1, an observable dipole anisotropy should be induced by the motion of the Earth around the Sun. The solar dipole effect provides an important check of the reliability of the analysis techniques presented earlier, as it verifies that the techniques are sensitive to a known dipole with an amplitude of roughly the same size as the structures in the equatorial skymap.

As discussed in Chapter 4, any seasonal variation of the solar dipole can cause a spurious anisotropy in equatorial coordinates and vice versa. We follow the example of [140] and [58] and use anti-sidereal time for an estimate of the error from seasonal variations on the amplitude of the sidereal anisotropy, and extended-sidereal time to estimate the systematic error on the solar dipole amplitude.

To measure the solar dipole anisotropy we estimate the reference level using a time window $\Delta t = 24$ hours, which maximizes the sensitivity to large-scale features. The data and reference maps are produced in a coordinate system where the latitude coordinate is

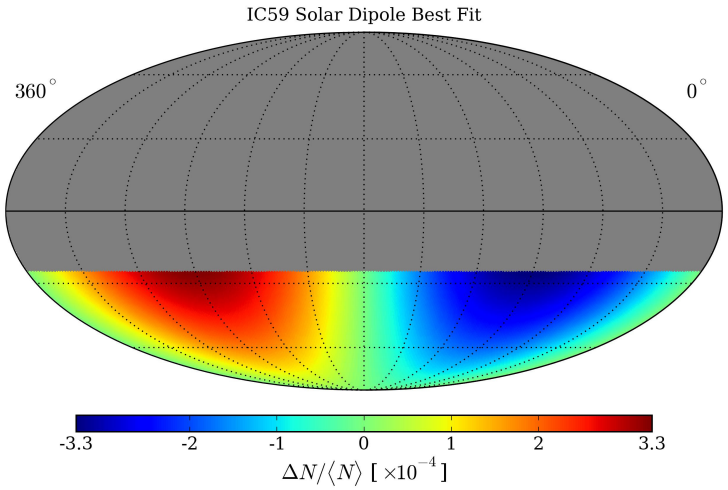

Figure 5.13: Best fit results to the IC59 data expressed in solar coordinates. In this coordinate system, the velocity vector of the motion of the Earth about the Sun is pointing at a longitude of 270°.

declination and the longitude coordinate represents the angular distance from the Sun in right ascension, defined as the difference between the right ascension of each event and the right ascension of the Sun. In this coordinate system the Sun's longitude is fixed at 0° and we expect, over a full year, an excess in the direction of motion of the Earth's velocity vector (at 270°) and a minimum in the opposite direction.

The data are fit using the dipole and quadrupole expansion given in Eq. (4.11). The quadrupole coefficients are found to be equivalent to zero within the fit uncertainties, so the fit is repeated with only a dipole term and a constant offset. The dipole describes the data well; the fit $\chi^2/\text{ndf} = 14207/14192$ corresponds to a χ^2-probability of 41.6%. The best fit coefficients are listed in Table 5.3. Only one free parameter, the p_y component of the dipole fit, differs significantly from zero. Hence, the dipole is pointing at a longitude of 270° within the equatorial plane of this coordinate system, following the expectation for a dipole in the cosmic-ray anisotropy caused by relative motion about the Sun.

Coefficient	Fit Value ($\times 10^{-4}$)
m_0	-0.029 ± 0.058
p_x	0.017 ± 0.142
p_y	-3.661 ± 0.142
p_z	-0.027 ± 0.072

Table 5.3: Coefficients of a dipole and constant offset fit to the IC59 solar coordinate data. The uncertainties are statistical.

The amplitude of the dipole is $(3.66 \pm 0.14_{\text{stat}} \pm 0.99_{\text{sys}}) \times 10^{-4}$. The systematic uncertainty is evaluated by fitting a dipole to the data in a coordinate system using extended-sidereal time. We have conservatively estimated this systematic uncertainty by taking the amplitude of the dipole in extended-sidereal coordinates. Within the large systematic error, the amplitude of the solar dipole agrees with the prediction.

5.4.2 Anti-Sidereal Time Analysis

As described in the previous section, we use the analysis of the data in the anti-sidereal time frame to study systematic effects caused by seasonal variations. For this test, we produce skymaps where anti-sidereal time is used instead of sidereal time in the coordinate transformation from local detector coordinates to "equatorial" coordinates. Skymaps produced in this way are subjected to the same analyses as the true equatorial maps. Neither the angular power spectrum nor the skymaps show any significant deviation from isotropy. In particular, no regions of significant excess or deficit are observed in the anti-sidereal skymaps for any smoothing scale. The systematic error bars shown in Fig. 5.11 are estimated by using the variation in anti-sidereal time as a measure of this error.

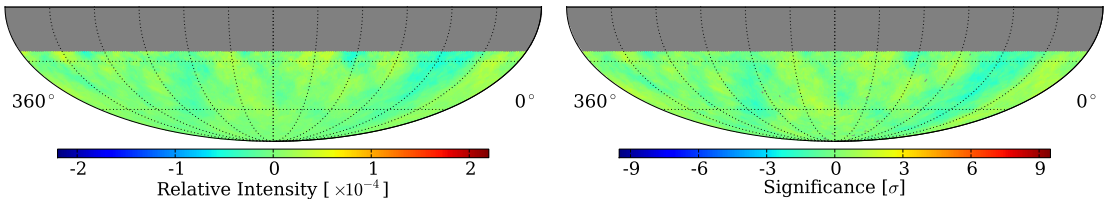

Figure 5.14: Relative intensity *(left)* and significance *(right)* map for a time window of 4 hours and an integration radius of 20°. The maps are represented in a system where the anti-sidereal, instead of the sidereal, time has been used to compute the coordinate transformation from local to equatorial.

5.5 Analysis of the Combined IceCube Data Set

The combination of all cosmic-ray data recorded by IceCube to date provides a large statistics sample that enables the study of the anisotropy at smaller amplitudes and angular scales.

Data from five configurations (IC22, IC40, IC59, IC69, and the first year of operation of IC86) have been used in this search. The final sample, collected over five years, consists of 150 billion cosmic-ray events. The contribution of each detector configuration is detailed in Table 5.4

Similarly to the IC59 study, an angular power spectrum of the relative intensity map (shown in Fig. 5.15a) is used to estimate the strength of the anisotropy over a wide range of angular scales. The spectrum shows excellent agreement with that calculated using IC59 data up to $\ell \sim 15$, where the IC59 spectrum enters the isotropic noise band (Fig. 5.4). It must be noted, however, that the IC59 events are also included but only contribute about 23% of the total sample size.

Since the average value of $\mathcal{C}_\ell$ for an isotropic map of N events is $\sim 1/N$ [141], the higher statistics lower the "noise floor" from $\langle \mathcal{C}_\ell \rangle \sim 10^{-10}$ in IC59 to $\langle \mathcal{C}_\ell \rangle \sim 10^{-11}$ in the combined

Detector	Start	End	Live-time (days)	No. of events ($\times 10^9$)
IC22	06/2007	04/2008	269.4	5.3
IC40	05/2008	05/2009	335.6	18.9
IC59	06/2009	06/2010	335.0	33.8
IC79	06/2010	05/2011	299.7	39.1
IC86	05/2011	05/2012	332.9	52.9
Total				150

Table 5.4: Detector configurations that were used to collect the data analyzed in this work.

set. This reveals power in the spectrum up to $\ell \sim 22$, which corresponds to angular structures in the sky smaller than 10°.

The presence of small scale anisotropy is also evident in the one-dimensional projection of relative intensity as a function of right ascension shown in Fig. 5.15 for the declination range $-75° < \delta < -35°$. A 3° binning was chosen for this plot to match the angular resolution of the cosmic-ray sample. The projection shows both smooth structures several tens of degrees wide (for instance, the large-scale minimum around $\alpha \sim 230°$) and a series of peaks of different widths. An interesting sharp edge is seen near $\alpha \sim 150°$ with a very small relative amplitude and a width well below 10°. This is the first evidence for the presence of such a small structure in the TeV cosmic-ray sky, and its existence could be linked to very local effects, since it is difficult to maintain such a collimated beam with cosmic rays propagating over long distances through the Galactic magnetic field.

In order to reveal the smaller scale anisotropy, the dipole and quadrupole terms of the spherical harmonic functions are fit and subtracted from the relative intensity map. The best fit coefficients are given in Table 5.5 for the spherical harmonic fit functions in Eq. 4.11 and agree with the IC59 results shown in Table 5.1. The residual maps are smoothed to search

for small-scale anisotropy. A map of relative intensity after the dipole- and quadrupole-subtraction in shown in Fig. 5.16 for a smoothing radius of 20°. The map shows excellent agreement with the corresponding IC59 map shown in Fig. 5.7.

Maps of relative intensity and pre-trial statistical significance are shown in Fig. 5.17 before (Figs. 5.17a and 5.17b) and after (Figs. 5.17c and 5.17d) the dipole and quadrupole subtraction procedure for a 5° smoothing radius. The high significance of the small-scale structure shown in the dipole- and quadrupole-subtracted maps indicates for the first time the presence of anisotropy in the flux of TeV cosmic rays at angular scales of about 5°, close to the angular resolution of IceCube for cosmic rays. The sharp edge found in Fig. 5.15b is seen as a band that extends along the $\alpha \sim 150°$ meridian with an amplitude of $\sim 2 \times 10^{-4}$. Note that this is at the location of the most significant structure found in IC59 (Region 1 in Fig.5.8) which had an optimal smoothing scale of 22°. In the 5° skymap it can be seen that Region 1 is in fact composed of two relative excesses separated by about 30° in right ascension.

Coefficient	Value ($\times 10^{-4}$)
m_0	-0.05 ± 0.82
p_x	3.01 ± 0.28
p_y	-2.84 ± 0.28
p_z	-0.08 ± 1.42
Q_1	-0.03 ± 0.64
Q_2	-2.69 ± 0.20
Q_3	-8.14 ± 0.20
Q_4	-2.01 ± 0.09
Q_5	-4.77 ± 0.09

Table 5.5: Dipole and quadrupole coefficients for the best fit to the relative intensity map. The indicated uncertainties are statistical only. A good agreement is found between these values and those shown in 5.1.

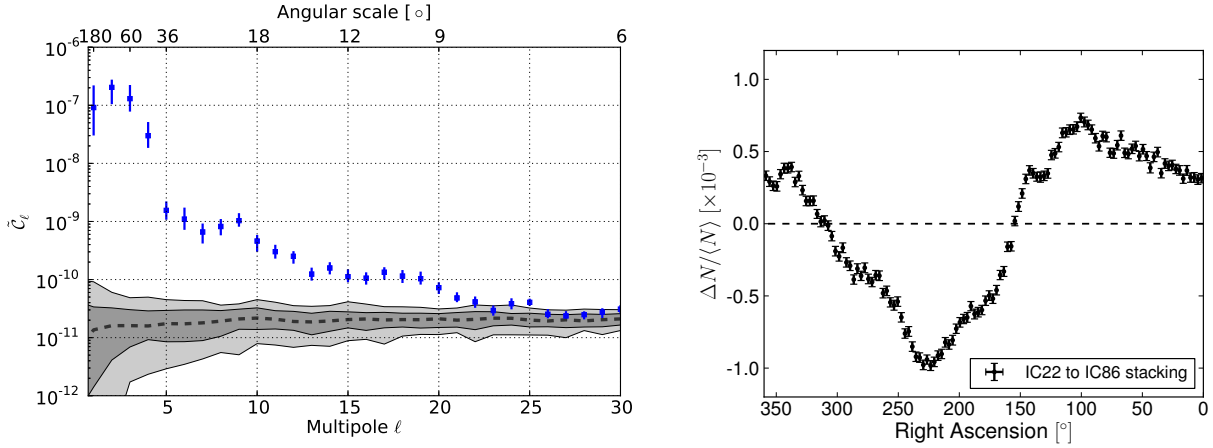

(a) Angular power spectrum.

(b) Relative intensity projection.

Figure 5.15: *Left:* Angular power spectrum of the unsmoothed relative intensity map for the full data set (IC22 to IC86.) Blue points show the power spectrum. Error bars are statistical only. The gray bands indicate the distribution of power spectra for a large sample of isotropic maps, showing the 68% (dark) and 95% containing interval. *Right:* One-dimensional projection of relative intensity as a function of right ascension for the combined IceCube data set. The uncertainties shown are only statistical.

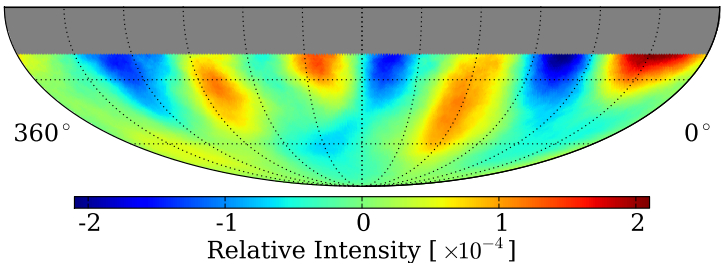

Figure 5.16: Dipole- and quadrupole-subtracted relative intensity map for a smoothing radius of 20°. The structure observed in this map shows good agreement with IC59 results (Fig. 5.7).

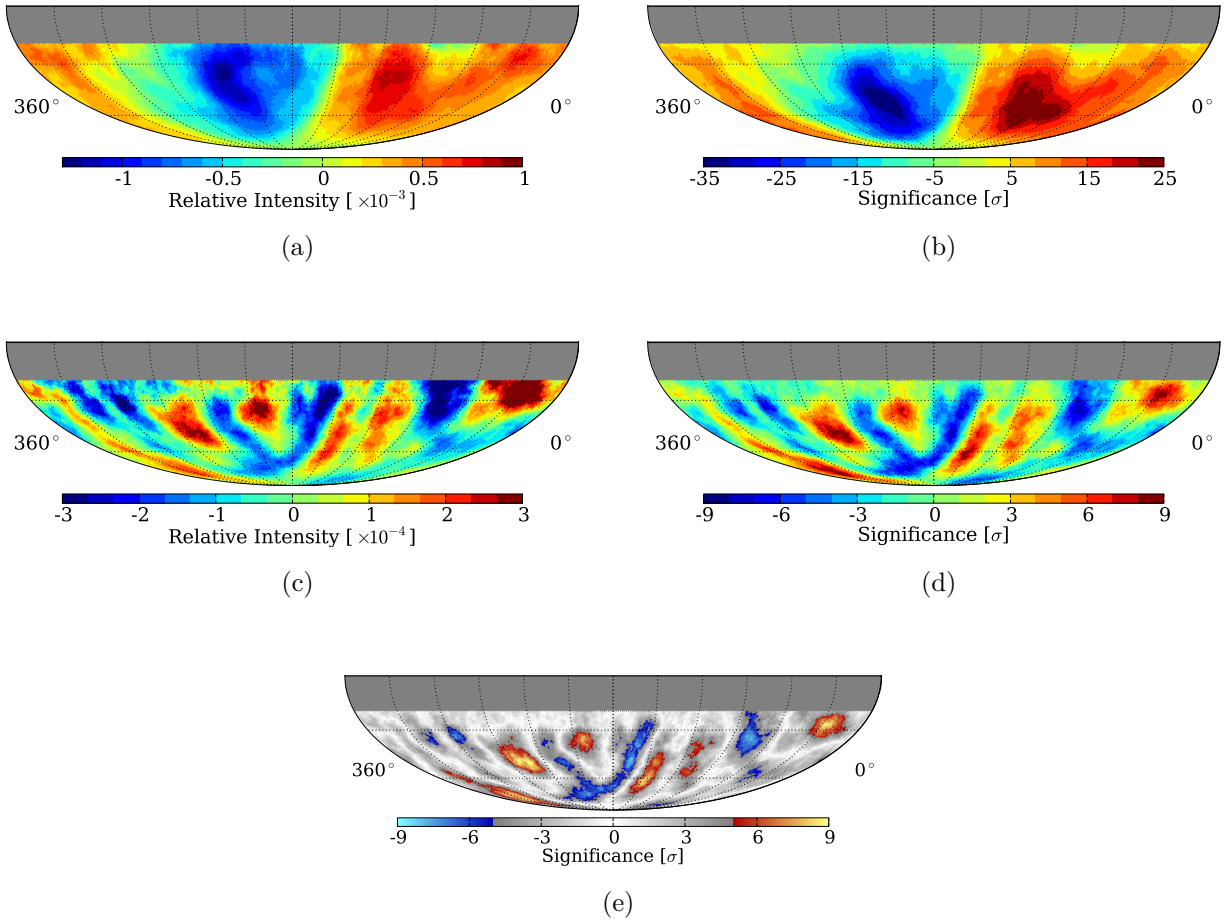

Figure 5.17: Relative intensity and pre-trial statistical significance maps in equatorial coordinates for the combined IceCube data set. The maps are shown before (Figs. 5.17a and 5.17b) and after (Figs. 5.17c and 5.17d) the dipole- and quadrupole subtraction procedure. A 5° smoothing radius was used for all maps. The maps show an anisotropic structure that is statistically significant at an angular scale of about 5°. In Fig.5.17e, the map of statistical significance shown in Fig. 5.17d has been highlighted to indicate excess (deficit) regions with pre-trial significances higher (lower) than 5σ (-5σ).

5.6 Discussion

Using 32 billion events recorded with IC59, we have shown that the arrival direction distribution of cosmic rays with a median energy of 20 TeV exhibits significant anisotropy on all scales up to $\ell = 12$ in the angular power spectrum. The power spectrum is dominated by a dipole and quadrupole moment, but also indicates the presence of significant structure on angular scales down to about 15°. These structures become visible in the skymap when the dominant dipole and quadrupole moments are either subtracted or suppressed. The residual skymap shows both significant excesses and deficits, with the most prominent ones reaching a post-trial significance of $5.3\,\sigma$ in IC59. The relative intensity of the smaller-scale structures are about a factor of 5 weaker than the dipole and quadrupole structure.

The anisotropy search was extended to smaller amplitudes and angular scales using the combined set of all IceCube data collected to date, which consists of 150 billion events. Significant structures are revealed by the analysis down to angular sizes of $\sim 5°$, near the angular resolution of the detector, which represents the first observation of anisotropy at these angular scales.

Together with data from the γ-ray experiments in the northern hemisphere, we now have an almost complete cosmic-ray map of the entire sky at TeV energies. Fig. 5.18 shows the combined IceCube and Milagro skymaps of small-scale anisotropy. For this map, all available IceCube data have been used and the analysis is performed using the method described in Section 5.3.3 with a smoothing radius of 10°. The combined skymap shows significant excess regions in both hemispheres. It is possible that the structure around right ascension 150° spans both hemispheres, as the drop in significances around declination $\delta = 0°$ could be an artifact of the smaller exposure of both detectors near $\delta = 0°$, which corresponds to a region close to the horizon for both detectors.

The strongest excess in the northern sky (region A in the Milagro map located near the celestial equator at $\alpha \sim 60°$, see Section 1.7.1) does not appear to continue to the southern sky. It is possible that since the median of the Milagro data set is about 1 TeV, and the

excess appears to have a cutoff at 10 TeV, the excess is not visible in the 20 TeV IceCube sky map.

There is currently no explanation for these local enhancements in the cosmic ray flux. We note that the two most significant excess regions in the southern sky (regions 1 and 2 in Tab. 5.2) are both located near the Galactic plane. In addition, the position of one of the excess regions (region 1) coincides with the location of the Vela pulsar at ($\alpha = 128.8°, \delta = -45.2°$). At a distance of about 300 pc [142], Vela is one of the closest known supernova remnants, and has long been considered a candidate source for Galactic cosmic ray acceleration. However, the Larmor radius of 10 TeV protons in a μG magnetic field is approximately 0.01 pc, many orders of magnitude smaller than the distance to Vela.

On the other hand, the small-scale structure of the anisotropy might simply be an effect of the turbulent interstellar magnetic field in our vicinity [143]. The spectrum of the magnetic field turbulence may have an imprint on the sizes and amplitudes of the observed small-scale anisotropy, and therefore on the angular power spectrum. The local interstellar magnetic field is thought to be associated to the Loop I shell expanding from the Scorpion-Centaurus Association and to be relatively regular up to several tens of parsec [144], i.e. the order of magnitude of the estimated proton mean free path in the interstellar medium [145]. Cosmic-ray protons with energy 1-10 TeV happen to have a gyro-radius of the order of the heliospheric size, therefore it is possible that the interstellar magnetic field perturbed by the heliosphere provides significant pitch angle scattering to influence and re-distribute the arrival directions [146, 147, 148]. It has been recently postulated that the existence of long-range electric fields in the heliosphere or in the local ISM could produce the small scale structure [149].

The study of cosmic ray arrival directions at TeV energies will continue to be a major ongoing research effort in IceCube. IceCube and the High Altitude Water Cherenkov (HAWC) γ-ray observatory [150] under construction in Mexico can be used to monitor the southern and northern hemisphere, respectively, with high sensitivity. The combined data sets will soon allow for all-sky power spectra and the analysis of the entire sky at all angular scales.

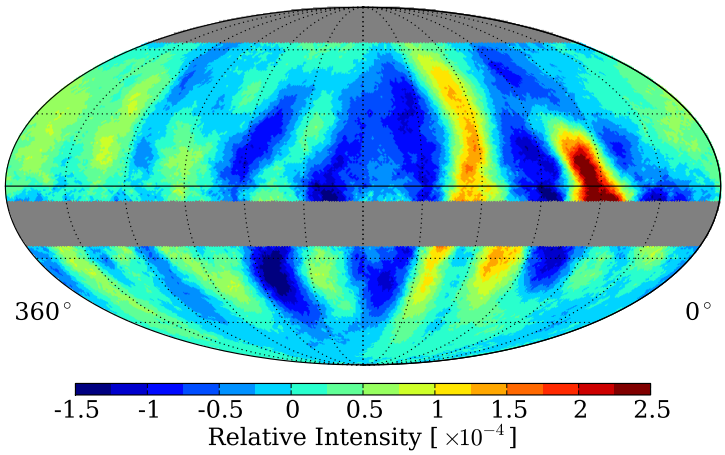

(a)

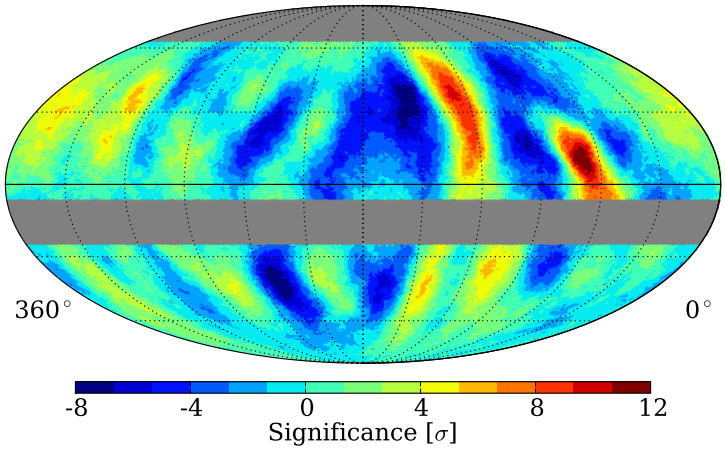

(b)

Figure 5.18: Combined maps of relative intensity (top) and significances (bottom) in the cosmic ray arrival direction distribution observed by Milagro in the northern hemisphere [64] and IceCube in the southern hemisphere (this analysis). Both maps have been smoothed with a 10° radius.

Chapter 6

Anisotropy as a Function of Energy

6.1 Introduction

The observation of cosmic ray anisotropy in both hemispheres at multi-TeV energies has been discussed in Chapters 1 and 5 of this work. The cosmic-ray sky at these energies is dominated by large scale structure of per-mille amplitude but also presents smaller features with typical sizes between 5° and 20° which is about a factor of five weaker in amplitude than the large scale pattern.

These observations can be explained, at least qualitatively, in the framework of diffusive transport of cosmic rays in our galaxy. As mentioned in Chapter 1, cosmic ray diffusion from recent (10...100 kyrs) nearby supernovae may produce anisotropy that would be observed on Earth as a dipole with its maximum possibly oriented towards the source. Depending on the geometrical parameters of the propagation, the observed large-scale anisotropy would be the result of the superposition of individual dipoles from different sources. In the absence of clear evidence of cosmic-ray acceleration in nearby sources, an important challenge is identifying which nearby supernovae may be contributing to the current cosmic-ray flux at Earth [63, 62]. For this reason, it is difficult to predict the orientation of the dipole anisotropy. However, all diffusion models predict a power-law increase in the amplitude of the anisotropy with energy. The study of the energy dependence may therefore provide information about the propagation of cosmic rays at TeV energies and higher.

In the Northern hemisphere, the EAS-TOP data contain weak evidence for an increase in the amplitude of the anisotropy as a function of energy, as well as a change of phase [69].

6.1.1 Study of the Energy Dependence with IceCube

The search for anisotropy at higher energies was extended to the southern hemisphere by IceCube [151] using DST data taken with the IC59 configuration. The anisotropy was explored in two energy bands: 20 TeV and 400 TeV. The bands were created by performing a cut on two variables available in the DST data stream: the reconstructed zenith angle of the events, and the number of triggered DOMs in the detector. The energy scale of the samples was determined by evaluating the effect of the cuts on simulated CORSIKA air showers with the polygonato model of spectrum and composition [20]. After cuts, the low-energy sample consists of 21 billion events with a median primary energy of 20 TeV. For this set, 68% of the events are contained in the 4 - 63 TeV range. The high-energy sample contains 0.58 billion events, with a median energy of 400 TeV and a 68% containing interval defined in the range 100 - 1258 TeV.

The anisotropy observed at 20 TeV is similar to that already described in other chapters of this work. A slight increase in the peak-to-peak amplitude of the anisotropy pattern is visible with respect to the sample without energy cuts presented in Chapter 5. The small deficit region identified as "region 6" in Chapter 5 centered around $\alpha \sim 75^\circ$ is apparently absent after cuts in the 20 TeV sky map. This change can be seen in the sky map shown in Fig. 6.1 which can be compared to the combined sky map for all IceCube data with no energy-dependent cuts shown in Fig. 5.17a. The relative intensity projections of the IC59 data before and after the low-energy cut are compared in Fig. 6.1 for the declination range $-40^\circ < \delta < -25^\circ$ where region 6 dominates.

In the 400 TeV skymap two important features are observed: an excess with a significance of 5.3σ and a optimal smoothing of 29° located at $(\alpha = 256.6^\circ, \delta = -25.9^\circ)$, and a deficit with a significance of -8.6σ and an optimal smoothing of 29° located at $(\alpha = 73.1^\circ, \delta = -25.3^\circ)$, both near the edge of the detector acceptance window. The amplitude of the deficit is about 10^{-3}. The anisotropy at 400 TeV differs in shape and strength from the anisotropy observed at 20 TeV and is no longer a superposition of large- and small-scale structures, but is rather dominated by the single deficit region. The presence of this feature is consistent with the

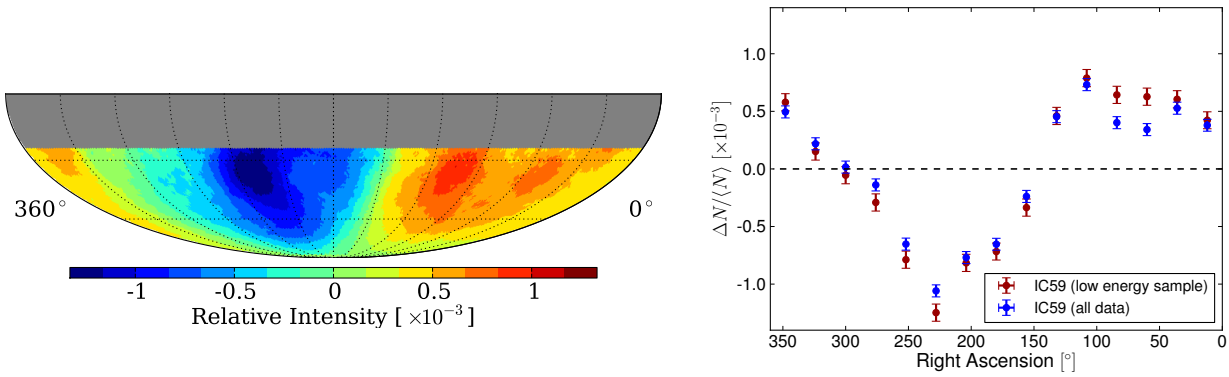

Figure 6.1: *Left*: Sky map of relative intensity for the low-energy IC59 sample with 10° smoothing. *Right:* Comparison between the relative intensity projections of the full IC59 data set (*all data*) and the subset of low-energy events (*low energy sample*) for the declination range $-40° < \delta < -25°$. The deficit identified as "region 6" in the multiple-angular scales analysis disappears after the energy cut.

change in relative intensity seen in the low-energy data set compared to the complete data set. The relative intensity projections for the 20 and 400 TeV samples are are shown in Fig. 6.2.

Since IceCube is only sensitive to the muonic component of the air showers, and low-energy muons are absorbed before they can reach the detector, the number of triggered DOMs in an IceCube cosmic ray event is only a poor estimator of the energy of the original primary particle. Above 1 TeV, the energy resolution is of order 0.5 in $\Delta \log(E)$, where E is the energy of the primary cosmic ray. The distribution of the difference between true and reconstructed shower energies has substantial tails, making it difficult to isolate a set of events with large median energy that is not contaminated by low-energy events.

6.1.2 Extending the Search to PeV Energies with IceTop

To extend the search for anisotropy to even higher energies, we use data from the IceTop which can record not only the muonic component of the air showers, but also the electromagnetic component, at ground level. With the sparse sampling of the shower front typical for air shower arrays, it also has a considerably higher detection threshold for cosmic rays than IceCube. The size and geometry of the array result in a threshold for reconstruction of air showers of approximately 300 TeV.

As an air-shower array, IceTop provides a more measured information per shower than IceCube. A study of cosmic-ray anisotropy with IceTop can therefore complement measurements with IceCube. With its high energy threshold, good energy resolution (about 0.1 in $\Delta \log(E)$), and sensitivity to the cosmic-ray composition, IceTop data are particularly useful for studying anisotropy at energies above 1 PeV. Due to the lower data rate, the full event information is stored, and a more careful offline reconstruction of the primary cosmic-ray properties is possible.

The accumulated IceTop data set is not yet large enough for a detailed study of per-mille anisotropy in several energy bins. However, the statistics collected between 2009 and 2012 are now sufficient to search for anisotropy in two energy bands centered at 400 TeV and 2 PeV. The 400 TeV data set can be compared to results based on downgoing muons in IceCube at a similar energy but for a different cosmic-ray composition model. With the 2 PeV data set, the search for anisotropy is extended to energies not previously explored. The remainder of this chapter deals with the observation of anisotropy with IceTop at both energies. These results were published in [152].

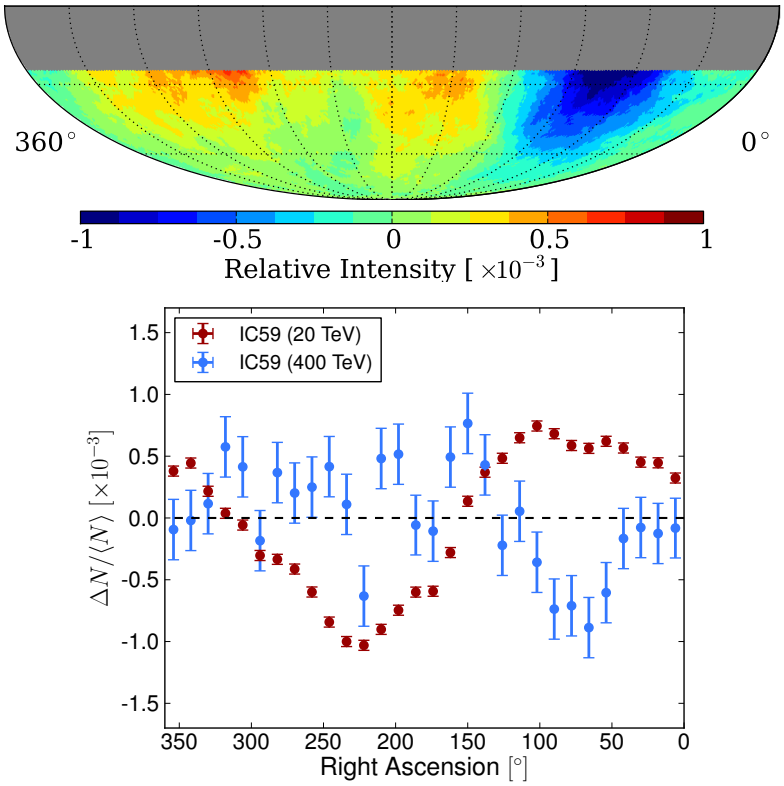

Figure 6.2: *Top*: Sky map of relative intensity for the high-energy IC59 sample with 25° smoothing. *Bottom:* Comparison between the relative intensity projections of the 20 TeV and 400 TeV IC59 data sets for the declination range $-75° < \delta < -25°$. The most significant feature is the wide deficit centered around $\alpha \sim 75°$.

6.2 Data Sets

The IceTop cosmic-ray air shower array was described in detail in Chapter 2. In this work, we use data taken during three periods: between May 2009 and May 2010 when the detector was operated in a 59-station configuration (IT59); between May 2010 and May 2011 when IceTop operated with 73 stations (IT73); and between May 2011 and May 2012 when the detector operated in its final 81-station configuration (IT81). The layout of these configurations is shown in Fig. 6.3.

Due to the limited bandwidth available for data transmission from the South Pole, events triggering less than eight stations were prescaled by a factor of eight during the operation of IT59, and by a factor of three during IT73 and IT81. Events triggering more than eight stations were not prescaled. This prescaling scheme was used to divide the data into two samples: a "low-energy" data set, containing events with at least three but less than eight stations triggered, and a "high-energy" data set that contains events where eight or more stations were triggered. From this point on, the low- and high- energy names refer to the IceTop data sets only and should not be confused with the low (20 TeV) and high (400 TeV) energy samples from the IceCube analysis.

During the operation of IT59, IT73, and the first year of IT81, a total of 3.55×10^8 events with more than 3 triggered stations were recorded. Of these events, 2.90×10^8 were classified as low-energy events while the high-energy sample contains the remaining 0.65×10^8 events. A zenith angle cut (described below) was used to remove misreconstructed events at large zenith angles. This cut reduced the final sample to 2.86×10^8 events in the low-energy set and 0.64×10^8 events in the high-energy sample.

As in the angular dependence study, the angular resolution of the reconstruction algorithm and the median energy of the data sets were determined by using simulated cosmic-ray air showers. CORSIKA events were generated and passed through a full simulation of the IceTop detector. The median energy of the samples determined using this simulation will depend on the assumptions made about the chemical composition of the primary cosmic

rays. The detailed primary composition has not been directly measured for energies beyond 100 TeV, but models that extrapolate existing measurements to higher energies indicate that in the energy range of this analysis, the cosmic ray flux consists mainly of protons, helium, and iron [19]. Their relative contribution is a function of energy, with helium and protons dominating around 100 TeV and iron becoming the dominant element above several tens of PeV. Given the uncertainties in the composition, we have generated only proton and iron showers as the two limiting cases for the chemical composition. The true median energy of the sample should be contained in the interval defined by these two cases.

The `ShowerPlane` angular reconstruction (Chapter 2) was used in the IceTop anisotropy analysis. From simulation we have determined the median angular resolution of this reconstruction to be 3° for both proton and iron showers for all detector configurations. The plane fit is well suited to our needs since it provides a resolution that is several times smaller than the typical angular scale of the anisotropic pattern ($> 20°$) without requiring a larger number of stations triggered which would reduce the size of the cosmic-ray sample. As shown in Fig. 6.4a, the resolution of the plane fit degrades rapidly for showers with zenith angles larger than 60°. For this reason, this analysis is limited to events with a reconstructed zenith angle smaller than 55°.

The median energies of the data sets were determined from the energy distribution of the simulated air showers which satisfy the same trigger conditions as events in the low- and high-energy data samples. The simulated energy distributions are shown in Fig.6.4b. The median energies and the 68% containing intervals for the two composition models for each energy band are shown in Table 6.1, which shows that the low-energy band has a median energy in the range 270 - 500 TeV, while the median energy for the high-energy sample should be contained in the range 1.6 - 2.2 PeV.

For both data samples, the median energy of the primary cosmic rays monotonically increases with zenith-angle, as illustrated in Fig. 6.5.

	Low energy		High energy	
Composition	$\tilde{E}$	68% interval	$\tilde{E}$	68% interval
Proton	0.27 PeV	0.11- 0.69 PeV	1.6 PeV	0.83 - 3.8 PeV
Iron	0.50 PeV	0.22 - 1.2 PeV	2.2 PeV	1.2 - 5.3 PeV

Table 6.1: Median energy and 68% containing interval in PeV for the two energy bands used in this work assuming that the cosmic rays consists of either protons or iron nuclei.

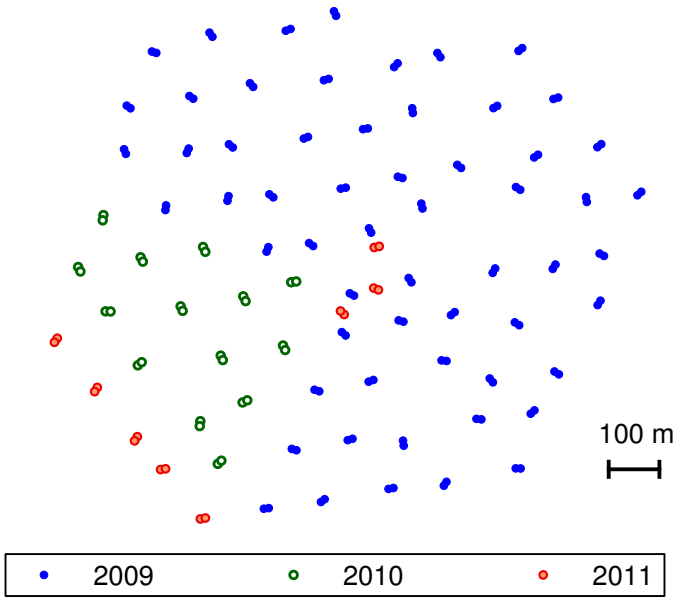

Figure 6.3: Detector configurations of the IceTop array, 2009-2011. IT59 comprised 59 stations deployed through January 2009 (blue circles). In 2009 and 2010 fourteen additional stations were deployed and the detector was operated in the IT73 configuration (blue and green circles). The remaining eight stations (red circles) were deployed in late 2010. The final IceTop configuration (IT81) consists of 81 stations and operated in 2011.

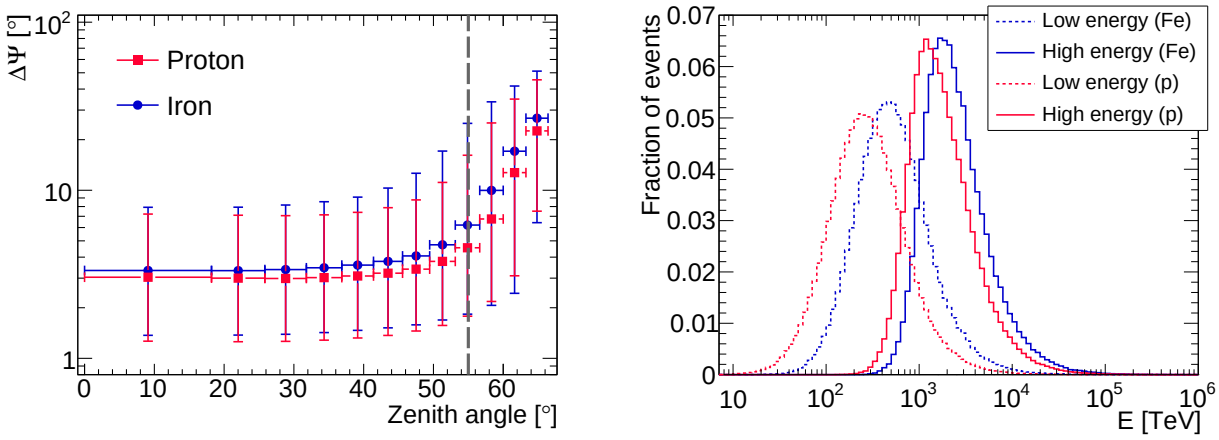

(a) IceTop angular resolution.

(b) IceTop cosmic ray energy distributions.

Figure 6.4: *Left:* Median opening angle $\Delta\Psi$ between reconstructed and true arrival direction as a function of reconstructed zenith angle θ. At large zenith angles the fraction of misreconstructed events increases. For this reason, a zenith cut was implemented that restricts the analysis to events with $\theta < 55°$ (dashed gray line). The error bars correspond to a 68% containing interval. IT59, IT73, and IT81 show the same dependence of angular resolution on reconstructed zenith angle. *Right:* Simulated energy distributions for all events in the low-energy (*dashed*) and high-energy (*solid*) data sets assuming all-iron (*blue*) and all-proton (*red*) compositions. The energy distributions are the same for the IT59, IT73 and IT81 configurations.

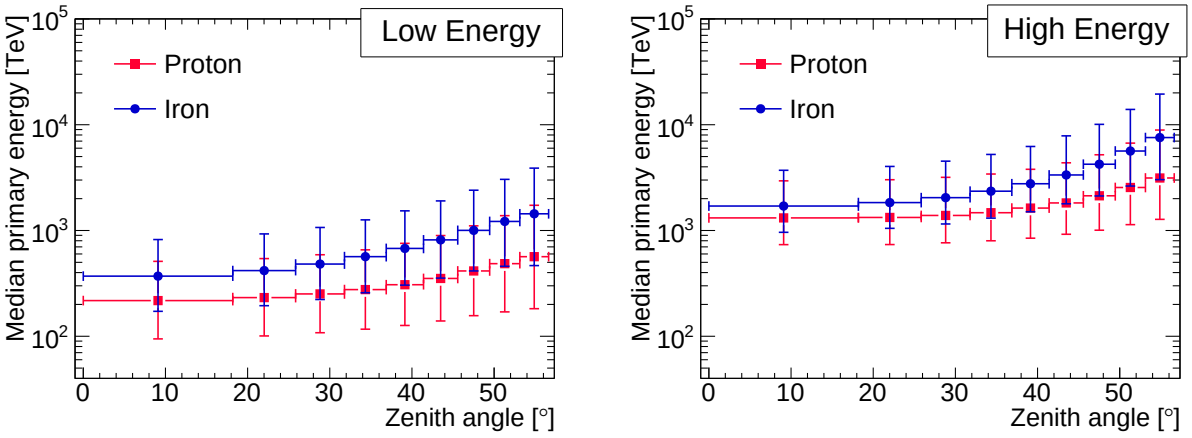

Figure 6.5: Median energy as a function of reconstructed zenith angle for the low-energy *(left)*, and high-energy *(right)* data sets for proton and iron cosmic-ray primaries. The error bars correspond to a 68% containing interval. IT59, IT73 and IT81 show the same energy dependence on the reconstructed zenith angle.

6.3 Analysis

A time-scrabling procedure with a 24 hours time window was used to estimate the isotropic reference map from the IceTop data. After the reference level estimation, a smoothing procedure was applied to the low- and high-energy maps for smoothing radii between 5° and 50° in 3° steps. A search for regions of high significance was performed on the resulting smoothed maps. The relative intensity and significance maps for the low- and high-energy data are shown in Fig. 6.6 for a representative smoothing radius of 20° where all the relevant features observed in these two energy ranges are visible.

The low-energy map is dominated by a strong deficit in relative intensity located at the same position as the 400 TeV deficit found in IceCube. The statistical significance of the deficit reaches a minimum of -8.5σ for a smoothing radius of 29° at a location around ($\alpha = 85.8°$, $\delta = -36.4°$). Since the search for this minimum is performed over about 10000 pixels in the map, and across all 16 different smoothing radii, there is a trials factor of at most 1.6×10^5 that reduces the post-trial significance of the deficit to 7.0σ. This correction for trials is conservative, since the pixels in the map are statistically correlated by the smoothing procedure, which results in a smaller effective number of trials than the maximum.

For the optimal smoothing radius of 29°, the relative intensity δI reaches a value of about -1.5×10^{-3} at the location of the greatest deficit ($\alpha = 83.7°$, $\delta = -35.7°$), near the edge of our exposure window. Differences in declination between the location of the maximum relative intensity and maximum significance are due to the fact that the statistical significance accounts for both signal strength and the declination-dependence of our statistics. This usually implies that the position of maximum significance is offset towards lower declination values where the statistics increase.

Also visible in the low-energy map is a region of excess flux located around ($\alpha = 182.9°$, $\delta = -55.9°$). The maximum pre-trial significance for this region is 5.3σ for a smoothing angle of 26°. The significance falls below $3\,\sigma$ after accounting for trials.

As the presence of the strong deficit introduces an underestimation of the isotropic reference level, it is possible that the excess observed in the low-energy data set is associated with the presence of the deficit region.

The high-energy map also shows statistically significant anisotropy which is dominated by a deficit located in the same approximate position as that observed in the low-energy data. The pre-trial significance of the deficit is $8.6\,\sigma$ ($7.1\,\sigma$ post-trials) for a smoothing angle of $35°$, with its minimum located at ($\alpha = 79.4°$, $\delta = -37.2°$). The main difference between the low- and high-energy deficits is that the value of δI for the greatest deficit in the high-energy sample is -2.3×10^{-3}, larger than its low-energy counterpart. This is evident in Fig. 6.7, where the relative intensity is projected onto the right ascension axis using the declination band $-75° < \delta < -35°$.

A second notable feature in the high-energy map is a wide excess region that reaches a peak significance of $5.9\,\sigma$ ($3.4\,\sigma$ post-trials) for a smoothing angle of $41°$. The excess does not appear to be concentrated in any particular part of the sky, but distributed across a wide band in right ascension. This is visible in the one-dimensional projection shown in Fig. 6.7, where the relative intensity reaches a plateau above $\alpha > 170°$ which is offset from zero by about 10^{-3}. As in the low-energy data set, such an excess could be associated with the presence of the observed deficit in the same declination band that introduces a bias in the reference-level estimation.

In order to characterize the observed anisotropic pattern, we attempted to fit the relative intensity projections of the data shown in Fig. 6.7 with the first terms (dipole and quadrupole) of a harmonic series. However, this choice of base functions does not fit the data well. For this reason, the fit is performed using the following Gaussian function:

$$\delta I(\alpha) = A e^{-(\frac{\alpha-\alpha_s}{\sqrt{2}\sigma})^2} + b \quad , \tag{6.1}$$

where α is right ascension, A is the amplitude, σ is the width, and α_s is the right ascension of the center of the deficit. The parameter b represents an overall offset in the reference level that can be introduced by the presence of a strong signal in the data.

	Low energy	**High energy**
A	$(-1.58 \pm 0.46 \pm 0.52) \times 10^{-3}$	$(-3.11 \pm 0.38 \pm 0.96) \times 10^{-3}$
α_s	$90.6^\circ \pm 6.8^\circ \pm 9.3^\circ$	$88.1^\circ \pm 6.8^\circ \pm 11.1^\circ$
σ	$21.3^\circ \pm 5.8^\circ \pm 7.6^\circ$	$43.1^\circ \pm 7.3^\circ \pm 13.1^\circ$
b	$(2.61 \pm 0.64 \pm 5.20) \times 10^{-4}$	$(9.37 \pm 1.96 \pm 9.60) \times 10^{-4}$
χ^2/dof	13.2/11	10.7/11

Table 6.2: Fit parameters obtained for both energy datasets for the Gaussian function given in Eq. 6.1. In all cases, the first quoted uncertainty is statistical while the second one corresponds to the systematics.

The results of these fits are shown in Table 6.2, and indicate that while the center point of the deficit for both data sets is consistently located at $\alpha_s \sim 90^\circ$, both the amplitude and the width are larger in the high-energy sample, with both values increasing by about a factor of two with respect to the low-energy case. The location of the deficit in the right ascension projection (Fig. 6.7) is consistent with its location in the skymap (Fig. 6.6), within statistical and systematic uncertainties, for both the low-energy and high-energy samples. Similarly, the amplitudes in relative intensity of the deficit agree well, when the overall offset b is taken into account.

The systematic uncertainty associated with each fit value was obtained from the systematic uncertainty of the relative intensity projection, shown as shaded boxes in Fig. 6.7. The systematic uncertainty of the projection was conservatively estimated as the maximum amplitude of the relative intensity distribution for each energy data set when analyzed in the anti-sidereal time frame (see Section 5.4).

The IceTop results at 400 TeV can be compared to the IC59 sky map with a similar energy. Note that while the IceTop median energy was obtained by assuming two limiting cases of primary chemical composition (all-proton or all-iron primaries only), the IceCube median energy was obtained assuming that the cosmic ray flux follows the polygonato composition

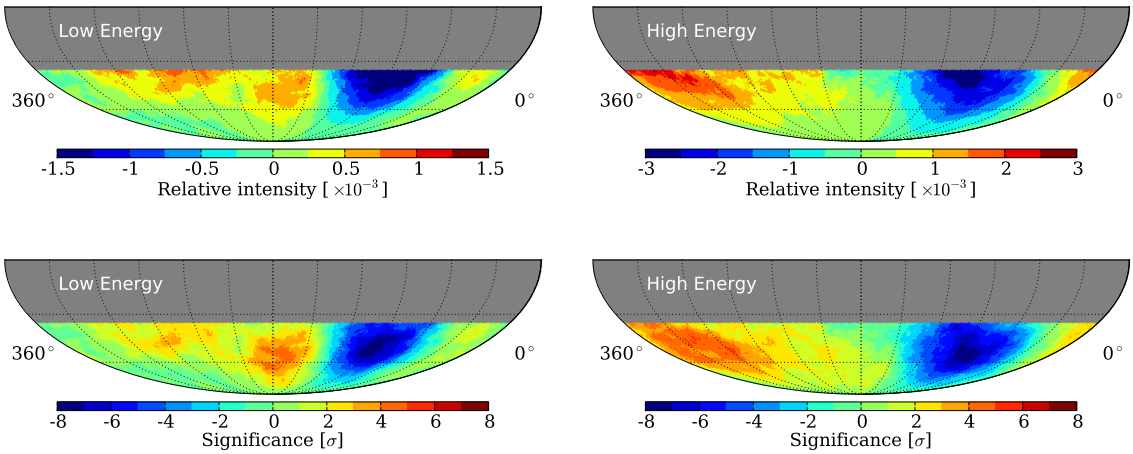

Figure 6.6: Relative intensity (*top*) and statistical significance (*bottom*) maps for the low-energy (*left*) and high-energy (*right*) data sets for a smoothing angle of 20°.

models [20], which in principle could lead to some differences in the actual median energy and the energy distribution of events in both samples.

The smoothing procedure described here was also used in the IceCube analysis, and the significance of the deficit was maximized for a smoothing radius of 29°, the same as the optimal smoothing angle for the low-energy IceTop data. Fig. 6.8 shows a comparison between the IceCube and IceTop relative intensity projections at 400 TeV. The location and amplitude of the deficits observed in both data sets agree given the current values of the statistical and systematic uncertainties associated with both measurements.

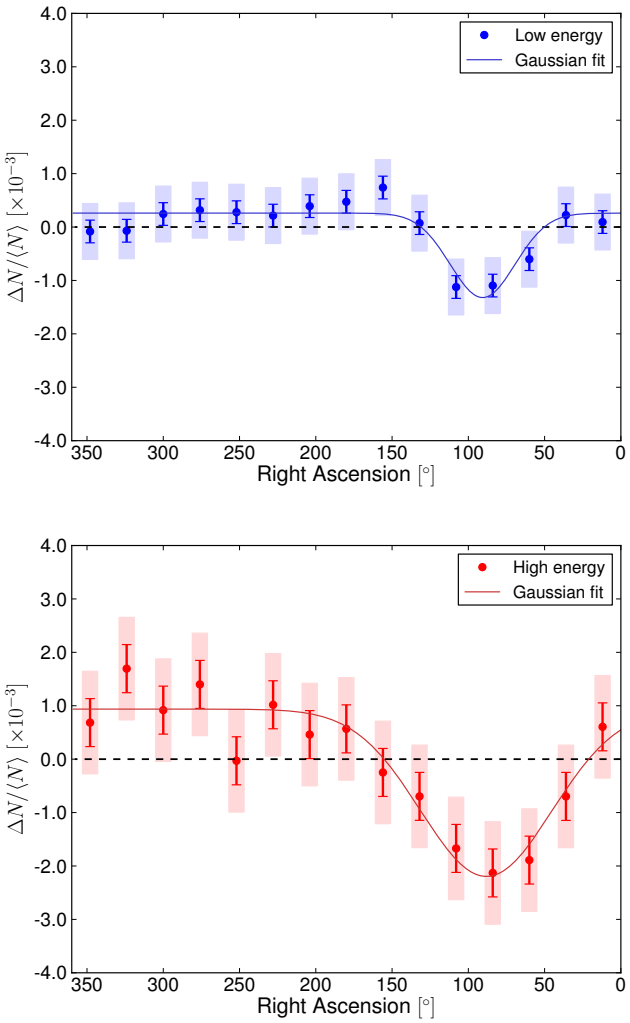

Figure 6.7: Relative intensity as a function of right ascension for the low-energy (*top*) and high-energy (*bottom*) data samples in the declination band $-75° < \delta < -35°$. The error bars are statistical while the colored boxes indicate the systematic uncertainty obtained from analyzing the same data in the anti-sidereal time frame (see Section 5.4 for details). The result of a fit using the Gaussian function given in Eq. 6.1 to both energy bands are also shown.

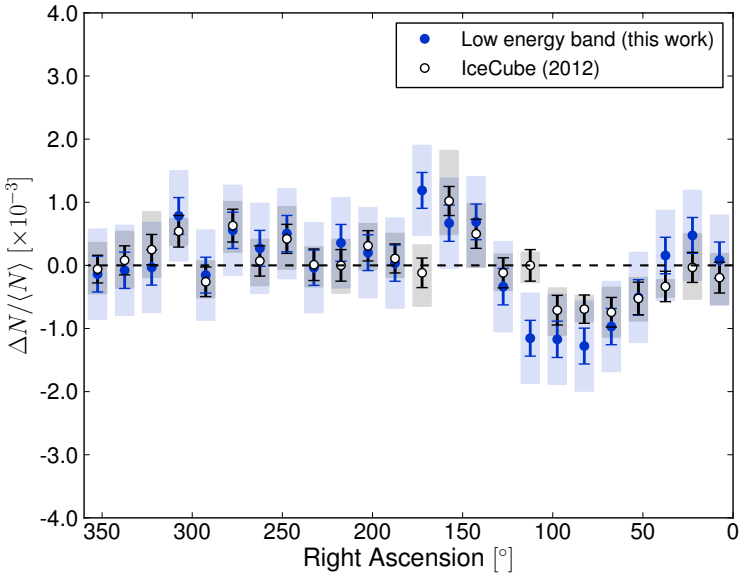

Figure 6.8: Comparison between the relative intensity projections for the IceTop low-energy sample (*blue filled circles*) and the IceCube 400 TeV sample (*black open circles*). The location and amplitude of both deficits are consistent given the statistical and systematic uncertainties. The declination range for the IceCube plot is $-75° < \delta < -25°$, slightly different from the IceTop one.

6.4 Systematic Uncertainties

A number of tests have been performed in order to quantify the systematic uncertainties associated with the observation of anisotropy in the IceTop data.

In the first study, the anisotropy search was performed on three independent data subsamples, each containing events recorded during the operation of the three different detector configurations IT59, IT73, and IT81 considered in this work. In this manner we can determine the possible systematic effect introduced by the changing geometry of the detector on the observed anisotropy.

The results of this comparison are shown in Fig. 6.9, where the relative intensity as a function of right ascension for the declination band $-75^\circ < \delta < -35^\circ$ is displayed for all three detector configurations and for the low- and high-energy samples separately. The anisotropy observed by all three configurations is consistent within statistical uncertainties.

Another test was performed to evaluate the impact of the seasonal variation of the cosmic-ray rate at the South Pole [139]. In this study, four different time periods were selected from the data: June through August, September through November, December through February, and March through May for each year of operation of the detector. These four data sets contain events taken with comparable detector geometries, but recorded during different phases of the seasonal variation cycle. The results of this study, shown in Fig. 6.10, indicate that the anisotropy observed in each of the four time periods is consistent within statistical uncertainties.

Other possible seasonal effects on the anisotropy are also investigated. First, an analysis was performed to look for anisotropy in the solar time frame. The dipolar anisotropy should have an amplitude of 4.7×10^{-4}. No anisotropy was observed using IceTop data. However, simulations of the solar dipole assuming the IceTop acceptance in local coordinates indicate that the current size of the data set is insufficient for a statistically significant observation.

We performed the anti-sidereal analysis on the combined three-year data set and obtained both skymaps and one-dimensional relative intensity projections for the low- and

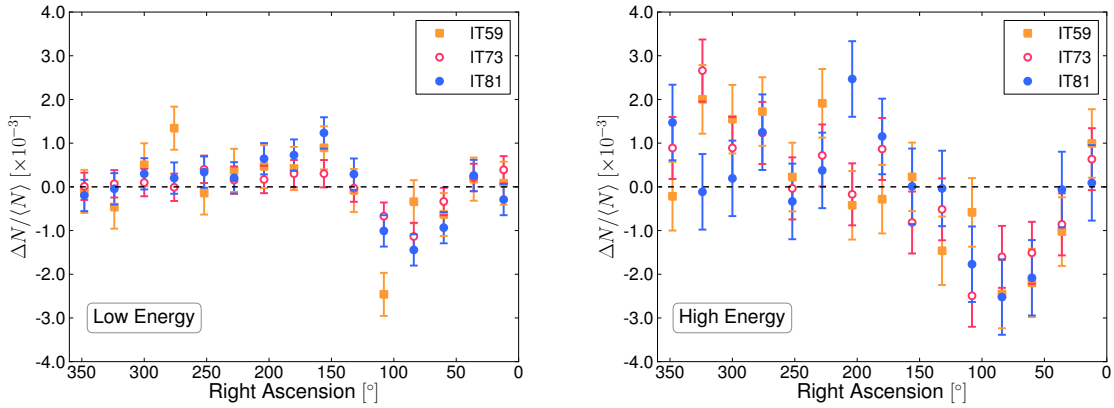

Figure 6.9: Relative intensity as a function of right ascension for the low-energy (*left*) and high-energy (*right*) data samples in the declination band $-75° < \delta < -35°$ for the three detector configurations of IceTop considered in this work (IT59, IT73, and IT81). For clarity, only statistical error bars are shown.

high-energy bands. The skymaps produced for the anti-sidereal frame do not exhibit any significant anisotropy that could indicate a possible systematic bias in the sidereal frame. The systematic uncertainty of the sidereal anisotropy due to seasonal variations, shown in Fig. 6.7, is obtained from the relative intensity projections in the anti-sidereal frame. This uncertainty is conservatively estimated as the maximum departure from the reference level of the anti-sidereal right ascension distribution.

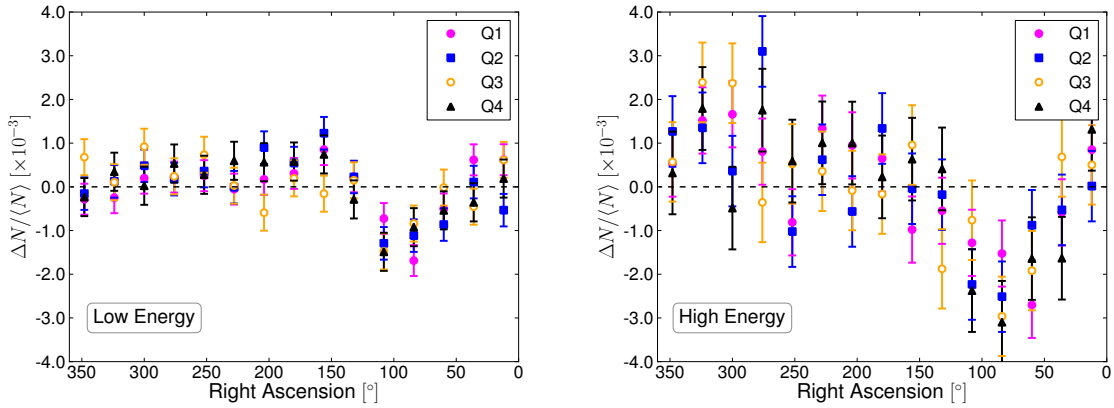

Figure 6.10: Relative intensity as a function of right ascension for the low-energy (*left*) and high-energy (*right*) data samples in the declination band $-75° < \delta < -35°$ for the three detector configurations of IceTop considered in this work (IT59, IT73, and IT81). For clarity, only statistical error bars are shown.

6.5 Conclusions

The study of cosmic ray arrival directions with IceCube and IceTop shows significant anisotropy at three different median energies, 20 TeV, 400 TeV, and 2 PeV. At 20 TeV the anisotropy is dominated by a large scale structure with subdominant small scale features that were extensively discussed in Chapter 5. At 400 TeV, the skymap is dominated by a single deficit region with an angular size of about 30°. This deficit region has been observed both by IceCube and IceTop with consistent results. IceTop data show that this anisotropy persists to 2 PeV.

The anisotropy in the southern sky at 400 TeV and 2 PeV is different in shape and amplitude from what is observed at 20 TeV. In the northern hemisphere, the EAS-TOP experiment has also found indications for an increasing amplitude and a change of phase between 100 TeV and 400 TeV in a harmonic analysis in right ascension that considers the first and second harmonic [69]. The IceTop anisotropy is not well-described by a sum of a dipole and a

quadrupole moment, so the results cannot be directly compared. However, both northern and southern hemisphere data seem to show qualitatively similar trends.

Although these results do not provide conclusive evidence for any particular model, they lend support to scenarios where the large-scale anisotropy is a superposition of the flux from a few nearby sources. The sparse spatial distribution and the different ages of nearby supernova remnants are expected to lead to a bumpy structure in the amplitude and sudden changes in the phase of the anisotropy as a function of energy [61]. Unfortunately, this energy dependence is dominated by details such as the geometry of the Galaxy, the location, age and injection spectrum of the sources, and the energy dependence of the cosmic-ray diffusion coefficient. While the predicted strength of the amplitude has the correct order of magnitude, further quantitative predictions are not possible at this point. In addition, in their simplest form, these models predict a dipolar anisotropy, whereas in most cases, the observed anisotropy cannot be described as a simple dipole, which also means that "amplitude" and "phase" are not well-defined. It has been recently proposed [153] that the IceTop observations at PeV could be interpreted as evidence for the onset of significant contribution of sources from the inner galaxy. Some local sources, such as the Monogem Ring SNR and Vela X could also be linked to the origin of this anisotropy.

If the anisotropy arises from cosmic ray scattering on the turbulence of the Galactic magnetic field close to Earth [143], these effects should be energy dependent since the relevant distance scales should change as particle energies increase from TeV to PeV. Nevertheless, our poor knowledge of interstellar magnetic fields prevents us from providing a more quantitative predictions that can be tested with data. A detailed measurement of the anisotropy might lead to a better understanding of these fields.

The observation of cosmic-ray anisotropy with IceTop opens up new possibilities for future studies that go beyond mapping the arrival direction distribution as a function of energy. Studies of the energy spectrum and composition of the cosmic ray flux in distinct regions of the southern sky can be performed.

IceTop is now in stable running mode in its complete configuration of 81 stations. In two years, the size of the cosmic ray data set available for anisotropy studies will be more than twice what was used in the analysis presented in this paper. Eventually, it will be possible to extend the analysis of cosmic-ray anisotropy to higher energies, specially above the cosmic-ray knee.

Chapter 7

Anisotropy as a Function of Time

7.1 Introduction

In this chapter we present a study of the time stability of the TeV anisotropy observed with IceCube and its predecessor experiment, AMANDA. Stability studies have been reported by the Tibet [56], and Milagro [58] collaborations with, so far, contradictory results. While Tibet observes no significant variation in the anisotropy from November 1999 to December 2008, Milagro reports a steady increase in the amplitude of the deficit region over a similar period of seven years (from July 2000 to July 2007). These stability studies can be extended to the southern hemisphere by analyzing the combined cosmic-ray data set collected by the AMANDA and IceCube neutrino telescopes over the course of 12 years (from 2000 through 2011). The stable operation environment and the good angular resolution of both detectors make this study possible.

The discovery of time modulation in the shape of the anisotropy pattern may provide clues about its origin. At TeV energies, the gyroradius of a proton in the μG-strength field of our galaxy is about 10^{-3} pc, which corresponds to scales of $\mathcal{O}(10^2)$ AU, similar to the size of the heliosphere. It has been argued [146] that given the similarity in these scales, it is possible that some of the observed structure in the anisotropy is due to scattering of cosmic rays in the outer heliosphere.

A possible evidence for such a heliospheric influence would be the observation of a variation in the anisotropy with the 11-year solar cycle during which the magnetic field of the Sun switches polarity. The combined AMANDA-IceCube data set covers the period from

approximately the maximum of solar cycle 23 to the first third of cycle 24, which started in January 2008 [1]. A graph of solar activity as a function of time (evidenced here by the solar radio flux at 10.8 cm) is shown in Fig. 7.1 together with a shaded region that indicates the time coverage of the combined data set. It has been predicted that the Sun will reach its maximum in activity for cycle 24 during mid-2013. Data being currently taken with IceCube will allow to expand the stability study to cover a full solar cycle. On much longer times scales (over thousands of years or more) a variation in the orientation and amplitude of the anisotropy is expected due to changes in the cosmic-ray flux due to nearby sources [155].

We present a study of the stability of the TeV anisotropy using AMANDA and IceCube data. The first observation of cosmic-ray anisotropy in AMANDA is documented in [156]. The analysis of AMANDA data presented in this chapter is based on the event selection developed for that work.

[1] `http://www.swpc.noaa.gov/SolarCycle/SC24/`

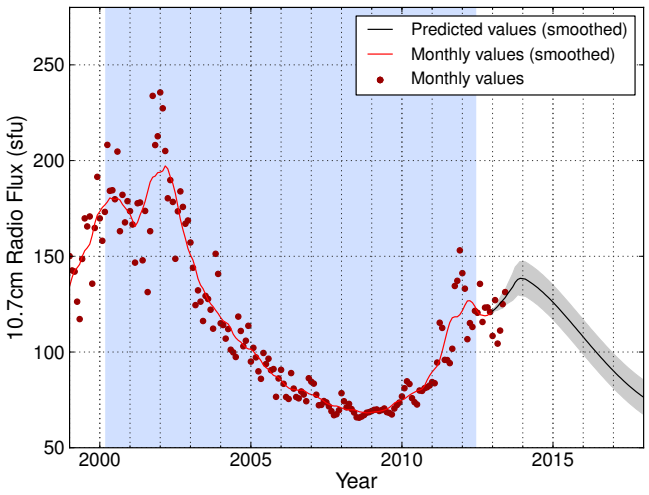

Figure 7.1: Time coverage of the combined AMANDA-IceCube data set (*blue band*) compared to measurements of the solar radio flux at a wavelength of 10.8 cm (*red points*) showing the change in solar activity over the last 14 years. A prediction for the solar maximum of cycle 24 is also shown as a gray band. Based on data taken from [154].

7.2 Data Sets

Data from the AMANDA-II detector and partial configurations of the IceCube detector starting with IC22 through the first year of IC86 were used in this stability study. Maintenance and deployment activities on both detectors during the austral summer naturally divide the data set into 12 periods of similar length that are studied individually and compared to a global average.

The date range, live-time, and sample size for each period is defined in Table 7.1. The number of events is calculated after applying a set of quality and stability cuts described in this section.

7.2.1 AMANDA

The AMANDA detector was described in detail in Chapter 2. For the anisotropy study, we use events from the `nano-dst` data stream which includes the result of the `DirectWalk` angular reconstruction applied to events passing the M24 trigger condition.

AMANDA was operated for a fraction of the year. Maintenance, calibration procedures, and the operation of other experiments at the South Pole caused rate instabilities and stops in the data acquisition process. Since these changes in rate may have an impact on the observed anisotropy, only data acquired under stable conditions are analyzed. Periods of unusually high or low rates are excluded. The data are divided in 5 minute long time slices and the event rate in each time slice is compared to the average event rate of the past 12 hours. Time slices in which the event rate deviates by more than 50% from the average rate are discarded.

For those events where the `DirectWalk` algorithm failed to find a solution for the most likely azimuth ϕ and zenith θ angles of the muon track, zero values would be returned for both coordinates. For this reason, a quality cut was implemented that removed events with $\theta < 0.2^\circ$ and $\phi < 0.1^\circ$. The events excluded by this cut represent 10% of the sample. The average event rate after cuts is approximately 60 Hz, seasonally modulated by about 15%.

Typical distributions of reconstructed angles and the event rate are shown in Fig. 7.2 for data recorded on MJD 51600 (February 26$^{\text{th}}$, 2000).

7.2.2 IceCube

Similarly to AMANDA, only periods where the detector data rate was stable are taken into account. The operation of IceCube was remarkably more stable than the operation of AMANDA. For this reason, stability cuts that remove periods with fluctuating rates have a smaller impact in IceCube than in AMANDA. IceCube events from the multi-angular scale analysis sample presented in Chapter 5 are used in this analysis. The number of events collected with each detector configuration of IceCube is given in Table 7.1. The correlation between detector and sample size is evident. The final size of the total sample is 163.4 billion events, which is strongly dominated by the IceCube contribution of 150 billion events.

Typical distributions of reconstructed angles and the event rate for the IC86 configuration are shown in Fig. 7.2 for data recorded on MJD 55744 (July 2$^{\text{nd}}$, 2011).

Period	**Detector**	**Start**	**End**	**Live-time (days)**	**No. of Events ($\times 10^9$)**	χ^2**/dof**	**p-value**
1	AM-II	02/13/2000	11/02/2000	213.4	1.4	11.3/15	0.73
2	AM-II	02/11/2001	10/19/2001	235.3	2.3	16.6/15	0.34
3	AM-II	01/01/2002	08/02/2002	169.2	2.4	26.0/15	0.04
4	AM-II	02/09/2003	12/17/2003	236.0	2.2	19.3/15	0.20
5	AM-II	01/05/2004	11/02/2004	225.8	2.5	14.3/15	0.50
6	AM-II	12/30/2004	12/23/2005	242.9	2.6	21.0/15	0.14
7	AM-II	01/01/2006	09/13/2006	213.1	2.4	24.4/15	0.06
8	IC22	06/01/2007	03/30/2008	269.4	5.3	45.2/15	7×10^{-5}
9	IC40	04/18/2008	04/30/2009	335.6	18.9	12.8/15	0.62
10	IC59	05/20/2009	05/30/2010	335.0	33.8	11.1/15	0.75
11	IC79	05/31/2010	05/12/2011	299.7	39.1	6.5/15	0.97
12	IC86	05/13/2011	05/14/2012	332.9	52.9	8.9/15	0.88

Table 7.1: Definition of each time period used in this analysis. AMANDA data sets are indicated as "AM-II," while IceCube data sets are marked as "IC" followed by the number of active detector strings during that time period. The number of live-days and recorded events is shown. Each time period is compared to the global twelve-year average using a χ^2-test. The χ^2 and the associated p-value for each period is also listed.

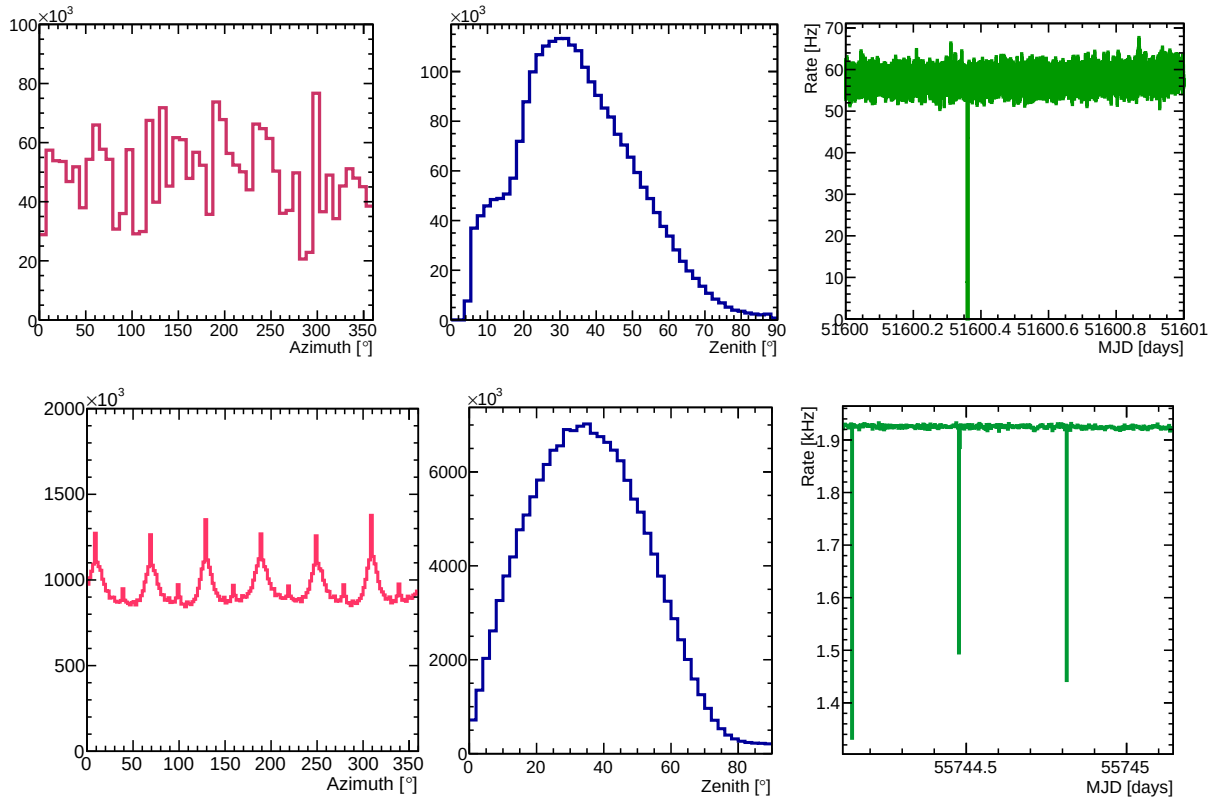

Figure 7.2: Distributions of reconstructed event directions in zenith and azimuth and event rate for a single day of AMANDA (*top*) and IceCube (*bottom*). The short gaps in the rate plots are due to a run stopping and a new one starting immediately afterwards.

7.3 Analysis

In this analysis, we compare the relative intensity profile from each individual period defined according to Table 7.1 to the global twelve-year profile. The relative intensity projections are obtained in the same manner as for other analyses presented in this work. First, a reference level map is obtained from data by time-scrambling the events using a time window of 24 hours, which makes the analysis sensitive to all angular scales.

Second, one-dimensional projections of the anisotropy maps are obtained by binning the right ascension coordinate α in 15 statistically-independent intervals. The relative intensity $\delta I(\alpha)$ in the j^{th} right-ascension bin is calculated from the number of events in the data and reference maps contained in the declination range $-85^\circ < \delta < -35^\circ$.

The agreement between each yearly profile δI_y and the global average $\langle \delta I \rangle$ is estimated by a χ^2-test using the following expression:

$$\chi^2_y = \sum_{j=1}^{j=15} \frac{(\delta I_y(\alpha_j) - \langle \delta I(\alpha_j) \rangle)^2}{\sigma^2_{\delta I} + \sigma^2_{\langle \delta I \rangle}} \ , \tag{7.1}$$

where the statistical uncertainties in the relative intensity of each bin are calculated according to Eq. 4.13. The combined uncertainty in the difference is obtained by adding the individual uncertainties in δI_y and $\langle \delta I \rangle$ in quadrature. The combined uncertainty in each bin is dominated by the uncertainty in each yearly period due to the relatively lower level of statistics. Only statistical uncertainties have been considered so far. A future analysis will account for systematic effects that may be caused by the incomplete time coverage of each period which could lead to distortions in the right ascension profile (for instance, due to interference of the solar dipole anisotropy with the anisotropy in equatorial coordinates as described in Chapter 5).

Finally, a p-value was calculated for each reduced χ^2 value. A list of p-values is given in Table 7.1. With the exception of Period 8, all p-values show a good agreement between individual periods and the global average, given the statistical uncertainties of each set. The large p-values for periods 11 and 12 are expected since the large relative size of both data

sets makes them dominate the global average profile. Period 8 corresponds to the start of regular operation of IceCube, where the detector operated with 22 active strings (about one quarter of its final size). Due to gaps in the data taking process and fluctuations in the trigger rate, it is possible that the discrepancy is related to detector effects. A preliminary study of the impact of these effects is presented in Section 7.4.1.

In parallel to the relative intensity profiles, sky maps of the anisotropy were produced. The maps shown in Fig. 7.3 exhibit significant large-scale structure of per-mille amplitude in the southern sky as already presented in Chapter 5. At first glance, the anisotropy shape appears to be stable across the twelve periods considered in this work.

A search for small scale anisotropy was performed using the same approach presented in Chapter 5, namely by fitting and subtracting the dipole and quadrupole modes of the spherical harmonic functions to the map. Unfortunately, the sizes of the data samples in the periods covered by AMANDA are too small to perform this study for each period individually. For this reason, we combined all data from AMANDA into a single map.

The results of the dipole and quadrupole fit are given in Table 7.2, where the notation for the fit coefficients follows the definition given in Eq. 4.11. The fit residuals were smoothed using a 20° circular window to increase the sensitivity to structures in that angular range. The relative intensity and significance maps after smoothing are shown in Fig. 7.5. Most of the excess and deficit regions reported in Chapter 5 are visible even in the combined AMANDA data set with a significance larger that $\sim 4\sigma$. The shape of the small-scale structure appears stable over the periods under study.

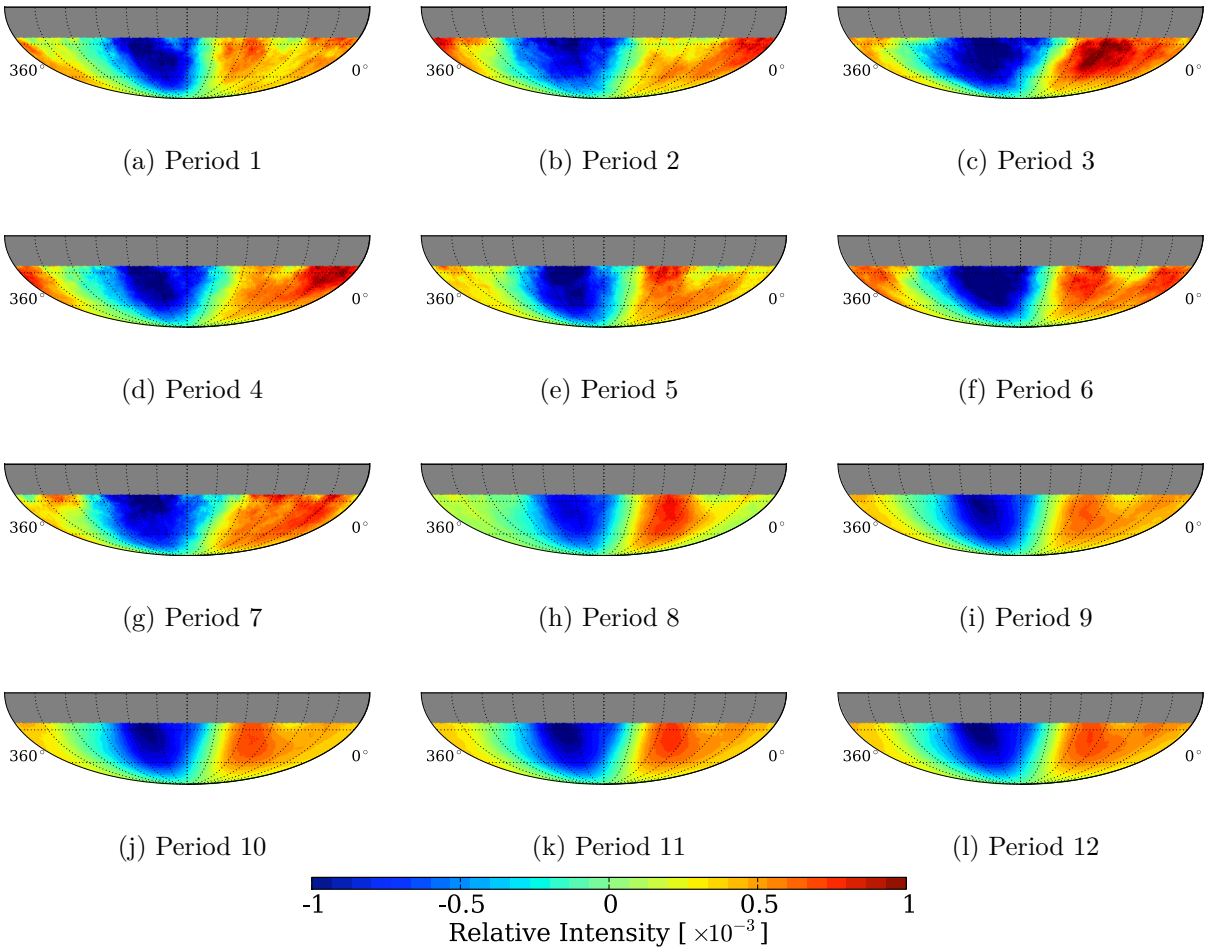

Figure 7.3: Two-dimensional relative intensity maps in equatorial coordinates of the cosmic-ray anisotropy for the 12 time periods covering the years from 2000 to 2012 (see Table 7.1). All maps have been smoothed using a circular window with a 20° angular radius.

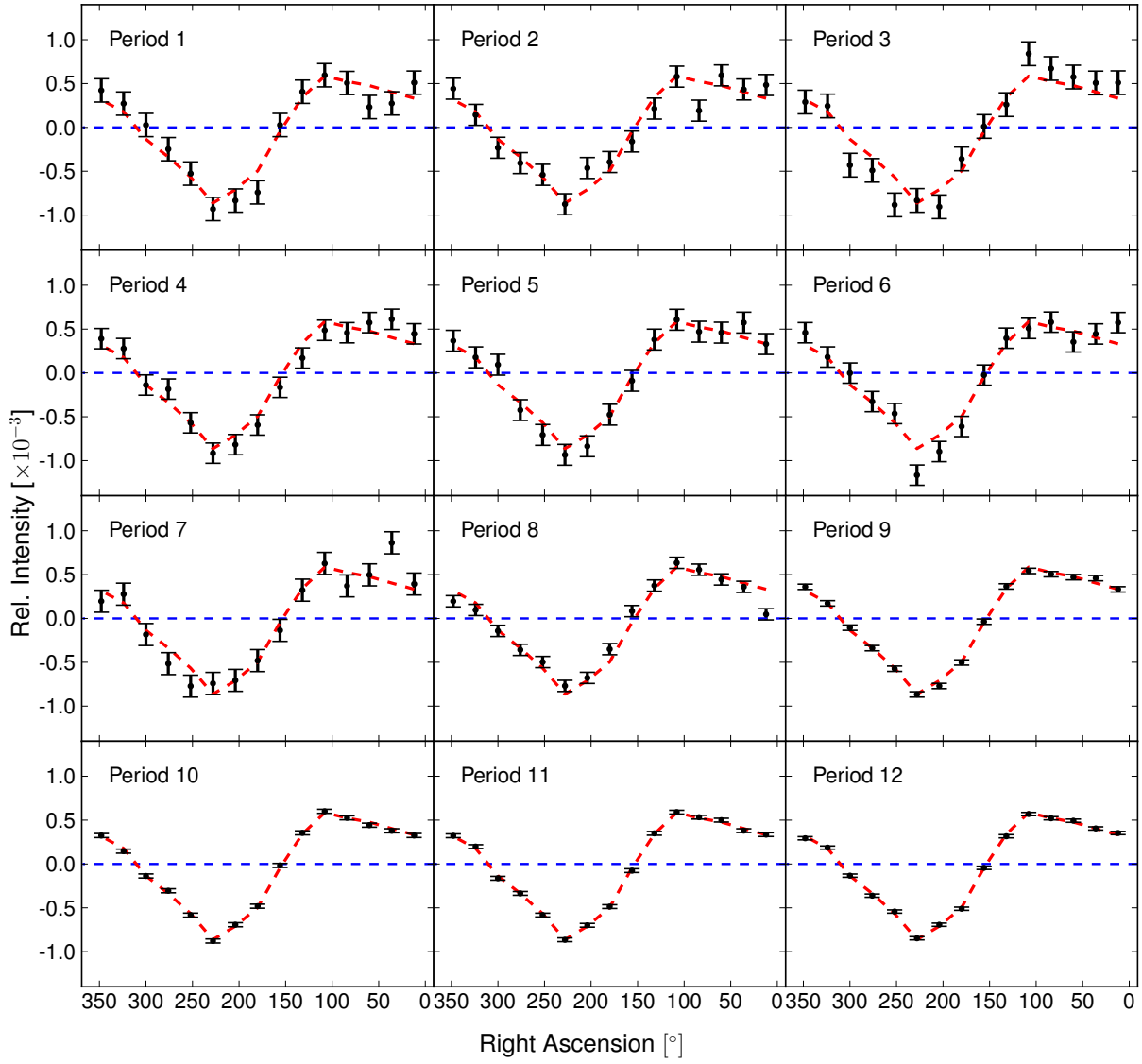

Figure 7.4: One-dimensional projections of relative intensity as a function of right ascension for the 12 time periods considered in this work. As a reference, the average profile for the entire data set is shown as a dashed blue line. The uncertainties shown are only statistical.

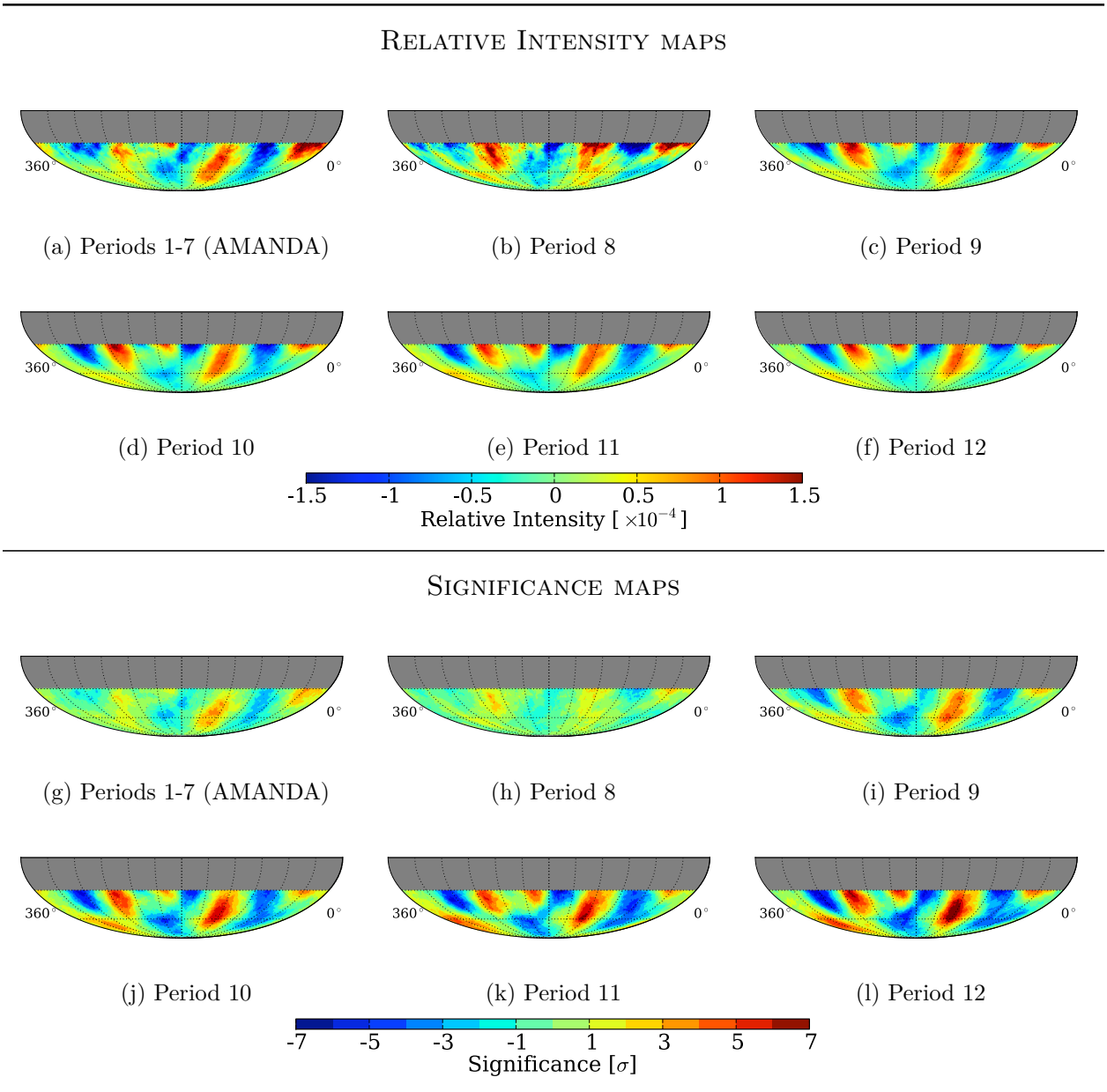

Figure 7.5: Relative intensity (*top*) and significance maps (*bottom*) of the dipole and quadupole fit residuals for a smoothing angle of 20°. The small scale reported in Chapter 5 is visible in all maps. The structure is already significant at the $\sim 4\sigma$ level in the AMANDA data and its significance increases for the larger data sets collected with IceCube.

Period	m_0	p_x	p_y	p_z	Q_1	Q_2	Q_3	Q_4	Q_5
1-7	-0.9 ± 6.6	3.2 ± 1.8	-5.5 ± 1.8	-1.5 ± 11.0	-0.5 ± 4.7	-3.6 ± 1.2	-9.9 ± 1.2	-1.4 ± 0.5	-4.0 ± 0.5
8	-0.2 ± 8.9	1.5 ± 2.3	-7.8 ± 2.3	-0.2 ± 14	-0.1 ± 6.4	-2.2 ± 1.6	-11 ± 1.6	-2.6 ± 0.6	-4.8 ± 0.6
9	0.6 ± 6.1	-0.5 ± 1.1	-5.6 ± 1.1	1.0 ± 10	0.4 ± 4.4	-5.1 ± 0.8	-9.8 ± 0.8	-1.7 ± 0.3	-5.3 ± 0.3
10	0.4 ± 0.6	1.3 ± 0.8	-3.7 ± 0.8	0.7 ± 1.1	0.3 ± 0.5	-3.7 ± 0.5	-8.7 ± 0.5	-2.3 ± 0.2	-5.5 ± 0.2
11	-0.4 ± 1.9	1.5 ± 0.8	-2.8 ± 0.8	-0.7 ± 3.3	-0.3 ± 1.4	-3.7 ± 0.5	-8.3 ± 0.5	-2.7 ± 0.2	-5.2 ± 0.2
12	-0.3 ± 0.5	3.0 ± 0.6	-1.4 ± 0.6	-0.5 ± 0.8	-0.2 ± 0.4	-2.8 ± 0.4	-7.2 ± 0.4	-2.2 ± 0.2	-4.8 ± 0.2

Table 7.2: Dipole and quadrupole fits for each period.

7.4 Systematic Studies

By definition, the χ^2-test used to test the stability of the anisotropy only takes into account statistical fluctuations of the relative intensity. Correlated fluctuations across different bins of the relative intensity would be ignored by this test. In order to search for such systematic changes in amplitude or phase of the anisotropy for different years we perform a second-order harmonic fit to the relative intensity profiles. The results of these fits are shown in Table 7.4. The evolution of the parameters as a function of time is shown in Fig. 7.6.

A possible change in the fit parameters with time was investigated by fitting the points in Fig. 7.6 with two linear functions: one representing a constant value (*red dashed line*), and a second one including a slope (*gray dashed line*). The improvement in the χ^2 of the fit after the inclusion of the slope parameter was evaluated (Table 7.3.) The resulting p-values for the fits indicate that no significant improvement results from adding the slope parameter. Therefore, we conclude that no significant change is observed in the four harmonic parameters with time.

Parameter	χ^2/dof (constant)	χ^2/dof (slope)	$\Delta\chi^2$	**p-value**
A_1	31.3 / 11	29.7 / 10	1.7	0.20
A_2	19.4 / 10	14.9 / 9	4.5	0.03
ϕ_1	45.8 / 11	45.5 / 10	0.3	0.56
ϕ_2	6.5 / 10	5.9 / 9	0.6	0.43

Table 7.3: χ^2 values for the fit of a zeroth (constant) or first (slope) order polynomial to the fit parameters as a function of time shown in Fig 7.6. The p-values associated with the χ^2 difference indicate that the inclusion of a slope does not improve the fit significantly, which implies that the fit parameters do not exhibit a systematic variation in the time period considered.

It must be noted that two data points (the second-order harmonic phase ϕ_2 and amplitude A_2) for Period 2 (year 2001) were excluded from the fit. As can be seen in Table 7.4, both the amplitude and the phase of the second-order harmonic have an opposite sign with respect to the rest of the periods. This is due to the degeneracy introduced by the periodic nature of the harmonic functions, where small changes in the data points to be fit may induce a large shift in the phase of one of the functions. To test this scenario, the χ^2 space of the fit as a function of the second-order harmonic parameters, shown in Fig. 7.7, was explored while keeping the first-order parameters constant. Even though the global χ^2 minimum found by the minimizer is located at the position reported in the table, a minimum of almost the same depth is found at $A_2 \sim -1.2 \times 10^{-4}$ and $\phi_2 \sim 54^\circ$ which is in better agreement with the rest of the periods.

7.4.1 Period 8

Period 8 corresponds to the operation of the first stable configuration of IceCube: IC22. The first detection of the large-scale anisotropy with IceCube was based on data collected with IC22 [89]. Due to the small size of the detector, its operation in parallel with AMANDA, and other common problems related to the start of normal operation of a detector, the operation of IC22 was less stable than that of later partial configurations of IceCube. These fluctuations could be the cause of the significant deviation of the observed anisotropy with respect to the global average.

A study was performed to search for possible reconstruction effects due to changes in the detector configuration during the time-scrambling period of 24 hours. For this purpose, distributions of reconstructed azimuth and zenith angles for the events were created for each half of each day of data taking. For each day, the zenith and azimuth histograms from each half were compared using a χ^2-test and events from days where the test p-value was less than 1.5% were removed from the sample. This cut removed 13% of the events from the sample, and resulted in the χ^2 value of 45/15 shown in Table 7.1 for the comparison to the global profile.

A comparison plot to the global profile is shown in Fig. 7.8 for the declination range $-85° < \delta < -35°$ after cuts. The largest deviation between the two profiles is observed in the bin that covers the right ascension range $0° < \alpha < 24°$. Excluding the bin in the calculation of the χ^2 improves the p-value from $\sim 10^{-4}$ to 0.05. The underfluctuation of this bin was also present in the IC22 analysis [89] that used a different reference level estimation (azimuthal weighting instead of time scrambling) as well as a different set of stability cuts. Two relative intensity profiles were generated for independent declination ranges, $-75° < \delta < -50°$ and $-50° < \delta < -25°$, and compared to the corresponding declination bands for the combined data set to better locate the region presenting the underfluctuation. This determined that the deviation is only present in the declination band $-75° < \delta < -50°$.

Even though it is possible that detector effects could cause this underfluctuation, it is difficult to produce a feature that is stable in sidereal coordinates for such a specific range in right ascension and declinations. Another possibility that was explored was the impact of changes in the rate. A more strict selection cut was applied where periods with a trigger rate that deviated by more than 7 Hz from the median daily trigger rate were removed. The resulting rate is shown in Fig. 7.9. This cut, however, did not improve the χ^2 of the comparison to the global profile significantly.

If the discrepancy between IC22 and the global data is present only for certain periods of time, this could point towards a detector-related origin of the deviation. An astrophysical origin of the variation is also possible, although less likely due to the much longer time scales usually expected for the variation of the anisotropy.

To test the time variation of the IC22 anisotropy, the χ^2 for the comparison to the global profile was performed individually for each month of IC22 data taking. The monthly χ^2 values are shown in Fig. 7.10 for 15 degrees of freedom. There appears to be a significant increase in the χ^2 for all months after October 2007, around the time when the seasonal increase in the muon trigger rate starts. Months before and after this time were identified as "good" and "bad" months, respectively. The χ^2/dof for the combined set of "good" months is 14.6/15, while the value for the "bad" months was 109/15. The cause of this change

in χ^2 is currently under investigation. Additional evidence that supports the hypothesis of a detector-related origin of the difference is the observation of anisotropy in the solar time-frame, shown in Fig. 7.11, that is inconsistent with the expected dipolar distribution of events in that coordinate frame.

Period	$A_1(\times 10^{-4})$	ϕ_1	$A_2(\times 10^{-4})$	ϕ_2	χ^2/dof	p-value
1	6.3 ± 0.5	$45.3° \pm 4.4°$	-3.1 ± 0.5	$37.1° \pm 4.4°$	9.2/10	0.51
2	6.1 ± 0.4	$50.0° \pm 4.1°$	1.2 ± 0.4	$-35.7° \pm 10.6°$	15/10	0.13
3	7.9 ± 0.5	$58.8° \pm 3.6°$	-1.8 ± 0.5	$41.8° \pm 7.9°$	10/10	0.44
4	6.9 ± 0.4	$43.0° \pm 3.5°$	-1.6 ± 0.4	$31.6° \pm 7.4°$	5.6/10	0.85
5	6.9 ± 0.4	$50.2° \pm 3.6°$	-2.4 ± 0.4	$38.5° \pm 5.1°$	4.6/10	0.92
6	7.1 ± 0.4	$46.2° \pm 3.4°$	-2.7 ± 0.4	$38.4° \pm 4.5°$	15/10	0.13
7	7.1 ± 0.5	$52.6° \pm 3.7°$	-1.2 ± 0.5	$44.7° \pm 11°$	15/10	0.12
8	5.6 ± 0.2	$63.4° \pm 2.4°$	-2.2 ± 0.2	$30.8° \pm 3.0°$	12/10	0.30
9	6.4 ± 0.1	$51.8° \pm 1.0°$	-2.1 ± 0.1	$36.0° \pm 1.5°$	33/10	2×10^{-4}
10	6.2 ± 0.1	$54.4° \pm 0.78°$	-2.2 ± 0.1	$35.5° \pm 1.1°$	64/10	5×10^{-10}
11	6.3 ± 0.1	$53.4° \pm 0.71°$	-2.0 ± 0.1	$34.6° \pm 1.1°$	74/10	7×10^{-12}
12	6.3 ± 0.1	$52.6° \pm 0.61°$	-1.9 ± 0.1	$34.1° \pm 1.0°$	89/10	9×10^{-15}

Table 7.4: Results of the second order harmonic fit to the relative intensity profiles from each year.

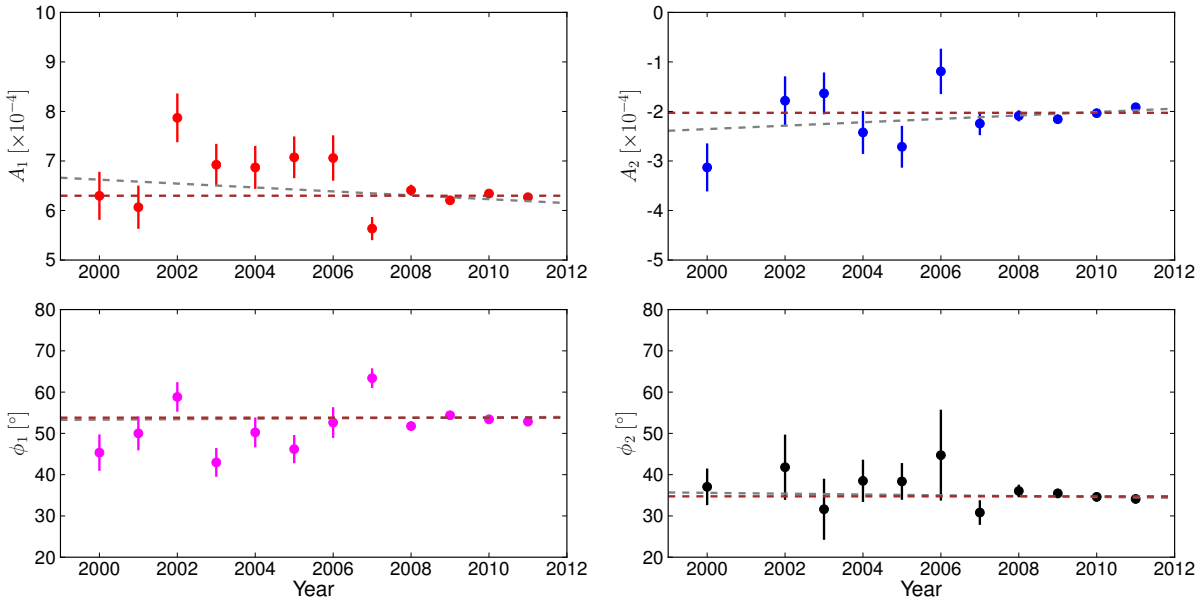

Figure 7.6: Stability of the harmonic fit parameters as a function of time. Two linear functions are fit to each set of points: a constant level (*red dashed line*) and a line with a slope parameter (*gray dashed line*). The small improvement in the χ^2 of the fit indicates that there is no significant time-dependence in the parameters.

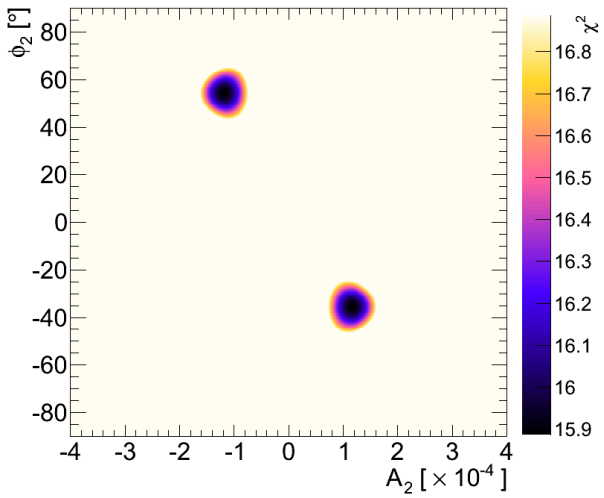

Figure 7.7: χ^2 space for the second-order harmonic parameters A_2 and ϕ_2. The minimum located at positive A_2 and negative ϕ_2 is mirrored in negative A_2 and positive ϕ_2 due to the degeneracy of the harmonic functions. The $\sim 90°$ phase shift is due to the periodicity of the second harmonic moment. The values of the first-order harmonic function (A_1 and χ_1) have been kept constant during the scan.

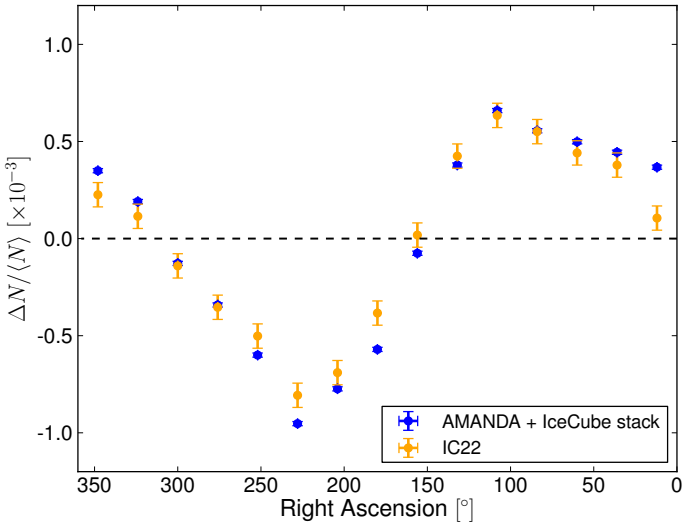

Figure 7.8: Comparison of relative intensity projections for IC22 (*orange*) and the global profile (*blue*). The most significant difference between the two distributions is in the right ascension bin covering the range $0° < \alpha < 24°$.

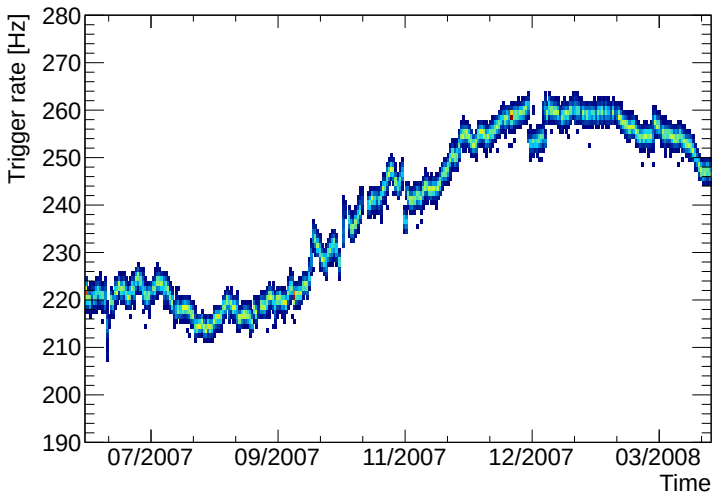

Figure 7.9: IC22 trigger rate after quality cuts as a function of time.

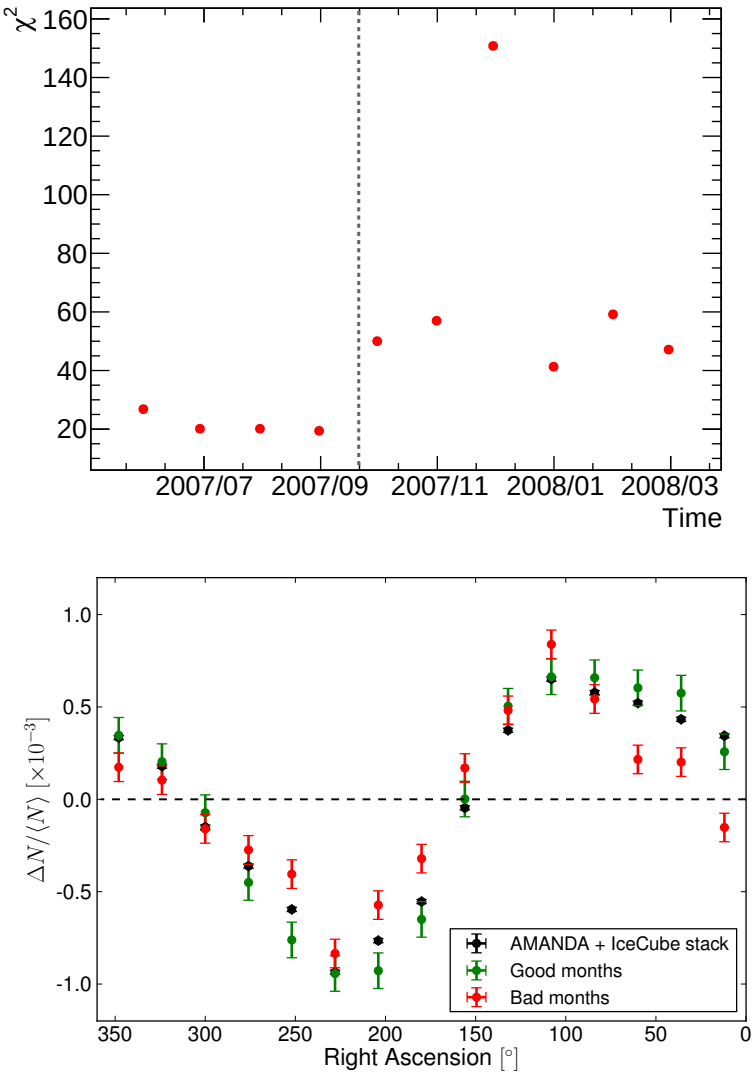

Figure 7.10: *Top:* χ^2 values for a monthly comparison of IC22 data to the global profile. An increase in the χ^2 is visible after October 2007. The vertical dashed line divides the data into "good" and "bad" months respectively before and after the line. *Bottom:* Comparison between the global relative intensity profile (*black*) and those for the "good" (*red*) and "bad" (*red*) months of IC22. The χ^2 for the "good" months show a good agreement with the global profile.

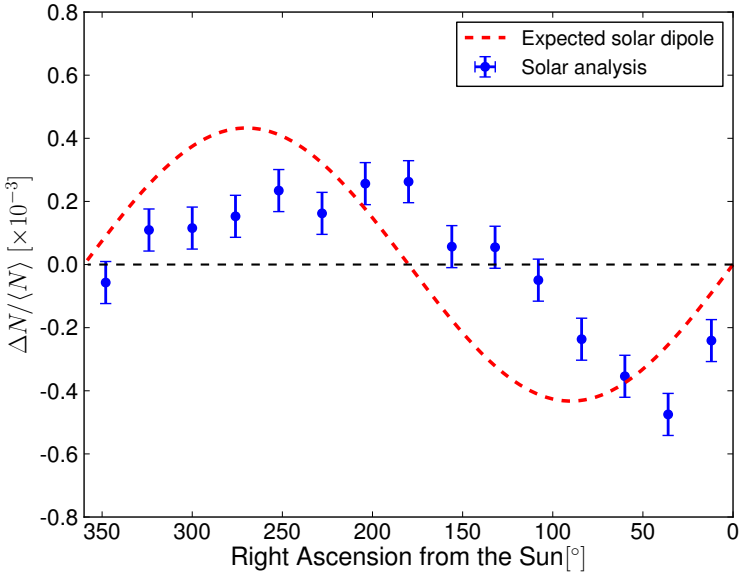

Figure 7.11: Analysis of the IC22 in the solar frame. The expected solar dipole shape is shown compared to the IC22 data. The observed disagreement may indicate the presence of atmospheric or detector related effects that could be distorting the expected dipole distribution.

7.5 Conclusions

A study of the stability of the TeV cosmic ray anisotropy over a period of twelve years was presented using data recorded with the AMANDA and IceCube detectors. The anisotropy is studied both at large angular and small scales. Small scales are studied in a similar way to what was presented in Chapter 5 by fitting and subtracting the dipole and quadrupole components of the spherical harmonic functions and then studying the fit residuals. No significant time variation in the observed anisotropy is found with the exception of period 8, which corresponds to the 22-string configuration of IceCube.

Since IC22 was the first year of regular operation of IceCube, instabilities in the detector configuration were common, which may have led to distortions in the observed anisotropy. Several stability studies are presented for IC22, with the purpose of ruling out detector-related effects that may be causing the observed deviation in the relative intensity profile. Further stability studies are currently under way to estimate the impact of these detector effects.

Chapter 8

Conclusions

The anisotropy in the arrival directions of TeV and PeV cosmic rays has been studied using a combined data set of about 170 billion cosmic-ray events collected with the IceCube, IceTop, and AMANDA detectors. The analyses presented in this work evaluate the dependence of the observed anisotropy on angular scale, cosmic-ray energy, and time.

The large-scale anisotropy detected by experiments in the northern hemisphere at TeV energies was observed for the first time in the southern sky using data from the 22-string configuration of the IceCube detector. In this work, a study of the anisotropy as a function of angular scale was presented using data from the 59-string configuration of IceCube. The analysis revealed that, besides the large-scale pattern, significant structure is present in the southern sky with typical angular sizes between 10° and 20°. An update on this study using all IceCube data available to date shows anisotropy at angular scales of $\sim 5°$, near the angular resolution of the detector for this type of events.

While the origin of the small-scale structure remains unknown, several models have been proposed to explain the observed flux enhancements. It is possible that the observed small-scale features are due to TeV cosmic rays scattering off the turbulence of the local interstellar magnetic field [143]. In that case, the angular power spectrum of the anisotropy could contain important information about the spectrum of the local magnetic field turbulence. Other works try to explain the small-scale anisotropy in terms of the interaction of TeV cosmic rays with the heliosphere, either through a magnetic scattering process [146, 147, 148], or through the existence of long-range electric fields [149].

More exotic scenarios have also been postulated where the small-scale excess regions are produced by a flux of strangelet particles produced in nearby neutron stars [157], or by the byproducts of the annihilation of dark matter particles in a nearby subhalo [158]. To test these models, a study of the primary composition of the cosmic-ray flux from the excess regions would be required.

The anisotropy was then studied in three energy bands, with median energies of 20 TeV, 400 TeV, and 2 PeV. Cosmic-ray data at 20 TeV is dominated by the already mentioned large-scale structure. IceTop data at 400 TeV and 2 PeV reveal anisotropic structure that is significantly different from that observed at lower energies. The large scale pattern observed at 20 TeV disappears at 400 TeV, and only a localized deficit region with a width of about 40° is observed. The IceTop deficit is consistent with an anisotropy measurement performed at a similar energy with IceCube data. At 2 PeV, the deficit is still present, although with an amplitude and width larger by about a factor of two. Besides the change in the characteristic size of the anisotropy from 20 TeV to 400 TeV and above, there is also a change in the phase of the anisotropy. While at 20 TeV the deficit region of the large-scale anisotropy has a minimum near $\alpha \sim 240°$, at 400 TeV this occurs near $\alpha \sim 70°$.

This sudden change in the orientation of the anisotropy has been interpreted in the literature [63] as being due to two different source populations that contribute to different energy ranges of the cosmic-ray flux. It is believed that at 20 TeV the flux is dominated by the contribution of nearby sources in the Orion arm of the Milky Way galaxy, while at higher energies sources located farther away in the Galaxy contribute to the flux, which forces the direction of the excess to point towards the Galactic Center. Recent results from the KASCADE-Grande [159] and Auger [160] detectors indicate that, while there is still no significant large-scale anisotropy detection, the best-fit phase of a dipole pattern to the data remains essentially constant between 3 PeV and 1 EeV at $\alpha \sim 240°$, in agreement with the IceCube/IceTop data above 400 TeV. The collection of larger data sets with the Auger and KASCADE-Grande experiments, and its combination with IceTop data at higher

energies, may help determine if the cosmic-ray anisotropy is indeed produced by an ensemble of Galactic sources.

The time stability of the anisotropy (for both large and small scales) was explored by combining data from AMANDA and IceCube. The combined data set covers a time span of 12 years (2000 through 2012). A modulation of the anisotropy in this time range could hint at a possible heliospheric influence on the propagation of TeV cosmic rays. No significant time variation of the anisotropy was observed, except for the case of data collected with the 22-string configuration of IceCube. That configuration marked the start of regular data acquisition with IceCube, and for this reason detector instabilities were common. The impact of these possible detector effects on the observed anisotropy are currently under study.

The combination of these studies with future work on the dependence of the anisotropy on cosmic-ray composition may provide information about the origin of the cosmic-ray anisotropy in particular and cosmic rays in general. Current and future direct-detection experiments such as AMS-2 [12], ISS-CREAM [161], or CALET [162] will collect large data sets that will allow detailed composition measurements of different parts of the sky for cosmic-ray energies up to tens of TeV. From the ground, square-kilometer arrays such as IceTop will continue to collect data to expand the search for cosmic-ray anisotropy above the cosmic-ray knee while also studying its composition dependence. The combination of these data sets with those collected by other experiments at higher energies such as KASCADE-Grande, Telescope Array, or the Pierre Auger Observatory will determine if a large-scale anisotropy is in fact present at energies above the cosmic-ray knee.

LIST OF REFERENCES

[1] V. F. Hess. Über Beobachtungen der durchdringenden Strahlung bei sieben Freiballonfahrten. *Phys. Z.*, 13:1084–1091, 1912.

[2] P. Auger, P. Ehrenfest, R. Maze, J. Daudin, and R. A. Fréon. Extensive Cosmic-Ray Showers. *Rev. Mod. Phys.*, 11:288–291, July 1939. doi:10.1103/RevModPhys.11.288.

[3] Y. Sekido and H. Elliot, editors. *Early History of Cosmic Ray Studies*, volume 118 of *Astrophysics and Space Science Library*, July 1985.

[4] D. J. Bird et al. Detection of a Cosmic Ray with Measured Energy well beyond the Expected Spectral Cutoff due to Cosmic Microwave Radiation. *Astrophys. J.*, 441:144–150, March 1995. arXiv:astro-ph/9410067, doi:10.1086/175344.

[5] Y. S. Yoon et al. Cosmic-ray Proton and Helium Spectra from the First CREAM Flight. *Astrophys. J.*, 728:122, February 2011. arXiv:1102.2575, doi:10.1088/0004-637X/728/2/122.

[6] R. Abbasi et al. All-Particle Cosmic Ray Energy Spectrum measured with 26 IceTop Stations. *Astropart. Phys.*, 44(0):40 – 58, 2013. doi:http://dx.doi.org/10.1016/j.astropartphys.2013.01.016.

[7] J. Abraham et al. Measurement of the Energy Spectrum of Cosmic Rays above 10^{18} eV using the Pierre Auger Observatory. *Phys. Lett. B*, 685:239–246, March 2010. arXiv:1002.1975, doi:10.1016/j.physletb.2010.02.013.

[8] J. Abraham et al. Observation of the Suppression of the Flux of Cosmic Rays above 4×10^{19} eV. *Phys. Rev. Lett.*, 101(6):061101, August 2008. arXiv:0806.4302, doi:10.1103/PhysRevLett.101.061101.

[9] K. Greisen. End to the Cosmic-Ray Spectrum? *Phys. Rev. Lett.*, 16:748–750, April 1966. doi:10.1103/PhysRevLett.16.748.

[10] G. T. Zatsepin and V. A. Kuz'min. Upper Limit of the Spectrum of Cosmic Rays. *Soviet J. Exp. Theor. Phys.*, 4:78, August 1966.

[11] H. S. Ahn et al. Discrepant Hardening Observed in Cosmic-ray Elemental Spectra. *Astrophys. J. Lett.*, 714:L89–L93, May 2010. arXiv:1004.1123, doi:10.1088/2041-8205/714/1/L89.

[12] M. Aguilar et al. First Result from the Alpha Magnetic Spectrometer on the International Space Station: Precision Measurement of the Positron Fraction in Primary Cosmic Rays of 0.5-350 GeV. *Phys. Rev. Lett.*, 110:141102, Apr 2013. doi:10.1103/PhysRevLett.110.141102.

[13] J. Abraham et al. Properties and Performance of the Prototype Instrument for the Pierre Auger Observatory. *Nucl. Instrum. Methods A*, 523:50–95, May 2004. doi:10.1016/j.nima.2003.12.012.

[14] J. J. Beatty and S. Westerhoff. The Highest-Energy Cosmic Rays. *Annu. Rev. Astron. Astrophys.*, 59:319–345, November 2009. doi:10.1146/annurev.nucl.58.110707.171154.

[15] J. A. M. Bleeker. *The Century of Space Science*. Springer, 2001.

[16] X. H. Sun, W. Reich, A. Waelkens, and T. A. Enßlin. Radio Observational Constraints on Galactic 3D-Emission Models. *Astron. Astrophys.*, 477:573–592, January 2008. arXiv:0711.1572, doi:10.1051/0004-6361:20078671.

[17] R. Abbasi et al. Cosmic Ray Composition and Energy Spectrum from 1-30 PeV using the 40-string Configuration of IceTop and IceCube. *Astropart. Phys.*, 42:15–32, February 2013. arXiv:1207.3455, doi:10.1016/j.astropartphys.2012.11.003.

[18] W. D. Apel et al. Kneelike Structure in the Spectrum of the Heavy Component of Cosmic Rays Observed with KASCADE-Grande. *Phys. Rev. Lett.*, 107(17):171104, October 2011. arXiv:1107.5885, doi:10.1103/PhysRevLett.107.171104.

[19] T. K. Gaisser. Spectrum of Cosmic-Ray Nucleons, Kaon Production, and the Atmospheric Muon Charge Ratio. *Astropart. Phys.*, 35:801–806, July 2012. arXiv:1111.6675, doi:10.1016/j.astropartphys.2012.02.010.

[20] J. R. Hörandel. On the Knee in the Energy Spectrum of Cosmic Rays. *Astropart. Phys.*, 19:193–220, 2003. arXiv:astro-ph/0210453, doi:10.1016/S0927-6505(02)00198-6.

[21] J. Abraham et al. Measurement of the Depth of Maximum of Extensive Air Showers above 10^{18} eV. *Phys. Rev. Lett.*, 104(9):091101, March 2010. arXiv:1002.0699, doi:10.1103/PhysRevLett.104.091101.

[22] D. Ikeda et al. Recent Results of the Energy Spectrum and Mass Composition from Telescope Array Fluorescence Detector. *J. Phys. Conf. Ser.*, 409(1):012097, 2013.

[23] K.-H. Kampert and M. Unger. Measurements of the Cosmic Ray Composition with Air Shower Experiments. *Astropart. Phys.*, 35:660–678, May 2012. arXiv:1201.0018, doi:10.1016/j.astropartphys.2012.02.004.

[24] E. Fermi. On the Origin of the Cosmic Radiation. *Phys. Rev.*, 75:1169–1174, Apr 1949. doi:10.1103/PhysRev.75.1169.

[25] C. Grupen. *Astroparticle Physics*. Springer, 2005. doi:10.1007/3-540-27670-X.

[26] A. M. Hillas. The Origin of Ultra-High-Energy Cosmic Rays. *Annu. Rev. Astron. Astrophys.*, 22:425–444, 1984. doi:10.1146/annurev.aa.22.090184.002233.

[27] F. Schüssler. *Top-Down Reconstruction of Ultrahigh Energy Air Showers measured with the Pierre Auger Fluorescence Detector*. PhD Thesis, Universität Karlsruhe (TH), 2005.

[28] J. Abraham et al. Upper Limit on the Cosmic-Ray Photon Fraction at EeV Energies from the Pierre Auger Observatory. *Astropart. Phys.*, 31:399–406, July 2009. arXiv:0903.1127, doi:10.1016/j.astropartphys.2009.04.003.

[29] K. Kotera and A. V. Olinto. The Astrophysics of Ultrahigh-Energy Cosmic Rays. *Annu. Rev. Astron. Astrophys.*, 49:119–153, September 2011. arXiv:1101.4256, doi:10.1146/annurev-astro-081710-102620.

[30] L. A. Anchordoqui and T. Montaruli. In Search of Extraterrestrial High-Energy Neutrinos. *Annu. Rev. Nucl. Part. Sci.*, 60:129–162, November 2010. arXiv:0912.1035, doi:10.1146/annurev.nucl.012809.104551.

[31] D. Paneque. Experimental Gamma-Ray Astronomy. *J. Phys. Conf. Ser.*, 375(5):052020, July 2012. doi:10.1088/1742-6596/375/1/052020.

[32] W. B. Atwood et al. The Large Area Telescope on the Fermi Gamma-Ray Space Telescope Mission. *Astrophys. J.*, 697:1071–1102, June 2009. arXiv:0902.1089, doi:10.1088/0004-637X/697/2/1071.

[33] M. Ackermann et al. Detection of the Characteristic Pion-Decay Signature in Supernova Remnants. *Science*, 339:807–811, February 2013. arXiv:1302.3307, doi:10.1126/science.1231160.

[34] W. Baade and F. Zwicky. Cosmic Rays from Super-novae. *Proceedings of the National Academy of Science*, 20:259–263, May 1934. doi:10.1073/pnas.20.5.259.

[35] V. L. Ginzburg and S. I. Syrovatskii. *The Origin of Cosmic Rays*. Gordon and Breach, 1964.

[36] A. A. Abdo et al. TeV Gamma-Ray Sources from a Survey of the Galactic Plane with Milagro. *Astrophys. J. Lett.*, 664:L91–L94, August 2007. arXiv:0705.0707, doi:10.1086/520717.

[37] S. Funk. The Status of Gamma-Ray Astronomy. In *Proc. of the 32nd ICRC*, Beijing, China, July 2011. arXiv:1204.4529.

[38] R. Abbasi et al. An Absence of Neutrinos Associated with Cosmic-Ray Acceleration in γ-Ray Bursts. *Nature*, 484:351–354, April 2012. arXiv:1204.4219, doi:10.1038/nature11068.

[39] A. W. Strong, I. V. Moskalenko, and V. S. Ptuskin. Cosmic-Ray Propagation and Interactions in the Galaxy. *Annu. Rev. Nucl. Part. Sci.*, 57:285–327, November 2007. arXiv:astro-ph/0701517, doi:10.1146/annurev.nucl.57.090506.123011.

[40] V. S. Berezinskiĭ, S. V. Bulanov, V. A. Dogiel, V. S. Ptuskin, and V.L. Ginzburg. *Astrophysics of Cosmic Rays*. North-Holland, 1990.

[41] T. K. Gaisser. *Cosmic Rays and Particle Physics*. Cambridge University Press, 1990.

[42] T. Stanev. *High Energy Cosmic Rays*. Springer-Praxis books in astrophysics and astronomy. Springer, 2004.

[43] A. Obermeier, P. Boyle, J. Hörandel, and D. Müller. The Boron-to-Carbon Abundance Ratio and Galactic Propagation of Cosmic Radiation. *Astrophys. J.*, 752:69, June 2012. arXiv:1204.6188, doi:10.1088/0004-637X/752/1/69.

[44] A. W. Strong, I. V. Moskalenko, T. A. Porter, G. Jóhannesson, E. Orlando, and S. W. Digel. The GALPROP Cosmic-Ray Propagation Code. In *Proc. of the 31st ICRC*, Łódź, Poland, July 2009. ID 0902. arXiv:0907.0559.

[45] C. Evoli, D. Gaggero, D. Grasso, and L. Maccione. Cosmic Ray Nuclei, Antiprotons and Gamma Rays in the Galaxy: a New Diffusion Model. *J. Cosmol. Astropart. Phys.*, 10:18, October 2008. arXiv:0807.4730, doi:10.1088/1475-7516/2008/10/018.

[46] G. R. Farrar, R. Jansson, I. J. Feain, and B. M. Gaensler. Galactic magnetic deflections and Centaurus A as a UHECR source. *J. Cosmol. Astropart. Phys.*, 1:23, January 2013. arXiv:1211.7086, doi:10.1088/1475-7516/2013/01/023.

[47] R. Jansson and G. R. Farrar. A New Model of the Galactic Magnetic Field. *Astrophys. J.*, 757:14, September 2012. arXiv:1204.3662, doi:10.1088/0004-637X/757/1/14.

[48] P. Abreu et al. A Search for Point Sources of EeV Neutrons. *Astrophys. J.*, 760:148, December 2012. arXiv:1211.4901, doi:10.1088/0004-637X/760/2/148.

[49] A. H. Compton and I. A. Getting. An Apparent Effect of Galactic Rotation on the Intensity of Cosmic Rays. *Phys. Rev.*, 47:817–821, Jun 1935. doi:10.1103/PhysRev.47.817.

[50] S. R. Majewski. Precision Astrometry, Galactic Mergers, Halo Substructure and Local Dark Matter. In W. J. Jin, I. Platais, and M. A. C. Perryman, editors, *IAU Symposium*, volume 248 of *IAU Symposium*, pages 450–457, July 2008. arXiv:0801.4927, doi:10.1017/S1743921308019790.

[51] L. Gleeson and W. Axford. The Compton-Getting effect. *Astrophys, Space Sci.*, 2:431–437, 1968. doi:10.1007/BF02175919.

[52] P. L. Biermann et al. The Origin of Cosmic Rays: Explosions of Massive Stars with Magnetic Winds and their Supernova Mechanism. *Astrophys. J.*, 725:184–187, 2010. arXiv:1009.5592, doi:10.1088/0004-637X/725/1/184.

[53] K. Nagashima, K. Fujimoto, and R. M. Jacklyn. Galactic and Heliotail-in Anisotropies of Cosmic Rays as the Origin of Sidereal Daily Variation in the Energy Region $< 10^4$ GeV. *J. Geophys. Res.*, 103:17429–17440, August 1998. doi:10.1029/98JA01105.

[54] K. Munakata et al. Large-Scale Anisotropy of the Cosmic-Ray Muon Flux in Kamiokande. *Phys. Rev. D*, 56:23–26, 1997. doi:10.1103/PhysRevD.56.23.

[55] M. Amenomori et al. Anisotropy and Corotation of Galactic Cosmic Rays. *Science*, 314:439–443, 2006. arXiv:astro-ph/0610671, doi:10.1126/SCIENCE.1131702.

[56] M. Amenomori et al. On Temporal Variations of the Multi-TeV Cosmic Ray Anisotropy using the Tibet III Air Shower Array. *Astrophys. J.*, 711:119–124, 2010. arXiv:1001.2646, doi:10.1088/0004-637X/711/1/119.

[57] G. Guillian et al. Observation of the Anisotropy of 10 TeV Primary Cosmic Ray Nuclei Flux with the Super-Kamiokande-I Detector. *Phys. Rev. D*, 75(6):062003, Mar 2007. doi:10.1103/PhysRevD.75.062003.

[58] A. A. Abdo et al. The Large Scale Cosmic-Ray Anisotropy as Observed with Milagro. *Astrophys. J.*, 698:2121–2130, 2009. arXiv:0806.2293, doi:10.1088/0004-637X/698/2/2121.

[59] S. Cui et al. Study on Large-Scale CR Anisotropy with ARGO-YBJ Experiment. In *Proc. of the 32nd ICRC*, Beijing, China, July 2011. ID 0041. doi:10.7529/ICRC2011/V01/0041.

[60] A. D. Erlykin and A. W. Wolfendale. The Anisotropy of Galactic Cosmic Rays as a Product of Stochastic Supernova Explosions. *Astropart. Phys.*, 25:183–194, 2006. arXiv:astro-ph/0601290, doi:10.1016/j.astropartphys.2006.01.003.

[61] P. Blasi and E. Amato. Diffusive Propagation of Cosmic Rays from Supernova Remnants in the Galaxy. II: Anisotropy. *J. Cosmol. Astropart. Phys.*, 1:11, January 2012. arXiv:1105.4529, doi:10.1088/1475-7516/2012/01/011.

[62] V. S. Ptuskin, F. C. Jones, E. S. Seo, and R. Sina. Effect of Random Nature of Cosmic Ray Sources - Supernova Remnants - on Cosmic Ray Intensity Fluctuations, Anisotropy, and Electron Energy Spectrum. *Adv. Space Res.*, 37:1909–1912, 2006. doi:10.1016/j.asr.2005.08.036.

[63] L. G. Sveshnikova, O. N. Strelnikova, and V. S. Ptuskin. Spectrum and Anisotropy of Cosmic Rays at TeV-PeV-energies and Contribution of Nearby Sources. *ArXiv e-prints*, January 2013. arXiv:1301.2028.

[64] A. A. Abdo et al. Discovery of Localized Regions of Excess 10-TeV Cosmic Rays. *Phys. Rev. Lett.*, 101:221101, 2008. arXiv:0801.3827, doi:10.1103/PhysRevLett.101.221101.

[65] L. Drury and F. Aharonian. The Puzzling Milagro Hot Spots. *Astropart. Phys.*, 29:420–423, 2008. arXiv:0802.4403, doi:10.1016/j.astropartphys.2008.04.007.

[66] M. Salvati and B. Sacco. The Milagro Anticenter Hot Spots: Cosmic Rays from the Geminga Supernova? *Astron. Astrophys.*, 485:527–529, July 2008. arXiv:0802.2181, doi:10.1051/0004-6361:200809586.

[67] M. A. Malkov et al. Probing Nearby CR Accelerators and ISM Turbulence with Milagro Hot Spots. *Astrophys. J.*, 721:750–761, 2010. arXiv:1005.1312, doi:10.1088/0004-637X/721/1/750.

[68] S. Vernetto et al. Sky Monitoring with ARGO-YBJ. In *Proc. of the 31st ICRC*, Łódź, Poland, July 2009. ID 0399. arXiv:0907.4615.

[69] M. Aglietta et al. Evolution of the Cosmic Ray Anisotropy above 10^{14} eV. *Astrophys. J. Lett.*, 692:L130–L133, 2009. arXiv:0901.2740, doi:10.1088/0004-637X/692/2/L130.

[70] T. Antoni et al. Large-Scale Cosmic-Ray Anisotropy KASCADE. *Astrophys. J.*, 604:687–692, April 2004. arXiv:astro-ph/0312375, doi:10.1086/382039.

[71] S. Over et al. Search for Anisotropy and Point Sources of Cosmic Rays with the KASCADE-Grande Experiment. In *Proc. of the 30th ICRC*, volume 4, pages 223–226, Mérida, Mexico, 2008.

[72] P. Abreu et al. Search for First Harmonic Modulation in the Right Ascension Distribution of Cosmic Rays detected at the Pierre Auger Observatory. *Astropart. Phys.*, 34:627–639, March 2011. arXiv:1103.2721, doi:10.1016/j.astropartphys.2010.12.007.

[73] P. Abreu et al. Large-scale Distribution of Arrival Directions of Cosmic Rays Detected Above 10^{18} eV at the Pierre Auger Observatory. *Astrophys. J. Suppl. Ser.*, 203:34, December 2012. arXiv:1210.3736, doi:10.1088/0067-0049/203/2/34.

[74] P. Abreu et al. Constraints on the Origin of Cosmic Rays above 10^{18} eV from Large-scale Anisotropy Searches in Data of the Pierre Auger Observatory. *Astrophys. J. Lett.*, 762:L13, January 2013. doi:10.1088/2041-8205/762/1/L13.

[75] N. Hayashida et al. The Anisotropy of Cosmic-Ray Arrival Directions around 10^{18} eV. *Astropart. Phys.*, 10:303–311, May 1999. arXiv:astro-ph/9807045, doi:10.1016/S0927-6505(98)00064-4.

[76] J. Abraham et al. Anisotropy Studies around the Galactic Centre at EeV Energies with the Auger Observatory. *Astropart. Phys.*, 27:244–253, April 2007. arXiv:astro-ph/0607382, doi:10.1016/j.astropartphys.2006.11.002.

[77] N. Hayashida et al. Updated AGASA Event List above 4×10^{19} eV. *Astrophys. J.*, 522:225, August 1999. (appendix). arXiv:astro-ph/0008102.

[78] R. U. Abbasi et al. Study of Small-Scale Anisotropy of Ultra-High-Energy Cosmic Rays Observed in Stereo by the High Resolution Fly's Eye Detector. *Astrophys. J. Lett.*, 610:L73–L76, August 2004. arXiv:astro-ph/0404137, doi:10.1086/423303.

[79] J. Abraham et al. Correlation of the Highest-Energy Cosmic Rays with Nearby Extragalactic Objects. *Science*, 318:938–, November 2007. arXiv:0711.2256, doi:10.1126/science.1151124.

[80] J. Abraham et al. Correlation of the Highest-Energy Cosmic Rays with the Positions of Nearby Active Galactic Nuclei. *Astropart. Phys.*, 29:188–204, April 2008. arXiv:0712.2843, doi:10.1016/j.astropartphys.2008.01.002.

[81] M.-P. Véron-Cetty and P. Véron. A Catalogue of Quasars and Active Nuclei: 12th Edition. *Astron. Astrophys.*, 455:773–777, August 2006. doi:10.1051/0004-6361:20065177.

[82] R. U. Abbasi et al. Search for Correlations between HiRes Stereo Events and Active Galactic Nuclei. *Astropart. Phys.*, 30:175–179, November 2008. arXiv:0804.0382, doi:10.1016/j.astropartphys.2008.08.004.

[83] P. Abreu et al. Update on the Correlation of the Highest Energy Cosmic Rays with Nearby Extragalactic Matter. *Astropart. Phys.*, 34:314–326, December 2010. arXiv:1009.1855, doi:10.1016/j.astropartphys.2010.08.010.

[84] P. Abreu et al. Anisotropy and Chemical Composition of Ultra-High Energy Cosmic Rays using Arrival Directions Measured by the Pierre Auger Observatory. *J. Cosmol. Astropart. Phys.*, 6:22, June 2011. arXiv:1106.3048, doi:10.1088/1475-7516/2011/06/022.

[85] T. Abu-Zayyad et al. Search for Anisotropy of Ultrahigh Energy Cosmic Rays with the Telescope Array Experiment. *Astrophys. J.*, 757:26, September 2012. arXiv:1205.5984, doi:10.1088/0004-637X/757/1/26.

[86] P. Abreu et al. Antennas for the Detection of Radio Emission Pulses from Cosmic-Ray Induced Air Showers at the Pierre Auger Observatory. *J. Instr.*, 7:11P, October 2012. arXiv:1209.3840, doi:10.1088/1748-0221/7/10/P10011.

[87] J. Alvarez-Muñiz et al. The MIDAS Telescope for Microwave Detection of Ultra-High Energy Cosmic Rays. *Nucl. Instrum. Methods A*, 719:70–80, August 2013. arXiv:1208.2734, doi:10.1016/j.nima.2013.03.030.

[88] Y. Takahashi et al. The JEM-EUSO Mission. *New J. Phys.*, 11(6):065009, 2009. doi:10.1088/1367-2630/11/6/065009.

[89] R. Abbasi et al. Measurement of the Anisotropy of Cosmic-ray Arrival Directions with IceCube. *Astrophys. J. Lett.*, 718:L194–L198, August 2010. arXiv:1005.2960, doi:10.1088/2041-8205/718/2/L194.

[90] D. Chirkin and W. Rhode. Propagating Leptons through Matter with Muon Monte Carlo (MMC). *ArXiv e-prints*, July 2004. arXiv:hep-ph/0407075.

[91] R. Abbasi et al. The Design and Performance of IceCube DeepCore. *Astropart. Phys.*, 35:615–624, May 2012. arXiv:1109.6096, doi:10.1016/j.astropartphys.2012.01.004.

[92] R. Abbasi et al. Calibration and Characterization of the IceCube Photomultiplier Tube. *Nucl. Instrum. Methods A*, 618:139–152, 2010. arXiv:1002.2442, doi:10.1016/j.nima.2010.03.102.

[93] R. Abbasi et al. The IceCube Data Acquisition System: Signal Capture, Digitization, and Timestamping. *Nucl. Instrum. Methods A*, 601:294–316, 2009. arXiv:0810.4930, doi:10.1016/j.nima.2009.01.001.

[94] M. G. Aartsen et al. Measurement of South Pole Ice Transparency with the IceCube LED Calibration System. *Nucl. Instrum. Methods A*, 711(21):73 – 89, May 2013. arXiv:1301.5361, doi:10.1016/j.nima.2013.01.054.

[95] M. Ackermann et al. Optical Properties of Deep Glacial Ice at the South Pole. *J. Geophys. Res. (Atmos.)*, 111(D10):13203, jul 2006. doi:10.1029/2005JD006687.

[96] D. Pandel. Bestimmung von Wasser- und Detektorparametern und Rekonstruktion von Myonen bis 100 TeV mit dem Baikal-Neutrinoteleskop NT-72. Diploma Thesis, Humboldt-Universität zu Berlin, 1996.

[97] D. Heck et al. CORSIKA: A Monte Carlo Code to Simulate Extensive Air Showers. *Forschungszentrum Karlsruhe Report FZKA 6019*, 1998. URL: http://www-ik.fzk.de/corsika/.

[98] R. Abbasi et al. IceTop: The Surface Component of IceCube. *Nucl. Instrum. Methods A*, 700:188–220, February 2013. arXiv:1207.6326, doi:10.1016/j.nima.2012.10.067.

[99] E. Andres et al. The AMANDA Neutrino Telescope: Principle of Operation and First Results. *Astropart. Phys.*, 13:1–20, March 2000. arXiv:astro-ph/9906203, doi:10.1016/S0927-6505(99)00092-4.

[100] J. Ahrens et al. Muon Track Reconstruction and Data Selection Techniques in AMANDA. *Nucl. Instrum. Methods A*, 524:169–194, 2004. arXiv:astro-ph/0407044, doi:10.1016/j.nima.2004.01.065.

[101] P. Steffen. Direct-Walk: A Fast Track Search Algorithm without Hit Cleaning. Technical Report AMANDA-IR/20010801, DESY, June 2001. URL: http://www-zeuthen.desy.de/~steffenp/direct_walk/.

[102] D. A. Chirkin. *Cosmic Ray Energy Spectrum Measurement with the Antarctic Muon and Neutrino Detector Array (AMANDA).* PhD Thesis, University of California, Berkeley, 2003.

[103] G. W. Clark. Arrival Directions of Cosmic-Ray Air Showers from the Northern Sky. *Phys. Rev.*, 108(2):450–457, Oct 1957.

[104] M. Ambrosio et al. Moon and Sun Shadowing Effect in the MACRO Detector. *Astropart. Phys.*, 20(2):145 – 156, 2003. arXiv:astro-ph/0302586.

[105] P. Achard et al. Measurement of the Shadowing of High-Energy Cosmic Rays by the Moon: A Search for TeV-Energy Antiprotons. *Astropart. Phys.*, 23(4):411 – 434, 2005. arXiv:astro-ph/0503472.

[106] A. Oshima et al. The Angular Resolution of the GRAPES-3 Array from the Shadows of the Moon and the Sun. *Astropart. Phys.*, 33(2):97 – 107, 2010.

[107] P. Adamson et al. Observation in the MINOS Far Detector of the Shadowing of Cosmic Rays by the Sun and Moon. *Astropart. Phys.*, 34(6):457 – 466, 2011. arXiv:1008.1719.

[108] B. Bartoli et al. Observation of the Cosmic Ray Moon Shadowing Effect with the ARGO-YBJ Experiment. *Phys. Rev. D*, 84:022003, Jul 2011. doi:10.1103/PhysRevD.84.022003.

[109] R. Abbasi et al. Time-integrated Searches for Point-like Sources of Neutrinos with the 40-string IceCube Detector. *Astrophys. J.*, 732(1):18, 2011. arXiv:1012.2137.

[110] M. G. Aartsen et al. Observation of the Cosmic-Ray Shadow of the Moon with IceCube. *ArXiv e-prints*, May 2013. arXiv:1305.6811.

[111] P. Wallace. The SLALIB library. *ASP Conf. Ser.*, 61:481, 1994. URL: http://star-www.rl.ac.uk/star/docs/sun67.htx/sun67.html.

[112] R. A. Meyers and S. N. Shore, editors. *Encyclopedia of Astronomy and Astrophysics*. Academic Press, 1989.

[113] T. Neunhöffer. Estimating the Angular Resolution of Tracks in Neutrino Telescopes based on a Likelihood Analysis. *Astropart. Phys.*, 25(3):220 – 225, 2006. arXiv:astro-ph/0403367, doi:DOI:10.1016/j.astropartphys.2006.01.002.

[114] Ahn, E.-J. and others. Cosmic-Ray Interaction Event Generator SIBYLL 2.1. *Phys. Rev. D*, 80:094003, 2009. arXiv:0906.4113, doi:10.1103/PhysRevD.80.094003.

[115] J.G. Roederer. *Dynamics of Geomagnetically Trapped Radiation*. Springer-Verlag, 1970.

[116] C. C. Finlay et al. International Geomagnetic Reference Field: the Eleventh Generation. *Geophys. J. Int.*, 183(3):1216–1230, 2010. doi:10.1111/j.1365-246X.2010.04804.x.

[117] N. A. Tsyganenko. A Model of the Near Magnetosphere with a Dawn-Dusk Asymmetry 1. Mathematical Structure. *J. Geophys. Res.*, 107:1179, 2002. doi:10.1029/2001JA000219.

[118] N. A. Tsyganenko. A Model of the Near Magnetosphere with a Dawn-Dusk Asymmetry 2. Parameterization and Fitting to Observations. *J. Geophys. Res.*, 107:1176, 2002. doi:10.1029/2001JA000220.

[119] L. Dorman. *Cosmic rays in Magnetospheres of the Earth and other Planets*. Springer-Verlag, 2009.

[120] G. Di Sciascio and R. Iuppa. Simulation of the Cosmic Ray Moon Shadow in the Geomagnetic Field. *Nucl. Instrum. Methods A*, 630(1):301 – 305, 2011. doi:DOI:10.1016/j.nima.2010.06.197.

[121] J. H. Cobb et al. Observation of a Shadow of the Moon in the Underground Muon Flux in the Soudan 2 Detector. *Phys. Rev. D*, 61(9):092002, Mar 2000. arXiv:hep-ex/9905036.

[122] R. Abbasi et al. Search for a Diffuse Flux of Astrophysical Muon Neutrinos with the IceCube 40-string Detector. *Phys. Rev. D*, 84:082001, Oct 2011. doi:10.1103/PhysRevD.84.082001.

[123] T.-P. Li and Y.-Q. Ma. Analysis Methods for Results in Gamma-Ray Astronomy. *Astrophys. J.*, 272:317–324, Sep 1983.

[124] J. Braun, J. Dumm, F. De Palma, C. Finley, A. Karle, and T. Montaruli. Methods for Point Source Analysis in High Energy Neutrino Telescopes. *Astropart. Phys.*, 29(4):299 – 305, 2008. arXiv:0801.1604, doi:DOI:10.1016/j.astropartphys.2008.02.007.

[125] J. Blumenthal. Measurements of the Shadowing of Cosmic Rays by the Moon with the IceCube Neutrino Observatory. Diploma Thesis, Rheinisch-Westfälische Technische Hochschule (RWTH) Aachen, 2011.

[126] R. Reimann. Untersuchungen mit Graphik-Prozessoren (GPU) zur Messung der Abschattung kosmischer Strahlung durch den Mond in IceCube. Diploma Thesis, Rheinisch-Westfälische Technische Hochschule (RWTH) Aachen, 2011.

[127] W. W. Kinnison et al. Search for $\mu^+ \to e^+\gamma$. *Phys. Rev. D*, 25(11):2846–2868, Jun 1982. doi:10.1103/PhysRevD.25.2846.

[128] M.O. Wascko. *Study of the Shadow of the Moon in Very High Energy Cosmic Rays with the Milagrito Water Cherenkov Detector*. PhD Thesis, University of California, Riverside, 2001.

[129] J. Meeus. *Astronomical Algorithms*. Willmann-Bell, 1998.

[130] F. J. M Farley and J. R. Storey. The Sidereal Correlation of Extensive Air Showers. *Proc. Phys. Soc. Sect. A*, 67(11):996, 1954. URL: http://stacks.iop.org/0370-1298/67/i=11/a=306.

[131] K. M. Gorski et al. HEALPix – a Framework for High Resolution Discretization, and Fast Analysis of Data Distributed on the Sphere. *Astrophys. J.*, 622:759–771, 2005. arXiv:astro-ph/0409513, doi:10.1086/427976.

[132] R. Iuppa and G. Di Sciascio. Time-Average-Based Methods for Multi-angular Scale Analysis of Cosmic-Ray Data. *Astrophys. J.*, 766:96, April 2013. arXiv:1301.1833, doi:10.1088/0004-637X/766/2/96.

[133] G. F. Smoot and P. M. Lubin. Southern Hemisphere Measurements of the Anisotropy in the Cosmic Microwave Background Radiation. *Astrophys. J.*, 234:L83–L86, Dec 1979.

[134] R. Abbasi et al. Observation of Anisotropy in the Arrival Directions of Galactic Cosmic Rays at Multiple Angular Scales with IceCube. *Astrophys. J.*, 740:16, October 2011. arXiv:1105.2326, doi:10.1088/0004-637X/740/1/16.

[135] R. Abbasi et al. Measurement of the Anisotropy of Cosmic Ray Arrival Directions with IceCube. *Astrophys. J.*, 718:L194, 2010. arXiv:1005.2960, doi:10.1088/2041-8205/718/2/L194.

[136] R. Ansari and C. Magneville. Partial CMB Maps: Bias Removal and Optimal Binning of the Angular Power Spectrum. *Mon. Not. Roy. Astron. Soc.*, 405:1421–1430, 2010. arXiv:0910.4623.

[137] I. Szapudi, S. Prunet, D. Pogosyan, A. S. Szalay, and J. R. Bond. Fast CMB Analyses via Correlation Functions. *Astrophys. J.*, 548:L115, 2001. arXiv:astro-ph/0010256.

[138] G. Chon et al. Fast Estimation of Polarization Power Spectra using Correlation Functions. *Mon. Not. Roy. Astron. Soc.*, 350:914, 2004. arXiv:astro-ph/0303414, doi:10.1111/j.1365-2966.2004.07737.x.

[139] S. Tilav et al. Atmospheric Variations as Observed by IceCube. In *Proc. of the 31st ICRC*, Łódź, Poland, July 2009. arXiv:1001.0776.

[140] M. Amenomori et al. New Estimation of the Spectral Index of High-Energy Cosmic Rays as determined by the Compton-Getting Anisotropy. *Astrophys. J.*, 672:L53–L56, 2008. arXiv:0711.2002.

[141] M. Ackermann et al. Searches for Cosmic-Ray Electron Anisotropies with the Fermi Large Area Telescope. *Phys. Rev. D*, 82(9):092003, November 2010. arXiv:1008.5119, doi:10.1103/PhysRevD.82.092003.

[142] P.A. Caraveo et al. The Distance to the Vela Pulsar gauged with HST Parallax Observations. *Astrophys. J.*, 561:930–937, 2001. arXiv:astro-ph/0107282.

[143] G. Giacinti and G. Sigl. Local Magnetic Turbulence and TeV-PeV Cosmic Ray Anisotropies. *Phys. Rev. Lett.*, 109(7):071101, August 2012. arXiv:1111.2536, doi:10.1103/PhysRevLett.109.071101.

[144] P. C. Frisch et al. The Interstellar Magnetic Field Close to the Sun. II. *Astrophys. J.*, 760:106, December 2012. arXiv:1206.1273, doi:10.1088/0004-637X/760/2/106.

[145] H. Yan and A. Lazarian. Cosmic-Ray Propagation: Nonlinear Diffusion Parallel and Perpendicular to Mean Magnetic Field. *Astrophys. J.*, 673:942–953, February 2008. arXiv:0710.2617, doi:10.1086/524771.

[146] P. Desiati and A. Lazarian. Anisotropy of TeV Cosmic Rays and Outer Heliospheric Boundaries. *Astrophys. J.*, 762:44, January 2013. arXiv:1111.3075, doi:10.1088/0004-637X/762/1/44.

[147] A. Lazarian and P. Desiati. Magnetic Reconnection as the Cause of Cosmic Ray Excess from the Heliospheric Tail. *Astrophys. J.*, 722:188–196, October 2010. arXiv:1008.1981, doi:10.1088/0004-637X/722/1/188.

[148] P. Desiati and A. Lazarian. Cosmic Rays and Stochastic Magnetic Reconnection in the Heliotail. *Nonlin. Proc. Geophys.*, 19:351–364, June 2012. arXiv:1205.3783, doi:10.5194/npg-19-351-2012.

[149] L. O'C. Drury. The Problem of Small Angular Scale Structure in the Cosmic Ray Anisotropy Data. In *Proc. of the 33rd ICRC*, Rio de Janeiro, Brazil, July 2013. ID 0012. arXiv:1305.6752.

[150] A. U. Abeysekara et al. On the Sensitivity of the HAWC Observatory to Gamma-Ray Bursts. *Astropart. Phys.*, 35:641–650, May 2012. arXiv:1108.6034, doi:10.1016/j.astropartphys.2012.02.001.

[151] R. Abbasi et al. Observation of Anisotropy in the Galactic Cosmic-Ray Arrival Directions at 400 TeV with IceCube. *Astrophys. J.*, 746:33, February 2012. arXiv:1109.1017, doi:10.1088/0004-637X/746/1/33.

[152] M. G. Aartsen et al. Observation of Cosmic-Ray Anisotropy with the IceTop Air Shower Array. *Astrophys. J.*, 765:55, March 2013. arXiv:1210.5278, doi:10.1088/0004-637X/765/1/55.

[153] A. D. Erlykin and A. W. Wolfendale. Cosmic Ray Anisotropies to 5 PeV. *J. Cosmol. Astropart. Phys.*, 4:6, April 2013. arXiv:1303.2889, doi:10.1088/1475-7516/2013/04/006.

[154] Solar Cycle Progression. http://www.swpc.noaa.gov/SolarCycle/. Accessed: 2013-06-05.

[155] M. Pohl and D. Eichler. Understanding TeV-band Cosmic-Ray Anisotropy. *Astrophys. J.*, 766:4, March 2013. arXiv:1208.5338, doi:10.1088/0004-637X/766/1/4.

[156] M. Gurtner. *Cosmic Ray Anisotropy Studies with AMANDA*. PhD Thesis, Bergische Universität Wuppertal, 2013 (planned).

[157] K. Kotera, M. A. Perez-Garcia, and J. Silk. Strangelets and the tevÐpev cosmic-ray anisotropies. *Phys. Lett. B*, 2013. (in press). arXiv:1303.1186, doi:10.1016/j.physletb.2013.07.010.

[158] J. P. Harding. The TeV Cosmic-Ray Anisotropy from Local Dark Matter Annihilation. *ArXiv e-prints*, July 2013. arXiv:1307.6537.

[159] C. Curcio et al. Search for Anisotropies in the Arrival Directions of Primary Cosmic Rays with the KASCADE-Grande Experiment. In *Proc. of the 33rd ICRC*, Rio de Janeiro, Brazil, July 2013. ID 0094.

[160] A. Sidelnik et al. Measurement of the First Harmonic Modulation in the Right Ascension Distribution of Cosmic Rays detected at the Pierre Auger Observatory: Towards the Detection of Dipolar Anisotropies over a Wide Energy Range. In *Proc. of the 33rd ICRC*, Rio de Janeiro, Brazil, July 2013. ID 0739.

[161] E. S. Seo et al. Cosmic Ray Energetics And Mass for the International Space Station (ISS-CREAM). In *Proc. of the 33rd ICRC*, Rio de Janeiro, Brazil, July 2013. ID 0629.

[162] S. Torii et al. The Calorimetric Electron Telescope (CALET) for High Energy Astroparticle Physics on the International Space Station. In *Proc. of the 33rd ICRC*, Rio de Janeiro, Brazil, July 2013. ID 0147.